

DISSERTATION

THE OPTICAL, CHEMICAL, AND PHYSICAL PROPERTIES OF AEROSOLS AND
GASES EMITTED BY THE LABORATORY COMBUSTION OF WILDLAND FUELS

Submitted by

Gavin R. McMeeking

Department of Atmospheric Science

In partial fulfillment of the requirements

For the Degree of Doctor of Philosophy

Colorado State University

Fort Collins, Colorado

Fall 2008

UMI Number: 3346483

INFORMATION TO USERS

The quality of this reproduction is dependent upon the quality of the copy submitted. Broken or indistinct print, colored or poor quality illustrations and photographs, print bleed-through, substandard margins, and improper alignment can adversely affect reproduction.

In the unlikely event that the author did not send a complete manuscript and there are missing pages, these will be noted. Also, if unauthorized copyright material had to be removed, a note will indicate the deletion.

UMI[®]

UMI Microform 3346483

Copyright 2009 by ProQuest LLC.

All rights reserved. This microform edition is protected against unauthorized copying under Title 17, United States Code.

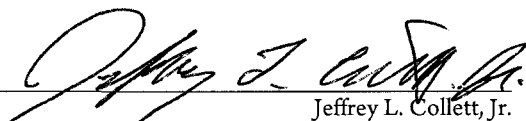
ProQuest LLC
789 E. Eisenhower Parkway
PO Box 1346
Ann Arbor, MI 48106-1346

COLORADO STATE UNIVERSITY

July 18, 2008

WE HEREBY RECOMMEND THAT THE DISSERTATION PREPARED UNDER OUR SUPERVISION BY GAVIN R. MCMEEKING ENTITLED THE OPTICAL, CHEMICAL, AND PHYSICAL PROPERTIES OF AEROSOL AND GASES EMITTED BY THE LABORATORY COMBUSTION OF WILDLAND FUELS BE ACCEPTED AS FULFILLING IN PART REQUIREMENTS FOR THE DEGREE OF DOCTOR OF PHILOSOPHY.

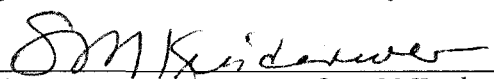
Committee on Graduate Work


Jeffrey L. Collett, Jr.


Christian D. Kummerow


Melissa L. Lunden


John Volckens


Adviser Sonia M. Kreidenweis


Department Head

ABSTRACT OF DISSERTATION

THE OPTICAL, CHEMICAL, AND PHYSICAL PROPERTIES OF AEROSOL AND GASES EMITTED BY THE LABORATORY COMBUSTION OF WILDLAND FUELS

Biomass burning is a major source of trace gases and particles that have a profound impact on the atmosphere. Trace gases emitted by fires include the greenhouse gases CO₂ and CH₄, as well as CO and volatile organic compounds that affect air quality. Particle emissions affect climate, visibility, the hydrologic cycle, and human health. This work presents measurements of trace gas and aerosol emissions from a series of controlled laboratory burns for various plant species common to North America. Over 30 fuels were tested through ~250 individual burns during the Fire Laboratory at Missoula Experiment.

Emission factors are presented as a function of modified combustion efficiency (MCE), a measure of the fire combustion conditions. The emissions of many trace gas and aerosol species depended strongly on MCE: smoldering-phase combustion dominated fires (low MCE) emitted roughly four times as much gas-phase hydrocarbon species and organic aerosols than flaming-phase dominated fires (high MCE). Inorganic aerosol emissions depended more strongly on plant species and components than on MCE.

Flaming-phase dominated fires tended to produce aerosol with high mass fractions of strongly light-absorbing elemental carbon. Smoldering-phase fires produced aerosol with large mass fractions of more weakly light absorbing organic carbon, but this material was found to have a strong wavelength dependence of absorption, greater than the inverse wavelength relationship typically assumed for light absorbing aerosol.

A two component model—featuring elemental carbon with a weak wavelength dependence but high mass-normalized absorption efficiency and organic carbon with a strong wavelength dependence but low mass-normalized absorption efficiency—is shown to represent the bulk absorption spectra of biomass burning aerosol. The results show that at wavelengths below ~450 nm, organic carbon light absorption could rival that of elemental carbon for aerosol dominated by organic carbon. If ignored, the light absorption by organic carbon can cause errors in predicted surface ultraviolet and visible radiation fluxes and photochemical photolysis rates in regions affected by biomass burning emissions. The dependence of spectral aerosol optical properties on combustion conditions means that fire behavior must be accurately assessed and predicted to ensure accurate emissions inventories and estimates of biomass burning atmospheric impacts.

Gavin R. McMeeking
Department of Atmospheric Science
Colorado State University
Fort Collins, CO 80523
Fall 2008

ACKNOWLEDGEMENTS

My adviser, Sonia Kreidenweis, has been instrumental to the completion of this work. She has been a constant source of support and guidance during my time in graduate school. I cannot thank her enough for her help over the years. I would also like to thank my committee for their time and service. Jeff Collett not only served on my committee, but has also acted almost as a co-adviser to me on the FLAME work presented here, but also on a number of other studies that did not make it into this dissertation. Tom Kirchstetter and Melissa Lunden were excellent and helpful hosts at LBNL, and provided me with another scientific perspective. Chris Kummerow and John Volckens had many helpful comments and asked many probing questions.

The FLAME results are the product of the efforts of many individuals in the Kreidenweis and Collett groups, as well as collaborators from Desert Research Institute, the Fire Sciences Laboratory, and the University of Nevada, Reno. The experiment ran smoothly thanks to the efforts of Kip Carrico and Cyle Wold, who seemed to be the first people anyone went to with a question about pumps, power, or lunch. My particular thanks to Kristin Lewis and Pat Arnott for sharing the photoacoustic data, Amy Sullivan and Mandy Holden for their analysis of the filter composition data, Steve Baker for gas canister data, Emily Lincoln for fuel property data, and Cyle Wold for real-time gas and scattering data. The work presented here has benefited from helpful discussions with Markus Petters, Kip Carrico, Hans Moosmüller, Amy Sullivan, Steve Baker, Tom Kirchstetter, Antony Chen, Tami Bond, and Judy Chow.

FLAME was supported by the Joint Fire Science Program under Project JFSP 05-3-1-06, which is funded by the United States Department of Agriculture and the National Park Service. We thank R. Cullin, D. Day, G. Engling, and L. Mazzoleni for their assistance in

collecting samples and P. Freeborn, E. Lincoln, and the FSL staff for their help during the burns. Charles McDade and Derek Day assisted with the IMPROVE samplers. FLAME fuels were provided by M. Chandler, J. Chong, D. Davis, G. Engling, G. Gonzalez, S. Grace, J. Hinkley, R. Jandt, R. Moore, S. Mucci, R. Olson, K. Outcalt, J. Reardon, K. Robertson, P. Spaine, and D. Weise.

My graduate work has been supported in part by a Graduate Research Environmental Fellowship (GREF) from the United States Department of Energy's Global Change Education Program (GCEP), the Department of Atmospheric Science at CSU, and by the National Park Service. GCEP supported my visits to LBNL, and countless workshops, orientations and conferences since my days as an undergraduate research student in the SURE program. My thanks to Mary Kinney and Milt Constantin for their help with travel, funding, and all the nuts and bolts.

Finally, I'd have long gone crazy without all my family and friends here and back home. Thanks Mom, Dad, Anne, Laura ... you've kept me sane (relatively speaking, of course). And thanks to everyone in the Kreidenweis group, indoor cats, and out.

TABLE OF CONTENTS

Chapter 1 Introduction.....	1
1.1 Roadmap	2
1.2 Light absorbing organic carbon (LAOC).....	3
1.3 Previous LAOC studies	5
1.4 Overview of several processes sensitive to aerosol optical properties	9
1.4.1 Tropospheric photochemistry.....	10
1.4.2 Visibility degradation.....	12
1.4.3 Climate.....	16
1.4.4 Thermal optical analysis-based carbonaceous aerosol measurements.....	17
1.4.5 Remote sensing applications.....	18
Chapter 2 Biomass burning	21
2.1 Combustion.....	22
2.2 Seasonal and spatial biomass burning patterns.....	26
2.3 Fire behavior and its relationship to emission factors.....	32
2.4 Global estimates of biomass burning emissions by species	34
2.5 Impacts of biomass burning emissions	36
Chapter 3 The Fire Laboratory at Missoula Experiment (FLAME)	41
3.1 Fuels.....	42
3.2 Experimental procedure.....	64
3.2.1 Burn procedure.....	64
3.2.2 Real-time gas measurements.....	68
3.2.3 Canister gas measurements.....	70
3.2.4 Annular denuder gas measurements.....	71
3.2.5 Ignition artifact testing.....	71
3.3 Fire behavior.....	73
3.3.1 Mass loss and energy release rates.....	73
3.3.2 Modified combustion efficiency.....	76
3.4 CO and CO ₂ emission factors	81
3.5 Hydrocarbon emission factors	85
3.6 Gas-phase nitrogen compound emissions	90
3.7 Summary	95
Chapter 4 Aerosol composition and optical properties.....	98
4.1 Aerosol measurements	102
4.1.1 Filter samples	102
4.1.2 Optical instruments	105
4.2 Aerosol composition.....	107
4.2.1 Bulk aerosol composition	107
4.2.2 Elemental and organic carbon composition.....	116
4.2.3 Inorganic species	121
4.3 Particulate emission factors	124
4.4 Carbon mass budgets and total observed organic carbon emissions.....	128
4.5 Aerosol optical properties.....	135
4.5.1 Fire-integrated emission factors and single-scattering albedo	138
4.5.2 Relationship with aerosols.....	141
4.5.3 Relationships between optical properties and aerosol composition (OC/EC).....	145

4.6 Summary	146
Chapter 5 A comparison of organic and elemental carbon measurement techniques	151
5.1 Methods for measuring organic and elemental carbon	151
5.2 Description of the filter samplers.....	153
5.3 Organic and elemental carbon analysis protocols	157
5.3.1 The IMPROVE_A protocol	157
5.3.2 The modified NIOSH 5040 / Sunset analyzer protocol	159
5.4 Organic gas adsorption artifacts.....	159
5.5 Total carbon, gravimetric and inorganic mass measurements	162
5.6 Measured organic and elemental carbon fractions.....	169
5.7 Summary and conclusions	176
Chapter 6 Wavelength dependence of aerosol light attenuation.....	179
6.1 Method.....	179
6.1.1 Filter samples and preparation.....	179
6.1.2 Optical system.....	180
6.1.3 Filter treatments	181
6.1.4 Filter samples from field measurements	182
6.2 Attenuation measurements.....	183
6.3 Quantifying the wavelength dependence of attenuation	186
6.4 Results for untreated samples.....	195
6.5 Results for front- and back-filter halves and treated filters.....	202
6.5.1 Front- and back-filter halves.....	202
6.5.2 Solvent-treatment results.....	205
6.6 Comparison of FLAME results with field measurements.....	212
6.7 Comparisons with photoacoustic spectrometer measurements during FLAME.....	218
6.8 Summary	227
Chapter 7 Linking aerosol optical properties, composition and fire combustion behavior.....	229
7.1 Angstrom exponent and aerosol composition	230
7.2 A simple, two-component model of Angstrom exponent behavior	233
7.3 Recommended optical properties for light absorbing organic carbon	238
7.3.1 Light attenuation.....	238
7.3.2 Light absorption	241
7.3.3 Optical properties of an OC-dominated sample.....	247
7.4 Angstrom absorption exponent and combustion conditions.....	249
7.4.1 Flaming and smoldering pine needle emissions	249
7.4.2 Fire-integrated MCE	250
7.5 Relationships between Angstrom exponents and single scatter albedo	251
7.6 Physical explanation of absorption spectral dependence – links to composition.....	254
7.7 Summary	260
Chapter 8 Conclusions and Future Work.....	263
8.1 Conclusions.....	263
8.2 Future work	267
References	271
Appendix A Carbonaceous aerosol measurements	290

LIST OF TABLES

Table 1.1 Carbonaceous aerosol terminology (from <i>Andreae and Gelencsér</i> [2006]).....	4
Table 1.2. Previous measurements of light absorbing organic carbon and spectrally dependent aerosol absorption in carbonaceous aerosols.....	7
Table 1.3 Selected remote sensing instruments/networks that provide aerosol information that depends on assumed aerosol optical properties.....	19
Table 2.1. Emission factors (g species per kg dry fuel matter) for selected particulate phase emissions and biomass burning classes.	34
Table 2.2 Biomass burning and biofuel emissions (from <i>Bond et al.</i> [2004])......	35
Table 3.1 Plant species that served as fuels during FLAME (all images are in the public domain).	44
Table 3.2 Individual burns during FLAME 1 and 2. Ignition methods are noted by: T = torch, P = pilot light, C = coils. Divide emission factors by fuel carbon fraction to obtain emission factors in units of g kg ⁻¹ carbon.	51
Table 3.3 Previously reported emission factors for CO, CO ₂ , CH ₄ , C ₂ H ₄ and C ₃ H ₆ from selected studies of natural fires and laboratory burns. Gases were measured using open path Fourier transform IR spectrometry (OP-FTIR), aircraft-based Fourier transform IR spectrometry (AFTIR), and gas chromatography with flame ionization detection (GC-FID).	81
Table 4.1 Previous laboratory studies of biomass combustion that reported aerosol composition, aerosol emission factors and/or optical properties (OC = organic carbon, EC = elemental carbon, f(RH) = relative humidity scattering growth factor, PAH = polycyclic aromatic hydrocarbon, HULIS = humic like substance, K = potassium, S = sulfur).....	100
Table 4.2 Filter-integrated combustion properties and aerosol emission factors during FLAME. TOOC = total observed organic carbon (see Section 4.4). ΣIN = sum of observed, water-soluble inorganic ions. RFM = sum of all speciated mass. See Appendix A for more emission factors.	109
Table 5.1 Configurations of the filter sampling systems that measured aerosol carbon composition during FLAME 1 chamber burns.	154
Table 6.1 Discrete measurement wavelengths of the optical instruments sampling during FLAME.	187
Table 6.2 Optical properties of LAOC produced by combustion sources. Discrete wavelengths or wavelength ranges are indicated by italic text. OC or mixed refers to the bulk classification of the carbonaceous material. PSAP = particle soot absorption photometer.....	200
Table 7.1 Elemental carbon mass attenuation efficiency (α_A), mass absorption efficiency (α_A) and the imaginary part of the complex refractive index (k) determined from Equation 7.5 at 870 nm. Elemental carbon data was taken from the NIOSH 5040/Sunset analyzer measurements from high volume filter samples (EC) or from the IMPROVE_A measurements from the IMPROVE PM _{2.5} filters (ECI).....	244
Table 7.2 Mean optical constants (± 1 standard deviation) for OC and EC measured on high volume filter samples during the FLAME 1 chamber burns. Optical data were taken	

from filter-based attenuation measurements and two photoacoustic spectrometers. OC mass absorption efficiencies were calculated by extrapolating the absorption from EC using an Angstrom absorption exponent of 0.8. The mass absorption efficiency of EC was calculated by assuming it was the only species responsible for absorption at 870 nm. The imaginary component of the complex refractive index (k) was calculated from Equation 7.5.....246

LIST OF FIGURES

Figure 1.1. Schematic depicting various classifications of carbonaceous aerosol and their relationship to molecular structure. Adapted from <i>Andreae and Gelencsér</i> [2006] and <i>Pöschl</i> [2003].	5
Figure 1.2 Illustration of several important atmospheric impacts of light absorbing organic carbon.	9
Figure 1.3 Global map of the percent decrease in $O_3 \rightarrow O(^1D)$ photolysis frequency, $J(O(^1D))$, predicted by the CHEM chemical transport model after including scattering and absorption of light by selected aerosol species. Taken from <i>Martin et al.</i> [2003].	12
Figure 1.4 Mean annual aerosol extinction (Mm^{-1}) determined from IMPROVE aerosol mass concentrations and mass extinction efficiencies for the period 1996-1998 (from the IMPROVE website: http://vista.cira.colostate.edu/IMPROVE).	14
Figure 1.5 Contours of annual mean organic matter (left) and ammonium sulfate (right) mass fractions of fine mass observed across the IMPROVE network during 2000. Aerosol organic matter is defined as measured organic carbon (OC) multiplied by 1.4 to account for non-carbon species in the organic material. (from <i>Malm et al.</i> [2004]; with permission).	15
Figure 2.1. Annual mean fire pixel density ($km^{-2} yr^{-1}$) adjusted for satellite overpass frequency from the Terra MODIS sensor over the period 2000-2005 (from <i>Giglio et al.</i> [2006b]; with permission).	27
Figure 2.2. Mean annual burned area derived from Terra MODIS active fire observations for the period 2001-2004. Blue shades correspond to regions where 0.1 to 1 percent of the $1^\circ \times 1^\circ$ pixel burned per year. Green shades correspond to 1 to 10 % pixel area yr^{-1} and orange/red shades indicate 30-100 % pixel area yr^{-1} . Uncertainties are on the order of 0.5 to 20 % pixel area yr^{-1} . Taken from <i>Giglio et al.</i> [2006b].	28
Figure 2.3 Mean fire radiative power (FRP, MW) retrieved from Terra MODIS observations over the period November 2000 to October 2005 (from <i>Giglio et al.</i> [2006a]; with permission).	31
Figure 2.4. Monthly distributions of major aerosol species in the northwest US during 2000 (in $\mu g m^{-3}$) (from <i>Malm et al.</i> [2004]; with permission).	39
Figure 3.1 Schematic of the US Forest Service Fire Sciences Laboratory combustion chamber and adjacent laboratory space, located in Missoula, Montana. Image is to scale. The locations of the fuel bed during stack and chamber burns are indicated.	65
Figure 3.2 Timeseries of excess CO_2 and CO (ppm) and THC (ppm C) mixing ratios measured in the stack during a test ethanol-only burn during FLAME 2 (burn 120). The fuel (ethanol) mass (in g C) measured using the fuel bed balance is plotted in gray on the right-hand-side axis. Time is in seconds from ignition time.	72
Figure 3.3 Instantaneous fuel mass loss rate (F) in $g s^{-1}$ and energy release rate (E) in kW as function of time for six burns during the FLAME 1 and 2 studies. Time is given as the time elapsed from ignition time. The transition time from flaming to smoldering combustion, determined visually, is shown by the vertical gray line. Note the left column	

plots feature a time period twice as long as that for the plots in the right column. Burn identifiers and fuel names given on each plot correspond values given in Table 3.2..... 74

Figure 3.4 Maximum instantaneous rates of energy release (E , kW) versus fuel mass loss (F , g s^{-1}) for FLAME stack burns. The linear least-squares regression to data is shown along with the coefficient of variation. Frequency distributions of the parameters are also shown..... 76

Figure 3.5 Excess CO and CO₂ mixing ratios (ppm) and modified combustion efficiency (MCE) as a function of time for six stack burns. CO₂ is plotted against the left-hand side axis and CO is plotted against the right-hand side axis. MCE is plotted against the outermost left-hand side axis. 78

Figure 3.6 Median modified combustion efficiencies (MCE) for fuel groups burned during FLAME 1 and 2, ranked in order of decreasing MCE. Horizontal bars indicate the range of MCE observed within a fuel class. Each median value is shaded to indicate the mean fuel moisture of the fuel group. Starred fuel groups (*) included flaming- and smoldering-phase only, heading and backing experiments..... 80

Figure 3.7 Real-time emission factors (EF) for CO, CO₂, NO (g kg^{-1} fuel) and THC (g C kg^{-1} fuel) for six sample burns. THC and NO emission factors are multiplied by a factor of five and ten, respectively. The transition from flaming to smoldering, identified visually, is indicated by the vertical gray line..... 83

Figure 3.8 Excess CO, CO₂ and total hydrocarbon (THC) mixing ratios measured by the real-time gas analyzers versus canister sample measurements by gas chromatography. The real-time THC measurements (in ppm C) are compared with the sum of C₂₋₄ hydrocarbon mixing ratios (in ppm C). FLAME 1 data are plotted with red circles, FLAME 2 data with blue squares. The dashed lines show the 1:1 line, and the solid lines give the linear least-squares regression of the real-time data onto the canister data..... 87

Figure 3.9 Emission factors for hydrocarbon gas species calculated from canister gas chromatography measurements as a function of modified combustion efficiency (MCE). Black lines indicate the linear least-squares regression of the emission factors onto MCE. Colored lines indicate regressions reported by previous studies. *Yokelson et al.* [2003] only observed MCE ranging from 0.92–0.98, but I have extended the regression over the range of MCE observed during FLAME. 90

Figure 3.10 Molar ratios of NH₃-to-NO_x emissions as a function of modified combustion efficiency (MCE) during FLAME and several biomass burning field and laboratory experiments. FLAME data are shaded to reflect the magnitude of the NO_x measurement, and therefore reflect the confidence in the measured ratio. Symbols plotted in red indicate laboratory measurements, symbols plotted in blue indicate field measurements, and symbols in green are representative values for savanna, tropical and extratropical forest fires given by *Andreae and Merlet* [2001]. The dashed line indicates the fit provided by *Goode et al.* [2000] for several sets of laboratory and field biomass burning measurements. The solid line gives the least-squares regression to FLAME data where total NO_x mass emissions were greater than 0.6 g NO. Note that this figure is truncated to better illustrate the majority of NH₃:NO_x data from our study and the

literature. A maximum NH ₃ :NO _x ratio of ~12 at an MCE of 0.82 was reported by Christian et al. [2003].	93
Figure 3.11 Scatter plot comparing fire-integrated NO and NO ₂ emission factors during FLAME, expressed as g NO kg ⁻¹ dry fuel consumed. NO and NO ₂ emission factors reported by three recent studies are also plotted. <i>Chen et al.</i> [2007] and <i>Freeborn et al.</i> [2008] examined emissions from several North American fuels burned at the Fire Science Laboratory and used the same NO _x analyzer featured here. Data presented by <i>Yokelson et al.</i> [2007a] were collected with an aircraft-based Fourier Transform Infrared Spectrometer (FTIR) over fires in Brazil. The 1:1 (solid) and 1:10 (dashed) lines are indicated.	96
Figure 4.1 The combustion chamber at the USFS Fire Sciences Laboratory in Missoula, Montana. The locations of the high volume and URG samplers and the fuel beds during chamber and stack experiments are indicated.	103
Figure 4.2 Schematic showing locations of optical instruments during FLAME stack (left) and chamber (right) burns. The layout for FLAME 1 is shown on the top half of the figure and the layout for FLAME 2 is shown in the bottom half.	107
Figure 4.3 Ternary plot comparing mass fractions of elemental carbon (EC), organic carbon (OC) and major inorganic species (K ⁺ , Na ⁺ , NH ₄ ⁺ , Mg, Ca, Cl, SO ₄ ²⁻ , NO ₃ ⁻).	114
Figure 4.4 Elemental-to-total carbon (EC/TC) ratios observed for emissions from (a) ponderosa pine and (b) chaparral/desert shrub fuels versus fire-integrated modified combustion efficiency (MCE). Ponderosa pine data include needle, branch, needles and branches, needle litter and duff burns. Samples collected during only flaming (high MCE) and smoldering (low MCE) combustion of ponderosa pine needles are indicated by the filled circles. Results reported by several laboratory-based biomass burning emissions studies listed in Table 4.1 are shown for comparison.	119
Figure 4.5 Emission factors as a function of modified combustion efficiency for: a) organic carbon (OC); b) elemental carbon (EC); c) total carbon (TC); d) chloride; e) potassium; f) total inorganics; g) reconstructed fine mass; and h) reconstructed fine mass including species associated with OC.	125
Figure 4.6 Carbon mass consumed versus carbon mass emitted during FLAME.	129
Figure 4.7 Combustion efficiency (CE) versus modified combustion efficiency (MCE) during FLAME.	130
Figure 4.8 Particulate emission factors as a function of combustion efficiency (CE) following Figure 4.5.	132
Figure 4.9 Total observed organic carbon (TOOC) emission factors during FLAME as a function of a) modified combustion efficiency and b) combustion efficiency.	134
Figure 4.10 Semi-log scatter plot showing organic carbon (OC) fractions of total observed organic carbon (TOOC) as a function of OC mass concentrations during FLAME.	135
Figure 4.11 Timeseries for uncorrected aerosol scattering coefficients measured at 450, 550, and 700 nm using a TSI 3-λ nephelometer and at 532 nm using a reciprocal nephelometer (colored lines). Aerosol light absorption at 532 nm measured using a photoacoustic spectrometer is shown by the thick black line. All optical data are plotted against the left-hand side axis. The black crosses indicate the real-time modified combustion efficiency,	

plotted against the right-hand side axis. The vertical gray line indicates the transition from flaming to smoldering combustion determined from visual observations of the fire. 138

Figure 4.12 Mass scattering efficiency ($\lambda = 532 \text{ nm}$) as a function of modified combustion efficiency for filter-integrated burns during FLAME 1..... 142

Figure 4.13 a) Mass scattering efficiency ($\lambda = 532 \text{ nm}$) and b) total carbon mass fraction as a function of Ångström exponent calculated from scattering measured at $\lambda = 450$ and 700 nm during FLAME 1..... 144

Figure 4.14 Mass absorption efficiency ($\lambda = 532 \text{ nm}$) as a function of modified combustion efficiency during FLAME 1. 145

Figure 4.15 Single scattering albedo at $\lambda = 532 \text{ nm}$ as a function of elemental carbon-to-total carbon ratios. 146

Figure 5.1 Carbon mass concentrations ($\mu\text{g C m}^{-3}$) measured on the primary and secondary IMPROVE $\text{PM}_{2.5}$ filters during FLAME 1 and 2. Organic carbon (OC) concentrations are shown by red circles and elemental carbon (EC) concentrations are shown by black squares. 161

Figure 5.2 Organic carbon (OC) measured on secondary (backup) IMPROVE filters normalized by OC measured on primary (front) IMPROVE filters as a function of the primary OC mass concentration during the FLAME 1 and FLAME 2 chamber burns. The sample with the unusually short collection time is highlighted in red. 163

Figure 5.3 Scatter plots showing total carbon (TC) in $\mu\text{g C m}^{-3}$ for each measurement technique and/or filter sampler during FLAME. Each scatter plot shares axes with the corresponding plots in its row or column. To find the comparison between any two measurements, locate the column and row for each technique. For example, plot C compares TC measured on IMPROVE PM_{10} samples using the IMPROVE_A protocol to TC measured by the semi-continuous Sunset analyzer using the modified NIOSH 5040 protocol. The least-squares linear regression and coefficient of determination (r^2) is given for each data pair. The dashed black line is the 1:1 line. 165

Figure 5.4 Gravimetric mass of particles with aerodynamic diameters less than $10 \mu\text{m}$ (PM_{10}) compared to gravimetric mass of particles with diameters less than $2.5 \mu\text{m}$ ($\text{PM}_{2.5}$) for IMPROVE filter samples during FLAME 1 and 2 chamber burns. Data for the duff emissions are highlighted by filled blue circles (see text for details). 166

Figure 5.5 The sum of $\text{PM}_{2.5}$ inorganic species measured on IMPROVE versus URG filter samples during FLAME 1 and 2..... 167

Figure 5.6 $\text{PM}_{2.5}$ mass reconstructed from Hi-vol carbon measurements and URG inorganic species (black circles) and $\text{PM}_{2.5}$ mass reconstructed from IMPROVE carbon and inorganic species (red squares) versus gravimetric mass measured on IMPROVE $2.5 \mu\text{m}$ samples during FLAME 1 and 2. Organic carbon concentrations have been multiplied by a factor of 1.5 to account for non-carbon species present in the organic aerosol..... 168

Figure 5.7 Scatter plot showing elemental carbon (EC) divided by total carbon (TC) for each measurement technique and/or filter sampler during FLAME. The short, dashed black line gives the 1:1 line and the two dashed gray lines show points where one measurement is double the magnitude of the other..... 170

Figure 5.8 Reflectance-based pyrolyzed organic carbon (POC) versus elemental carbon (EC) measured on the IMPROVE PM _{2.5} filter samples during FLAME. Each value is normalized by the corresponding total carbon (TC) concentration measured on the filter.	172
Figure 5.9 Transmittance- and reflectance-based pyrolyzed organic carbon (TPOC, RPOC) concentrations ($\mu\text{g C m}^{-3}$) measured on the IMPROVE PM _{2.5} filter samples using the IMPROVE-A protocol. The solid line shows the 1:1 line. Error bars indicate the uncertainty in each measurement calculated from Equation 5.2.....	173
Figure 5.10 Elemental carbon (EC) fractions of total carbon (TC) measured on IMPROVE PM _{2.5} filters. EC was corrected for pyrolyzed organic carbon using reflectance (EC_R) and transmittance (EC_T). The short dashed line indicates the 1:1 line and the long dashed lines show regions where one measurement disagreed with the other by a factor of two.	174
Figure 5.11 Transmittance- and reflectance-based pyrolyzed organic carbon (TPOC, RPOC) concentrations ($\mu\text{g C m}^{-3}$) versus apparent elemental carbon (EC_a) concentrations measured on the IMPROVE PM _{2.5} secondary filters. EC_a is defined as the carbon evolving at the three EC temperature plateaus and is not corrected for RPOC. TPOC is shown by the black circles and RPOC is given by the red squares. The solid line gives the 1:1 line.	175
Figure 6.1 Spectrum of light intensity (counts second ⁻¹) emitted by the light emitting diode (LED) bundle that served as the light source during the FLAME 2 sample attenuation measurements.....	181
Figure 6.2 Attenuation plotted as a function of wavelength (nm) for two punch samples taken from the FLAME 1 longleaf pine needle chamber burn (burn 115, filter 51). There are actually five spectra plotted, but individual replicates from single punches are indistinguishable.	185
Figure 6.3 Values of the Angstrom absorption exponent (\AA_a) predicted by Mie theory for size distributions of varying count median diameter (nm) for a range of imaginary refractive indices. The real part of the refractive index is fixed at 1.55 and the geometric standard deviation of the size distribution is 1.5. Reprinted with permission from Bond [2001].	188
Figure 6.4 Attenuation as a function of wavelength (bottom) and $\ln(\text{ATN})$ as function of $\ln(\lambda)$ (top) measured for a ceanothus emissions sample (burn 118, filter 54). The solid red line indicates the linear least-squares regression to the log-transformed data in both coordinate systems. The regression coefficient (\AA_{ATN}) and 95% confidence limits are indicated. The dashed line indicates ATN predicted for $1/\lambda$ relationship extended from the measured $\text{ATN}(\lambda_r = 880 \text{ nm})$	189
Figure 6.5 Attenuation as a function of wavelength (bottom) and $\ln(\text{ATN})$ as function of $\ln(\lambda)$ (top) measured for an Alaskan duff emissions sample (burn 106, filter 42). The red line indicates the linear least-squares regression to the log-transformed data for $360 < \lambda < 1000 \text{ nm}$ in both coordinate systems. The green line shows the fit given by a non-linear regression to the data assuming a power-law functionality. The blue line indicates is a non-linear regression fit, but restricted to the UV-visible (UV-VIS) wavelength range:	

360 < λ < 750 nm. The orange line is the fit provided by the weighted sum of two power laws fit to different regions of the spectrum (see text for details). The dashed line indicates ATN predicted for $1/\lambda$ relationship extended from the measured ATN($\lambda_r = 880$ nm). The solid circles indicate $\ln(ATN)$ values at $\lambda = 370$ and 880 nm..... 191

Figure 6.6 Scatter plots comparing Ångström attenuation exponents obtained from a) linear regression of log-transformed attenuation (ATN) as a function of log-transformed wavelength (\AA_{ATN-L}) and non-linear regression of ATN(λ) assuming a power-law functionality (\AA_{ATN}), b) non-linear regression over the UV-VIS and entire measurement spectra, c) non-linear regression and \AA_{ATN} calculated from Equation 4.2 at $\lambda = 405$ and 870 nm, and d) non-linear regression and the low-wavelength exponent (\AA_l) obtained from non-linear regression assuming ATN is a function of weighted power laws (see text for details). 194

Figure 6.7 Attenuation coefficients (ATN) as a function of wavelength for three biomass burning aerosol samples collected during FLAME: ponderosa pine duff (top), lodgepole pine needle and litter (middle) and chamise (bottom). Dashed lines give the attenuation coefficient predicted from a $1/\lambda$ attenuation dependence on wavelength normalized to ATN at a reference wavelength of 880 nm. Inset photographs are pictures of each filter sample taken in the laboratory with a digital camera 196

Figure 6.8 Attenuation Ångström exponents (\AA_{ATN}) observed for untreated, bulk filter samples of biomass burning emissions. Attenuation as a function of wavelength data for each sample were fit to a power-law using non-linear regression to obtain values of \AA_{ATN} . See Chapter 3 for a complete description of the fuels. Data are ranked in order of increasing \AA_{ATN} 198

Figure 6.9 (top) Light attenuation measured as a function of wavelength on whole (thick black), front-half (thin black) and back-half (red) filter samples of burning rice straw emissions (burn 104, filter 40). The blue line gives the difference between ATN measured on the front- and back-filter halves, which an estimate of the ATN due to particles (see text for details). The dashed line shows the ATN predicted by a $1/\lambda$ dependence based on ATN measured at $\lambda = 880$ nm on the front-filter half. (bottom) Fraction of total ATN attributable to an estimate of ATN by gas-phase species plotted as a function of wavelength for the same sample shown in (a)..... 204

Figure 6.10 Attenuation (ATN) versus wavelength for whole filters (thick black line) and the front- (thin black line) and back-halves (red line) of filters for eight different fuels burned during FLAME. The difference between the front and back filter ATN measurements is shown by the blue line. The dashed line indicates the ATN expected from a $1/\lambda$ relationship extended from ATN measured on the front filter half at 880 nm. 206

Figure 6.11 Attenuation (ATN) versus wavelength (a) for the untreated rice straw emissions sample (black line) and samples treated with acetone (red and orange lines), hexane (green line), and de-ionized water (blue line). The dashed line in (a) indicates ATN predicted from a $1/\lambda$ relationship from ATN measured at $\lambda = 880$ nm on the untreated sample. ATN normalized by the untreated ATN values is also plotted as a function of wavelength (b), with the same color scheme..... 208

- Figure 6.12 Attenuation (ATN) versus wavelength for untreated (black line) and filter samples treated with acetone (red line), hexane (green line) and de-ionized water (blue line). The dashed line indicates the ATN expected from a $1/\lambda$ relationship extended from ATN measured on the untreated filter at 880 nm.210
- Figure 6.13 Attenuation (ATN) plotted as a function of wavelength for two filter samples collected in Houston, Texas on 19 September 2006 (black) and 20 August 2006 (red). The start times for each filter collection period are indicated. The dashed lines give ATN predicted from ATN at 880 nm with a $1/\lambda$ wavelength dependence.213
- Figure 6.14 Ångström attenuation exponents (\hat{A}_{ATN}) determined by non-linear regression (a) and attenuation (ATN) measured at 880 nm versus time for filter samples collected during TexAQS – GoMACCS. The dashed line indicates $\hat{A}_{ATN} = 1$, the values expected for pure black carbon. ATN data are plotted as horizontal lines matching the start and end sample collection times. The two samples shown in Figure 6.13 are highlighted in red. The empty blue circles indicate ATN observed for field blanks collected during the study. Filter samples from the period 27 August to 15 September were not available..214
- Figure 6.15 Attenuation plotted against wavelength for two filter samples collected at Blodgett Forest Research Station.216
- Figure 6.16 Aethalometer measured \hat{A}_{ATN} ($\lambda = 370, 880$ nm) observed at Blodgett Forest Research Station (a) and Yosemite National Park (b) in 2002. The dashed line indicates $\hat{A}_{ATN} = 1$, equivalent to a $1/\lambda$ dependence of ATN.....217
- Figure 6.17 Ångström exponents from attenuation measured on filters (\hat{A}_{ATN}) and absorption measured *in situ* using photoacoustic spectrometers (\hat{A}_a). Exponents were calculated using Equation 4.2 for ATN/absorption measured at wavelengths of 405 and 870 nm (filled circles) and 532 and 870 nm (hollow circles). Error bars represent $\pm 5\%$ uncertainty, reported by *Lewis et al.* [in press]. The 1:1 line is also indicated.....222
- Figure 6.18 Values of the particle loading factor ($R(ATN)$) for correcting Aethalometer ATN coefficients to absorption coefficients, assuming a ‘shading factor’, $f = 1.2$ as a function of ATN (black line). Corrected ATN is shown in red on the right axis, assuming the filter scattering correction factor (C^*) is equal to one. The dashed red line indicates the values where $ATN = ATN$ corrected, i.e. $R(ATN) = 1$225
- Figure 6.19 Scatter plots comparing attenuation (ATN) Ångström exponents (\hat{A}_{ATN}) calculated from measured ATN on untreated FLAME bulk filter samples using Equation 4.2 at the wavelength pairs indicated in the axis labels. The wavelength pairs correspond to the measurement wavelengths of: a) photoacoustic spectrometer and $2-\lambda$ Aethalometer, b) short and long wavelength regions of the spectrum, c) photoacoustic and TSI integrating nephelometer, and d) two sets of photoacoustic measurements. Absorption Ångström exponents determined from photoacoustic measurements (as opposed to ATN at the same wavelengths) are also shown in d) as red squares. The 1:1 relationships are indicated by a dashed lines.226
- Figure 7.1 Ångström attenuation exponents (A_{ATN}) for bulk FLAME samples versus elemental-to-total carbon (EC/TC) ratios (measured using the NIOSH 5040/Sunset analyzer protocol) on a) normal coordinates and b) semi-log coordinates. The dashed line in a) indicates an EC/TC ratio of zero, i.e., no EC above detection limits.....231

Figure 7.2 Elemental-to-total carbon (EC/TC) ratios measured on IMPROVE PM _{2.5} filters using the IMPROVE_A thermal optical analysis protocol versus Angstrom attenuation exponent (A_{ATN}). Data are plotted on the same axes as Figure 7.2.	233
Figure 7.3 Mass attenuation efficiency (α_{ATN}) spectra for organic carbon (OC) and elemental carbon (EC) calculated assuming Angstrom attenuation exponents of 5.0 for OC and 0.75 for EC and α_{ATN} for OC is 0.1 m ² g ⁻¹ and for EC is 10 m ² g ⁻¹ at 550 nm.....	235
Figure 7.4 Attenuation as a function wavelength calculated from Equation 7.1 for a two-component aerosol consisting of organic (OC) and elemental carbon (EC) in a 9:1 ratio (elemental-to-total carbon ratio of 0.1). The attenuation for the two-component mixture is shown by the thick red line, the attenuation from EC in the mixture is shown by the thin black line, and the attenuation from OC in the mixture is shown by the thin green line. The fraction of the total ATN due to ATN by OC is shown by the dashed green line and plotted on the right-hand side axis.	236
Figure 7.5 Measured (symbols) and modeled attenuation Angstrom exponents (A_{ATN}) as a function of elemental carbon / total carbon ratios measured on FLAME Hi-vol samples using a modified NIOSH/Sunset analyzer thermal optical analysis protocol. The solid blue line gives the modeled A_{ATN} values for the best-fit parameters to the data (see text). The dashed blue lines represent upper and lower extremes.	237
Figure 7.6 Measured light attenuation coefficients (b_{ATN}) for the bulk sample (black line) and estimates of the OC and EC b_{ATN} (solid red and blue lines, respectively) and mass attenuation efficiencies (α_{ATN} , dashed red and blue lines, respectively) as functions of wavelength for ponderosa pine needle emissions (filter 35) during FLAME 1.....	239
Figure 7.7 Light attenuation coefficients (b_{ATN}) measured on FLAME 1 filter samples versus light absorption coefficients (b_A) measured by two photoacoustic spectrometers at 405, 532 and 870 nm. The solid, dashed, and dotted lines indicate $b_{ATN}:b_A$ ratios of 1:1, 2:1 and 5:1, respectively.....	242
Figure 7.8 Attenuation as a function of wavelength measured on filter samples of ponderosa pine needle flaming combustion emissions (red lines) and smoldering combustion emissions (blue lines). Non-linear regression power law fits to the data are shown by the dashed lines and the attenuation Ångström exponents are also given for each sample.....	250
Figure 7.9 Attenuation Angstrom exponent versus fire- and filter-integrated modified combustion efficiency for selected FLAME samples/burns. Solid line indicates the linear least-squares regression to the data.	252
Figure 7.10 Absorption Ångström exponents calculated from absorption measured at 405 and 870 nm as a function of single scattering albedo (ω_0) at 405 nm (adapted from <i>Lewis et al.</i> [in press]). Measurements for emissions from the flaming and smoldering-phase combustion of ponderosa pine needles are highlighted.....	253
Figure 7.11 Tauc plot illustrating the band gap relationship with $E_g = 1.85$ eV with the measured spectra for Alaskan duff emissions (see text for details).	258
Figure 7.12 Mass-normalized bulk absorption efficiency (β) as a function of wavelength for: a) a band gap, $E_g = 1.65$ eV (recommended by <i>Sun et al.</i> [2007], b) filter-based measurements of the acetone-soluble fraction of OC in aerosol collected over savannah fires in Africa, reported by <i>Kirchstetter et al.</i> [2004], c) study-averaged FLAME OC	

absorption efficiency determined from filter measurements, d) study-averaged FLAME
OC absorption efficiency determined from photoacoustic spectrometer measurements,
and e) three spectra measured for OC-dominated Alaskan dust emissions collected
during FLAME 1 and 2.261

NOTATION INDEX

A	light absorption
A_f	filter area
ANOVA	analysis of variance
ATN	light attenuation (through filter)
ATN_g	light attenuation due to gases
ATN_{EC}	light attenuation due to elemental carbon
ATN_{OC}	light attenuation due to organic carbon
\dot{A}_a	light absorption Ångström exponent
\dot{A}_s	light scattering Ångström exponent
\dot{A}_{ATN}	light attenuation Ångström exponent (determined by non-linear regression)
\dot{A}_{ATN-L}	light attenuation Ångström exponent determined by linear regression
α_A	mass absorption efficiency
α_{ATN}	mass attenuation efficiency
α_e	mass extinction efficiency
b_a	light absorption coefficient
b_{aeth}	corrected aethalometer light absorption coefficient
b_{ap}	aerosol light absorption coefficient
b_{ag}	gas light absorption coefficient
b_{ATN}	light attenuation coefficient
b_{ep}	aerosol light extinction coefficient
b_{eg}	gas light extinction coefficient
b_{sp}	aerosol light scattering coefficient
b_{sg}	gas light scattering coefficient
BC	black carbon
BFRS	Blodgett Forest Research Station
C	aethalometer correction factor for multiple-light scattering by filter

	fibers
C_i	carbon fraction from IMPROVE thermal optical analysis measurements
C^*	modified Aethalometer correction factor that includes particle light scattering
c_p	constant-pressure specific heat of air
CE	combustion efficiency
CMD	count median diameter
CTM	chemical transport model
CV	coefficient of variation
D_{ae}	particle aerodynamic diameter
D_p	particle physical diameter
DI	de-ionized water
E	photon energy
E_t	fire thermal energy release rate
E_{tot}	total thermal energy released
EC	elemental carbon
EC_a	apparent elemental carbon
EC_r	reflectance-corrected elemental carbon
EC_t	transmittance-corrected elemental carbon
EFX	emission factor for species 'X'
FLAME	Fire Laboratory at Missoula Experiment
F	fuel bed mass loss rate
F_a	actinic flux
FID	flame ionization detection
GC-FID	gas chromatography with flame ionization detection
H	heat of combustion
H_f	fire-integrated heat of combustion
Hi-vol	high volume filter sampler
HULIS	humic-like substance

IDL	Interface Design Language
IMPROVE	Interagency Monitoring of Protected Visual Environments
k	imaginary component of the complex refractive index
λ	wavelength
I	intensity
I_0	blank intensity
I_r	reference intensity
$I_{r,0}$	reference intensity at time of blank measurement
LAOC	light absorbing organic carbon
LBNL	Lawrence Berkeley National Laboratory
LED	light emitting diode
LOD	level of detection
m	mass
m_0	initial fuel mass (prior to burn)
m_f	final fuel/ash mass (after burn)
MCE	modified combustion efficiency
MDL	minimum detection level
MFC	Mass Flow Controller
MILAGRO	Megacity Initiative: Local and Global Research Observations
n	real component of the complex refractive index
NIR	near infrared
NIST	National Institute for Standards and Technology
OC	organic carbon
ω_0	single scattering albedo
PM _{2.5}	particulate matter with aerodynamic diameter < 2.5 μm
PM ₁₀	particulate matter with aerodynamic diameter < 10 μm
POC	pyrolyzed organic carbon
POM	particulate organic mass
PSAP	particle soot absorption photometer

PTR-MS	proton transfer reaction mass spectrometry
Q	flow rate
Q_a	light absorption efficiency
Q_s	light scattering efficiency
R(ATN)	correction factor for Aethalometer data accounting for the ‘shadowing’ effect
R-POC	reflectance-measured pyrolyzed organic carbon
RFM	reconstructed fine mass
r^2	coefficient of determination
ρ_{air}	air density
σ_a	light absorption cross section
σ_s	light scattering cross section
SAFARI	South African Regional Science Initiative
SOA	secondary organic aerosol
t_s	sample time
T	temperature
T_s	stack air temperature
T-POC	transmittance-measured pyrolyzed organic carbon
TexAQSGoMACCS	Texas Air Quality Field Study II – Gulf of Mexico Atmospheric Composition and Climate Study
TC	total carbon
TOR	thermal optical reflectance
TOT	thermal optical transmittance
Tr	light transmission
UV	Ultraviolet
v_s	stack air velocity
VOC	Volatile Organic Compound
WSOC	water-soluble organic carbon

Chapter 1 Introduction

Biomass burning is a dynamic process that emits large concentrations of trace gases and particles to the atmosphere, but the mechanisms that control these emissions and their properties are poorly quantified and understood [*Reid et al., 2005b*]. Fires emit light absorbing organic carbon (LAOC), which may have large impacts on surface radiation fluxes in the ultraviolet and visible spectral regions, that are not currently accounted for in models or included in emissions inventories [*Kirchstetter et al., 2004*].

The focus of this work is quantifying the relationships between biomass burning emissions, including LAOC, and fire combustion conditions for a large range of plant species common to fire-impacted regions in the United States. Previous work has shown that these emissions have major impacts on climate, visibility and tropospheric chemistry, but have not included the effects of LAOC [e.g., *Kirchstetter et al., 2004; Roden et al., 2006*]. Ignoring its impacts will lead to errors in predicted climate forcing, tropospheric trace species concentrations, visibility and measurements of atmospheric species [*Andreae and Gelencser, 2006*]. This work seeks to reduce the uncertainties in the optical properties of LAOC in biomass burning emissions by examining data from a unique series of controlled biomass burning experiments. It relates these properties to combustion conditions and fuel in the aim of including them in chemical transport, radiative transfer and visibility models.

1.1 Roadmap

The remainder of this introduction gives an overview of processes in the atmosphere that can be affected by biomass burning emissions, with a focus on the impacts of light absorbing organic carbon. Chapter 2 provides background on the spatial and temporal distributions of biomass burning on global scales and discusses current estimates of biomass burning emission impacts on climate and visibility.

Chapter 3 introduces the Fire Lab at Missoula Experiments (FLAME 1 and 2), which took place in late-spring in 2006 and 2007 at the Fire Science Laboratory in Missoula, Montana. These two studies provided the bulk of biomass burning aerosol samples I investigate here. It includes descriptions of the fuels, including their origin and moisture conditions and quantifies their combustion behavior. It also organizes fuels into rough classes dominated by flaming or smoldering combustion, or a mixture of the two. The chapter also gives a brief overview of the instrumentation that operated during each of the studies and the data they provided. It also characterizes burns by their combustion behavior and reports observed emissions of trace gases.

In Chapter 4, I present observations of bulk aerosol properties, including mass concentrations, composition, light scattering, and light absorption. Chapter 5 discusses the OC and EC results in greater detail with a focus on possible measurement artifacts and uncertainties.

Chapter 6 introduces the wavelength-dependent light absorption measurements that are used to identify and characterize LAOC in the FLAME samples. This chapter discusses the effect of different solvent-rinses on LAOC optical properties, and relates these to make some general conclusions about the composition of LAOC. Data are also compared to independent measurements of the wavelength dependence of absorption made by photoacoustic

spectrometers during the studies. Chapter 7 combines the aerosol composition and fire behavior results to the absorption measurements. I demonstrate the effectiveness of a simple two-component mixture of strongly absorbing, but weakly wavelength dependent EC and weakly absorbing, but strongly light dependent OC that describes the bulk sample properties during FLAME. The relationship of EC/TC ratio and absorption wavelength dependence are also linked to combustion conditions, showing that greater fractions of smoldering combustion during a burn produced more OC and more strongly wavelength dependent light absorption.

1.2 Light absorbing organic carbon (LAOC)

Carbonaceous particles are a major component of tropospheric aerosols, making up ~50% of the fine particle loading in the lower atmosphere [Poschl, 2003]. They constitute 20 to 60% of the total fine mass in the continental US on an annual basis [Malm *et al.*, 2004]. Their contribution can be higher in the tropics during periods of widespread biomass burning events [Formenti *et al.*, 2003; Reid *et al.*, 1998; Reid *et al.*, 2005a]. Predictions of the radiative impacts of these particles rely on measurements of OC and EC concentrations and their optical properties because of the complexity of the particle organic composition.

Table 1.1 Carbonaceous aerosol terminology (from *Andreae and Gelencsér* [2006])

Term	Symbol	Definition
elemental carbon	EC	Poorly defined, conventional term for near-elemental soot carbon, often used interchangeably with 'black carbon' or 'apparent elemental carbon'.
apparent elemental carbon	EC _a	Operationally defined as the fraction of carbon oxidized above a specific temperature threshold that may be corrected for pyrolyzed carbon.
black carbon	BC	Poorly defined conventional term describing carbon with optical properties similar to soot carbon.
equivalent black carbon	BC _e	Operationally defined as the concentration of strongly light absorbing soot-like material that results in an observed signal from a light absorption instrument, such as an aethalometer.
soot	-	A black or brown substance formed by incomplete combustion.
soot carbon	C _{soot}	Fine particle aggregates of graphene-dominated spherules with minor concentrations of oxygen and hydrogen produced by combustion.
brown carbon	C _{brown}	Light-absorbing organic matter (other than C _{soot}).
light absorbing carbon	LAC	Light-absorbing carbonaceous material (C _{soot} + C _{brown}).
organic carbon	OC	Operationally defined as the fraction of carbon that evolves in a non-oxidizing atmosphere at specific temperature thresholds.
light absorbing organic carbon	LAOC	The fraction of OC that absorbs light.

The operationally defined OC and EC components depend on the measurement protocol and not on predetermined characteristics, making nomenclature in this field a challenge. Table 1.1 lists several definitions common to the carbonaceous aerosol literature as discussed by *Andreae and Gelencsér* [2006]. The LAOC term is introduced here to describe the fraction of OC (as determined using thermal-optical techniques) that absorbs light. It is essentially a measurable version of brown carbon (C_{brown}) analogous to the relationship between apparent elemental carbon (EC_a) and EC.

Figure 1.1, originally shown by *Pöschl* [2003] and modified by *Andreae and Gelencsér* [2006], illustrates the difficulties of making bulk classifications of carbonaceous material present in the atmosphere. The 'rainbow' of optical properties, shown on the right-hand side of the figure, ranges from non-absorbing, or 'white carbon' to strongly absorbing, or 'black carbon' particles. The left-hand side of the figure shows the carbonaceous material on the basis of its thermo-chemical classification, ranging from non-refractory material (OC) to refractory

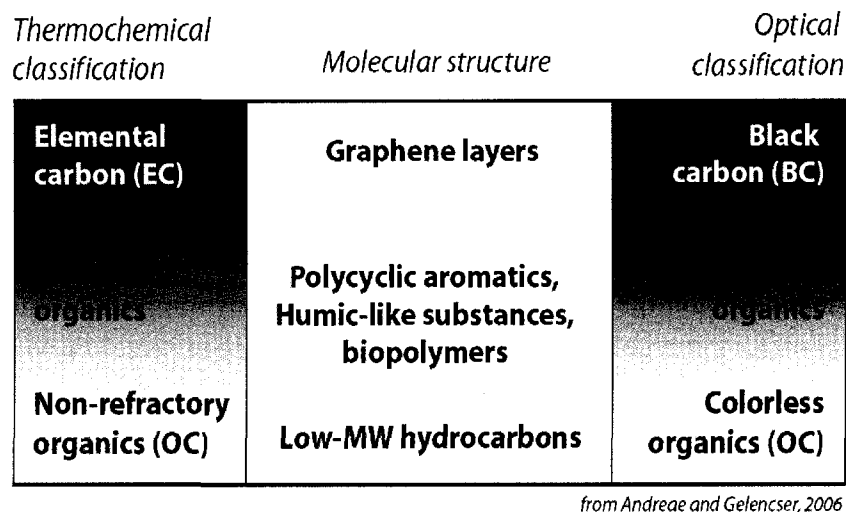


Figure 1.1. Schematic depicting various classifications of carbonaceous aerosol and their relationship to molecular structure. Adapted from *Andreae and Gelencsér [2006]* and *Pöschl [2003]*.

material (EC). Though molecular composition changes drive the behavior in these classification regimes, they are not necessarily linked, particularly in the intermediate range between the extremes in composition. For example, estimates of BC mass absorption efficiency (a_a) range between 3 and 16 m² g⁻¹ [*Bond and Bergstrom, 2006*], even though these samples (primarily from diesel engine and spark discharge sources) should contain primarily near-elemental soot carbon.

1.3 Previous LAOC studies

Researchers began investigating aerosol light absorption, primarily by soot and mineral dust, in the early 1970s [*Bond and Bergstrom, 2006*]. In the late 1970s and 1980s field studies examined the relationship between particle mass and light absorption. The IMPROVE program included light absorption by carbonaceous particles (by proxy through measurements of EC) in its visibility estimates [*Malm et al., 1994*]. During this time light absorbing aerosols were beginning to be included in climate models [*Chung and Seinfeld, 2002; Cooke et al., 1999; Haywood and Shine, 1995; Haywood et al., 1997; Koch, 2001; Penner et al., 1998*]. It became clear

that light absorbing carbonaceous aerosols could be a significant contributor to anthropogenic climate change, particularly after *Jacobson* [2001] estimated the BC radiative forcing at 0.54 W m^{-2} , roughly a fourth of that estimated for greenhouse gases. The magnitude and even the sign of the carbonaceous aerosol impact on climate continues to be debated [*Penner et al.*, 2003].

Researchers have focused less attention on LAOC because it is thought to have a weaker climate impact than BC [*Bond and Bergstrom*, 2006]. LAOC has a much stronger wavelength dependence than BC and its mass-normalized absorption efficiency (a_A) increases sharply towards the UV, so LAOC absorption of UV could be important for photochemistry [*Andreae and Gelencsér*, 2006]. Further, the high abundance of LAOC may counteract its low a_A to some degree [*Hoffer et al.*, 2006; *Kirchstetter et al.*, 2004], so its climate and visibility impacts may be significant.

Several studies that have identified and characterized spectral light absorption by carbonaceous aerosol-dominated samples are listed in Table 1.2. *Patterson and McMahon* [*Patterson and McMahon*, 1984] were among the first to observe a strong spectral dependence of light absorption in atmospheric aerosols. They examined the emissions produced by the smoldering combustion of biomass fuels. *Bond et al.* [*Bond et al.*, 1999b; *Bond et al.*, 2002] found similar absorption dependence in particles emitted by residential and industrial coal combustion, particularly during early phases of burning. It is thought that during these combustion processes, partially aromatized carbon, formed through pyrolysis, volatilizes from the fuel bed and later condenses in the smoke plume [*Mukai and Ambe*, 1986]. Other studies have noted a strong wavelength dependence in combustion emissions, particularly those from biomass burning [e.g., *Kirchstetter et al.*, 2004; *Roden et al.*, 2006]. Other forms of LAOC may

Table 1.2. Previous measurements of light absorbing organic carbon and spectrally dependent aerosol absorption in carbonaceous aerosols.

	Reference	Source (study)	Comments
BIOMASS BURNING	Patterson and McMahon [1984]	smoldering pine needles	
	Foot and Kilsby [1989]	straw burning	
	Kirchstetter et al. [2004]	savannah burning (SAFARI)	decrease in spectral dependence following acetone extraction of OC
	Schnaiter et al. [2004]	laboratory corn stem burning	-
	Roden et al. [2006]	wood-burning cookstoves	stronger spectral dependence during smoldering phase of combustion
	McMeeking et al. [2006]	smoke-impacted haze, western United States (YACS)	increase in UV absorption when observation site impacted by smoke
	Chand et al. [2006]	smoke-impacted haze, Amazon basin (LBA-SMOCC)	stronger spectral dependence during periods with highest particle concentrations
	Lukacs et al. [2007]	European smoke-impacted samples (residential wood and agricultural burning)	determined concentrations of C_{brown} using an optical method calibrated using HULIS samples
	Clarke et al. [2007]	biomass burning plumes over eastern North America (INTEX/ICARTT)	stronger spectral dependence compared to urban pollution plumes; linked to refractory OC
	Sandradewi et al. [2008]	ambient aerosol in a mountain valley (residential wood burning)	strong spectral dependence of absorption at night
Lewis et al. [in review]	controlled biomass combustion (FLAME 1)	stronger spectral dependence in particles emitted by fuels dominated by smoldering combustion	
COMBUSTION	Bond et al. [1999]	industrial lignite burning	spectral dependence correlated with burning rate
	Bond et al. [2002]	residential coal combustion	
	Schnaiter et al. [2003]	spark-discharge soot	
	Lawless et al. [2004]	tobacco smoke	
	Schnaiter et al. [2006]	propane combustion	spectral dependence increased when OC fraction ~50% of TC.
HULIS	Havers et al. [1998]	ambient aerosol (Germany)	alkaline-extractable fraction
	Varqa et al. [2001]	ambient aerosol (Hungary)	
	Hoffer et al. [2006]	Amazon basin (LBA-SMOCC)	examined properties of HULIS extracted from biomass burning-impacted samples

include humic-like substances (HULIS).

There are many measurements of combustion aerosol, which may contain LAOC [Engling et al., 2006b; Formenti et al., 2003; Mayol-Bracero et al., 2002], but there are few measurements which tie specific compounds in biomass combustion aerosol to their light absorbing properties. A handful of studies have hypothesized that the light absorbing properties of carbonaceous aerosol were due either to nitrated and aromatic compounds [Jacobson, 1999] or differing levels of aromatization [Bond, 2001]. The composition of HULIS has been

examined more closely, with a number of studies [*Decesari et al., 2006; Hoffer et al., 2004*] noting a large number of humic and fulvic acids in smoke aerosol. Humic and fulvic acids represent a large number of individual compounds, but they share a number of physical properties, including water-solubility and extremely high-molecular weight [*Graber and Rudich, 2006*].

Biogenic materials and their low temperature combustion products are another important source of light absorbing organic carbon. These possibly include microbial particles (e.g., bacteria, fungi, algae), plant debris, and humic-like substances (HULIS) [*Andreae and Crutzen, 1997*]. HULIS have chemical and physical properties similar to humic substances, which are a complex class of refractory organic molecules produced by the microbial degradation of plant material [*Havers et al., 1998*] [*Havers et al., 1998*]. They are important in biogeochemical cycles [*Cronan and Aiken, 1985*] and their chemical [*Hoffer et al., 2004; Mayol-Bracero et al., 2002*] and optical [*Havers et al., 1998*] properties and interactions with water [*Fuzzi et al., 2001; Gelencser et al., 2003*] have been investigated. HULIS may form through heterogeneous reactions with dienes (e.g., isoprene) in the presence of sulfuric acid [*Limbeck et al., 2003*] or through organic compound reactions on sulfuric acid particles at low humidity [*Hegglin et al., 2002*].

Tolocka et al. [2004] proposed that oligomers are important in secondary organic aerosol (SOA) formation, and that particles with oligomeric molecules could absorb light. Further investigations have shown that oligomers appear to be important in the early stages of biogenic SOA formation and SOA aging processes [*Gross et al., 2006; Heaton et al., 2007*]. Depending on the prevalence of these oligomer-dependent mechanisms, SOA could be a major source of LAOC given its potential production from numerous volatile organic compound

(VOC) sources.

1.4 Overview of several processes sensitive to aerosol optical properties

LAOC has an impact on several important atmospheric radiation-related processes, which are illustrated in Figure 1.2. Light absorption by LAOC reduces the amount of UV radiation at the surface. This radiation initiates a large number of photochemical reactions that partly determine concentrations of ozone and other trace gases. LAOC can degrade visibility, affect climate, and alter the optical properties of cloud droplets, which affects their radiative impacts and lifetimes [Andreae and Gelencser, 2006]. Ignoring LAOC can cause errors when

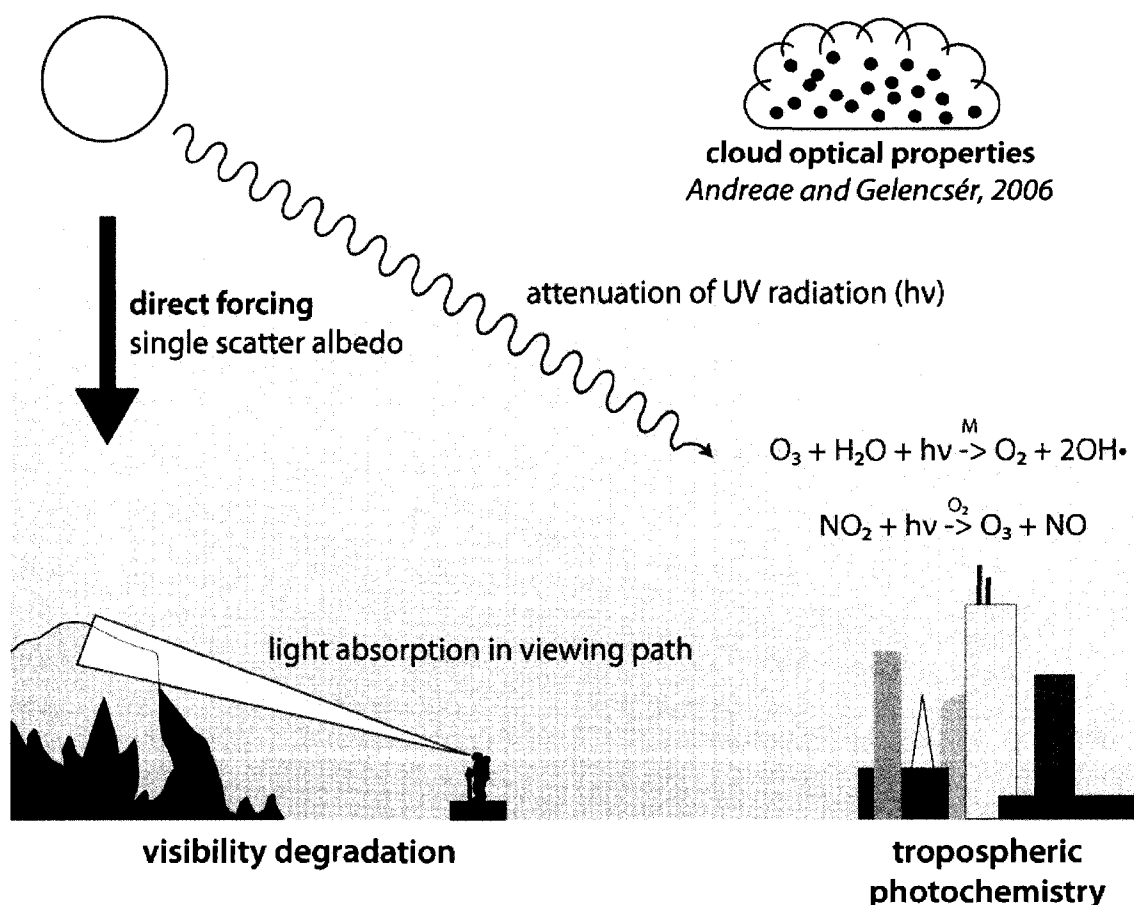


Figure 1.2 Illustration of several important atmospheric impacts of light absorbing organic carbon.

extrapolating absorption-based measurements of aerosol properties to other wavelengths and retrievals from remote sensing measurements.

1.4.1 *Tropospheric photochemistry*

The absorption of electromagnetic radiation by molecules, primarily in the ultraviolet (UV) and visible wavelengths, drives many important chemical reactions in the troposphere. Molecules become electronically excited after absorbing light and can dissociate or directly react to form free radicals or more stable species. The free radicals produced by photochemical reactions can be involved in hundreds of reactions that produce other trace species. The trace species produced may be toxic to humans and plants and/or absorb radiation in the infrared and thus act as greenhouse gases.

The formation of these species, their atmospheric lifetimes, and their concentrations are partially determined by photolysis rates. The photolysis rate constant depends on the amount of light absorbed by the molecule and the probability that it dissociates or reacts with another species following absorption. The amount of light absorbed by a molecule in the atmosphere depends on the amount of light that reaches it, the actinic flux (F_a), and on its ability to absorb the radiation, which is quantified through the quantum yield and absorption cross section. The quantum yield and absorption cross section are intrinsic properties of the molecule and can be measured in the laboratory, but the spectral actinic flux depends on sun geometry and atmospheric conditions and is more difficult to determine. The optical properties of the gases and particles in the atmosphere play a critical role in determining the number of photons available for photolysis, so any attempt to predict the concentrations, distributions, and lifetimes

of trace gas species in the troposphere will require an accurate description of the radiative processes in the atmosphere.

Jacobson [1999] noted that reduced UV flux could impact ozone chemistry and hypothesized that nitrated and aromatic aerosols were responsible for the reduction of UV surface fluxes in the Los Angeles region. He found that ozone mixing ratios were 5-8% lower in the presence of high aerosol loadings. Including UV-absorbing aerosol in model column simulations showed that it accounted for approximately 25% of the UV attenuation, but still over predicted UV irradiances by 25% at a rural site [*Jacobson*, 1999]. Other groups have examined the role of aerosol on UV fluxes in specific regions [*Vuilleumier et al.*, 2001a; *Vuilleumier et al.*, 2001b]. *Krotkov et al.* [2005] compared modeled and measured UV irradiances over Greenbelt, Maryland for a 17-month period. They found changes in the aerosol $\omega_0(\lambda)$ between the summer and winter seasons and when aerosol loadings were high. *Krotkov et al.* [2005] found that the highest aerosol loadings were associated with the passage of a smoke plume, thought to be of Siberian origin.

Martin et al. [2003] determined the net aerosol effect on photolysis rates on a global scale by incorporating aerosol scattering and absorption into the CHEM chemical transport model (CTM). They did not include any impacts from LAOC, but noted it could be important. Figure 1.3 shows the percent change in the $O_3 \rightarrow O(^1D)$ photolysis frequency predicted by GEOS-CHEM after including aerosol scattering and absorption effects [*Martin et al.*, 2003]. It decreased by ~5% over most of the northern hemisphere, mostly due to mineral dust. In biomass burning regions the photolysis frequency decreases by a factor of 2, attributed mostly to BC. Depending on the strength of LAOC absorption, the decrease could be even higher. Other

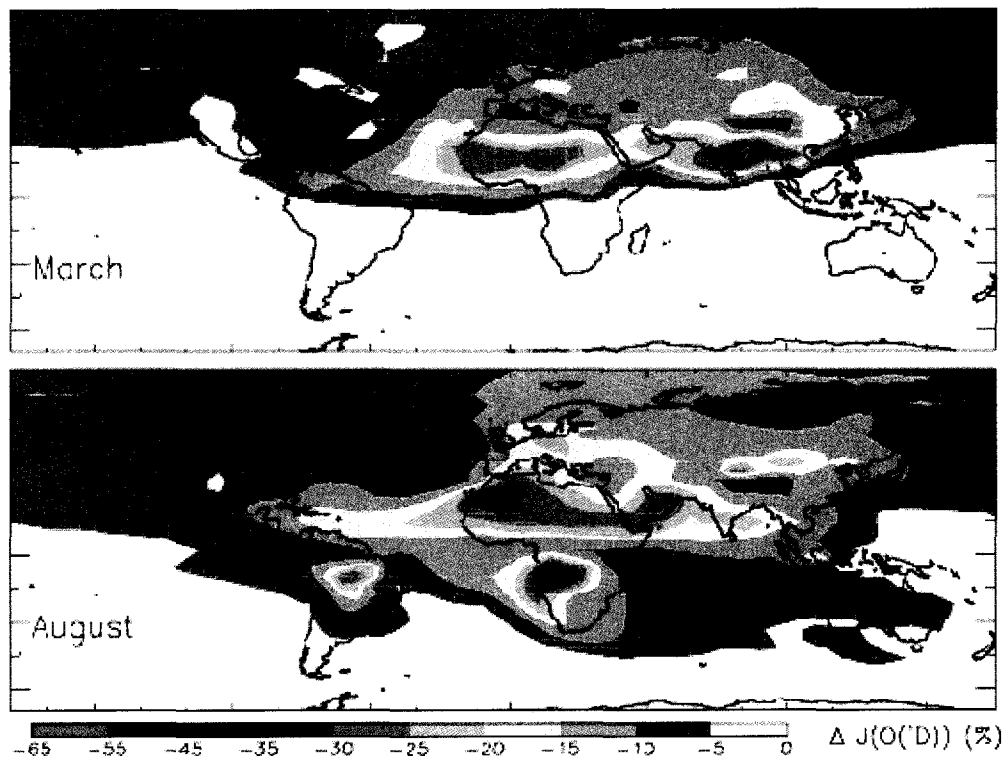


Figure 1.3 Global map of the percent decrease in $O_3 \rightarrow O(^1D)$ photolysis frequency, $J(O(^1D))$, predicted by the CHEM chemical transport model after including scattering and absorption of light by selected aerosol species. Taken from *Martin et al.* [2003].

regions with high BC concentrations, e.g., India and Europe, saw large decreases as well, but these were not separated into biomass burning and other sources. *Martin et al.* [2003] also determined the effect of reduced photolysis frequency on concentrations of OH, CO, NO_x ($NO + NO_2$) and O_3 . The hydroxyl radical was reduced over northern Africa by 25-50% and by 5-25% throughout the NH. Reduced OH concentrations lead to increased CO and NO_x lifetimes, and the model predicted increases in [CO] of 5-15 ppbv (5-10%) over the NH. The effect was larger downwind of fires, with increases of 20-75 ppbv.

1.4.2 Visibility degradation

Visibility is an important air quality component from both psychological and practical perspectives. The human experience of scenic beauty, particularly in wildlife areas and national

parks, is closely related to the clarity of the viewing experience. The 1990 Amendments to the Clean Air Act established the Regional Haze Rule, which requires the reduction of pollution in protected areas, returning to natural visibility conditions by 2064. Severe visibility degradation can have direct economic consequences in addition to purely aesthetic ones. For example, poor visibility can impair or prevent air travel when airports are heavily polluted, e.g., Los Angeles International Airport during wildfire events in October 2003.

Visibility can be quantified in terms of the visual range, which is proportional to the contrast between a target located some distance from the observer and the background scene. Contrast between the target and scene is reduced by the extinction of light along the viewing path and by the scattering of background light into the viewing path. Aerosols and gases between the viewer and target reduce contrast by scattering and absorbing light. As the distance between an observer and the target increases, more particles and gas molecules are included in the viewing path and the contrast between the target and background scene decreases. The contrast can also be reduced if the concentration of particles and/or gases in the viewing path increases.

Visual range is related to the extinction coefficient (b_{ext}), which can be expressed as a sum of the contributions by scattering and absorption from gases and particles:

$$b_{ext} = b_{sg} + b_{ag} + b_{sp} + b_{ap} \quad 1.1$$

The scattering by gases is predicted by Rayleigh theory, and is only a function of atmospheric pressure [Bohren and Huffman, 1983]. In the continental United States it varies between a maximum of $\sim 12 \text{ Mm}^{-1}$ at sea level to a value of $\sim 8 \text{ Mm}^{-1}$ at 4000 m above sea level. The absorption of light at visible wavelengths by gases is dominated by NO_2 . It can be important in plumes and in urban areas, but tends to be a minor contribution to visibility degradation in

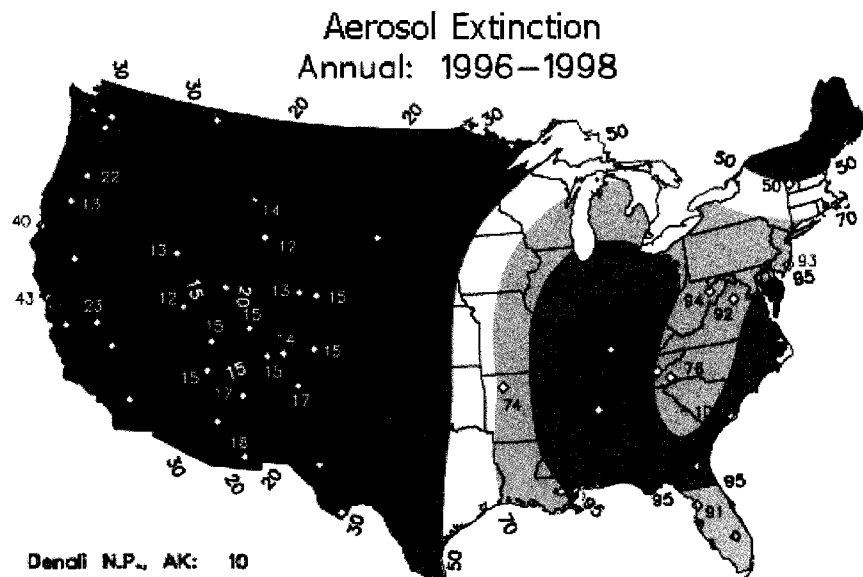


Figure 1.4 Mean annual aerosol extinction (Mm^{-1}) determined from IMPROVE aerosol mass concentrations and mass extinction efficiencies for the period 1996-1998 (from the IMPROVE website: <http://vista.cira.colostate.edu/IMPROVE>).

remote regions. In non-urban regions, extinction is dominated by the contribution from particles [Malm *et al.*, 1994].

The annual mean aerosol extinction over the continental United States for the period 1996 to 1998 is shown in Figure 1.4. The highest extinction values occur in the Ohio River valley and southeastern United States, regions with high sulfur and volatile organic compound (VOC) emissions coupled with high relative humidity. The lowest values are observed in the intermountain west, a region with low anthropogenic emissions and relative humidity. The relative contribution of sulfate and carbonaceous particles in these two regions is different. Figure 1.5 shows the fractions of particulate organic matter, defined as OC multiplied by a factor of 1.4 to account for the associated non-carbon species, and sulfate relative to reconstructed fine mass observed across the IMPROVE network in 2000. In the west, carbonaceous particles have a higher contribution to fine mass and in the east sulfate is a larger component. This is largely

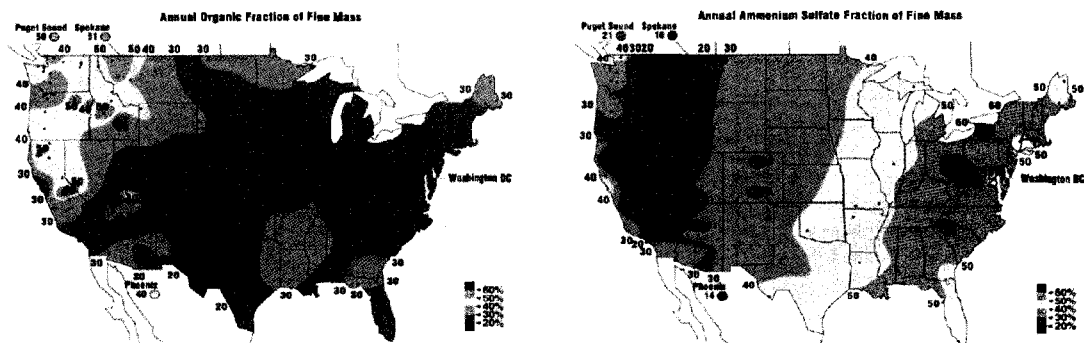


Figure 1.5 Contours of annual mean organic matter (left) and ammonium sulfate (right) mass fractions of fine mass observed across the IMPROVE network during 2000. Aerosol organic matter is defined as measured organic carbon (OC) multiplied by 1.4 to account for non-carbon species in the organic material. (from *Malm et al.* [2004]; with permission).

due to the importance of wildfires and biogenic emissions in the west and coal-fired power plant emissions in the east. Note that both of these figures have been prepared before the increase in the particulate organic matter-to-OC ratio recommended by *Malm and Hand* [2007], which would increase both the contribution by organic particles to fine mass and the total extinction in these areas.

Information about aerosol optical properties from a number of specific sources is needed to accurately determine the contributions by both natural and anthropogenic sources to visibility degradation [Watson, 2002]. The treatment of carbonaceous aerosols is particularly problematic due to the large number of individual organic species falling into this class of particles and their uncertain optical properties [Malm et al., 2004]. These particles also have many sources, including primary emissions from biological and anthropogenic processes and secondary formation following the oxidation of gaseous precursors [Seinfeld and Pandis, 1998]. Any further information about the physical and optical properties of these particles will aid efforts to assess their impacts, and any characteristics that could help distinguish between carbonaceous aerosol sources would also be of value.

1.4.3 Climate

Direct radiative forcing by aerosols is one factor that influences climate and is a source of uncertainty in efforts to predict future climate change [Forster *et al.*, 2007]. Radiative forcing is defined by the most recent Intergovernmental Panel on Climate Change (IPCC) assessment report as the rate of energy change per unit area of the globe, at the top of the atmosphere, caused by a specific forcing agent [Forster *et al.*, 2007]. Our understanding of the direct aerosol effect has improved since the 2001 IPCC report, but the range of estimates of its true value remains large ($\sim 1 \text{ W m}^{-2}$), and the direct aerosol effect remains an important source of uncertainty in climate change predictions.

Aerosol optical properties are often parameterized by the single scattering albedo (ω_0), specific extinction coefficient (a_e), and scattering phase function (P) [Bohren and Huffman, 1983]. Many climate models parameterize these properties for individual aerosol classes, typically sulfates, organic carbon, black carbon, and mineral dust [Chung and Seinfeld, 2002; Koch, 2001; Koch *et al.*, 2007; Myhre *et al.*, 2003]. This type of information can be used to prioritize emission reductions to mitigate climate change, but requires accurate information about optical properties for each aerosol class. Light absorption by aerosols is dominated by the contributions from BC and mineral dust, though the mineral dust contribution is about 1-2 orders of magnitude lower than that of BC [Bond and Bergstrom, 2006]. Light absorption by organic carbon is not usually included in direct radiative forcing estimates, but could be important given the large emissions of OC from biomass burning globally. Sun *et al.* [2007] noted the simple forcing efficiency (at a wavelength of 550 nm) presented by Bond and

Bergstrom [2006] is negative for a 150 nm particle with a refractive index of $1.55 + 0.05i$ and positive if the refractive index is $1.55 + 0.06i$.

1.4.4 *Thermal optical analysis-based carbonaceous aerosol measurements*

Thermal optical analysis (TOA) methods are filter-based measurement approaches that are sensitive to aerosol optical properties. Instead of relying on attenuation to determine particle mass, TOA methods combine measurements of evolved carbon gases with optical observations to characterize carbonaceous aerosol present in a sample. TOA techniques typically involve a two-stage heating procedure, first heating the sample in an oxygen-free atmosphere to volatilize OC, then adding oxygen to combust EC.

The quantification of OC and EC is not always straightforward because some OC can pyrolyze in the initial oxygen-free heating step, forming pyrolyzed organic carbon (POC) or 'char'. The POC can evolve during the second portion of the analysis and be incorrectly identified as EC. The formation of POC causes the filter to darken because the process converts material that usually does not absorb light into a form that does. Light transmittance through [Birch and Cary, 1996] or reflectance from [Chow et al., 1993; Chow et al., 2007] the filter is monitored during heating to correct for POC. It is usually quantified by identifying the point at which the transmittance or reflectance returns to its original value prior to the OC heating steps.

It is unclear if the species responsible for the light absorption by organic carbon are classified as OC or EC by TOA methods, nor is it known if LAOC is prone to charring [Andreae and Gelencser, 2006]. Current TOA protocols measure the filter transmission or reflectance at a single wavelength, usually 632 nm (the wavelength produced by a HeNe laser), which is less

sensitive to light absorption by LAOC because it is weakly absorbing at this wavelength compared to EC. The instrument is 'blind' to the evolution of this material, so it is impossible to determine how much of it evolves in the non-oxidizing and oxidizing atmospheres and classified as OC or EC. The presence of this material may be responsible for the large disagreements in measurements of the EC-content of total carbon ($TC = OC + EC$) in biomass burning aerosol [Watson *et al.*, 2005].

1.4.5 Remote sensing applications

Remote sensing techniques are a valuable tool for understanding earth processes and evaluating the performance of model predictions of weather and climate. Ground-based systems acquire information about the state of the atmosphere and its constituents at a high time resolution and at great distances, which are difficult to obtain with other techniques. Instruments mounted on satellites obtain similar information on a global scale. They require a number of assumptions to infer aerosol properties from measured radiances, so much effort has been invested in developing accurate aerosol retrievals [Dubovik *et al.*, 2002; Holben *et al.*, 1998; King *et al.*, 1999; Remer *et al.*, 2005; Yamasoe *et al.*, 1998]. Table 1.3 lists several remote sensing platforms with some details on their measurement methods and times of operation. The earliest sensors were designed for applications such as weather forecasting and ozone detection, but it was realized that the aerosol interferences provided useful information. Newer designs have focused on measuring aerosol properties specifically, and these more sophisticated instruments can provide much more detailed information, even over bright surfaces.

The MODERate Resolution Imaging Spectroradiometer (MODIS) retrieval algorithms

Table 1.3 Selected remote sensing instruments/networks that provide aerosol information that depends on assumed aerosol optical properties.

Instrument Full name	Platforms	Dates	Major aerosol products	Reference(s)
MODIS moderate resolution imaging spectro-radiometer	Terra, Aqua	2000-present, 2002-present	optical depth, effective radius, fine mode fraction	<i>Kaufman et al.</i> [1997] <i>Remer et al.</i> [2005]
MISR multi-angle imaging spectroradiometer	Terra	2000-present	optical depth (particularly over bright surfaces), particle size and shape	<i>Diner et al.</i> [1998]
POLDER polarization and directionality of the earth's reflectance	ADEOS-1, -2, PARASOL	1996-97, 2002-03	optical depth, shape, surface vs. atmospheric reflectance	<i>Deuzé et al.</i> [2000; 2001]
TOMS total ozone mapping spectrometer	Nimbus-7, Meteor-3, ADEOS-1, EarthProbe	1978-94, 1996-97,	optical depth, UV absorbing aerosols (smoke + dust), single scatter albedo	<i>Herman et al.</i> [1997] <i>Torres et al.</i> [2002]
AVHRR advanced very high resolution radiometer	multiple polar orbiters	1978-present	"radiatively equivalent" optical depth over oceans	<i>Husar et al.</i> [1997]
CALIOP cloud-aerosol lidar with orthogonal polarization	CALIPSO	2006-present	Backscatter profiles of cloud and aerosol layers	<i>Winker et al.</i> [2007]
OMI Ozone monitoring instrument	Aura	2004-present	optical thickness, single-scatter albedo	<i>Levell et al.</i> [2006]
MFRSR Multifilter rotating shadowband radiometer	UV-B ground network	1992-present	optical depth, size, direct-diffuse ratios	<i>Alexandrov et al.</i> [2002]
AERONET aerosol robotic network	ground network	1993-present	optical depth, size, refractive index, shape	<i>Holben et al.</i> [1998]

illustrate the main methods behind retrievals and the role aerosol optical properties play in them. MODIS instruments are aboard two satellites, Terra and Aqua, which cross the equator at 10:30 and 13:30 local time, and achieve global coverage approximately every 1-2 days [*Kaufman et al.*, 1997]. They are passive sensors, measuring radiances over 36 channels, ranging from 0.44 to 15 μm , of which seven in the range 0.47 to 2.13 μm are used to retrieve aerosol properties.

Different algorithms retrieve aerosol properties over ocean and land. The ocean retrievals are thought to be more accurate because of the uncertainties introduced by bright surfaces, e.g. snow, ice, deserts [*Kaufman et al.*, 1997; *Remer et al.*, 2005]. Both algorithms require calibrated, geolocated surface reflectances, a cloud mask product, and meteorological data [*Remer et al.*, 2005]. The algorithms take the surface reflectances and the measured TOA

reflectances as inputs in a lookup table to obtain aerosol optical thickness. The lookup tables are constructed using radiative transfer models with prescribed aerosol populations based on a number of possible emission sources. The optical properties assumed for these particle classes have a strong impact on retrieving aerosol information accurately.

Chapter 2 Biomass burning

The term biomass burning includes a broad range of combustion processes that involve high-temperature oxidation of biological materials. It is related to fossil fuel burning in that both involve the combustion of carbonaceous material, but biomass burning tends to be far less efficient compared to fossil fuel burning, more widespread, and has both natural and anthropogenic sources. Biomass burning includes natural wildfires, which are prevalent in temperate and boreal zones, agricultural and land clearing burning, prescribed fires, burning of biofuel for energy purposes, and the combustion of biomass waste products, such as trash burning at incinerators. It produces gas- and particle-phase emissions, or smoke, including carbon dioxide (CO_2), carbon monoxide (CO), water vapor (H_2O), other trace gases and particles, as well as LAOC. The emissions of these species depend strongly on combustion conditions, which are related to fuel properties (e.g., moisture), air temperature and relative humidity [Reid *et al.*, 2005b].

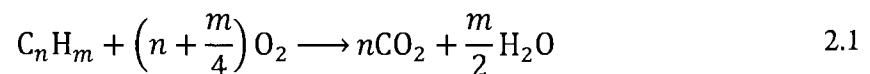
The fire literature is extensive, ranging from studies on fire behavior itself to those linking the history of fire occurrence to long-term climate variability. It features contributions from ecologists, biologists, climatologists, atmospheric scientists, soil scientists and chemists. In this section, I focus on the factors driving biomass burning emissions, their geographic distribution and seasonality, and a general picture of their bulk physical and chemical properties. When possible, I give the most recent estimates for both open-field fires, which includes

wildfires, agricultural burning in fields, and prescribed fires, and controlled or indoor fires, which include burning for domestic energy use (e.g., heating, cooking).

The fire triangle is commonly used to communicate wildfire behavior to the public, with the three sides representing heat, fuel and oxygen, all required to sustain the fire. Heat is required not only to ignite the fire, but also to maintain and spread it (via both radiative and convective heat transfer), because heat removes moisture and preheats the fuel. Characteristics of the fuel that affect fire behavior include its moisture content, shape, size, quantity and how it is distributed over the landscape. Of course, fires also require oxygen to support the chemical oxidation processes during combustion, although some conversion of fuel to fire products occurs even in the absence of oxygen.

2.1 Combustion

The complete combustion of a simple hydrocarbon fuel requires the complete oxidation of the fuel into carbon dioxide and water [*Flagan and Seinfeld, 1988*] :



Based on equation 2.1, for every mole of fuel burned, $4.78(n + m/4)$ moles of air are needed because oxygen is roughly 20% of air on a mole basis. This coefficient gives the stoichiometric ratio of fuel to air, but in non-premixed flames (such as those in wildfires), the ratio of fuel to air varies widely, from very fuel-lean to very fuel-rich combustion occurring in different regions of the burning mixture. Equation 2.1 shows only the overall mass balance, and does not describe the actual sequence of reactions occurring during combustion. Furthermore, combustion reactions only occur in the gas phase, so if C_nH_m represents a solid or liquid, volatilization must

first occur.

Combustion of solid biomass consists of several stages, beginning with ignition, proceeding to flaming and smoldering combustion, then to purely smoldering combustion and finally to extinction [Andreae and Merlet, 2001]. Water and volatile compounds (including alcohols, terpenes, etc.) are released at the beginning of the combustion process during an initial drying/distillation stage. During this time the fuel bed temperature increases to ~ 500 K [Morvan et al., 2000]. Further heating of the fuel bed to temperatures between 600 and 800 K causes thermal cracking of fuel molecules or pyrolysis. Pyrolysis is the chemical decomposition of organic materials when heated in the absence of oxygen. During this stage volatile matter (hydrocarbons) are released from the fuel bed and char is formed (material that does not undergo further pyrolysis). The char is subsequently oxidized through a series of slower, surface area-limited oxidation processes. Modeling of fire propagation through a bed of solid fuel, as occurs in biomass burning, is difficult but represents an urgently-needed tool for fire management. Morvan et al. [2000] present a numerical model aimed at predicting the rate of propagation of a fire through a forest fuel bed and apply it to an idealized case of fire propagation through a bed of pine needle litter. Their results (for the one case considered) show that radiative heat transfer is more important than convective heat transfer in controlling fire propagation.

The complex mixture of volatile gases emitted during pyrolysis can mix with air and ignite. Initiation of the combustion mechanism begins with the formation of hydrocarbon radicals ($R\cdot$) by either the abstraction of a hydrogen atom by oxygen:



or by thermally induced dissociation [*Flagan and Seinfeld, 1988*]:



Both reactions are endothermic, so ignition requires the input of heat. The hydrocarbon radicals react rapidly with oxygen to form hydroperoxy radicals ($RO_2\cdot$), which can dissociate to form additional free radicals, including the hydroxyl radical ($OH\cdot$). At temperatures above 1200 K, the hydroxyl radical concentration is high enough to participate in a large number of reactions generating $H\cdot$, $O\cdot$, and $OH\cdot$. Thus, combustion processes generate a large pool of highly reactive radicals that continue to break down fuel molecules. Note that these reactions are strongly dependent on the temperature of the gases, which governs the kinetics of the reactions. Heat generated by the exothermic radical reactions increases the temperature of the fuel bed and allows the fire to propagate.

The flame produced during the flaming-phase of combustion represents the reaction front created by the diffusion of energy and free radicals from the hot gases into the cooler, unreacted gases [*Flagan and Seinfeld, 1988*]. An idealized flame consists of a central core containing pure gas-phase fuel surrounded by a region in which fuel diffuses outward and air diffuses inward. The main reaction zone occurs where the mixture of air and fuel is closest to its stoichiometric ratio (i.e., that given by Equation 2.1). In these regions the flame temperature can reach ~ 2300 K [*Flagan and Seinfeld, 1988*]. The visible light from the flame is due to

chemiluminiscent reactions (in the fuel-rich region) and the emission of thermal radiation from the soot formed in the flame (closer to the stoichiometric ratio).

The mixing of air and fuel in the flame zone can be turbulent due to the relatively high velocities of the buoyant gases escaping the fuel bed. Carbon monoxide and gas-phase hydrocarbons can escape oxidation in the flame in fuel-rich regions where mixing is relatively poor. Soot can be formed in flames following chemical reactions that create larger hydrocarbon molecules, including PAHs, that are eventually large enough to form particles and continue to grow by chemical reactions at their surface [*Flagan and Seinfeld, 1988*]. Soot formation is linked to the molar proportion of carbon to oxygen, and depends on flame type, temperature, and the fuel itself [*Flagan and Seinfeld, 1988*]. In diffusion flames associated with biomass combustion, there is no oxygen in the pyrolysis zone that can oxidize the newly-formed soot, so soot formation increases with temperature because the pyrolysis rate is higher.

The emission of volatile compounds slows as the fuel is depleted, so the chain reactions responsible for maintaining the free radical pool in, and high temperature of, the combustion region slow. The flame extinguishes and the lower-temperature smoldering phase begins. The smoldering phase of combustion features surface oxidation of the char formed during the flaming-stage of combustion. The rate of smoldering combustion depends strongly on the rate of oxygen transport to the combustion region. It is hypothesized that oxygen adsorbed onto the surface creates partially oxidized carbon species that desorb and then may be further oxidized in the gas phase [*Warnatz et al., 1996*]. Temperatures surrounding the fuel bed and in the combustion zone of the emitted gases are lower (~500 K), and the radical-based chain reaction processes are slower during this phase of combustion, so more partially-oxidized gases can

escape further oxidation and be emitted to the atmosphere [Yokelson *et al.*, 1997]. Thus during smoldering combustion, emissions of CO and partially oxidized pyrolysis products increase [Andreae and Merlet, 2001]. For this reason, the distinction between flaming and smoldering combustion phase contributions to the overall fuel combustion, quantified through the combustion efficiency, is extremely important and will be discussed extensively throughout this work.

2.2 Seasonal and spatial biomass burning patterns

Natural and human-initiated biomass burning occurs throughout the world during all times of the year. Most human-initiated fires occur in developing countries in the tropics, where fire is used as a land management tool, clearing forest for agricultural use, as well as for pest control, nutrient mobilization, domestic energy use, and charcoal production [Crutzen and Andreae, 1990]. Agricultural burning also occurs in developed countries, but at a smaller scale [McCarty *et al.*, 2007]. Wildland, or 'natural' forest fires, have been shaping the landscape since the evolution of plant species, and today are the dominant form of biomass burning in temperate and boreal regions. Prescribed burning has become more widely used as a land management tool in these regions in recent years with the realization that decades of fire suppression have perturbed natural ecosystems in some areas [Allen *et al.*, 2002; Brown and Bradshaw, 1994].

Early estimates of global biomass burning activity relied on extrapolating data from studies focused on smaller regions using survey and demographic data [Crutzen and Andreae, 1990; Hao and Liu, 1994; Lioussé *et al.*, 1996]. Increased sophistication in satellite retrievals and improvements in satellite instrumentation provided a new source of data allowing

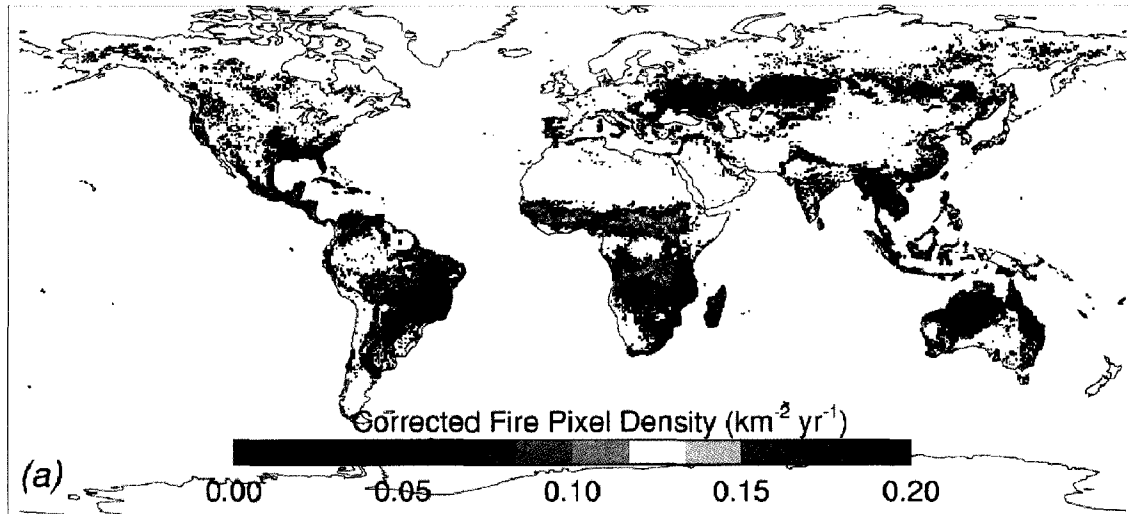


Figure 2.1. Annual mean fire pixel density ($\text{km}^2 \text{yr}^{-1}$) adjusted for satellite overpass frequency from the Terra MODIS sensor over the period 2000-2005 (from Giglio *et al.* [2006b]; with permission).

improvements in open-field biomass burning activity estimates [Ito and Penner, 2004]. These include burned-area [Giglio *et al.*, 2006b; Gregoire *et al.*, 2003; Kaufman *et al.*, 2003; Roy *et al.*, 2002; Simon *et al.*, 2004] and active fire count [Giglio *et al.*, 2006a; Kaufman *et al.*, 2003; van der Werf *et al.*, 2006] products.

Figure 2.1 presents Terra MODIS area corrected fire pixel density for the period 2001-2006 [Giglio *et al.*, 2006a]. The fire pixel density is simply the gridded fire counts normalized by the expected equatorial coverage in a calendar month containing no missing observation [Giglio *et al.*, 2006a]. The highest fire pixel densities are observed in Brazil and regions just to the north and south of the equator in Africa, but fire is widespread in southeast Asia, Australia, Central and North America, and central Asia. A similar pattern is shown by Figure 2.2, which shows Terra MODIS mean annual burned area from Giglio *et al.*, [2006b].

Humans burn biomass in the tropics to shift agriculture, convert forest into cropland, remove agricultural waste, and heat and cook in their homes [Crutzen and Andreae, 1990]. With

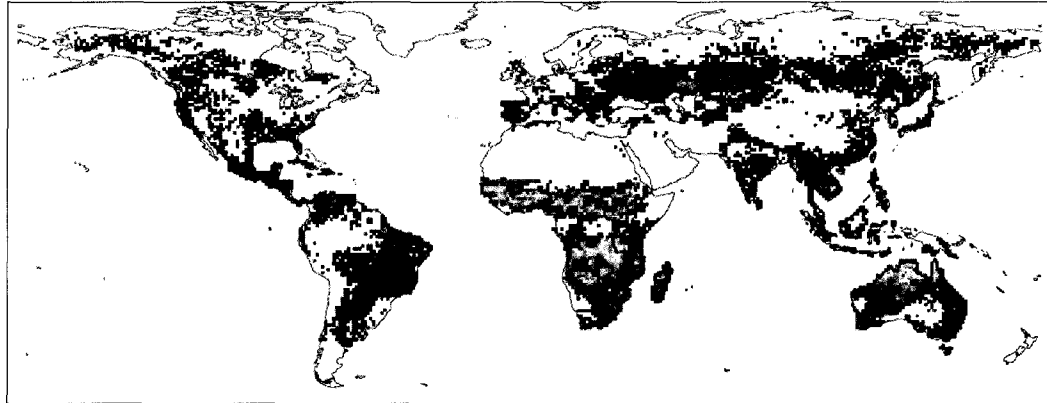


Figure 2.2. Mean annual burned area derived from Terra MODIS active fire observations for the period 2001-2004. Blue shades correspond to regions where 0.1 to 1 percent of the $1^\circ \times 1^\circ$ pixel burned per year. Green shades correspond to 1 to 10 % pixel area yr^{-1} and orange/red shades indicate 30-100 % pixel area yr^{-1} . Uncertainties are on the order of 0.5 to 20 % pixel area yr^{-1} . Taken from *Giglio et al.* [2006b].

the exception of domestic use, the timing of the burning is closely linked to precipitation patterns. For example, a strong seasonal shift in burning in Africa coincides with different phases of the dry season. Farmers cut the forest undergrowth and trees at the beginning of the dry season, leave it to dry for a brief period of time, and burn this material to prepare land for agricultural use. After several years the farmer may move to a new plot of land, allowing the forest to grow back. This process is known as shifting agriculture or 'slash-and-burn' farming. The land use change is permanent if the cleared region is used for pasture or human settlement, in which case the process is referred to as deforestation. *Crutzen and Andreae* [1990] estimated the carbon released globally by shifting agriculture practices was between 500 and 1000 Tg C per year and that by permanent deforestation between 200 and 700 Tg C yr^{-1} . Savannah and brushland burning (again done for agricultural practices) is another important type of biomass burning that occurs in the tropics, particularly in Africa, releasing between 400 and 2400 Tg C yr^{-1} [*Crutzen and Andreae*, 1990].

Natural fire plays an important part in maintaining the carbon balance and ecology of boreal forests [Johnson *et al.*, 1998]. It begins the pattern of succession in the forest, regulating the ecosystem primary production, and controls soil carbon and moisture levels and hence soil respiration [O'Neill *et al.*, 2002a; Zhuang *et al.*, 2002]. Boreal fire is more episodic than in the tropics, partly because many of these fires are ignited by lightning and are less influenced by human activities [French *et al.*, 2002]. They are prevalent throughout the dryer regions of continents in the northern hemisphere, including Alaska, Canada, Scandinavia and parts of Russia. There is speculation that climate change impacts could result in increased boreal fire activity because of warmer, drier conditions.

Burned areas from single events in boreal regions tend to be much larger than other areas due to the large fuel loading and the absence of human suppression or management efforts. Vegetation consumed by boreal fires includes spruces, firs and the 'organic mat' or duff layer, made up of the mosses, lichens, plant litter and organic soils found on/in the forest floor. The duff layer contains a large fraction of the ecosystem's carbon storage, so it is an important contribution to the emissions in boreal forest fires [French *et al.*, 2002]. Boreal fires are significantly more intense than in the tropics, with more frequent crown fires. Fire radiative power, a measure of combustion intensity, determined by Terra MODIS, is higher for boreal regions compared to the tropics, as illustrated in Figure 2.3.

In natural wildfires a flame front passes through the fuel bed followed by a lengthy smoldering period, sometimes lasting weeks, before the fire is completely extinguished [Andreae and Merlet, 2001]. Most studies of fire behavior are limited to individual events or fuel samples [Bond *et al.*, 1999b; Chakrabarty *et al.*, 2006; Christian *et al.*, 2003; Hille and Stephens, 2005;

Roden et al., 2006; Stephens and Moghaddas, 2005]. Less quantitative, but global, data are available from the MODIS fire radiative power (FRP) product [*Giglio et al., 2006a*]. Fires burned for agricultural purposes and in the tropics have lower FRP, suggesting they are less intense and more controlled than extra-tropical burning. Regions dominated by grassland, as in savannahs in Africa and Brazil and parts of western Australia feature high FRP and intense, but short lived burning events [*Giglio et al., 2006a*]. Boreal regions, especially those in North America, feature intense crown fires that have high FRP [*Wooster and Zhang, 2004*].

Biomass burning in temperate regions as a whole represents substantially less carbon emitted to the atmosphere than that emitted from burning in either boreal or tropical zones, but occurs in close proximity to developed nations where air quality and visibility are more strictly regulated. Wildfires, prescribed burning and agricultural waste burning are important influences on air quality in these regions. The fire season in the NH peaks in the late-summer (August-October) when fuels are dry. The fire activity in temperate zones features more interannual variability than in the tropics [*Duncan et al., 2003*] and is linked to major climate patterns, such as El Niño – Southern Oscillation (ENSO) [*Collins et al., 2006; Kitzberger et al., 2007*].

Severe wildfire activity has increased in the western United States in recent years, possibly due to land management practices or climate change [*Westerling et al., 2006*]. The 20th century saw an aggressive fire suppression strategy implemented throughout the western United States, which reduced the frequency of large fires [*Savage and Swetnam, 1990*]. This led to changes in forest structures and biomass density that resulted in more intense wildfires in the last few years, altering the natural fire regime. In some regions the perturbations to the natural fire regime are minor, such as in the Northern Rockies, while in other locations the effects of fire

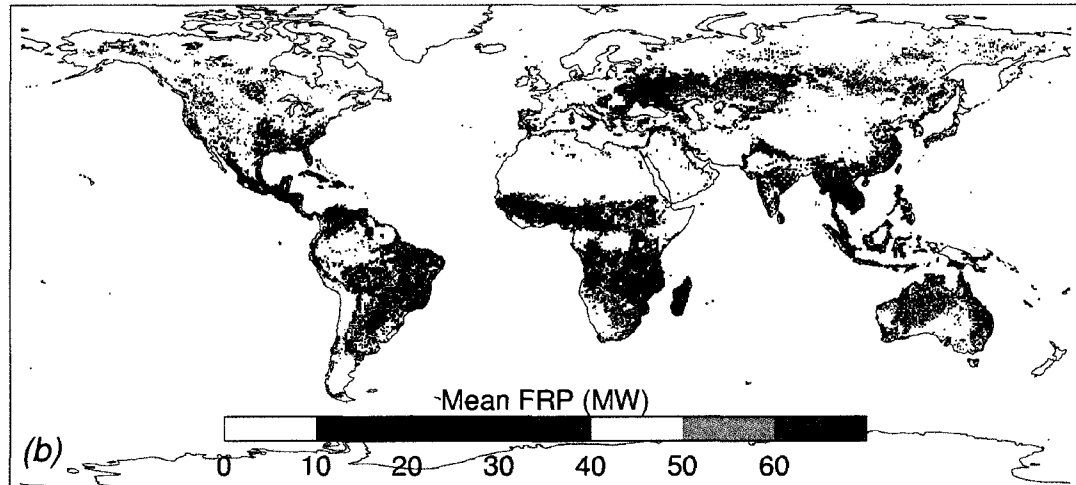


Figure 2.3 Mean fire radiative power (FRP, MW) retrieved from Terra MODIS observations over the period November 2000 to October 2005 (from Giglio et al. [2006a]; with permission).

suppression on the ecosystem are more severe, such as the southern Sierra Nevada [Westerling et al., 2006].

Changes in natural climate variations, such as drought-frequency, may also be playing a role in modifying fire behavior. Westerling et al. [2006] found that warming combined with an earlier spring is resulting in increased fire severity in the western United States. Holden et al. [2007] show that variability in the timing and amount of precipitation during the southwestern US fire season dramatically influenced fires in the Gila National Forest. Climate variability also has a strong impact. There are strong links between ENSO-induced droughts in the western US and southeastern Asia and fire season severity [Collins et al., 2006; Giglio et al., 2006a; van der Werf et al., 2006]. Kitzberger et al. [2007] found relationships between phases of the Pacific Decadal Oscillation (PDO) and Atlantic Multi-decadal Oscillation (AMO) and fire activity using tree-ring fire scar data going back to ~1550.

Biomass is also burned under controlled conditions outdoors to clear agricultural waste

and indoors for domestic heating and cooking purposes. Both represent significant fractions of biomass burning activity. For example, *McCarty et al.* [2007] found that agricultural burning accounted for 16% of the biomass burning activity in the southeastern US in 2004, with ~1.8 million acres burned, comparable to the area burned by wildfires in the US during less severe fire seasons.

Domestic biomass burning of wood, grasses, and other organic materials, often referred to as biofuel, accounts for ~35% of energy consumption in developing countries and ~15% globally [*Crutzen and Andreae*, 1990]. *Fernandes et al.* [2007] estimated that 2460 Tg of biofuel were consumed globally in 2000 based on current residential fuel use patterns and population data. Wood fuels made up the majority of the biofuel consumed for residential purposes (69%), followed by crop residues (25%). Fuel consumption was highest in east Asia, south Asia, and Africa, combining to 73% of global residential biofuel consumption [*Fernandes et al.*, 2007].

2.3 Fire behavior and its relationship to emission factors

Understanding of the spatial distribution of biomass burning alone is not sufficient to determine the impacts of fire on climate, atmospheric chemistry and visibility. It must be combined with a quantitative description of emissions, preferably as a function of fuel and combustion intensity [*Andreae and Merlet*, 2001]. The mass (m) of species x produced by the combustion of a specific mass of dry fuel (m_{biomass}) is known as the emission factor, EF_x [*Andreae and Merlet*, 2001]. It is given (in units of g kg^{-1}) as:

$$EF_x = \frac{m_x}{m_{\text{biomass}}} = \frac{m_x}{m_c} [C]_{\text{biomass}} \quad 2.4$$

where $[C]_{\text{biomass}}$ is the concentration of carbon in the biomass consumed by fire and m_c is the

mass of carbon emitted, including CO₂, CO, gas-phase hydrocarbons, and particulate carbon. The emission factors of species that contain only carbon, hydrogen, and oxygen are dominated by the combustion process because the carbon content of fuel varies only over a limited range, while the emissions of other trace species, such as those containing nitrogen or sulfur, are controlled by both fuel composition and combustion conditions [Andreae and Merlet, 2001].

Carbonaceous species (carbon and other elements associated with the carbon) dominate the particle phase emissions (~80-90%), but appreciable concentrations of inorganic species, such as potassium, chlorine, and calcium, are also present [Reid et al., 2005b]. Reports show organic and black/elemental carbon make up ~55% and ~8% of total particulate emissions, respectively [Cachier et al., 1995; Ferek et al., 1998; Reid et al., 2005b; Yamasoe et al., 2000]. The ratio between OC and BC/EC is sensitive to combustion conditions, with more OC emitted by smoldering combustion compared to flaming combustion [Reid et al., 2005b]. Measurements of the individual organic compounds in smoke are incomplete, identifying only 5-20% of the carbonaceous species [Reid et al., 2005b]. They suggest that thermal decomposition products of the lignin and cellulose making up woody material are important. Carbohydrates, such as levoglucosan, are thought to make up as much as 10% of fresh smoke particle mass [Engling et al., 2006a; Gao et al., 2003].

Measurements of flaming and smoldering phase emission factors are rare, primarily because it is difficult, if not impossible, to separate these phases during measurements of natural wildfires [Andreae and Merlet, 2001]. Instead researchers have reported integrated emissions observations for specific vegetation classes, which typically have characteristic ratios of flaming and smoldering combustion. These can vary considerably within a vegetation class, however,

Table 2.1. Emission factors (g species per kg dry fuel matter) for selected particulate phase emissions and biomass burning classes.

Vegetation class or fire type	PM _{2.5} (g kg ⁻¹)	Organic carbon (g kg ⁻¹)	Black carbon (g kg ⁻¹)	Reference
Savannah/Grassland	5.4 ± 1.5	3.4 ± 1.4	0.48 ± 0.18	Andreae and Merlet, 2001 (AM2001)
Tropical forest	9.1 ± 1.5	5.2 ± 1.5	0.66 ± 0.31	AM2001
Extra-tropical forest	13.0 ± 7.0	8.6-9.7	0.56 ± 0.19	AM2001
Biofuel	7.2 ± 2.3	4.0 ± 1.2	0.59 ± 0.37	AM2001
Cooking fuel	8.5 ± 1.6	4.0 ± 0.9	1.5 ± 0.3	Roden et al., 2006
Agricultural waste	3.9	3.3	0.69 ± 0.13	AM2001

because of the range of moisture conditions, fuel structure, winds and terrain [Andreae and Merlet, 2001].

Andreae and Merlet [2001] reviewed several biomass burning studies to determine emission factors of PM_{2.5}, OC and BC for several biomass burning types, summarized in Table 2.1. Extra-tropical forests have the highest emission factors for PM_{2.5} and OC and agricultural waste produces the most BC per unit mass, but not significantly more than other vegetation classes. Andreae and Merlet [2001] note that aerosol emission factors, particularly from agricultural waste and biofuel burning, are uncertain. For example, Roden et al. [2006] estimated emission factors of 8.5 ± 1.6 (PM_{2.5}), 4.0 ± 0.9 (OC), 1.5 ± 0.3 (EC) g kg⁻¹ fuel for biomass fuel burned during domestic cooking. They note that the testing procedure and use of accelerants influenced the magnitude of EF and suggest that differences between laboratory- and field-based estimates may be a result. These uncertainties propagate when calculating total biomass burning emissions (multiplying EFs by biomass burning inventories), which is discussed in the next section.

2.4 Global estimates of biomass burning emissions by species

Andreae and Merlet [2001] presented estimates of global biomass burning emissions of

Table 2.2 Biomass burning and biofuel emissions (from *Bond et al. [2004]*).

Reference	Year	BIOMASS/BIOFUEL		FOSSIL FUEL	
		BC (Tg yr ⁻¹)	OC (Tg yr ⁻¹)	BC (Tg yr ⁻¹)	OC (Tg yr ⁻¹)
Penner et al., 1993	1980	6.0	-	6.6	-
Liousse et al., 1996	1984	5.6	45	6.6	28
Andreae and Merlet, 2001	-	4.8	36	5.1	10.0
Bond et al., 2004	1996	5.0	31	3.0	2.4

many trace species, including PM_{2.5}, OC and EC/BC, by combining late-1990s published emission factors and an unpublished inventory of global burning. They found 16.1 Tg yr⁻¹ for PM_{2.5} emitted by savannah and grassland burning, 12.0 Tg yr⁻¹ by tropical forest burning, 8.3 Tg yr⁻¹ by extra-tropical forest burning, 19.4 Tg yr⁻¹ by biofuel use, and 2.1 Tg yr⁻¹ by agricultural residue burning, totaling to ~58 Tg yr⁻¹. EC and OC emissions were estimated at 4.8 and 36.1 Tg yr⁻¹. *Bond et al. [2004]* provided updated inventories for OC and EC emitted by combustion processes, including biomass burning, for 1996. They determined open biomass burning emissions by region from their own review of published data, government reports to the United Nations, FAO statistics, and the *Andreae and Merlet [2001]* emission factors. Global TC emissions, excluding the contribution by biofuel consumption, were estimated at 28.3 Tg yr⁻¹ compared to 28.2 Tg yr⁻¹ reported by *Andreae and Merlet [2001]*. Table 2.2 summarizes biomass burning, biofuel and fossil fuel emissions estimates reported by these recent studies and earlier inventories commonly used in chemical transport models. Note that the OC and BC emissions from biomass burning are similar to or greater than those produced from fossil fuel combustion, depending on the emission inventory used. This is primarily due to the higher efficiency of fossil fuel combustion compared to biomass burning.

Satellite data have provided more information about global fire occurrence, spatial extent, seasonality and combustion intensity [*Giglio et al., 2006a; Giglio et al., 2006b*]. These

have not yet been included in a comprehensive global inventory in the same vein as *Lioussé et al.* [1996] or *Bond et al.* [2004], but are beginning to appear in regional-scale studies. *Ito et al.* [2007] combined a biogeochemical model with MODIS burned area product to determine CO and BC emissions from south African grasslands and woodlands. *Venkataraman et al.* [2006] performed a similar analysis for India. *Heald et al.* [2003] used AVHRR fire count data over Asia to construct daily-resolved fire maps, which they combined with climatologic emission factors and a chemical transport model (GEOS-Chem) to determine CO emissions.

2.5 Impacts of biomass burning emissions

In this section I give an overview of recent work examining the visibility and photochemical impacts of biomass burning. Aerosols have a short atmospheric lifetime—on the order of a week—so the biggest impacts of particulate biomass burning emissions tend to be regional in nature. That said, several studies have noted significant long-range transport of smoke from source regions [*Damoah et al.*, 2004; *Forster et al.*, 2001; *Kreidenweis et al.*, 2001; *Wotawa and Trainer*, 2000]. For this reason, the following sections discuss the impacts of emissions on regional and global scales.

The discussion in this section is limited to visibility impacts of biomass burning in North America because the majority of visibility studies have focused on this region. There are two major reasons for this: a) implementation of the Regional Haze Rule (RHR) by the United States Environmental Protection Agency, and b) the majority of the areas regulated by the RHR are located in the western US, a region that sees frequent wildland fire activity. Biomass burning emissions have impacts on visibility outside this region, but are rarely studied from a visibility

point of view because these impacts are not considered as important as the climate or health impacts. Other studies have examined transboundary transport of fire emissions from Canada to the US and Europe [Colarco *et al.*, 2004; Wotawa and Trainer, 2000] and from Mexico and Central America to the US [Kreidenweis *et al.*, 2001; Mendoza *et al.*, 2005].

Several studies have linked episodic fire events to reductions in visibility. Phuleria *et al.* [2005] and Mühle *et al.* [2007] examined the impacts of fires in Southern California in 2003 that caused the closure of Los Angeles International Airport. Green *et al.* [2007] used positive matrix factorization to show that approximately half of the organic mass in the Columbia River Gorge during hazy periods with high fire activity was due to biomass burning. McMeeking *et al.* [2005] linked fires in the Pacific northwest to visibility degradation in Yosemite National Park in 2002 and McMeeking *et al.* [2006] determined that these fires affected a broad region in California, Oregon and Washington.

Determining the more widespread, long-term impacts of biomass burning on visibility is difficult because measurements common in episodic studies are too localized and expensive to be performed continuously in sensitive areas. Malm *et al.* [2004] report high concentrations of OC and EC at IMPROVE sites in western US parks and wilderness areas during the late-summer and early-fall of 2000. Figure 2.4 depicts monthly concentrations of major aerosol species at IMPROVE sites in the Pacific northwest. Malm *et al.* [2004] attribute the large increase in organics during late-summer and early-fall determined by their study to wild and prescribed fires in the northern Rockies, northern California and Oregon and the northwest. Extreme concentrations of aerosol fine mass have also been tied to increases in total carbon (TC = OC + EC) likely due to wildland fires [Ames and Malm, 2001].

There are other sources of organics besides biomass burning, however, notably SOA formation from biogenic precursors, which are widespread in the western and southeastern US. This limits the diagnostic power of measurements of OC alone. In addition it is difficult to distinguish between anthropogenic and biogenic combustion sources if only OC and EC measurements are used. *Bench and Herckes* [2004] examined the ratios of carbon isotopes in aerosol samples to determine the age of carbonaceous aerosol material collected at Yosemite National Park in 2002 and showed that the majority of variation in TC concentrations was driven by 'modern' or biogenic carbon sources as opposed to 'old' or fossil fuel carbon sources. This indicated a strong biogenic influence on aerosol concentrations in the park, but could not distinguish biogenic SOA and biomass burning sources, as both contain 'modern' carbon.

McKenzie et al. [2006] introduced a modeling approach to simulate smoke impacts in the northwestern US, first predicting fire outbreaks using meteorological data and fuel inventories, then determining emissions from these fires, and predicting the plume distribution during the events. They showed that their technique has promise, but is only in the development stages and has not yet been applied to larger regions. *Park et al.* [2003] determined the contributions from different source types to annual mean carbon concentrations in the United States by adjusting emissions in a chemical transport model (GEOS-Chem) to match IMPROVE site observations. They combined these with a climatological fire inventory to show that fires contributed 0.48 and 0.32 $\mu\text{g C m}^{-3}$ to the mean carbonaceous aerosol concentrations in the western and eastern United States, respectively. Recent modeling efforts have shown that variability in OC in the western US is driven by wildfire activity [*Spracklen et al.*, 2007].

Park et al. [2007] analyzed IMPROVE data from 2001-2004 to quantify the impacts of fires and biofuel combustion on carbonaceous aerosol concentrations in the United States. They used non-soil potassium (K) measured at IMPROVE sites as a biomass combustion tracer. To separate the contributions from biofuel use, *Park et al.* [2007] examined gridded satellite burn area data. They derived burning contributions to TC by multiplying seasonal non-soil K values by emissions ratio, which they calculate at each IMPROVE site by correlating TC and non-soil K. Wildland fires contributed 22% of the observed annual mean TC in the west and 7% in the east [*Park et al.*, 2007]. Including emissions from prescribed fires and biofuel use increases the biomass burning contribution to ~50% of the observed annual mean TC concentrations. *Park et*

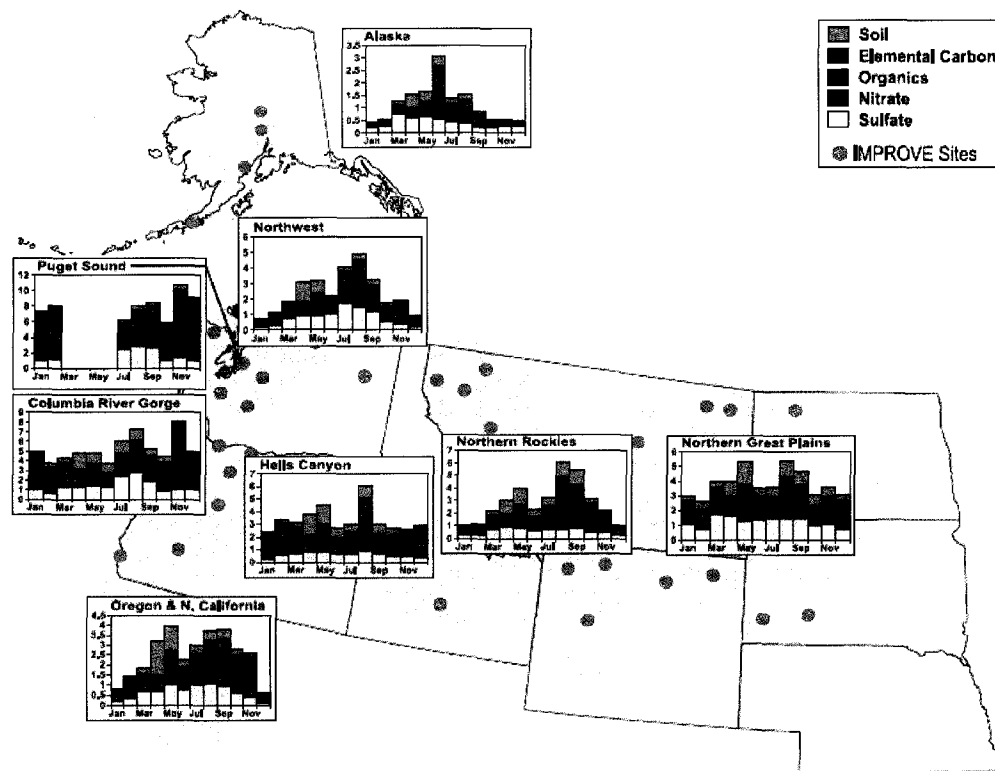


Figure 2.4. Monthly distributions of major aerosol species in the northwest US during 2000 (in $\mu\text{g m}^{-3}$) (from *Malm et al.* [2004]; with permission).

al. [2007] expect that decreasing anthropogenic emissions will lead to even higher contributions by biomass burning to aerosol concentrations in the US. *Spracklen et al.* [2007] noted an increasing trend in OC concentrations in the western US, which is likely due to increases in fire activity, reported by *Westerling et al.* [2006]. These findings suggest that biomass burning will assume more importance in future visibility estimates.

Chapter 3 The Fire Laboratory at Missoula Experiment (FLAME)

The wide range of fuels and fuel conditions consumed by fires leads to large variability in fire behavior, complicating efforts to quantify and predict fire emissions. These efforts require accurate biomass burning inventories and fuel-based emission factors (EF), which relate the mass of fuel burned to the mass of a species emitted. Aircraft-based measurements provide observations of integrated fire emissions with a large spatial extent [e.g., *Haywood et al.*, 2003; *Reid et al.*, 1998], but have difficulty capturing the full time evolution of the biomass burning activity. Field measurements generally suffer from poor information regarding fuels and fire combustion behavior. Laboratory measurements of biomass burning emissions, such as those presented in the following chapters, allow for systematic explorations of the relationship between emissions and the range of combustion behavior displayed by different fuels and their components and moisture conditions. They are a useful tool for determining emission factors, which are expressed as the mass of a species emitted for a given mass of fuel consumed, because the total emissions are readily captured [*Yokelson et al.*, 1996]. Emission factors can be used with fire prediction models to estimate biomass burning emission impacts on local and regional air quality or visibility [*Hodzic et al.*, 2007; *McKenzie et al.*, 2006; *Wiedinmyer et al.*, 2006]. Laboratory-based EF measurements are not complicated by the potentially significant concentrations of background gas and aerosol species present in the field, e.g., dust or biogenic secondary organic aerosol.

The Fire Laboratory at Missoula Experiment (FLAME) was a series of laboratory combustion experiments performed at the U.S. Forest Service's Fire Sciences Laboratory (FSL), located in Missoula, Montana. FLAME was a multi-investigator project conducted to determine the chemical, physical and optical properties of trace gas and aerosol emissions and their impacts on the atmosphere. FLAME 1 took place in May-June 2006 and FLAME 2 took place in May-June 2007. Earlier studies performed at the FSL examined fire combustion behavior [Freeborn *et al.*, 2008], trace gas emissions [Christian *et al.*, 2004; Goode *et al.*, 1999; Yokelson *et al.*, 1996; Yokelson *et al.*, 1997] and aerosol emissions [Chakrabarty *et al.*, 2006; Chen *et al.*, 2006; Chen *et al.*, 2007; Engling *et al.*, 2006a; Freeborn *et al.*, 2008]. FLAME expanded on this work by adding or improving measurements of aerosol properties including EFs for marker compounds, particle size distributions, refractive index, hygroscopicity, cloud condensation nuclei (CCN) and ice nuclei (IN) activity, aerosol optical properties, and relative humidity-dependence of aerosol light scattering. These results will be reported elsewhere [e.g., Carrico *et al.*, submitted; Lewis *et al.*, submitted; Sullivan *et al.*, submitted]. Here I introduce the experiments by describing the ~30 unique fuels tested in ~250 burns, characterize their combustion behavior, and present the results for trace gas emissions. The chapter aids the interpretation of the other FLAME observations and provides a common basis for linking FLAME results to field measurements of fire behavior and regional and global biomass burning inventories.

3.1 Fuels

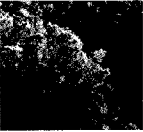
The components (leaves, sticks, and branches) of ~30 unique plant species were burned individually and in various combinations during FLAME 1 and 2. Fuel selection was based on

models indicating fuels that are frequently consumed by fires in the western and southeastern United States. According to a recent Western Regional Air Partnership (WRAP) emissions inventory, four National Fire Danger Rating System (NFDRS) fuel models account for 75% of total PM_{2.5} emissions in the western U.S. They include: California mixed chaparral generally 30 years or older (model B); mature closed chamise stands and oakbrush fields of Arizona, Utah, and Colorado and young, closed stands and mature, open stands of California mixed chaparral (model F); hemlock-Sitka spruce, Coast Douglas-fir, and wind thrown or bug-killed stands of lodgepole pine and spruce (model G); and immature scrub oak and desert shrub associations in the West, and the scrub oak-wire grass type in the Southeast (model T). The selected fuels are listed in Table 3.1.

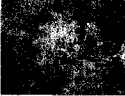
Chaparral is a highly diverse ecosystem that is distributed from Baja California to south-central Oregon and accounts for approximately 6% of the area of California [Keeley and Davis, 2007]. Chaparral-dominated regions coincide with many highly populated areas in California, most notably the Los Angeles and San Diego metropolitan regions, underscoring the need for accurate emission inventories for chaparral fuels. For example, Clinton *et al.* [2006] estimated that ~80% of the fuels consumed by a series of major wildfires in southern California during 2003 were shrubs and duffs. These fires emitted approximately 6 million tons of CO₂ and 0.5 million tons of CO to the atmosphere. The dominant species within the chaparral ecosystem include chamise (*Adenostoma fasciculatum*) and species in the *Ceanothus* and *Arctostaphylos* genera [Keeley and Davis, 2007]. We tested three fuels representing this ecosystem: chamise, hoaryleaf ceanothus (*Ceanothus crassifolius*), and Eastwood's manzanita (*Arctostaphylos glandulosa*). Samples were collected from the San Jacinto Mountains, about 150 km east of Los

Angeles, California (see Table 3.1).

Table 3.1 Plant species that served as fuels during FLAME (all images are in the public domain).

Common name	Scientific name	Picture	Sampling location(s)	Carbon content (%)	Nitrogen content (%)
Alaskan duff	-	-	Tok, Alaska	31	0.5
black spruce	<i>Picea mariana</i>		Fairbanks, AK	55	0.6
chamise	<i>Adenstoma fasciculatum</i>		San Jacinto Mountain, CA	49	1.0
common reed	<i>Phragmites australis</i>		Cameron Prairie NWR, LA	49	0.5
Douglas fir	<i>Pseudotsuga menziesii</i>		Missoula, MT	54	0.5–0.9
gallberry	<i>Ilex coriacea</i> <i>Ilex glabra</i>		Sandhill Crane NWR, MI St. Marks NWR, FL Osceola National Forest, FL	56	0.8
grass	<i>various species</i>	-	Missoula, MT	42	3.0
Gray's rabbitbrush	<i>Ericameria nauseosa</i>		UT	46	1.1
hickory	<i>Carya nutt</i>		Hillsborough, NC	48	2.1
hoaryleaf ceanothus	<i>Ceanothus crassifolius</i>		San Jacinto, CA	48	1.3
kudzu	<i>Pueraria Montana</i>		Athens, GA	47	3.6

lodgepole pine	<i>Pinus contorta</i>		Missoula, MT	42–50	0.3–1.2
longleaf pine	<i>Pinus palustris</i>		North Carolina, Sandhill Crane NWR, MI St. Marks NWR, FL Camp Lejeune, NC	52	1.1
manzanita	<i>Arctostaphylos glandulosa</i>		San Jacinto, CA	48	0.8
needlegrass rush	<i>Juncus roemerianus</i>		St. Marks NWR, FL	49	1.1
palmetto	<i>Serenoa repens</i>		St. Marks NWR, FL Osceola NF, FL Sandhill Crane NWR, MS	51	1.0
peltophorum	<i>Peltophorum inerme</i>	-	Puerto Rico	48	0.8
ponderosa pine	<i>Pinus ponderosa</i>		Missoula, MT	46–49	0.04–1.3
Puerto Rican fern	<i>Dicranopteris pectinata</i>	-	Puerto Rico	46	0.4
rhododendron	<i>Rhododendron minus</i>	-	-	51	0.6
rice straw	<i>Oryza sativa</i>		Douliou City, Taiwan	39–46	0.6–0.9
sagebrush	<i>Artemisia tridentate</i>		Salt Lake City, UT Missoula, MT	47–51	1.5–2.1
sea hibiscus	<i>Hibiscus tiliaceus</i>	-	Puerto Rico	-	-
Smooth cord grass	<i>Spartina alterniflora</i>		St. Marks NWR, FL		
sugar cane	<i>Saccharum officinarum</i>	-	Guangdon Province, China	48	1.3
Swamp sawgrass	<i>Cladium mariscus</i>		Big Branch Marsh NWR, LA	48	2.1
teak	<i>Tectona grandis</i>		Puerto Rico	44	0.8

titi	<i>Cyrilla racemiflora</i>		St. Marks NWR, FL	54	0.9
turkey oak	<i>Quercus laevis</i> Walt.		Hillsborough, NC Camp Lejeune, NC	53	1.3
Utah juniper	<i>Juniperus osteosperma</i>		UT	49	0.9
wax myrtle	<i>Myrica cerifera</i>		Sandhill Crane NWR, FL St. Marks NWR, FL	48–53	1.1–1.4
white spruce	<i>Picea glauca</i>		Fairbanks, AK	52	0.8
wiregrass	<i>Aristida beyrichiana</i>		Sandhill Crane NWR, MS St. Marks NWR, FL Camp Lejeune, NC	48	0.5

Montane and subalpine coniferous forests cover major portions of the Sierra Nevada and Cascade ranges [Fites-Kaufman *et al.*, 2007], and inland regions of the northwestern U.S. [Franklin, 1988] and northern Rocky Mountains [Peet, 1988]. This region encompasses many federal ‘Class 1’ areas that are protected by the RHR. Species from this ecosystem tested during FLAME included: ponderosa pine (*Pinus ponderosa*), logdepole pine (*Pinus cortata*), and Douglas-fir (*Pseudotsuga menziesii*). We burned needles, branches, combinations of needles and branches, as well as litter (dead needles and cones from the forest floor) and duff (litter and a portion of the uppermost layers of soil). These species were collected from several rural locations near Missoula, Montana.

Sagebrush rangeland ecosystems are one of the most widespread in the intermountain west, comprising nearly 64 million ha, primarily in eastern Oregon, southern Idaho, Nevada and Utah [West and Young, 2000]. In addition to big sagebrush (*Artemisia tridentate*), we also burned

two other woody species found from this region: Gray's rabbitbrush (*Chrysothamnus nauseosus*) and Utah juniper (*Juniperus osteosperma*). Samples were collected near Salt Lake City, Utah. Sagebrush samples were collected from two other areas: an urban setting near the Salt Lake City airport and a rural setting near Missoula, Montana.

Land managers in the southeastern U.S. prescribe burns to reduce the risk of wildfires, to control understory vegetation in order to regenerate desirable species, and to benefit wildlife and fire-dependent plant species [Stanturf *et al.*, 2002]. An estimated 900 to 1700 kha of forest, rangeland and cropland are burned each year [Haines *et al.*, 2001], but wildfires also occur in this region, primarily a result of arson or carelessness. We burned several species common to the coastal plain region of the southeastern U.S., including longleaf pine (*Pinus palustris*), and understory shrubs such as saw palmetto (*Serenoa repens*), gallberry (*Ilex glabra*), and wax myrtle (*Myrica cerifera*). During periods of prolonged drought, fire can spread to dry savannah and wetland ecosystems, so we also examined several species of grass found in the southeastern U.S., including titi (*Cyrilla racemiflora*), sawgrass (*Cladium mariscus*), common reed (*Phragmites australis*), wiregrass (*Aristida beyrichiana*) and black needlerush (*Juncus roemerianus*). We also burned kudzu (*Pueraria lobata*), an invasive species that is frequently the target of control efforts, which include prescribed burning.

Most of the southeastern fuels we tested were collected from multiple locations, listed in Table 3.1. They included: a) Cameron Prairie National Wildlife Refuge (NWR), located ~30 km south of Lake Charles, LA; b) Big Branch Marsh NWR on the north shore of Lake Pontchartrain, LA; c) Sandhill Crane NWR, located about ~65 km west of Mobile, AL; d) St. Marks NWR, located ~30 km south of Tallahassee, FL; e) Osceola National Forest (NF),

located 70 km west of Jacksonville, FL; f) Camp Lejeune, located ~10 km east of Jacksonville, NC; and g) a rural area just outside Hillsborough, NC. Kudzu was collected from just south of the University of Georgia campus in Athens, GA.

We examined several fuels collected from fire-impacted regions outside the conterminous United States. Boreal forest fires are a major source of carbon to the atmosphere [Kasischke *et al.*, 1995], and their emissions have major impacts on the atmosphere on local and global scales [e.g., French *et al.*, 2002; O'Neill *et al.*, 2002b; Pfister *et al.*, 2008; Stohl *et al.*, 2006; Trentmann *et al.*, 2006]. White spruce (*Picea glauca*) and black spruce (*Picea mariana*) are ubiquitous conifer species in boreal forests and are commonly found in spruce-feathermoss forests that dominate the southern boreal forest zone, which includes a large portion of Alaska [Elliot-Fisk, 1988]. We tested spruce samples collected within ~50 km of Fairbanks, Alaska. Wildfires and prescribed burns affect belowground biomass in addition to shrubs and trees, so we also burned samples taken from forest floor, which consisted of the uppermost layer of soil with live and dead feathermoss (*Pleurozium schreberi*).

We burned a mixture of plants from the tropics, a region that dominates biomass burning emissions on global scales [Andreae and Merlet, 2001]. Teak (*Tectona grandis*), sea hibiscus (*Hibiscus tiliaceus*), peltophorum (*Peltophorum inerme*), sacky sac bean (*Inga laurina*), and fern (*Decranopteris pectinata*) samples were collected from Puerto Rico. Two agricultural waste products that are burned after harvest were collected in Asia: rice straw (*oryza sativa*) from Taiwan and sugar cane (*saccharum officinarum*) from the Guangdong province of China.

Powders of pure lignin and cellulose, two major components of plant material, were also combusted. We tested mechanically processed ponderosa pine sticks in three different sizes to

study relationships between fuel surface area and volume. We refer to these as small (0.32 x 0.32 x 25.4 cm), medium (0.64 x 0.64 x 25.4 cm) and large (1.27 x 1.27 x 25.4 cm) sticks. The sticks were arranged in an eight-layered lattice before ignition. We also burned a mixture of unidentified grass species collected from a site outside of the FSL.

We attempted to examine potential surface deposition influences on emissions by spraying several chamise and sagebrush (MT) clippings with 1 L of 0.045 g L⁻¹ ammonium sulfate (NH₄SO₂) or with 1 L of 0.072 g L⁻¹ potassium chloride (KCl) solutions. These concentrations were selected in order to coat the plants with approximately 50 times the concentrations measured for these species during FLAME 1. We also tested sagebrush clippings collected near Salt Lake City, Utah that were ‘cleaned’ with de-ionized water (DI) to remove surface contaminants from the leaves and branches of the plant. The cleaning procedure consisted of immersing the clippings in 10 L of de-ionized water for 1 minute.

A selection of fuels were dried through conditioning in an environmental chamber maintained between 35° and 40° C for 48–72 hours. Other fuels were not dried beyond the drying that occurred during shipping and storage—I refer to these as ‘fresh’ fuels. A sample from each fuel was weighed to determine its mass, dried (in some cases for a second time) at a higher temperature in the environmental chamber, and weighed a second time. The change in sample mass was attributed to the loss of water from the sample. The mass of water lost was equal to the sample fuel moisture, expressed as a weight percent. We did not burn samples that were dried through this procedure; these samples were only used to determine the fuel moisture of the samples we did burn. The fuel moistures for the fuel samples burned during each experiment are given in Table 3.2 as a dry weight percent. The moisture contents for most fuels (following

drying) were roughly 10%. The moisture content of the samples tested during FLAME did not necessarily reflect their moisture contents in the field due to the loss of water during shipping and storage.

Table 3.2 Individual burns during FLAME 1 and 2. Ignition methods are noted by: T = torch, P = pilot light, C = coils. Divide emission factors by fuel carbon fraction to obtain emission factors in units of g kg^{-1} carbon.

ID	Plant	Component(s) and/or location	Fuel carbon fraction	Fuel mass (g)	Ash mass (g)	Moisture (%)	Ignition meth.	E_{\max} (kW)	F_{\max} (g s^{-1})	MCE	Emission factors (g kg^{-1} dry fuel)								
											CO ₂	CO	CH ₄	C ₂ H ₄	C ₃ H ₆	NO	NO ₂		
FLAME 1 stack burns													-	-	-	-	-	-	-
0	ponderosa pine	needle liter	-	241	11	11.3	P	0	-	-	-	-	-	-	-	-			
1	cellulose	filter	-	176	-	-	T	0	-	-	-	-	-	-	-	-			
2	cellulose	filter	0.45	174	-	-	T	6.3	0.5	0.983	1621	18	-	-	-	-			
3	cellulose	filter	0.45	181	-	-	T	5.7	0.6	0.971	1595	30	-	-	-	-			
4	cellulose	filter, potassium doped	0.45	179	-	-	T	8.4	0.7	-	-	-	-	-	-	-			
5	cellulose	filter, potassium doped	0.45	216	1	-	T	3.6	0.5	-	-	-	-	-	-	-			
6	cellulose	filter, potassium doped	0.45	180	-	-	T	7.6	0.7	0.916	-	-	-	-	-	-			
7	cellulose	filter, potassium doped	0.45	185	4	-	T	2.7	0.5	0.837	1381	171	-	-	-	-			
8	cellulose	filter, potassium doped	0.45	188	8	-	T	2.3	0.4	-	-	-	-	-	-	-			
9	cellulose	filter, potassium doped	0.45	182	3	-	T	9.3	1.2	0.9	1483	105	-	-	-	-			
10	cellulose	powder	0.45	136	3	-	T	2.2	0.3	0.936	1436	62	-	-	-	-			
11	cellulose	powder	0.45	143	4	-	T	1.7	0.6	-	-	-	-	-	-	-			
12	cellulose	powder	0.45	137	3	-	T	2.5	0.4	-	-	-	-	-	-	-			
13	Montana grass	dry	0.42	50	9	5.0	P	9.3	0.7	-	-	-	-	-	-	-			
14	Montana grass	dry	0.42	50	8	13.0	P	10.2	1	-	-	-	-	-	-	-			
15	Montana grass	dry	0.42	50	7	6.9	P	11.5	1.5	0.933	1409	64	4.2	8.4	-	-			
16	Montana grass	fresh	0.42	196	98	74.0	T	2.5	1.6	0.816	1151	165	-	-	-	-			
17	Montana grass	fresh	0.42	180	97	76.2	T	2.9	0.4	0.839	955	117	-	-	-	-			

ID	Plant	Component(s) and/or location	Fuel carbon fraction	Fuel mass (g)	Ash mass (g)	Moisture (%)	Ignition meth.	E _{max} (kW)	F _{max} (g s ⁻¹)	MCE	Emission factors (g kg ⁻¹ dry fuel)					
											CO ₂	CO	CH ₄	C ₂ H ₄	C ₃ H ₆	NO
18	Montana grass	torch time > 1/2 burn time	0.42	174	111	94.0	T	1.6	0.3	-	-	-	-	-	-	-
19	torch	torch emissions test	0.45	14	-	-	T	1.5	24.1	0.999	-	-	-	-	-	-
20	rice straw		0.43	202	29	12.6	P	18.2	2	0.863	1306	132	-	-	-	-
21	rice straw		0.43	201	30	13.0	P	17.4	1.8	0.872	1311	123	9.3	6.6	-	-
22	rice straw		0.43	201	30	9.9	P	24.1	2.5	0.886	1359	111	-	-	-	-
23	ponderosa pine duff		0.46	251	132	13.9	T	3.3	0.3	0.864	1381	138	-	-	-	-
24	ponderosa pine duff		0.46	251	82	14.6	T	3.6	0.4	0.912	1506	92	-	-	-	-
25	ponderosa pine duff		0.46	251	82	14.7	T	4.7	0.5	-	-	-	-	-	-	-
26	ponderosa pine	needle litter	0.49	250	24	9.5	P	26.7	2.1	0.928	1639	80	-	-	-	-
27	ponderosa pine	needle litter	0.49	250	18	9.5	P	25.7	2	0.918	1617	92	-	-	-	-
28	ponderosa pine	needle litter	0.49	250	26	9.2	P	15.8	1.6	0.92	1623	90	-	-	-	-
29	ponderosa pine	needle litter	0.49	240	27	10.4	P	14.9	1.5	0.897	1560	114	-	-	-	-
30	ponderosa pine	needle litter	0.49	239	27	9.6	P	17.1	1.7	0.908	1596	103	4.4	5.1	-	-
31	ponderosa pine	needle litter	0.49	236	26	9.9	P	19.2	1.6	0.926	1630	83	-	-	-	-
32	ponderosa pine	needle litter	0.49	234	22	9.8	P	21.5	1.9	0.923	1630	86	-	-	-	-
33	ponderosa pine	needle litter	0.49	251	25	9.7	P	20.9	1.8	0.933	1647	75	-	-	-	-
34	ponderosa pine	needle litter	0.49	249	33	10.0	P	17.2	1.4	0.943	1671	64	-	-	-	-
35	ponderosa pine	needle litter	0.49	244	34	10.5	P	13.4	1.2	0.914	1608	96	-	-	-	-
36	ponderosa pine	poor CO ₂ CO ₂ response	-	238	30	10.4	P	-	-	-	-	-	-	-	-	-
37	ponderosa pine	needle litter	0.49	249	30	9.4	P	-	-	0.933	1641	75	-	-	-	-
38	ponderosa pine	needle litter	0.49	253	31	9.6	P	17.1	1.5	0.921	1612	89	-	-	-	-
39	ponderosa pine	needle litter	0.49	249	25	10.1	P	25.6	2.1	0.931	1639	77	-	-	-	-

ID	Plant	Component(s) and/or location	Fuel carbon fraction	Fuel mass (g)	Ash mass (g)	Moisture (%)	Ignition meth.	E _{max} (kW)	F _{max} (g s ⁻¹)	MCE	Emission factors (g kg ⁻¹ dry fuel)						
											CO ₂	CO	CH ₄	C ₂ H ₄	C ₃ H ₆	NO	NO ₂
40	ponderosa pine	needle litter	0.49	251	28	10.9	P	19	1.4	0.908	1597	103	-	-	-	-	-
41	ponderosa pine	needle litter	0.49	250	39	10.0	P	11.9	0.9	0.876	1498	135	-	-	-	-	-
42	ponderosa pine	branches, small, dead	0.48	155	24	9.6	T	5.4	0.5	0.945	1646	61	-	-	0.37	0.34	-
43	ponderosa pine	branches, small, dead	0.48	156	24	9.4	T	4.3	0.4	0.958	1674	47	1.3	10.9	-	0.37	0.32
44	ponderosa pine	branches, small, dead	0.48	148	26	9.0	T	4.6	0.4	0.933	1631	74	-	-	-	0.52	0.19
45	ponderosa pine	branches, large, dead	0.48	285	47	9.3	T	5.7	0.6	0.956	1665	49	-	-	-	0.36	0.33
46	ponderosa pine	branches, large, dead	0.48	273	37	9.1	T	5.9	0.5	0.958	1675	46	1.0	2.7	-	0.3	0.25
47	ponderosa pine	branches, large, dead	0.48	281	50	9.3	T	7.8	0.7	0.948	1655	58	-	-	-	0.34	0.2
48	ponderosa pine	branches, small, fresh	0.48	244	81	43.4	T	4.2	0.4	0.923	-	-	-	-	-	-	-
49	ponderosa pine	branches, small, fresh	0.48	248	109	50.5	T	4.7	0.3	0.902	-	-	-	-	-	-	-
50	ponderosa pine	branches, small, fresh	0.48	246	50	45.7	T	5.6	0.4	0.937	-	-	-	-	-	-	-
51	ponderosa pine	needles, fresh	0.52	245	74	60.7	T	4.6	0.5	0.873	1578	146	-	-	-	0.31	-
52	ponderosa pine	needles, fresh	0.52	245	23	57.5	T	3.4	0.9	0.881	1549	159	5.1	6.0	1.67	0.04	-
53	ponderosa pine	needles, fresh	0.52	240	22	57.9	T	32.9	0.9	0.877	1562	140	-	-	-	0.32	-
54	ponderosa pine	branches, large, fresh	0.48	251	167	63.0	T	4.9	0.7	-	-	-	-	-	-	-	-
55	ponderosa pine	torch time > 1/2 burn time	0.48	249	193	72.0	T	5.2	-	-	-	-	-	-	-	-	-
56	ponderosa pine	branches, large, fresh	0.48	252	180	66.7	T	2	-	-	-	-	-	-	-	-	-
57	lodgepole pine	needle litter, poor CO ₂ response	-	251	53	13.7	P	0	-	-	-	-	-	-	-	-	-
58	lodgepole pine	needle litter	0.45	249	37	15.6	C/T	7.9	0.7	0.921	1493	81	-	-	-	0.45	0.33
59	lodgepole pine	needle litter	0.45	251	50	15.1	C/T	7.6	0.7	0.919	1470	82	3.6	4.1	-	0.47	0.37
60	lodgepole pine	needles, fresh	0.50	250	82	83.7	T	5.6	0.9	0.869	1507	144	-	-	-	0.23	0.19

ID	Plant	Component(s) and/or location	Fuel carbon fraction	Fuel mass (g)	Ash mass (g)	Moisture (%)	Ignition meth.	E _{max} (kW)	F _{max} (g s ⁻¹)	MCE	Emission factors (g kg ⁻¹ dry fuel)						
											CO ₂	CO	CH ₄	C ₂ H ₄	C ₃ H ₆	NO	NO ₂
61	lodgepole pine	needles, fresh	0.50	249	130	90.6	T	2.5	0.9	0.862	1508	154	5.1	20.0	-	0.48	0.25
62	lodgepole pine	needles, fresh	0.50	251	33	76.4	T	4.8	1	0.87	1481	140	-	-	-	0.34	0.07
63	lodgepole pine	branches, dead	0.48	251	23	9.1	T	11.8	-	0.946	1644	60	-	-	-	0.24	0.31
64	lodgepole pine	branches, dead	0.48	251	31	9.3	T	12.7	-	0.942	1651	65	0.9	1.9	-	0.22	0.29
65	lodgepole pine	branches, dead	0.48	249	21	9.0	T	14.5	-	0.951	1668	55	-	-	-	0.24	0.21
66	lodgepole pine duff		0.42	250	101	24.1	C/T	3.5	-	0.936	1419	61	-	-	-	0.46	0.21
67	lodgepole pine duff		0.42	251	79	20.1	C/T	1.6	0.4	0.932	1398	65	7.9	12.2	-	0.22	0.29
68	lodgepole pine duff		0.42	250	115	23.0	C/T	3.2	0.4	0.929	1406	69	-	-	-	0.46	0.8
69	rice straw		0.43	239	37	9.9	P	46.9	3.8	0.917	1421	82	-	-	-	0.48	0.45
70	rice straw	poor CO ₂ CO ₂ response	-	200	35	10.1	P	-	-	-	-	-	-	-	-	-	-
71	rice straw		0.43	254	38	9.0	P	25.7	-	0.91	1376	87	-	-	-	0.48	0.38
72	palmetto	leaves	0.48	253	18	11.7	P	40.9	-	0.92	1608	89	-	-	-	1.01	0.44
73	palmetto	leaves	0.48	250	27	11.2	P	34.4	-	0.912	1589	98	-	-	-	0.93	0.33
74	palmetto	leaves	0.48	251	15	9.9	P	29.3	2.6	0.916	1598	93	-	-	-	0.95	0.4
75	chamise	leaves, dry	0.45	227	14	8.7	P	21.1	2.1	0.886	1426	117	-	-	-	1.06	0.27
76	chamise	leaves, dry	0.45	250	12	19.6	P	24.6	2.6	0.898	1447	105	-	-	-	1.07	0.34
77	chamise	leaves, dry	0.45	245	12	17.9	P	15.9	1.6	0.894	1444	110	4.6	3.2	-	0.95	0.45
78	chamise	branches, dry	0.45	232	104	35.0	P	5.2	0.6	0.929	1515	74	-	-	-	0.51	0.49
79	chamise	branches, dry	0.45	251	75	30.7	P	6.2	0.6	0.928	1505	74	2.8	4.2	-	0.44	0.47
80	chamise	branches, dry	0.45	252	49	34.3	P	6.9	0.5	0.884	1432	119	-	-	-	0.25	0.39
81	chamise	leaves, fresh	0.45	243	49	52.2	T	8.2	1.2	0.87	-	-	-	-	-	-	-
82	chamise	leaves, fresh	0.45	248	27	56.0	T	11.1	1.5	0.828	-	-	-	-	-	-	-

ID	Plant	Component(s) and/or location	Fuel carbon fraction	Fuel mass (g)	Ash mass (g)	Moisture (%)	Ignition meth.	E _{max} (kW)	F _{max} (g s ⁻¹)	MCE	Emission factors (g kg ⁻¹ dry fuel)						
											CO ₂	CO	CH ₄	C ₂ H ₄	C ₃ H ₆	NO	NO ₂
83	chamise	leaves, fresh	0.45	255	41	60.4	T	10.8	1.3	0.896	-	-	4.5	5.7	2.63	-	-
84	chamise	branches, fresh	0.45	242	51	23.9	T	4.9	0.4	0.917	1495	86	-	-	-	0.45	0.56
85	chamise	branches, fresh	0.45	243	65	49.7	T	6.2	0.5	0.931	1514	72	1.8	4.1	-	0.46	0.72
86	chamise	branches, fresh	0.45	257	56	50.0	T	5.2	0.7	0.932	1514	71	5.3	8.4	-	0.41	0.58
87	manzanita	leaves, fresh, torch time > 1/2 burn time	-	250	97	101.0	T	0	-	-	-	-	-	-	-	-	-
88	manzanita	leaves	0.45	250	51	107.0	T	4.8	0.6	0.911	-	-	-	-	-	-	-
89	manzanita	leaves	0.45	250	56	75.4	T	5.1	0.7	0.91	1448	91	-	-	-	0.28	0.45
90	manzanita	branches, fresh	0.45	250	24	70.5	T	5.2	1	0.887	1425	116	-	-	-	0.34	0.41
91	manzanita	branches, fresh	0.45	250	27	67.8	T	7.5	0.9	0.891	1432	112	2.5	2.3	1.75	0.41	0.45
92	manzanita	branches, fresh	0.45	250	28	62.9	T	6.1	0.9	0.881	1411	121	-	-	-	0.35	0.51
93	manzanita	leaves, dry	0.45	250	32	59.8	T	4.4	0.7	0.867	1331	130	-	-	-	0.34	0.61
94	manzanita	leaves, dry	0.45	250	17	52.5	T	7.7	1	0.879	1371	120	9.1	8.6	3.68	0.35	0.44
95	manzanita	leaves, dry	0.45	250	16	55.2	T	3.8	0.8	0.863	1337	135	-	-	-	0.44	0.52
96	chamise	branches, leaves, dry	-	250	19	19.1	P	0	-	-	-	-	-	-	-	-	-
97	chamise	branches, leaves, dry	0.45	250	26	16.5	P	14	1.1	0.941	1542	62	-	-	-	0.94	0.31
98	chamise	branches, leaves, dry	0.45	250	16	19.4	P	25.5	2.3	0.927	1519	76	1.5	2.1	0.61	0.96	0.41
99	chamise	branches, leaves, dry	0.45	251	18	19.2	P	29.4	2.3	0.938	1542	65	-	-	-	1.03	0.28
FLAME 1 chamber burns																	
100	ponderosa pine	needles, branches	0.49	108	4	9.6	P	-	-	0.964	1320	31	2.9	12.1	-	0.53	0.3
101	chamise		0.51	301	18	11.8	P	-	-	0.942	1751	68	1.3	3.1	3.55	1.71	0.37
102	ponderosa pine	needles, litter, branches	0.49	200	15	10.3	P	-	-	0.937	1645	70	2.1	1.9	1.98	0.61	0.73

ID	Plant	Component(s) and/or location	Fuel carbon fraction	Fuel mass (g)	Ash mass (g)	Moisture (%)	Ignition meth.	E _{max} (kW)	F _{max} (g s ⁻¹)	MCE	Emission factors (g kg ⁻¹ dry fuel)								
											CO ₂	CO	CH ₄	C ₂ H ₄	C ₃ H ₆	NO	NO ₂		
103	chamise		0.51	202	16	14.4	P	-	-	0.947	1761	63	1.1	2.6	1.83	1.72	0.67		
104	rice straw		0.43	208	35	8.1	P	-	-	0.942	1469	58	1.2	1.7	0.84	0.71	0.47		
105	ponderosa pine duff	duff	0.46	201	94	13.9	T	-	-	0.915	1506	89	1.7	3.0	1.17	0.44	0.83		
106	Alaskan duff		0.36	193	97	9.2	T	-	-	0.902	1160	80	2.8	5.7	1.82	-	0.49		
107	manzanita		0.50	200	7	11.0	P	-	-	0.969	1766	36	0.9	2.6	1.08	0.88	0.45		
108	juniper	foilage, sticks	0.49	209	11	8.7	P	-	-	0.956	1713	51	0.2	0.7	-	2.18	0.18		
109	sage and rabbitbrush	foilage, sticks	0.45	199	17	9.1	P	-	-	0.935	1529	68	1.3	1.5	2.23	1.43	0.46		
110	lignin	powder	0.45	195	12	17.0	T	-	-	0.974	1561	27	1.1	1.9	-	0.15	0.83		
111	lodgepole pine	litter, twigs, 55 g consumed in chamber	0.49	203	55	13.7	P	-	-	0.965	1685	39	3.6	3.2	-	0.7	1.22		
112	Puerto Rican fern		0.46	192	18	12.8	P	-	-	0.943	1571	60	1.7	2.3	2.1	0.8	0.52		
113	chamise		0.51	200	14	12.3	P	-	-	0.94	1746	70	1.3	2.8	1.17	2.09	0.33		
114	wax myrtle	branches, foilage	0.50	200	48	13.6	P	-	-	0.927	1667	84	3.0	6.8	4.66	0.99	1.05		
115	longleaf pine	needles	0.50	80	7	16.4	P	-	-	0.972	1753	32	2.1	9.6	5.51	0.6	1.26		
116	Puerto Rico mixed woods 1	sticks	0.45	101	17	16.8	T	-	-	0.952	-	-	1.7	0.8	0.77	-	-		
117	palmetto	leaves	0.48	200	13	10.4	P	-	-	0.946	1664	60	1.6	0.6	-	1.3	0.78		
118	ceanothus		0.50	200	19	24.3	P	-	-	0.926	1678	86	2.0	1.2	1.3	1.55	1.12		
FLAME 2 stack burns																			
119	ponderosa pine	needles, test	-	250	-	-	C	-	-	-	-	-	-	-	-	-	-		
120	ethanol	test	0.45	~15	0	-	C	8	0.5	0.985	1225	12	-	-	-	0.3	0.2		
121	ethanol	test	0.45	~15	0	-	C	6.4	0.4	0.983	1189	13	-	-	-	0.07	0.26		
122	propane torch	test	0.45	-	-	-	T	1.6	0	0.994	1226	5	-	-	-	0.09	0.55		

ID	Plant	Component(s) and/or location	Fuel carbon fraction	Fuel mass (g)	Ash mass (g)	Moisture (%)	Ignition meth.	E _{max} (kW)	F _{max} (g s ⁻¹)	MCE	Emission factors (g kg ⁻¹ dry fuel)						
											CO ₂	CO	CH ₄	C ₂ H ₄	C ₃ H ₆	NO	NO ₂
123	propane torch	test	0.45	-	-	-	T	1.2	0	0.996	1583	4	-	-	-	0.24	0.73
124	ponderosa pine	needles, test	-	250	-	-	C	0	-	-	-	-	0.0	0.0	0	-	-
125	ponderosa pine	needles, test	-	247	-	-	C	0	-	-	-	-	0.0	0.0	0	-	-
126	palmetto	leaves, MS	0.51	247	21	7.1	C	32.9	3.4	0.951	1732	56	1.1	1.0	0.22	-	-
127	palmetto	leaves, MS	0.51	257	25	-	C	31.2	2.7	0.924	1652	87	2.1	1.2	0.33	-	-
128	palmetto	leaves, FL inland, coils left on	-	253	20	6.3	C	0	-	-	-	-	0.0	0.0	0	-	-
129	palmetto	leaves, FL inland	0.52	240	22	-	C	43.5	3.5	0.934	1687	76	2.1	1.1	0.47	-	-
130	palmetto	leaves, FL coastal	0.51	265	20	5.0	C	51.4	3.8	0.945	1717	63	1.8	1.3	0.47	-	-
131	palmetto	leaves, FL coastal	0.51	245	21	-	C	32.6	3.1	0.942	1694	66	2.7	1.7	0.55	5.19	-
132	gallberry	MS	0.56	197	15	6.0	C	41.2	3.6	0.95	1864	63	2.3	1.6	0.49	7.35	-
133	gallberry	MS	0.56	225	6	-	C	68.4	4.3	0.945	1871	69	2.6	1.9	0.49	-	-
134	longleaf pine	needles, MS	0.50	250	64	6.4	C	17.5	1.9	0.927	1555	78	3.2	1.7	0.59	4.11	-
135	longleaf pine	needles, MS	0.50	249	33	-	C	23.1	2.3	0.925	1573	81	-	-	-	4.01	-
136	oak	leaves, NC	0.50	106	2	8.1	C	47.6	2.9	0.937	1616	69	1.4	2.7	0.62	-	-
137	oak	leaves, NC	0.50	145	30	-	C	38.3	2.3	0.944	1667	62	1.0	1.8	0.33	-	-
138	hickory	leaves, NC	0.48	141	36	7.8	C	53.2	4.1	0.93	1566	75	3.0	2.0	0.55	-	-
139	hickory	leaves, NC	0.48	98	9	-	C	28.3	3.5	0.937	1600	69	2.4	1.8	0.54	-	-
140	wiregrass	MS	0.48	201	24	5.4	C	26.4	2.4	0.961	1687	44	0.8	0.5	0.21	3.8	-
141	wiregrass	MS	0.48	26	57	-	C	25.4	2.4	0.962	1674	42	0.6	0.3	-	3.25	-
142	titi		0.54	168	30	7.8	C	52.3	3.7	0.942	1825	71	1.8	1.1	-	7.64	-
143	titi		-	152	35	-	C	0	-	-	-	-	0.0	0.0	-	-	-
144	common reed		0.49	255	199	76.7	C	9.4	1.3	0.948	1650	58	1.3	2.7	-	9.57	-

ID	Plant	Component(s) and/or location	Fuel carbon fraction	Fuel mass (g)	Ash mass (g)	Moisture (%)	Ignition meth.	E _{max} (kW)	F _{max} (g s ⁻¹)	MCE	Emission factors (g kg ⁻¹ dry fuel)						
											CO ₂	CO	CH ₄	C ₂ H ₄	C ₃ H ₆	NO	NO ₂
145	common reed		0.49	248	202		C	9.8	0.9	0.967	1663	36	1.9	2.7	-	6.64	-
146	wax myrtle	MS	0.50	200	32	13.3	C	55.3	5.2	0.916	1646	96	2.0	1.5	0.42	-	-
147	wax myrtle	MS	0.50	188	20		C	42	3.3	0.902	1553	107	3.9	2.9	0.81	6.21	-
148	kudzu	GA	0.47	197	107	99.2	C	10.8	2.1	0.859	1121	117	6.1	7.7	2.11	5.72	-
149	kudzu	GA	0.47	221	138		C	7.6	2	0.855	1071	116	3.6	9.1	2.43	7.35	-
150	palmetto and gallberry	MS	0.54	246	32	23.1	C	14.3	2	0.916	1701	99	2.8	2.7	0.73	4.77	-
151	palmetto and gallberry	MS	0.54	252	23		C	25.6	3.1	0.911	1613	101	6.5	2.9	1.32	5.09	-
152	longleaf pine and wiregrass	127 g LLP, 90 g WG	0.52	244	32	6.8	C	21.7	2.1	0.922	1701	92	2.6	1.0	0.53	4.13	-
153	longleaf pine and gallberry		0.52	0.52	29		C	16.1	1.5	0.932	-	-	2.5	1.7	-	-	-
154	oak and hickory	leaves	0.49	101	10	10.7	C	24	2.8	0.939	1582	66	2.3	2.4	0.75	9.56	-
155	oak and hickory	leaves	-	161	15		C	0	-	-	-	-	0.0	0.0	0	-	-
156	ponderosa pine	needles	0.52	25	2	9.9	C	1.8	0.3	-	-	-	0.5	0.2	-	-	-
157	ponderosa pine	needles	0.52	250	152		C	50.6	3.9	0.907	1526	99	6.1	2.9	1.59	3.2	-
158	ponderosa pine	needles, Nox saturated	0.52	2360	111	9.2	C	203.3	20.2	0.935	-	-	3.5	1.3	0.77	-	-
159	ponderosa pine	needles	0.52	80	7		C	18.5	1.7	0.903	1465	100	6.0	4.3	1.67	4.64	-
160	ponderosa pine	needles, Nox saturated	0.52	502	30		C	90.5	6.4	0.939	1659	68	4.5	2.0	1.04	-	-
161	black spruce	dry	0.45	244	20	12.8	C	47.4	4	0.962	1565	39	1.0	0.8	0.42	-	-
162	black spruce	dry	0.45	244	29		C	42.7	3.1	0.941	1522	61	0.9	0.9	0.37	5	-
163	black spruce	fresh	0.45	250	14	22.5	C	29.5	2.8	0.957	1536	44	1.0	1.4	0.36	4.72	-
164	black spruce	fresh	0.45	250	17		C	34.1	3	0.951	1509	49	1.2	1.4	0.38	4.94	-
165	Douglas fir	needles	0.54	250	150	42.1	C	8.2	1.1	0.845	1387	162	3.9	6.1	2.02	4.53	-

ID	Plant	Component(s) and/or location	Fuel carbon fraction	Fuel mass (g)	Ash mass (g)	Moisture (%)	Ignition meth.	E _{max} (kW)	F _{max} (g s ⁻¹)	MCE	Emission factors (g kg ⁻¹ dry fuel)						
											CO ₂	CO	CH ₄	C ₂ H ₄	C ₃ H ₆	NO	NO ₂
166	Douglas fir	needles	0.54	250	25		C	5.9	0.7	0.86	1278	133	4.3	7.8	2.44	3.43	-
167	Douglas fir	branches	0.54	252	228	51.2	C	7.8	1	0.922	1620	88	-	-	-	1.49	3.27
168	Douglas fir	branches	0.54	279	240		C	7.4	1.1	0.936	1561	68	-	10.0	-	1.6	3.17
169	Douglas fir	branches, dry	0.54	51	51	20.7	C	33.3	-	0.926	1781	91	-	11.0	4.89	2.7	1
170	Douglas fir	branches, fresh	0.54	250	57	47.6	C	13.7	1.8	0.87	1418	135	6.4	11.3	3.35	3.97	1.75
171	Douglas fir	branches, fresh	0.54	260	20		C	13.6	2	0.892	1571	121	3.0	7.0	2.09	4.36	1.49
172	Douglas fir	needles, dry	-	250	151	27.5	C	0	-	-	-	-	0.0	0.0	0	-	-
173	Douglas fir	needles, dry	0.54	251	55	20.9	C	12.5	1.4	0.922	1729	93	1.6	3.1	1.12	4.23	-
174	manzanita		0.50	277	31	28.3	C	26.7	2.9	0.921	1606	88	-	-	-	4.34	-
175	manzanita		0.50	253	27		C	30.6	3.4	0.914	1580	95	2.7	3.0	0.9	5.07	-
176	ceanothus		0.50	253	34	15.4	C	52.1	4.6	0.902	1577	109	1.2	2.3	0.32	7.05	-
177	ceanothus		0.50	257	34		C	48	4.1	0.911	1613	100	2.0	1.7	0.45	-	-
178	ponderosa pine	sticks, 0.32 x 0.32 x 25.4 cm, 8-layer cake	0.54	253	4	6.9	C	20.8	1.7	0.965	1893	44	0.6	0.7	-	0.78	-
179	ponderosa pine	sticks, 0.32 x 0.32 x 25.4 cm, 8-layer cake	0.54	250	0		C	24.6	1.7	0.97	1868	37	0.6	1.0	-	0.74	-
180	ponderosa pine	sticks, 0.64 x 0.64 x 25.4 cm, 4-layer cake	0.52	250	0	7.7	C	15.7	1	0.964	1806	44	1.5	0.7	-	1.01	-
181	ponderosa pine	sticks, 0.64 x 0.64 x 25.4 cm, 4-layer cake	0.52	250	12		C	19.6	1.4	0.966	1790	41	0.8	0.5	-	0.89	-
182	ponderosa pine	sticks, 1.27 x 1.27 x 25.4 cm, 4-layer cake	0.52	260	17	7.8	C	9.9	1.2	0.954	1773	55	0.4	0.7	-	0.86	-
183	ponderosa pine	sticks, 1.27 x 1.27 x 25.4 cm, 4-layer cake	0.52	259	6		C	12.8	0.9	0.961	1800	46	1.0	0.5	-	1.05	-
184	sagebrush	UT	0.47	255	133	33.3	C	31.4	1.9	0.905	1438	96	1.3	1.0	0.45	5.77	-
185	sagebrush	UT, washed	0.48	249	128	21.2	C	40.6	3.3	0.892	1437	111	3.8	6.4	1.19	6.75	-

ID	Plant	Component(s) and/or location	Fuel carbon fraction	Fuel mass (g)	Ash mass (g)	Moisture (%)	Ignition meth.	E _{max} (kW)	F _{max} (g s ⁻¹)	MCE	Emission factors (g kg ⁻¹ dry fuel)						
											CO ₂	CO	CH ₄	C ₂ H ₄	C ₃ H ₆	NO	NO ₂
186	chamise		0.51	259	36	22.1	C	65.5	5.4	0.91	1657	104	1.4	1.7	0.34	-	-
187	rice straw	test	-	130	16	10.2	C	0	-	-	-	-	-	-	-	-	-
188	chamise		-	251	36		C	0	-	-	-	-	-	-	-	-	-
189	chamise	washed	0.51	176	20	27.4	C	42.8	3.6	0.897	1632	119	-	-	-	8.26	-
190	chamise	washed	0.51	163	18		C	37.8	3.3	0.918	1672	95	1.1	1.7	0.39	6.4	-
191	ponderosa pine	needles, flaming	0.55	200		8.2	C	33	-	0.991	1968	12	-	-	-	0.08	-
192	ponderosa pine	needles, flaming	0.55	130			C	23.9	-	0.993	1936	9	-	-	-	0.15	-
193	ponderosa pine	needles, flaming	0.55	134			C	33.7	-	0.994	1957	8	-	-	-	0.13	-
194	ponderosa pine	needles, flaming	0.55	152			C	38	2.4	0.994	1969	8	-	-	-	0.28	-
195	ponderosa pine	needles, flaming	0.55	150			C	-	-	0.991	1977	11	-	-	-	0.19	-
196	ponderosa pine	needles, flaming, feeding	0.55	50			C	-	0	0.985	1935	19	-	-	-	3.41	-
197	ponderosa pine	needles, flaming, feeding	0.55	50			C	0	0	0.981	1938	23	0.2	0.5	0.18	3.2	-
198	ponderosa pine	needles, smoldering	0.55	300			C	11.1	0.6	0.807	1551	236	-	-	-	2.17	-
199	ponderosa pine	needles, smoldering	0.55	302			C	11	0.3	0.777	1425	260	-	-	-	2.11	-
200	ponderosa pine	needles, smoldering	0.55	2500			C	34.7	1.5	0.802	1150	181	-	-	-	1.84	-
201	ponderosa pine	needles, smoldering, feeding	0.55	2500			C	2	0.7	0.725	1254	303	-	-	-	0.99	-
202	rice straw	flaming	0.45	1500		11.0	C	133.1	11.4	0.977	1583	24	-	-	-	0.88	-
203	rice straw	smoldering	0.45	1500	179	7.8	C	-0.5	1.5	-	-	-	-	-	-	-	-
204	ponderosa pine	needles, heading	0.45	250	14	9.1	P	23.4	3.2	0.944	1484	56	1.9	0.9	0.46	3.79	-
205	ponderosa pine	needles, heading	0.45	250	17		P	21.9	2.6	0.934	1485	67	1.8	1.1	0.58	3.89	-
206	ponderosa pine	needles, backing	0.45	250	12	8.7	P	12.7	1.2	0.944	1502	56	3.1	2.0	0.59	4.74	-
207	ponderosa pine	needles, backing	0.45	250	12		P	13.5	1.3	0.948	1500	52	0.8	1.2	0.5	4.09	-

ID	Plant	Component(s) and/or location	Fuel carbon fraction	Fuel mass (g)	Ash mass (g)	Moisture (%)	Ignition meth.	E _{max} (kW)	F _{max} (g s ⁻¹)	MCE	Emission factors (g kg ⁻¹ dry fuel)						
											CO ₂	CO	CH ₄	C ₂ H ₄	C ₃ H ₆	NO	NO ₂
208	sagebrush	heading	0.5	250	36	23.6	P	18.5	-	0.862	1412	144	-	12.0	4.41	5.75	-
209	sagebrush	heading	0.50	250	31		P	14.5	2.2	0.859	1387	145	6.0	5.3	1.95	4.71	-
210	sagebrush	backing	0.50	257	30	23.7	P	15.7	2.2	0.874	1462	134	6.8	5.0	1.69	5.81	-
211	sagebrush	backing	0.50	257	25		P	16	2.6	0.888	1505	120	6.3	4.4	1.43	5.87	-
212	sagebrush	coated with ammonium sulfate	0.51	160	19	9.4	C	53.2	5.4	0.898	1602	116	5.3	3.4	1.35	-	-
213	sagebrush	coated with ammonium sulfate	0.54	270	18	11.2	C	59.6	6.4	0.925	1800	93	2.3	2.0	-	-	-
214	sagebrush	coated with potassium chloride	0.50	270	19	16.3	C	58.7	5.8	0.878	1537	136	4.8	3.5	1.4	-	-
215	sagebrush	coated with potassium chloride	0.55	250	20	11.8	C	82	6.3	0.93	1845	88	1.3	2.1	0.32	6.8	-
216	sagebrush	MT	0.46	250	23	30.7	C	43.3	4.2	0.867	1365	133	6.9	6.7	2.26	5.7	-
217	sagebrush	MT	0.46	250	24	27.6	C	26.9	3.2	0.837	1234	153	7.5	6.7	2.28	4.94	-
218	rice straw		0.43	250	31	8.0	C	26.2	2.8	0.926	1423	73	3.4	1.5	0.67	5.38	-
219	rice straw		0.43	250	31		C	41.5	4.6	0.918	1387	79	2.5	1.7	0.48	4.48	-
220	turkey oak	leaves	0.53	250	6	8.5	C	60.4	5.4	0.89	1602	126	5.1	3.8	1.17	6.5	-
221	turkey oak	leaves	0.53	250	8		C	51.8	4.9	0.881	1558	133	6.8	4.9	1.57	6.15	-
222	charcoal	US, test	-	250			C	0	-	-	-	-	0.0	-	-	-	-
223	black needle rush and saw grass		0.50	247	26	32.7	C	24.9	2.6	0.912	1619	99	3.4	2.9	-	4.01	-
224	black needle rush and saw grass		0.50	254	16		C	20.3	2.7	0.87	1458	139	5.8	3.3	0.69	3.53	-
225	saw grass		0.48	175	13	14.9	C	42.9	4.2	0.895	1510	113	3.4	1.8	-	6.31	-
226	saw grass		0.48	165	54		C	68.9	5.3	0.906	1533	101	3.4	2.1	-	5.46	-
227	Alaskan duff		0.36	170	70	10.9	C	4.6	0.4	0.743	765	168	-	-	-	1.57	-
228	Alaskan duff		0.36	116	34		C/T	4.7	-	0.858	973	103	-	-	-	2.53	-
229	charcoal	United States	0.65	505	223	4.1	C/T	1.5	-	0.811	1825	271	-	-	-	7.07	-

ID	Plant	Component(s) and/or location	Fuel carbon fraction	Fuel mass (g)	Ash mass (g)	Moisture (%)	Ignition meth.	E _{max} (kW)	F _{max} (g s ⁻¹)	MCE	Emission factors (g kg ⁻¹ dry fuel)							
											CO ₂	CO	CH ₄	C ₂ H ₄	CaH ₆	NO	NO ₂	
230	charcoal	Asian	0.72	503	209	5.7	C/T	7.5	-	0.841	1951	235	-	-	-	-	0.85	-
231	coil	30 s	-	-	-	-	-	-	-	-	-	-	-	-	-	-	-	-
232	coil	1 min	-	-	-	-	-	-	-	-	-	-	-	-	-	-	-	-
233	coil	15 s	-	-	-	-	-	-	-	-	-	-	-	-	-	-	-	-
FLAME 2 chamber burns																		
234	ponderosa pine	needles, test	-	250	11	8.7	C	-	-	-	-	-	-	-	-	-	-	-
235	longleaf pine and wiregrass	100 g LLP, 50 g WG, venting	0.52	150	36	5.6	C	-	-	0.978	1696	25	1.8	1.0	0.45	2.06	-	-
236	black needle grass	venting during run	0.49	150	13	5.6	C	-	-	-	-	-	6.9	6.0	-	-	-	-
237	oak and hickory	leaves	0.49	101	8	7.4	C	-	-	0.953	-	-	2.1	2.7	0.67	-	-	-
238	Douglas fir	needles and branches	0.54	100	4	4.5	C	-	-	0.944	1863	70	1.5	0.5	0.11	8	-	-
239	Douglas fir	needles and branches	-	100	17	12.1	C	-	-	-	-	-	0.0	0.0	0	-	-	-
240	palmetto	leaves, FL coastal	0.51	105	14	5.6	C	-	-	0.958	1781	50	1.0	0.9	-	3.77	0.33	-
241	palmetto	MS	0.51	105	18	5.5	C	-	-	0.958	1781	49	1.6	1.2	-	2.97	0.83	-
242	rice straw		0.43	100	20	8.3	C	-	-	0.961	1491	39	1.4	0.5	0.15	3.4	-	-
243	Alaskan duff		0.36	87	29	9.7	C/T	-	-	0.906	1066	71	1.3	0.8	0.34	-	1.15	-
244	rhododendron		0.51	100	5	10.6	C	-	-	0.961	1783	46	1.8	1.2	-	3.87	-	-
245	black spruce		0.53	101	39	5.0	C	-	-	0.974	1809	31	0.1	1.7	1.1	0.98	3.18	-
246	Douglas fir	branches, dry	0.54	50	27	14.1	C	-	-	0.94	-	-	3.4	1.1	-	-	-	-
247	Alaskan duff		0.36	40	21	12.2	C	-	-	0.927	1205	60	2.8	1.1	-	-	1.47	-
248	wiregrass	FL	0.48	50	5	7.8	C	-	-	0.973	-	-	0.4	-	-	-	-	-
249	chamise		0.51	100	5	5.5	C	-	-	0.946	-	-	0.9	1.1	-	-	-	-

ID	Plant	Component(s) and/or location	Fuel carbon fraction	Fuel mass (g)	Ash mass (g)	Moisture (%)	Ignition meth.	E _{max} (kW)	F _{max} (g s ⁻¹)	MCE	Emission factors (g kg ⁻¹ dry fuel)						
											CO ₂	CO	CH ₄	C ₂ H ₄	C ₃ H ₆	NO	NO ₂
250	black needlerush	FL	-	50	5	7.3	C	-	-	-	-	0.0	0.0	-	-	-	
251	sagebrush	MT	0.50	250	16	7.8	C	-	-	0.945	1709	63	2.7	1.2	0.36	5.46	
252	longleaf pine	needles, MS	0.50	250	135	8.9	C	-	-	0.949	1677	57	0.5	1.4	0.92	4.04	
253	gallberry	MS	-	50	5	4.5	C	-	-	-	-	-	0.0	-	-	-	
254	sugar cane		0.48	50	4	9.4	C	-	-	0.977	-	-	0.8	0.9	-	-	
255	white spruce		0.52	50	13	38.3	C	-	-	0.971	-	-	1.7	-	-	-	

3.2 Experimental procedure

The experiments were performed at the U.S. Forest Service's combustion testing facility at the Fire Sciences Laboratory in Missoula, Montana, depicted in Figure 3.1. The main combustion chamber is a square room measuring 12.4 x 12.4 x 19.6 m high with a total volume of ~3000 m³. An exhaust stack located at the center of the room extends from 2.1 m above the floor and runs up to the chamber ceiling. An inverted funnel at the bottom of the exhaust stack narrows from a 3.6 m diameter opening to the 1.6 m stack diameter [Christian *et al.*, 2003]. Sampling ports that pass through the walls of the exhaust stack are located ~15.5 m above the floor, and are accessed from a platform running around the stack near the chamber ceiling. Several sampling ports located in the chamber wall connected the combustion room to adjacent laboratory space where instruments were located during a portion of the experiments.

3.2.1 Burn procedure

Two major classes of experiments were performed during FLAME: stack burns and chamber burns. All burns are listed in Table 3.2. The combustion chamber was pressurized with temperature- and humidity-conditioned air drawn from outside of the building. This forced air in the chamber up through the exhaust stack during each stack burn. Emissions from the fuel bed, located directly beneath the inverted funnel, traveled up through the exhaust stack to the platform sample ports. Turbulence in the stack mixed emissions. We measured the air velocity and temperature in the stack at the location of the gas sampling ports using a Kurz Model 455 hot-wire anemometer. We measured mean flow velocities in the exhaust stack of approximately 3.6 m s⁻¹ during FLAME 1 and 2, which yields a Reynolds number on the order of 4×10^5 , well

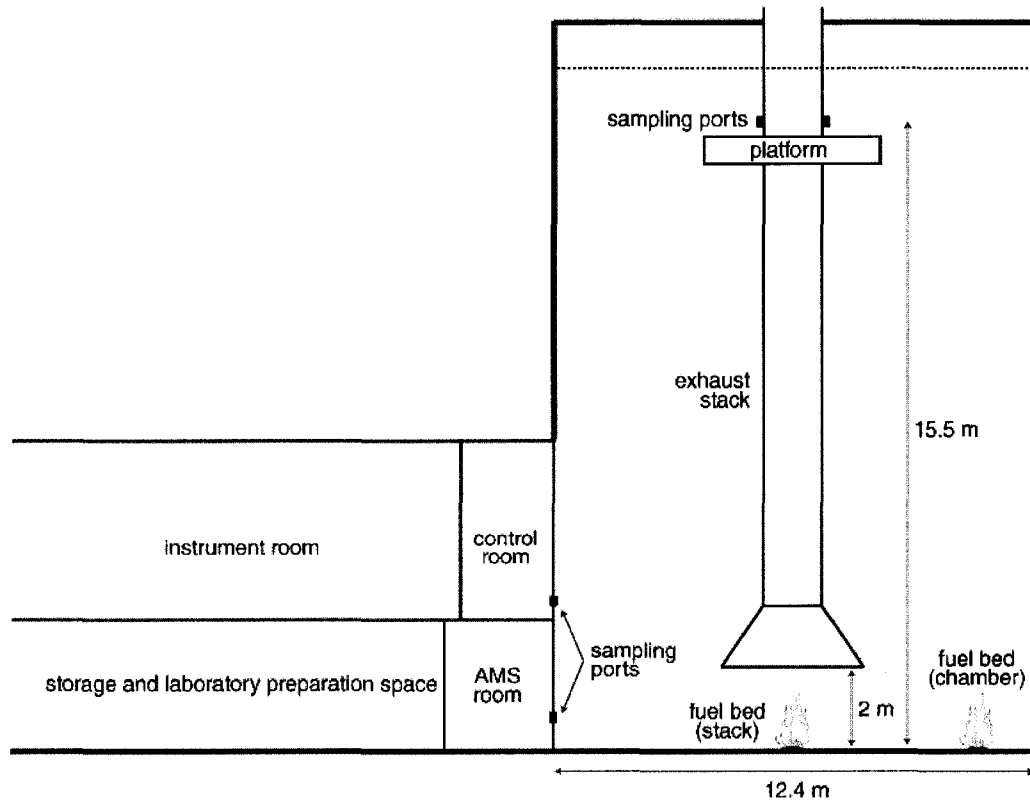


Figure 3.1 Schematic of the US Forest Service Fire Sciences Laboratory combustion chamber and adjacent laboratory space, located in Missoula, Montana. Image is to scale. The locations of the fuel bed during stack and chamber burns are indicated.

within the turbulent regime. *Christian et al.* [2004] reported three observations to demonstrate that emissions are well mixed before reaching the sampling ports. First, they measured the temperature profile across the stack at the sampling height and found it was constant. Second, CO_2 , CO and total hydrocarbon (THC) mixing ratios measured optically across the path spanning the stack agreed with point measurements [*Goode et al.*, 1999]. Finally, mixing ratios of reactive species determined using proton transfer reaction mass spectrometry (PTR-MS) were constant across the stack cross-section.

During chamber burns the combustion room was sealed by closing the exhaust stack, forcing biomass burning emissions to mix with the room air and remain 'trapped' in the chamber. This provided lower species concentrations and longer sampling periods (~2 hours)

compared to those possible during stack burns, which typically lasted from five to ten minutes. The fuel bed was placed about halfway between the exhaust stack and the chamber wall during these burns. The combustion chamber was vented with conditioned outdoor air partway through several chamber experiments to dilute trace gas and aerosol concentrations. A large circulation fan operated in one corner of the chamber to facilitate mixing.

The majority of samples burned during stack experiments were placed on a 46 x 61 cm horizontal metal tray covered with an inert, ceramic heat shield. For experiments that tested emissions from inclined fuel beds, we used a longer (91 x 25 cm), specially-built stand that was tilted 21° with respect to the horizontal. Fuels were stacked horizontally on the fuel bed to facilitate ignition, except for two large fuel mass burns (~2500 g). During these experiments, the fuels were stacked in a cylindrical, wire cage to keep the material confined to the fuel bed during the burn. For all burns, the fuel bed was placed on a Mettler-Toledo PM34 balance to monitor its mass as a function of burn time. The initial fuel mass (m_0) and final residual or 'ash' mass (m_f), listed in Table 3.2 for each burn, were measured with a higher sensitivity PM34-K balance (Mettler-Toledo). Initial fuel masses ranged from 25 to 2500 g depending on the objective of the experiment and desired emission concentrations; most were between 100 and 250 g.

We ignited the fuel bed using several methods, depending on the fuel and its moisture level. During FLAME 1, the dry fuels were easily ignited using a butane pilot lighter applied briefly to the edge of the fuel bed. Higher moisture level fuels required the application of a propane torch or heated metal coils for a longer period of time, in some cases continuously, to maintain the fire. These ignition methods often resulted in a propagating flame front that moved through the fuel bed and simultaneous flaming and smoldering combustion in different parts of

the fuel bed. Based on our experiences in the first study, we modified the fuel bed used in FLAME 2 to provide a more evenly distributed ignition source [Sullivan *et al.*, submitted]. Fuels were placed on a lattice of heating tape that was soaked with ~25 mL of ethanol. An electrical current passed through the tapes, heating them and causing the ethanol to vaporize and eventually ignite, together with the fuel.

In total, 256 experimental burns took place during FLAME, including stack, chamber, and test burns. Test burns were performed to verify ignition method suitability for various fuels, to measure possible ignition method artifacts, and to calibrate instruments. Table 3.2 gives the components of the plant or plants that were burned during each burn, the ignition method, and the fuel moisture content. The times for the flaming and smoldering combustion phases, shown in Table 3.2, were identified based on a subjective determination of the point after which no flames were visible by observers during the experiment. These were verified from video recordings of each burn. We performed three replicate burns for each fuel type during FLAME 1 stack burns and two replicate burns during FLAME 2. With the exception of several chamise burns, there were no replicate chamber burns during either study. We did burn the same fuel several times in other chamber burns, but these are not classified as replicate burns because fuel mass was not held constant.

We designed several subsets of burns to examine particular aspects of fuel properties or combustion behavior believed to affect emissions. These experiments tested: a) flaming and smoldering combustion of ponderosa pine needles and rice straw; b) ponderosa pine needles with different fuel masses; c) homogeneous and heterogeneous samples of ponderosa pine, chamise, manzanita, Douglas fir and lodgepole pine components; d) high and low fuel moisture

for ponderosa pine, lodgepole pine, chamise, manzanita, black spruce, and Douglas fir; e) combinations of Utah sagebrush and rabbitbrush, Puerto Rican mixed woods, palmetto and gallberry, longleaf pine and wiregrass, oak and hickory and black needlerush and saw grass; f) fuel bed orientation for ponderosa pine needles and sagebrush; g) fuel dimension for ponderosa pine sticks; h) surface treatments (KCl and $(\text{NH}_4)_2\text{SO}_4$, rinsing) of sagebrush and chamise; i) identical plant species from different geographical locations; and j) dilution/ventilation of Utah sagebrush and longleaf pine needle emissions.

3.2.2 Real-time gas measurements

Real-time measurements of CO_2 , CO, H_2O , THC, NO, and NO_2 were made at ~2 second resolution. Carbon dioxide and water vapor mixing ratios were measured with a Li-Cor Model 6262 non-dispersive infrared gas analyzer. The instrument has a maximum range of 1000 ppm and a precision of ± 1 ppm at 350 ppm. Carbon monoxide mixing ratios were measured using a Thermo Environmental Model 48C variable-range gas filter correlation analyzer. The instrument precision was $\pm 1\%$ of the full scale. Low and high concentration CO_2 and CO standards (CO_2 : 362 and 499 ppm; CO: 0.5 and 2.7 ppm) were passed through the analyzers prior to burn ignition. These data provided calibration curves needed to process the raw data. THC mixing ratios were measured using flame ionization detection by a Thermo Environmental Model 51 analyzer. The instrument was calibrated at the beginning of each day during the experiments using a mixed hydrocarbon calibration standard consisting of CH_4 , C_2H_4 and C_3H_8 at 8.1 ppm concentration.

Reactive odd-nitrogen ($\text{NO}_x = \text{NO} + \text{NO}_2$) mixing ratios were measured with a Thermo

Environmental Model 42 chemiluminescence analyzer at concentrations up to 2000 ppb with a precision of ± 0.5 ppb. The instrument responds to the emission of light resulting from the electronic relaxation of NO_2 formed from the reaction of NO with O_3 . To measure total NO_x , ambient NO_2 is first transformed to NO using a heated molybdenum converter. NO_2 is given by the difference between NO_x and NO . We observed high (>2000 ppb) NO_x concentrations during several FLAME 2 burns that saturated the analyzer. We do not report NO_x data for these burns. In some cases the NO measurement was valid, but the larger NO_x signal was at or above the instrument saturation limit, resulting in unreliable NO_2 data, so we only report NO observations in these cases.

The gas analyzers were located on the measurement platform at the top of the exhaust stack during the stack burns and drew sample through ports in the stack. During chamber burns, they operated in a control room adjacent to the combustion chamber and drew sample through a port in the wall of the chamber. The carbon gas analyzers sampled the smoke using aluminum lines and the other analyzers sampled using Teflon lines. The analyzer drew sample from a dilution system during the FLAME 1 stack burns and directly from the stack during FLAME 2. During chamber burns the analyzer sampled directly from the chamber. In all cases the THC analyzer collected sample through stainless steel lines.

The THC analyzer sampled from a dilution tank during FLAME 1 stack burns. We adjusted the flow of N_2 gas into the tank using a mass flow controller. The flow controller settings varied by burn depending on the level of dilution required to maintain two nephelometers that were also drawing sample from the dilution system below saturation. Dilution factors were determined from $[\text{CO}_2]$ measured simultaneously in the stack and dilution

tank and ranged from 15:1 (N₂:sample) to zero dilution.

3.2.3 Canister gas measurements

Canister samples of emissions drawn directly from the stack and chamber were analyzed by Dr. Steve Baker of the FSL for CO₂, CO, methane and C₂-C₄ gases with a Hewlett Packard model 5890 Series II gas chromatograph. The CO₂ and CO analysis uses a 1 ml sample loop to inject the sample, a 1/8" diameter x 6 foot Carbosphere (Alltech) column to separate CO₂, CO, and air with a helium carrier gas at a flow rate of 16 ml min⁻¹. After separation in the column the sample enters a nickel catalyst methanizer (375° C), that converts the CO₂ and CO to CH₄, and then a flame ionization detector (FID) at 350° C. The oven temperature program is isothermal at 100° C. The C₁-C₄ analyses are performed using a 0.25 ml sample loop, a 0.53 mm x 30 m GS-Q (J&W Scientific) column with a helium carrier gas at 6 ml min⁻¹. The oven temperature program for this analysis is 30° C for 6 minutes, then increasing by 10° C min⁻¹ to a final temperature of 90° C for 8 minutes.

Chromatogram data were processed by Hewlett Packard ChemStation II software. A set of gas standards bracketing the sample concentrations were analyzed with each set of samples to construct a standard curve for each compound. Based on the integrated peak areas, the sample concentrations were calculated from the standard curves. Duplicate analyses were performed every sixth sample to quantify measurement precision error. National Institute of Standards and Technology (NIST) primary standards of CO₂, CO, and CH₄ were analyzed as samples to measure overall accuracy.

3.2.4 Annular denuder gas measurements

We measured ammonia (NH_3) and nitric acid (HNO_3) emitted from fires using annular denuders. The denuders operated in series with a filter sampling system connected to stack sampling ports during stack burns or sitting on the floor of the chamber during chamber burns. The sample flow was nominally 10 lpm. The HNO_3 denuder was coated with 10 ml 0.1% sodium chloride in a 1:9 methanol/water solution and the NH_3 denuder was coated with 10 ml 1% citric acid in methanol [Lee *et al.*, 2004]. Coated denuders were dried by passing N_2 gas through them for ~10 minutes. After sampling, each denuder was extracted using 10 ml of deionized water. Extracts were analyzed using a Dionex DX-500 series ion chromatograph. Details of the analysis procedure are given by Lee *et al.* [2004]. Minimum detection limits (MDL) for each species were determined from blank samples. Values below the MDL are not reported.

3.2.5 Ignition artifact testing

To account for ignition artifacts, we performed several tests to measure emissions from the ethanol-tape and propane torch used to light fuels, listed in Table 3.2. During the ethanol tests, we soaked the heating tape with ~15 g ethanol. Figure 3.2 shows excess mixing ratios ($[\text{X}]_{\text{observed}} - [\text{X}]_{\text{background}}$; denoted by ' Δ ') for THC, CO, and CO_2 , and fuel mass as a function of time for an ethanol test burn (burn 120, Table 3.2). The fuel mass increased about 90 s before ignition when ~17 g ethanol was applied to the heating coils. ΔTHC increased about 60 s prior to ignition, probably due to ethanol evaporating from the coils. At ignition, fuel mass rapidly decreased and we observed a ~20 s pulse of THC and CO_2 . CO and NO_x emissions from the

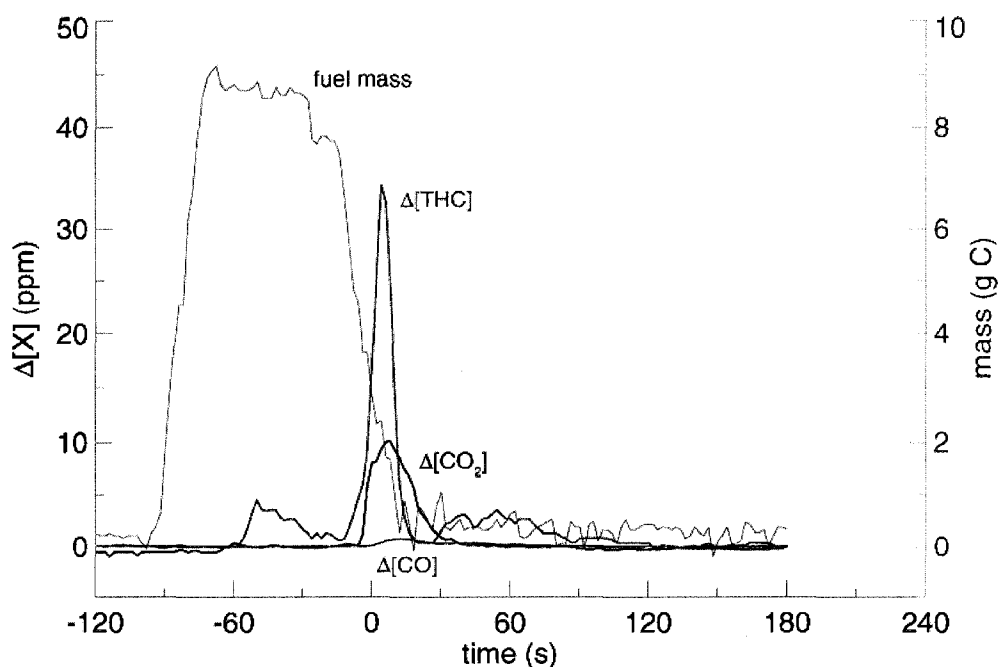


Figure 3.2 Timeseries of excess CO_2 and CO (ppm) and THC (ppm C) mixing ratios measured in the stack during a test ethanol-only burn during FLAME 2 (burn 120). The fuel (ethanol) mass (in g C) measured using the fuel bed balance is plotted in gray on the right-hand-side axis. Time is in seconds from ignition time.

ethanol tests were negligible. The propane torch produced a negligible amount of THC, CO , and NO , but did emit $70\text{-}90 \text{ mg CO}_2 \text{ s}^{-1}$ while operating.

I adjusted the total mass of CO , CO_2 and THC emitted for burns that used the ethanol-coil ignition system by subtracting the mean of the total emissions for each species during the two ethanol-coil test burns (0.13 g CO , 12.5 g CO_2 , 1.2 g THC). In general, the mass of plant material burned was 5-10 times greater than the mass of ethanol consumed during the ignition procedures. Exceptions were burns featuring low fuel masses conducted during FLAME 2 chamber burns. Emission data for burns that featured the propane torch ignition method were adjusted by subtracting the total torch emissions, which were determined by multiplying the time the torch was on by the species emission rate. Burns that required the torch to be applied to

maintain combustion for a period greater than half of the total burn time are omitted in the analyses.

3.3 Fire behavior

Fire behavior during FLAME depended on fuel components, moisture, mass, and the fuel bed orientation. I evaluated combustion conditions during each stack burn using ‘instantaneous’ (10-second averaged data) and fire-integrated modified combustion efficiency (MCE), energy release rates (E_t), and fuel-bed mass loss rates (F). The decrease in fuel bed mass resulted from both the combustion of dry biomass and the vaporization of water in the fuel, but for simplicity I refer to this mass loss as the fuel mass loss. The fuel mass, fluid velocity (v_s), and stack temperature (T_s) data obtained at two-second resolution were averaged to 10-second intervals prior to calculation of rates to reduce noise in their time derivatives.

3.3.1 Mass loss and energy release rates

The thermal energy release rate for each stack burn was approximated using measured stack temperatures and mass flow rates [Freeborn *et al.*, 2008]:

$$E_t = c_p \rho_{air} \Delta T_s Q \quad 3.1$$

I assumed air was the working fluid, and thus c_p was the constant pressure specific heat of air ($c_p = 1.012 \text{ J g}^{-1} \text{ K}^{-1}$), ρ_{air} was the air density ($\rho_{air} = 1204 \text{ g m}^{-3}$) and ΔT_s is the difference between the temperature measured in the stack and its mean value prior to ignition. Integrating the thermal energy release rate over the entire burn gives an estimate of the thermal energy released by the fire (E_{tot}); dividing it by the dry mass of fuel consumed yields an estimate of the effective heat of combustion (H_t) for the fuel. The true heats of combustion (H) for many woods and foliage

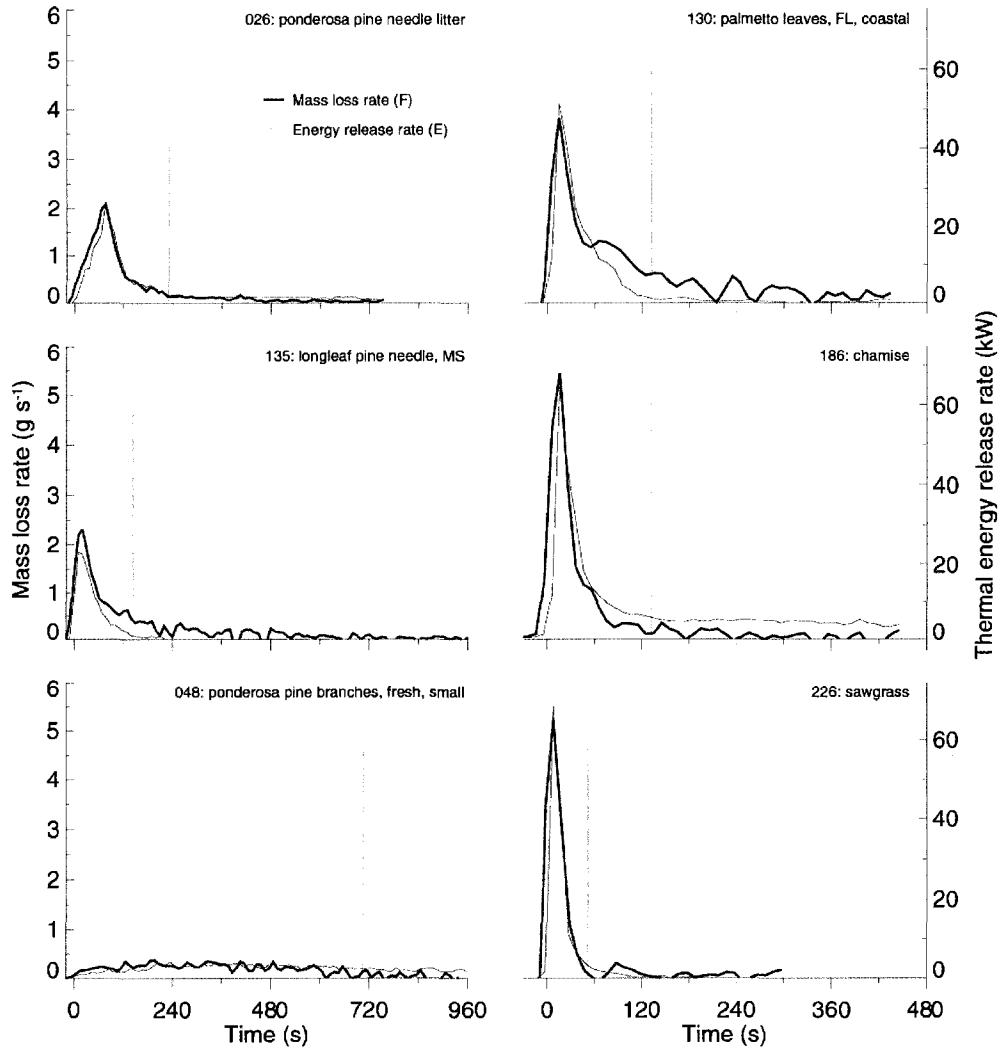


Figure 3.3 Instantaneous fuel mass loss rate (F) in g s^{-1} and energy release rate (E) in kW as function of time for six burns during the FLAME 1 and 2 studies. Time is given as the time elapsed from ignition time. The transition time from flaming to smoldering combustion, determined visually, is shown by the vertical gray line. Note the left column plots feature a time period twice as long as that for the plots in the right column. Burn identifiers and fuel names given on each plot correspond values given in Table 3.2.

have been measured using oxygen bomb calorimetry [e.g., *Shafizadeh and Degroot, 1976*]. Our estimates of H_f are lower than these values because we performed open burns with natural levels of oxygen that featured incomplete combustion processes.

Figure 3.3 shows observations of F , in g s^{-1} , and E_t , in kW, for six burns during FLAME 1 and 2 stack experiments. Thermal energy release and mass loss rates were highly correlated during the burns, indicating the amount of thermal energy released per unit mass of fuel

consumed was relatively constant. The relationship was also consistent when comparing burns to each other, with ~ 10 kJ energy released for every gram of biomass consumed. Values of F and E_t reached their maximum values near the same time, within two minutes of the ignition time, for all of these burns except for fresh pine branches. The higher moisture content in this fuel inhibited the flaming phase of combustion resulting in much lower values of F and E_t compared to the other fuels depicted in Figure 3.3. This fuel also required application of the propane torch for a long period of time to sustain a flame. The chamise and saw grass burns had the largest maximum values of F (~ 5.5 g s $^{-1}$) and E_t (~ 70 kW) of the six burns. The range of values of F and E_t I observed was similar to that found with similar experimental designs [Freeborn *et al.*, 2008; Yokelson *et al.*, 1996].

There was a strong correlation between maximum values of F and E_t observed during stack burns ($r^2 = 0.95$), shown in Figure 3.4. The slope of a least-squares linear fit to the data gives a study-wide estimate of H_f of 11.6 ± 0.2 MJ kg $^{-1}$ (regression coefficient ± 1 -sigma uncertainty estimates). The frequency distributions of the maximum values of E_t and F are also shown in Figure 3.4. Median values of F and E_t were 1.84 g s $^{-1}$ and 17.1 kW, respectively. The maximum values of F and E_t were not strong functions of the fraction of fuel consumed nor fuel moisture. They are listed in Table 3.2. The largest values of E_t were usually observed for low moisture content fuels. The mean maximum E_t for fuels with moisture contents greater than 40% of dry weight was 6.7 ± 5.4 kW (mean ± 1 standard deviation) compared to 28.3 ± 35.2 kW for fuels with moisture contents less than 40%.

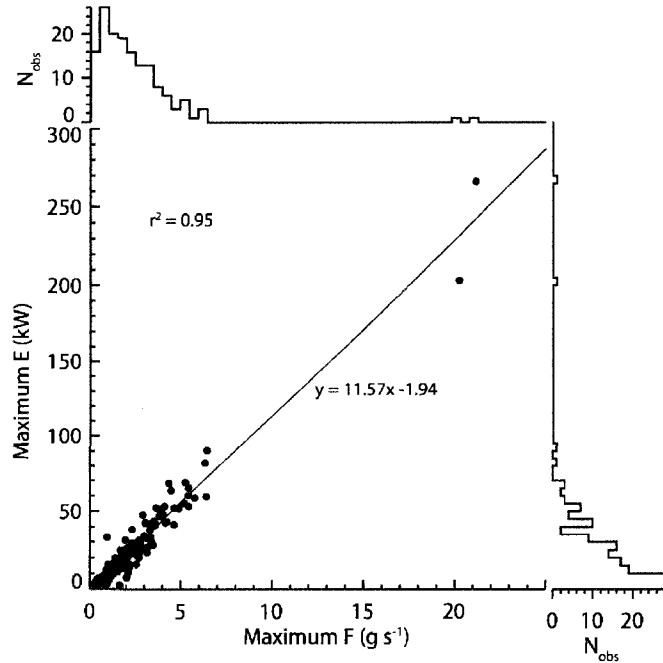


Figure 3.4 Maximum instantaneous rates of energy release (E , kW) versus fuel mass loss (F , g s^{-1}) for FLAME stack burns. The linear least-squares regression to data is shown along with the coefficient of variation. Frequency distributions of the parameters are also shown.

3.3.2 Modified combustion efficiency

Combustion behavior can be quantified using molar combustion efficiency (CE), defined as the ratio of the moles of CO_2 emitted by the fire to the moles of all carbon species emitted by the fire. Measuring the entirety of carbon species emitted is difficult, particularly during non-laboratory studies, and has not been as widely reported compared to MCE. I used MCE, which depends solely on the molar ratio of the emitted CO and CO_2 , as the standard measure of combustion efficiency for the vast majority of results presented in this work. It is given by [Ward and Radke, 1993]:

$$\text{MCE} = \frac{\Delta[\text{CO}_2]}{\Delta[\text{CO}] + \Delta[\text{CO}_2]} \quad 3.2$$

where $\Delta[\text{CO}_2]$ and $\Delta[\text{CO}]$ are the excess mixing ratios of CO_2 and CO in the stack or chamber.

I assumed the ambient concentrations of CO and CO_2 were equal to their mean values

measured in the stack or chamber immediately prior to ignition (usually from 120 to 10 seconds before ignition). MCE was calculated on both instantaneous and fire-integrated bases. For stack burns I determined the fire-integrated MCE for each burn by dividing the total mass of CO₂ (in g C) emitted during the fire by the total mass of CO₂ plus CO (in g C) emitted during the fire. For chamber burns, I computed the mean MCE during the 5-minute period between 30 and 35 minutes following ignition to represent the fire's combustion behavior. I chose this period based on the average time it took for concentrations of CO and CO₂ in the chamber to stabilize. The next chapter compares MCE to CE, after I have introduced the carbonaceous aerosol measurements.

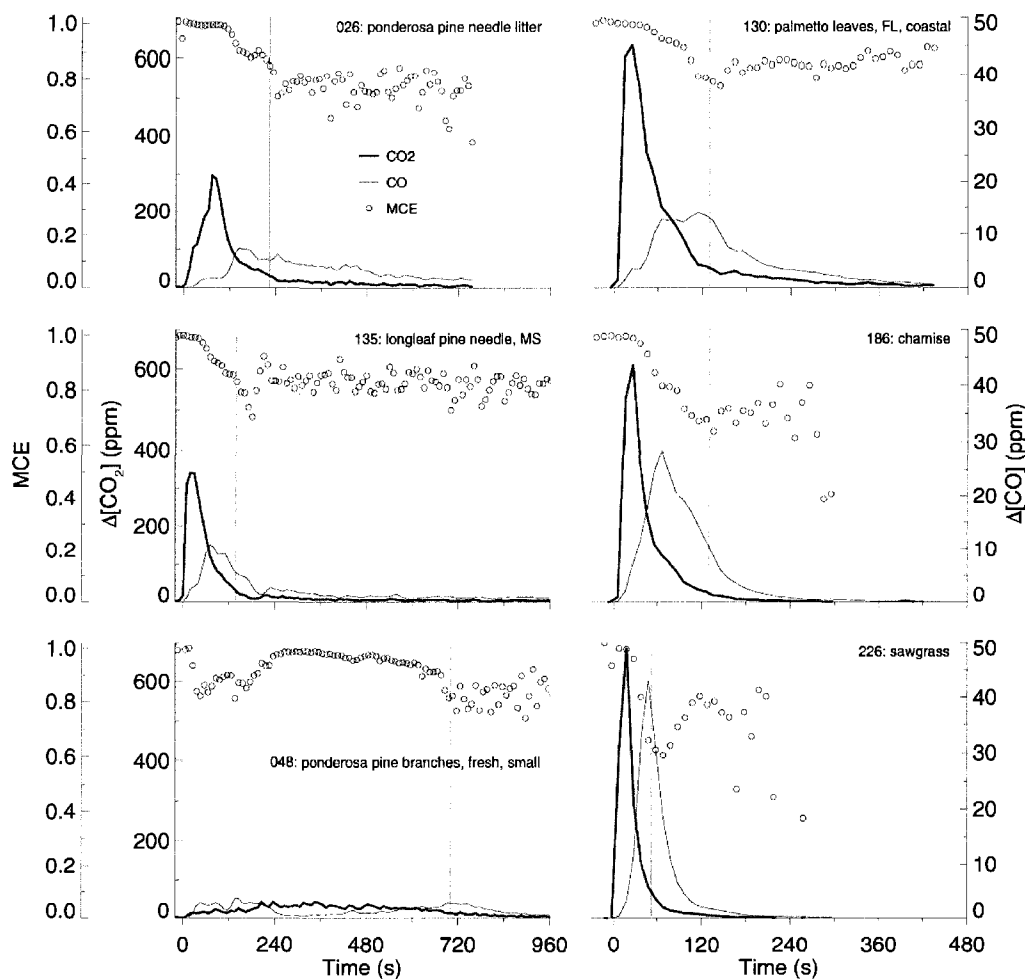


Figure 3.5 Excess CO and CO₂ mixing ratios (ppm) and modified combustion efficiency (MCE) as a function of time for six stack burns. CO₂ is plotted against the left-hand side axis and CO is plotted against the right-hand side axis. MCE is plotted against the outermost left-hand side axis.

Figure 3.5 shows $\Delta[\text{CO}]$, $\Delta[\text{CO}_2]$, and MCE for six burns during FLAME. The peak emission for $\Delta[\text{CO}_2]$ during these burns was about 20-60 times the peak $\Delta[\text{CO}]$ emissions in terms of absolute mass and about 15-40 times larger on a carbon mass basis. The majority of CO and CO₂ emissions during these burns occurred during flaming dominated-combustion in the first few minutes of the burns. Carbon dioxide emission rates were strongly tied to energy release and fuel mass consumption rate (compare with Figure 3.3), reflecting the strong relationship between carbon consumption and the release of oxidized carbon species and heat. Carbon monoxide emissions peaked before the visual transition to smoldering combustion during the

pine, palmetto, and chamise burns, reflecting the gradual transition from flaming to smoldering combustion that was not captured by the single transition time value. All six burns feature a 1-2 minute transition period when MCE drops from values of 0.98-1.0 to values near 0.8. Combustion conditions varied within the fuel bed during the transition period, with portions of the fuel being consumed by flaming combustion and others being consumed by smoldering combustion. *Chen et al.* [2007] observed similar shifts in MCE during the FLAME pilot study.

Table 3.2 lists the fire-integrated MCE for each burn performed during FLAME 1 and 2. I also presented these data grouped by fuel type and component in Figure 3.6 to aid interpretation of the results because of the large number of samples in the table. In general, groups of fuels with the highest mean fuel moistures had the lowest median MCE values and vice versa. Burns featuring common reed (*Phragmites australis*) were exceptions to this pattern. This fuel burned with a short flaming phase that was not followed by a noticeable smoldering phase. For the rest of the burns, the mixture of fresh Montana grasses collected outside the laboratory had the lowest median MCE. The study average integrated MCE was 0.92 ± 0.04 (mean ± 1 standard deviation), but this value reflects the choice of fuels we tested rather than being a representative value for natural fires. The range of MCE observed within a given fuel group primarily reflected the fuel moisture variability within the group. For example, burning 'fresh' ponderosa pine needles had an integrated MCE of 0.86, while burning 'dry' ponderosa pine needles had an MCE of 0.94. The ranges shown in Figure 3.6 also provide an indication of the variability between replicate burns. For example, for 15 replicate ponderosa pine needle litter burns (~250 g of fuel each), we calculated integrated MCE values ranging from 0.88 to 0.94 with a mean of 0.92 ± 0.02 .

My observations of integrated MCE for the FLAME burns are similar to previous laboratory and field measurements listed in Table 3.3. *Yokelson et al.* [2007a] observed MCE values ranging from 0.88 to 0.94 in open biomass burning plumes over Brazil. Fires in pine-dominated forests surrounding Mexico City produced smoke with MCE between 0.90 and 0.97

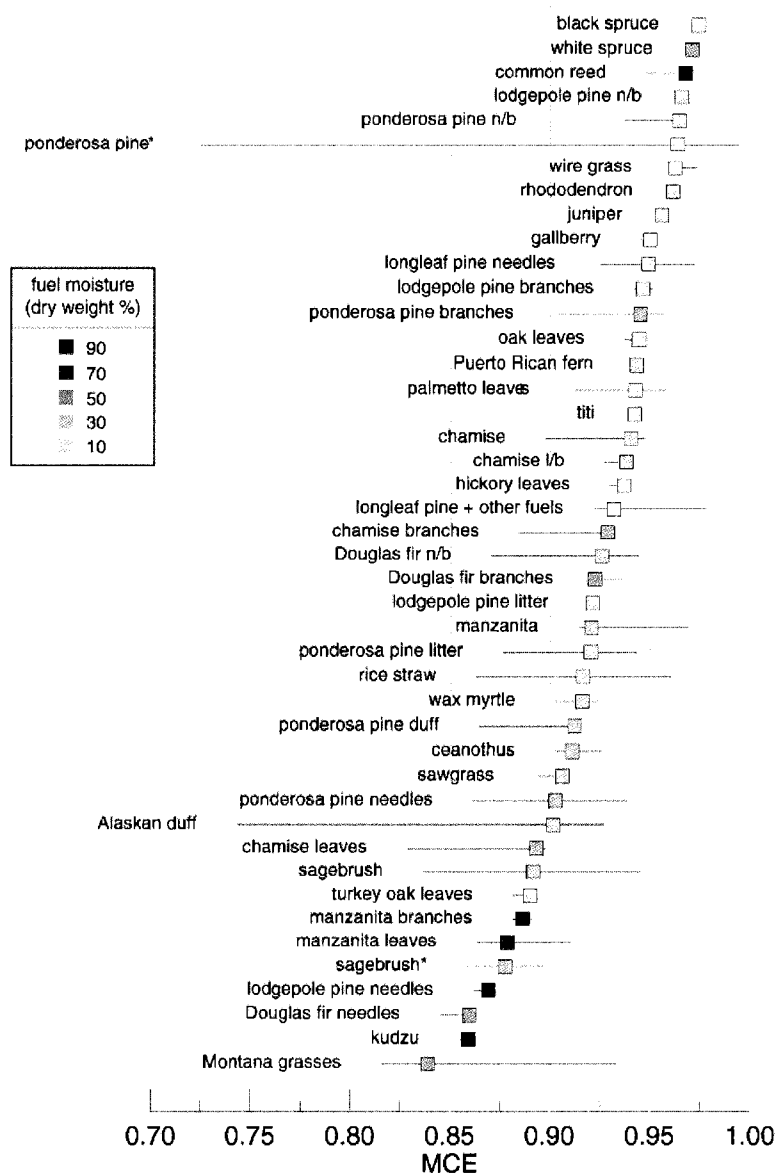


Figure 3.6 Median modified combustion efficiencies (MCE) for fuel groups burned during FLAME 1 and 2, ranked in order of decreasing MCE. Horizontal bars indicate the range of MCE observed within a fuel class. Each median value is shaded to indicate the mean fuel moisture of the fuel group. Starred fuel groups (*) included flaming- and smoldering-phase only, heading and backing experiments.

Table 3.3 Previously reported emission factors for CO, CO₂, CH₄, C₂H₄ and C₃H₆ from selected studies of natural fires and laboratory burns. Gases were measured using open path Fourier transform IR spectrometry (OP-FTIR), aircraft-based Fourier transform IR spectrometry (AFTIR), and gas chromatography with flame ionization detection (GC-FID).

Study	Location/Fuel/ Method	MCE range (mean)	Emission factors (g kg ⁻¹ fuel)					NO _x (as NO)
			CO	CO ₂	CH ₄	C ₂ H ₄	C ₃ H ₆	
Bertschi et al. [2003]	smoldering logs and belowground biomass (OP-FTIR)	0.85–0.90	110–165	1440–1610	2.4–23.2	0.3–2.4	0.4–2.4	-
Sinha et al. [2003]	savannah fires in Africa (GC-FID)	0.90–0.98 (0.94)	25–120 (70)	1620–1790 (1700)	0.6–2.5 (1.7)	0.2–1.1 (0.6)	0.1–0.5 (0.2)	2.4–4.1 (3.3)
Christian et al. [2003]	Indonesian fuels at the FSL (OP-FTIR)		50–210	1220–1700	0.9–20.8	0.5–2.8	0.2–3.9	0.6–1.7 ^a
Yokelson et al. [2003]	savannah fires in Africa (AFTIR)	0.92–0.98 (0.94)	30–105 (71.5)	1640–1780 (1703)	0.6–3.6 (2.2)	0.7–1.6 (1.2)	-	2.4–4.6 (3.4)
Christian et al. [2007]	smoldering logs in Brazil (OP-FTIR)	0.79 ± 0.06	230 ± 65	1340 ± 120	17.1 ± 10.0	1.4 ± 0.8	1.4 ± 1.1	-
Yokelson et al. [2007a]	Brazil (AFTIR)	0.88–0.94 (0.91)	60–135 (100)	1570–1680 (1620)	3.4–7.5 (5.7)	0.5–1.5 (1.0)	0.1–0.7 (0.5)	0.6–4.9 (1.4)
Yokelson et al. [2007b]	pine-dominated forests near Mexico City (AFTIR)	0.90–0.97 (0.93)	30–110 (80)	1610–1750 (1660)	2.8–6.9 (5.0)	0.4–1.4 (0.9)	0.2–0.9 (0.5)	4.2–10 (7.4)
Chen et al. [2007]	North American wildland fuels at the FSL	0.95–0.99	15–60	1460–1760	-	-	-	0.7–8.7 (3.3)
Andreae and Merlet [2001] ¹	extratropical forest (summary of published data)	0.90	105 ± 35	1570 ± 130	4.7 ± 1.9	1.1 ± 0.6	0.6 ± 0.2	3.0 ± 1.4
FLAME	North American wildland fuels at the FSL (GC-FID)	0.75–0.98 (0.88)	20–180 (65)	770–1980 (1560)	0.1–11.0 (2.7)	0.1–20.0 (3.1)	0.1–5.5 (1.2)	0.1–15 (4.2)

^aOnly reported NO emission factor.

during MILAGRO (Megacity Initiative Local and Global Research Observations) [Yokelson *et al.*, 2007b]. Sinha *et al.* [2003] observed MCE ranging from 0.90–0.98 over savannah fires in southern Africa. Other laboratory combustion experiments for biomass fuels produced MCE values of 0.97–0.98 for African savannah fuels (dambo grass and miombo), and 0.81–0.95 for Indonesian fuels, including peat, rice straw, and Alang-alang [Christian *et al.*, 2003].

3.4 CO and CO₂ emission factors

Figure 3.7 gives emission factors for CO, CO₂, NO and THC (EFX), calculated

assuming fuel carbon fraction in the fuel is constant throughout the burn, as a function of burn time for the six example burns described previously. In general, the maximum $EFCO_2$ was observed during the earlier periods of the burn when flaming phase combustion was dominant. During this period $EFCO_2$ approached 1700 g kg^{-1} fuel, near the upper limit resulting from the complete combustion of the carbon in the fuel. This is also reflected by MCE values near 1.0 during these periods, as shown in Figure 3.5.

$EFCO_2$ decreased as combustion began to transition to smoldering combustion, reaching values between 1000 and 1500 g kg^{-1} fuel. The smoldering-phase $EFCO_2$ displayed more variability between fuels compared to the variability during the flaming-phase. Unlike $EFCO_2$, $EFCO$ and $EFTHC$ were highest during the later stages of the burns when smoldering-phase combustion dominated. $EFCO$ and $EFTHC$ were usually correlated during the burns. $EFCO$ was between 100 - 250 g kg^{-1} fuel and $EFTHC$ was between 50 and 100 g C kg^{-1} fuel during smoldering combustion. $EFNO$ were more variable between burns, likely due to the varying N-content of the fuels, with peak values near 50 - 80 g NO kg^{-1} .

Table 3.2 lists fire-integrated EF that reflect the relative contributions from flaming and smoldering combustion. The study mean $EFCO_2$ was $1560 \pm 196 \text{ g kg}^{-1}$ dry fuel (mean ± 1 standard deviation), near the $1569 \pm 131 \text{ g kg}^{-1}$ dry fuel value recommended by Andreae and Merlet [2001] for extratropical forests. Emission factors were higher for the subset of fuels with moisture contents below 20% ($\sim 1510 \text{ g kg}^{-1}$ dry fuel). An Alaskan duff stack burn (burn 227) had the lowest $EFCO_2$ I observed, $\sim 770 \text{ g kg}^{-1}$ dry fuel, reflecting its low carbon content (31%) and the dominance of smoldering combustion during the burn (MCE = 0.74). The highest $EFCO_2$ was observed for the flaming-phase ponderosa pine needle stack burn (burn 195; ~ 1980

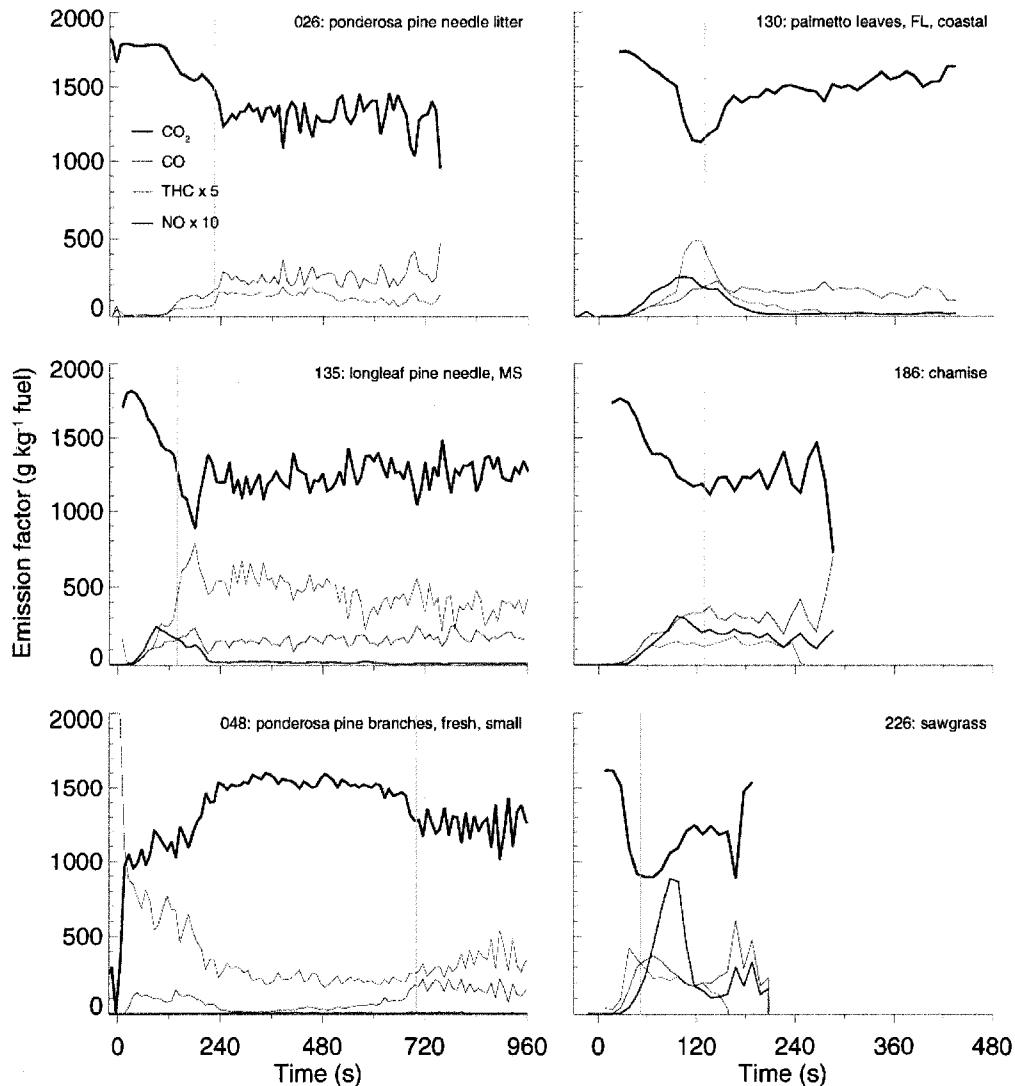


Figure 3.7 Real-time emission factors (EF) for CO, CO₂, NO (g kg⁻¹ fuel) and THC (g C kg⁻¹ fuel) for six sample burns. THC and NO emission factors are multiplied by a factor of five and ten, respectively. The transition from flaming to smoldering, identified visually, is indicated by the vertical gray line.

g kg⁻¹ dry fuel), which had a relatively large carbon content (55%) and high MCE (0.99). Other fuels with high EFCO₂ included white and black spruce, chamise, manzanita, juniper, and longleaf pine litter (dead needles and twigs).

The study mean EFCO was 81 ± 38 g kg⁻¹ dry fuel, somewhat lower than the value recommended by *Andreae and Merlet* [2001] for extratropical forests, 107 ± 37 g kg⁻¹ dry fuel. The lowest EFCO we observed were ~6-10 g kg⁻¹ dry fuel for flaming-phase combustion of

ponderosa pine. We observed EFCO as high as 250 g kg⁻¹ dry fuel for smoldering-phase combustion of ponderosa pine. Other notable high-EFCO fuels included fresh Montana grasses (120-150 g kg⁻¹ dry fuel), fresh lodgepole pine needles (140-150 g kg⁻¹ dry fuel) and sagebrush (100-150 g kg⁻¹ dry fuel). Consistent with the comparison to EFCO₂, our EFCO for ponderosa pine needles, sagebrush, and Montana grasses are higher than those reported by *Chen et al.* [2007] for similar fuels, reflecting the difference in combustion observed during the two studies.

Table 3.3 lists the range and/or study-average values for EFCO and EFCO₂ reported for previous laboratory and field biomass burning experiments. These studies varied in the fuels they burned (savannah grasses, North American wildland fuels, tropical biomass, peat, dung), location (combustion laboratory, Africa, Brazil), and in their measurement methods (Fourier transform IR spectrometry, gas chromatography). Combustion conditions during FLAME varied more than any of the studies listed in Table 3.3, reflecting the large number and variety of fuels we tested. As a result, the emission factors reported by these studies fell within the range of FLAME observations. It is difficult to compare study-averaged emission factors reported by different studies, particularly those that examine more than one type of fire regime, e.g., savannah fires. The FLAME study-average reflects the choice of fuels we tested, and the number of times we tested them, so the average emission factors did not necessarily compare with any previous study-averaged values.

The combustion conditions also varied within individual experiments that examined specific fuel types, as evident from the large ranges listed in Table 3.3, which led to considerable differences in CO and CO₂ emission factors. To estimate burn-to-burn variability during FLAME, I compared MCE and emission factors measured for 16 replicate burns (15 burns had

valid data) of ponderosa pine needle litter samples. The fuel moisture ($9.9 \pm 0.5\%$) and initial fuel mass (246 ± 6 g) of these samples was kept relatively constant. MCE ranged from 0.88 to 0.94 with a mean of 0.92 ± 0.02 . The mean EFCO₂ was 1614 ± 41 g kg⁻¹ (mean \pm 1 standard deviation) and for EFCO was 91 ± 18 g kg⁻¹. The variability in EFCO was higher than the variability in EFCO₂ because the emission factor for CO was more sensitive to variations in the smoldering combustion conditions, consistent with the findings of *Chen et al.* [2007].

Previous biomass burning studies and the analysis of the replicate ponderosa pine needle litter burns during FLAME show that combustion conditions were variable during biomass combustion. MCE and emission factors vary by 5–15%, even when such parameters as fuel type, fuel moisture, and fuel mass are controlled for. At first, this calls into question the representativeness of the FLAME data (and other biomass burning studies). The remainder of this work, however, will attempt to show that despite the large range of combustion conditions, even among replicate burns, the *relationships* between combustion conditions and trace gas and aerosol emissions, are surprisingly robust. It will focus on links between combustion conditions, quantified through MCE, and emissions, rather than on what controls the combustion conditions. This approach has been applied to trace gas measurements in the laboratory [*Christian et al.*, 2003; *Yokelson et al.*, 2008], but to a lesser extent for particles and their physical and optical properties.

3.5 Hydrocarbon emission factors

Gas-phase hydrocarbon species measured during FLAME included the real-time measurements of THC by the flame ionization detector-based analyzer and the canister

measurements of C₁₋₄ hydrocarbons by gas chromatography. The following hydrocarbons were quantified: CH₄ (methane), C₂H₂ (ethyne or acetylene), C₂H₄ (ethene), C₂H₆ (ethane), C₃H₆ (propene), C₃H₈ (propane), three isomers of C₄H₈ (butene), and C₄H₁₀ (n-butane). I calculated the concentration of measured non-methane hydrocarbons (NMHC) by summing the concentrations of the C₂₋₄ hydrocarbons. Background samples were collected in several canisters throughout the day during the experiments. Fluctuations in the CO₂ (and in some cases CO) background in the room varied on a shorter time period than the sampling interval for the background canisters. Excess mixing ratios for each species were calculated by subtracting the most recent background sample concentrations from the ambient value observed in the burn sample canister. I averaged the real-time CO, CO₂ and THC measurements over the canister sampling periods to compare the two methods.

Figure 3.8 compares excess mixing ratios of CO, CO₂ and THC measured by the real-time analyzers and those measured for the canisters by GC-FID. Excess mixing ratios of CO and CO₂ measured by each technique were in good agreement for the vast majority of the samples ($r^2 = 0.95, 0.96$ for CO₂ and CO, respectively). The mean of all measured values for the real-time $\Delta[\text{CO}]$ measurements was 3.6 ± 3.5 ppm and for the canisters it was 3.2 ± 2.5 ppm, or about 10% lower. The means for $\Delta[\text{CO}_2]$ were 55.2 ± 92.9 ppm for the real-time measurements and 54.1 ± 44.5 ppm for the gas canisters, or about 2% lower. A few samples had very large disagreements in CO and/or CO₂ measured by the two techniques, due to large differences in the background concentrations used to correct these samples. The good agreement between these two independent measurement methods provides greater confidence in the accuracy of the measurements, provided the background concentration of CO and CO₂ in the room during

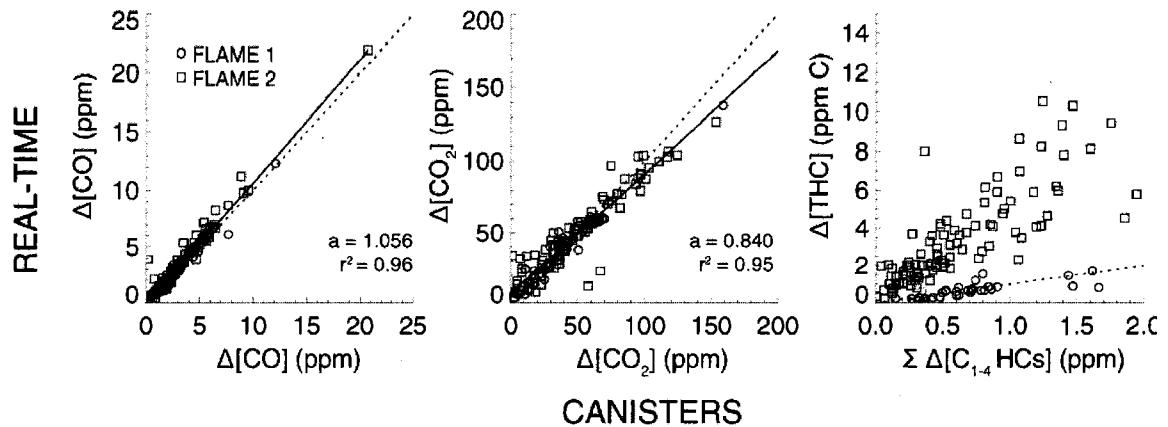


Figure 3.8 Excess CO, CO₂ and total hydrocarbon (THC) mixing ratios measured by the real-time gas analyzers versus canister sample measurements by gas chromatography. The real-time THC measurements (in ppm C) are compared with the sum of C₂₋₄ hydrocarbon mixing ratios (in ppm C). FLAME 1 data are plotted with red circles, FLAME 2 data with blue squares. The dashed lines show the 1:1 line, and the solid lines give the linear least-squares regression of the real-time data onto the canister data.

the burn matched that measured in the background gas canister samples.

The agreement in $\Delta[\text{CO}]$ and $\Delta[\text{CO}_2]$ measured by the two methods did not depend on the study, i.e., FLAME 1 data were similar to FLAME 2 data. The comparison between THC measured by the real-time instruments and the sum of NMHC + CH₄ (denoted by ΣC_{1-4}) was a different story, however. As Figure 3.8 shows, the real-time THC measurements were ~5 times higher than ΣC_{1-4} measured in the gas canisters during FLAME 2, but agreed well during FLAME 1. Previous biomass burning emissions measurements performed at the FSL have shown that THC and ΣC_{1-4} typically agree well [S. Baker, personal communication], so the large disagreements between THC and ΣC_{1-4} observed during FLAME 2 was probably due to a measurement bias during FLAME 2. The origin of this bias is unknown and troubling. Both instruments were calibrated with NIST traceable standards, so a large drift in the response of the flame ionization detector of either instrument seems an unlikely explanation for the disagreement. The disagreement could not have originated from an issue related to the canister versus real-time averaging procedure, because good agreement was observed for CO and CO₂.

If, for example, the real-time measurements were averaged over too long or short a time period, the CO and CO₂ measurements should show a similar bias. I used the canister data as the standard measure of gas phase hydrocarbons, rather than the THC measurements, because a) they provide information on individual hydrocarbons, which are much more common to the literature, b) they have similar concentrations for FLAME 1 and FLAME 2 burns of similar masses and fuels, and c) had emission factors similar to previously published values.

I calculated emission factors for each gas-phase species measured in the gas canisters using the same method as described in Section 2.3. Gas-phase hydrocarbon emissions are strongly related to combustion conditions [Yokelson *et al.*, 1996], so I plotted the emission factors as a function of MCE in Figure 3.9. The canisters were not necessarily sampled over the entire duration of the burn, so the emission factors were plotted against MCE calculated from the canister CO and CO₂ measurements, rather than the 'fire-integrated' MCE values reported in Table 3.2.

Emission factors for CH₄ ranged from approximately 0–11 g kg⁻¹ fuel (Figure 3.9a), from 0–5 g kg⁻¹ fuel for C₂H₂, from 0–40 g kg⁻¹ fuel for C₂H₄, from 0–8 g kg⁻¹ for C₂H₆, from 0–15 g kg⁻¹ fuel for C₃H₆ and 0–4 g kg⁻¹ fuel for C₃H₈. Concentrations for C₄ hydrocarbons were below the instrument detection limits for all but a handful of burns, so I did not calculate emission factors for them. Individual hydrocarbon emission factors were a strong function of MCE during FLAME. Canister samples with high MCE, reflecting a greater contribution by flaming-phase combustion, had lower hydrocarbon emission factors compared to samples with low MC that had a greater contribution by smoldering-phase emissions. The MCE explains over half of the variability in the emission factors for all of the hydrocarbon species with the exception of C₂H₄

(Figure 3.9e). The outliers at high MCE were probably due to errors in the calculation of MCE due to incorrect background concentration measurements. NMHC and $\Sigma C_{1,4}$ emission factors were also a strong function of MCE because the individual species that contributed to them were strong functions of MCE. The dominant hydrocarbon species, in order of decreasing carbon mass emission factor, were C_2H_4 , CH_4 and C_3H_6 .

Concentrations of gas phase hydrocarbons have been measured previously in both field- and laboratory-based biomass burning studies. Robert Yokelson and colleagues from the University of Montana and the FSL have carried out a series of open-path and fourier-transform IR spectroscopy (FTIR) measurements for a large number of laboratory and field fires over the last decade. These results are summarized in Table 3.3. *Yokelson et al.* [2003] regressed fire-averaged emission factors for CH_4 , C_2H_2 , and C_2H_4 against MCE measured from an aircraft over savannah fires in Africa. *Christian et al.* [2003] burned African savannah and Indonesian peat fuels at the FSL and performed a similar regression. Their results are compared with FLAME measurements in Figure 3.9 (shown by the solid red and blue lines). *Yokelson et al.* [2003] measured slightly higher emission factors for CH_4 , but obtained a similar regression against MCE as observed during FLAME. The FLAME and *Christian et al.* [2003] regressions were in nearly perfect agreement. The FLAME emission factors for C_2H_2 and C_2H_4 were higher than the *Yokelson et al.* [2003] and *Christian et al.* [2003] regressions predicted. The *Yokelson et al.* [2003] regressions were calculated for burns that had MCE ranging from only 0.91–0.97 compared to ~0.75–0.98 during FLAME. Several of the FLAME burns had C_2H_2 and C_2H_4 emission factors that agreed with the *Yokelson et al.* [2003] and *Christian et al.* [2003] regressions over the range of MCE they measured.

3.6 Gas-phase nitrogen compound emissions

NO_x ($\text{NO} + \text{NO}_2$) emission factors are a function of both combustion behavior and fuel nitrogen content [e.g., *Lobert et al.*, 1991]. Laboratory and field measurements have shown that NO_x is emitted primarily through flaming combustion and NH_3 is emitted primarily by

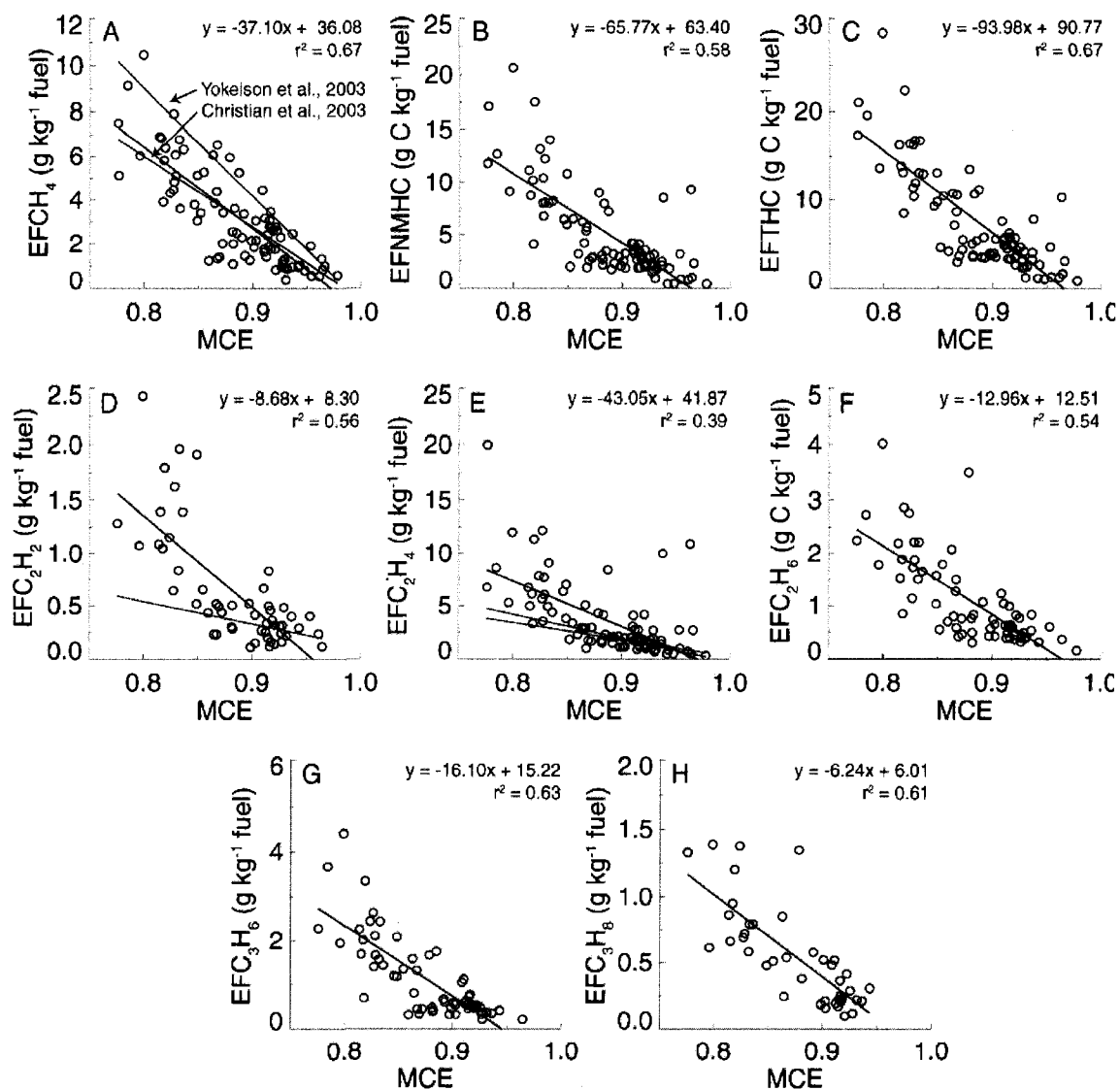


Figure 3.9 Emission factors for hydrocarbon gas species calculated from canister gas chromatography measurements as a function of modified combustion efficiency (MCE). Black lines indicate the linear least-squares regression of the emission factors onto MCE. Colored lines indicate regressions reported by previous studies. *Yokelson et al.* [2003] only observed MCE ranging from 0.92–0.98, but I have extended the regression over the range of MCE observed during FLAME.

smoldering combustion [Goode *et al.*, 2000; Lobert *et al.*, 1991; Yokelson *et al.*, 1996]. In the oxygen-rich flaming environment, NH_3 is rapidly oxidized to NO and NO_2 , while in the oxygen-poor smoldering environment more NH_3 escapes. Despite this, emissions factors for individual nitrogen emissions are not strongly correlated with MCE and instead have a greater dependence on fuel nitrogen content [Andreae and Merlet, 2001; Lobert *et al.*, 1991]. Previous studies have demonstrated a strong relationship between MCE and the molar ratio of NH_3 to NO_x (expressed as NO) emissions [Goode *et al.*, 2000], where the ratio removes the dependence on fuel nitrogen contents.

Figure 3.10 compares the relationship between NH_3/NO_x molar ratios and MCE observed during FLAME and other recently published observations. FLAME data points are shaded according to the absolute NO_x mass emissions to illustrate increasing uncertainty in the molar $\text{NH}_3:\text{NO}_x$ ratios calculated for low NO_x cases. The linear least-squares regression to the high-confidence data (defined as having absolute NO_x emissions greater than 0.6 g) indicated NH_3 makes up the majority of the identified N emissions below an MCE ~ 0.85 . Many burns departed from this fit, but most correspond to burns with low NO_x emissions and high uncertainties in the calculated $\text{NH}_3:\text{NO}_x$ molar ratios.

Figure 3.10 also illustrates the fit provided by Goode *et al.* [2000] to several sets of biomass burning observations published in the 1980s and 1990s. $\text{NH}_3:\text{NO}_x$ molar ratios during FLAME were about a factor of two lower than those reported and summarized by Goode *et al.* [2000] at similar MCE. Goode *et al.* [2000] treated all NO_x emissions as NO because NO_2 mixing ratios were below their instrument's detection limits. They justified this by pointing to evidence that NO_2 emissions are rarely more than 10% of total NO_x emissions. Recent

measurements, such as those presented in Figure 3.11, which compares NO and NO₂ measurements, indicate that the NO₂ contribution to total NO_x produced by fires can be much higher than 10%. In fact, Figure 3.11 suggests that the 10% assumption is a lower limit. Interestingly, the high-confidence FLAME data agreed with the *Goode et al.* [2000] fit if only NH₃:NO molar ratios were considered. Several other sets of NH₃ and NO_x measured with open-path and aircraft-based Fourier Transform Infrared Spectrometry (FTIR) published this decade also deviated significantly from the *Goode et al.* [2000] fit [*Yokelson et al., 2007a; Yokelson et al., 2007b*].

I also calculated emission factors for NO and NO₂ following the same approach used to calculate CO, CO₂ and hydrocarbon emission factors. Fire-integrated NO emission factors ranged from 0.04 to 9.6 g kg⁻¹ dry fuel, with a study mean and standard deviation of 2.6 ± 2.4 g kg⁻¹ dry fuel. There was a large difference between the FLAME 1 averaged EFNO (0.7 ± 0.5 g kg⁻¹) compared to the FLAME 2 averaged EFNO (3.9 ± 2.4 g kg⁻¹). This could have been due to the larger number of N-rich grasses and other plants we tested during FLAME 2. Due to instrument malfunction, no NO₂ measurements were valid during FLAME 2, so I assumed the relationship between NO and NO₂ emissions was consistent with the FLAME 1 data. The FLAME 1 averaged emission factors for NO₂ were 0.4 ± 0.3 g kg⁻¹, lower than EFNO measured during FLAME 1 or FLAME 2.

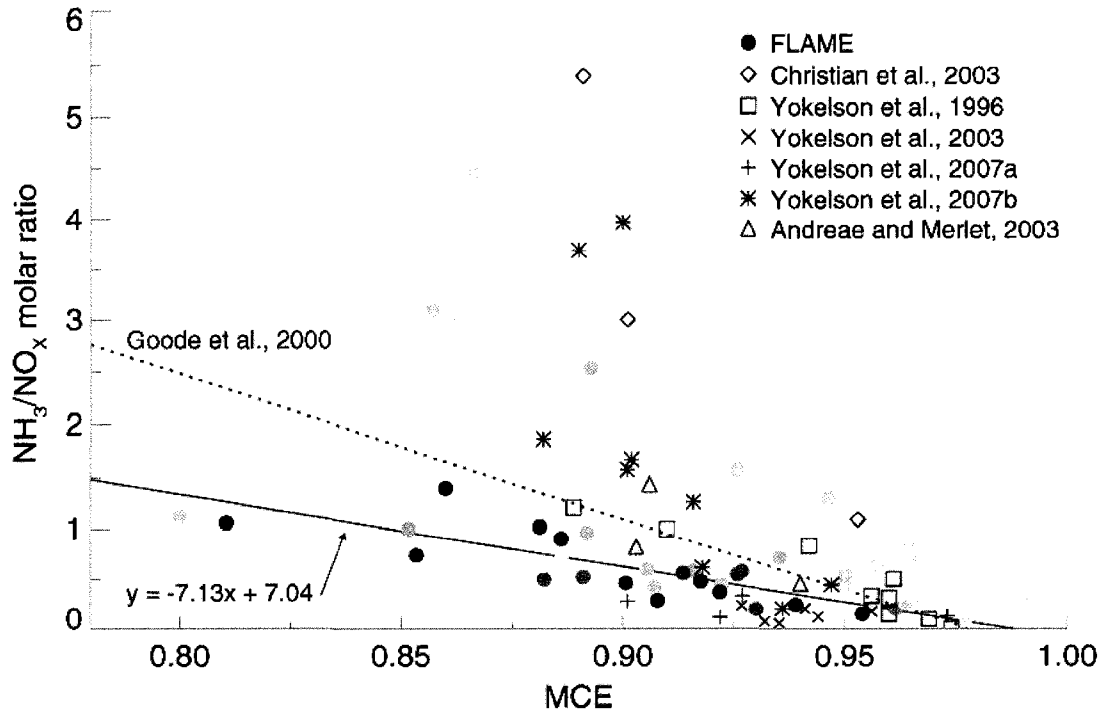


Figure 3.10 Molar ratios of NH₃-to-NO_x emissions as a function of modified combustion efficiency (MCE) during FLAME and several biomass burning field and laboratory experiments. FLAME data are shaded to reflect the magnitude of the NO_x measurement, and therefore reflect the confidence in the measured ratio. Symbols plotted in red indicate laboratory measurements, symbols plotted in blue indicate field measurements, and symbols in green are representative values for savanna, tropical and extratropical forest fires given by Andreae and Merlet [2001]. The dashed line indicates the fit provided by Goode et al. [2000] for several sets of laboratory and field biomass burning measurements. The solid line gives the least-squares regression to FLAME data where total NO_x mass emissions were greater than 0.6 g NO. Note that this figure is truncated to better illustrate the majority of NH₃:NO_x data from our study and the literature. A maximum NH₃:NO_x ratio of ~12 at an MCE of 0.82 was reported by Christian et al. [2003].

Figure 3.11 compares emission factors for NO and NO₂ (expressed as NO) calculated during FLAME and reported by three recent biomass burning emission studies [Chen et al., 2007; Freeborn et al., 2008; Yokelson et al., 2007a]. All four data sets show considerable scatter due to the complex relationships governing NO_x emissions and subsequent chemistry taking place in the smoke plume, e.g., the rapid reaction of NO and O₃ to form NO₂. This is the main reason why NO and NO₂ emissions are frequently reported as NO_x emissions. Unfortunately, the lack of NO₂ data during FLAME 2 limited my ability to report NO_x emissions. Instead I assumed that NO₂ emissions during FLAME 2 were in the same proportion to NO emissions as

during FLAME 1, a molar ratio of ~ 0.6 . Multiplying the FLAME 2 NO emissions by this factor yielded a FLAME-average EF_{NO_x} (as NO) of 4.2 ± 4.0 g NO kg⁻¹ fuel, within the range of previously reported values listed in Table 3.3.

Yokelson et al. [2007b] speculated that unusually high NO_x emissions from fires near Mexico City may have been due to deposition of N-containing pollutants to the vegetation (primarily pine trees). The chamise, manzanita, ceanothus and some of the sagebrush samples we burned were collected from polluted regions near Salt Lake City, Utah and east of Los Angeles, California, but these fuels did not display higher emission factor for nitrogen species as observed for the Mexico City fires, despite having a similar MCE. There was no significant difference between EF_{NO} or EF_{NH_3} for sagebrush collected from Salt Lake City (a polluted environment) and near Missoula, Montana (a clean environment). The plant species burned near Mexico City were more sensitive to nitrogen deposition and had higher fuel N content compared to those we tested. The higher levels of pollution in Mexico City versus Los Angeles or Salt Lake City could also have a larger impact on the surrounding vegetation.

Additional measurements of other potentially important N species emitted by fires, such as alkyl nitriles and amines, could help to explain the variations in the NH₃:NO molar ratios shown in Figure 3.10 and reduce the uncertainties associated with their emissions. The form of reactive nitrogen species emitted from fires has important implications for smoke plume aging and local fire impacts. NO_x is important in tropospheric ozone production and NO₂ can react with the hydroxyl radical to form nitric acid (HNO₃). Tropospheric ozone is a greenhouse gas and a regional-scale pollutant that is toxic to humans, plants and animals. It also plays an important role in determining the oxidant pool in the smoke plume as it ages. The majority of

NH₃ reacts with acids such as sulfuric acid (H₂SO₄) or HNO₃ to form ammonium salts that are a major component of aerosols. This acts to increase the effective particulate matter emission factor for fires with low MCE, and therefore potentially yield stronger impacts on direct radiative forcing and visibility.

3.7 Summary

We carried out a series of combustion experiments using a variety of fuels and fuel components to examine aerosol and trace gas emissions. This chapter provided background for the experiment, giving a detailed description of the experimental design and the fuels we tested. It characterized the burns based on their energy release and combustion efficiency, and reported emission factors for CO₂, CO, NO_x and C₁₋₄ hydrocarbons. I estimated energy release rates for each burn from the measured temperature increase in the stack and compared them to fuel mass consumption rates. These were highly correlated, and indicated an effective heat of combustion on the order of 12 MJ kg⁻¹ fuel.

I quantified the combustion conditions during each burn using MCE, which was typically 0.97-1.0 during the flaming-phase of combustion and between 0.6 and 0.85 during the smoldering-phase of combustion. There was a wide range in MCE over both studies, with minimum values near 0.6–0.75 and maximum values approaching 1.0, a range which brackets field observations. Our study mean MCE was 0.92, in good agreement with field observations for fires near Mexico City [Yokelson *et al.*, 2007b], in the coastal plain of North Carolina [Yokelson *et al.*, 1999], and Alaska [Goode *et al.*, 2000], regions with plant species similar to those we tested, but I stressed that comparisons between study-averaged values were not particularly

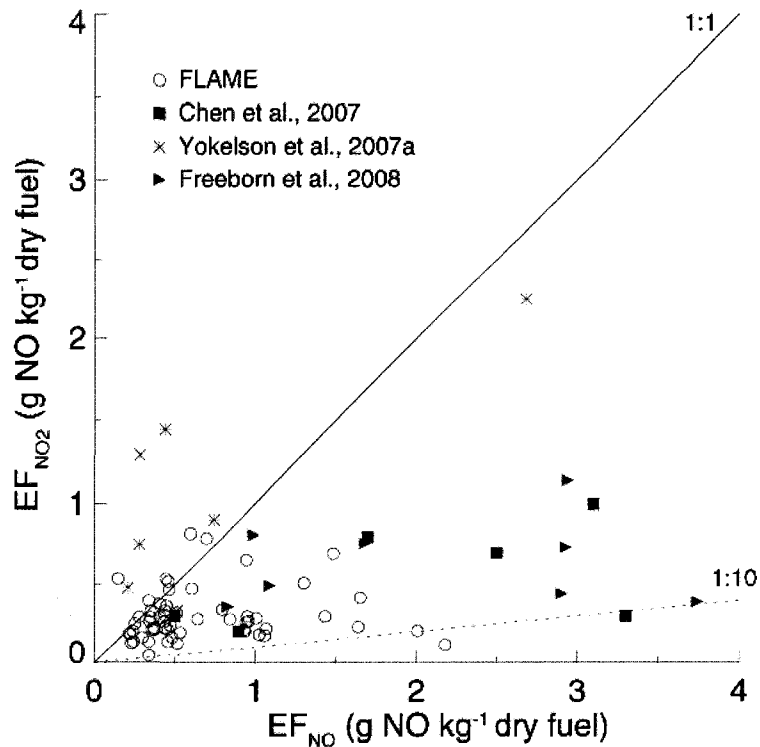


Figure 3.11 Scatter plot comparing fire-integrated NO and NO₂ emission factors during FLAME, expressed as g NO kg⁻¹ dry fuel consumed. NO and NO₂ emission factors reported by three recent studies are also plotted. *Chen et al.* [2007] and *Freeborn et al.* [2008] examined emissions from several North American fuels burned at the Fire Science Laboratory and used the same NO_x analyzer featured here. Data presented by *Yokelson et al.* [2007a] were collected with an aircraft-based Fourier Transform Infrared Spectrometer (FTIR) over fires in Brazil. The 1:1 (solid) and 1:10 (dashed) lines are indicated.

useful. Rather, the relationships between emissions, their properties and parameters such as MCE should be the focus of emissions studies similar to FLAME. The emissions of many trace gases and particulate matter are strongly related to MCE, so the similarity in our study averaged MCEs and those observed in the field suggests that our laboratory observations are representative of fresh emissions from real fires.

The wide range of fire-integrated MCE observed during FLAME reflected the variety of plant species we tested and the large number of burns that were carried out. In general, fuels with high moisture contents featured stronger contributions from smoldering combustion and lower MCE, while dry fuels had more flaming combustion and higher MCE. The variability in

MCE observed for the combustion of different components of the same species, different masses of the same fuel species, and different orientation of same fuel species all underscore the need to report biomass burning emission properties referenced to fire-integrated MCE.

Chapter 4 Aerosol composition and optical properties

Most of the smoke optical property and chemical composition measurements previously reported were made during wildland fires from the ground or from aircraft [*Reid et al., 2005a; Reid et al., 2005b* and references herein], making it difficult to link aerosol properties to specific fuels or combustion conditions. Measurements of flaming and smoldering phase emission factors are rare, primarily because it is difficult, if not impossible, to separate these phases during measurements of natural wildfires [*Andreae and Merlet, 2001*]. Laboratory biomass burning studies are useful for quantifying biomass burning emissions because all of the smoke emitted by the fire is captured, allowing for the complete characterization of the emissions. More instrumentation is employed than typically feasible in the field or onboard an aircraft. Fuel properties—moisture content, mass, and composition—are known, so emission factors can be determined more accurately and as a function of fuel moisture. Different components of the plant can be burned to determine their influence on total plant emissions.

A serious disadvantage of laboratory studies is the possibility that laboratory fire emissions do not match those produced by fires in the field [*Yokelson et al., 2008*]. Laboratory studies cannot readily measure changes in smoke concentrations or composition associated with aging. Concentrations in the laboratory are often higher than those observed in the field. This eases measurements of trace compounds with lower sensitivity instruments and improves counting statistics, but the large concentrations have implications for the gas-particle

partitioning of organic species [*Lipsky and Robinson, 2006; Robinson et al., 2007*]. Semi-volatile organic species that are identified in the particle phase at high particle concentrations in the laboratory may reside in the gas-phase at the lower particle mass concentrations observed in the atmosphere more distant from the source.

Table 4.1 lists several recent laboratory-based measurements of biomass burning emissions that examined aerosol optical properties. Many laboratory-based studies have examined wood smoke optical properties, but were focused on emissions from wood-burning stoves or fireplaces. Earlier studies (not listed in Table 4.1) only examined emissions from one or two individual fuels as part of a larger emissions characterization study [e.g., *Hildemann et al., 1991*]. Most laboratory-based emissions studies have focused on aerosol composition, especially organic composition, and did not measure optical properties concurrently. Others characterized emissions from agricultural waste fuels rather than fuels typically consumed in prescribed or wildland fires. The resulting subset of laboratory studies focused on characterizing the latter group of fuel species is small. *Hays et al. [2002]* sampled emissions from several wildland fire fuels in the EPA's combustion test facility and compared aerosol size distributions and composition to combustion behavior, but did not make optical measurements. *Chand et al. [2005]* and *Freeborn et al. [2008]* measured aerosol optical properties, but did not measure aerosol composition. I found only two previous studies that reported aerosol optical and chemical properties measured simultaneously in a laboratory: *Christian et al. [2003]*, who presented a limited set of aerosol composition and light scattering measurements for ~10 different African, Indonesian, and North American fuels and the FLAME pilot study [*Chen et al., 2007*].

Table 4.1 Previous laboratory studies of biomass combustion that reported aerosol composition, aerosol emission factors and/or optical properties (OC = organic carbon, EC = elemental carbon, $f(\text{RH})$ = relative humidity scattering growth factor, PAH = polycyclic aromatic hydrocarbon, HULIS = humic like substance, K = potassium, S = sulfur).

Study	Fuels burned	Reported properties
<i>Rogge et al.</i> [1998] ¹	pine, oak, synthetic log	mass, organic species inc. levoglucosan
<i>Oros and Simoneit</i> [1999]	eucalyptus, hemlock, rye grasses	mass, OC, EC, organic species including levoglucosan
<i>Schauer et al.</i> [2001] ¹	pine, oak, eucalyptus	mass, OC, EC, ionic species, elements including K, organic species including levoglucosan
<i>Oros and Simoneit</i> [2001a]	apache pine, California redwood, Douglas fir, white pine, lodgepole pine, Montezuma pine, hemlock, noble fir, silver fir, ponderosa pine, cedar, Sitka spruce, white spruce	mass, OC, EC, organic species including levoglucosan
<i>Oros and Simoneit</i> [2001b]	Dwarf birch, eucalyptus, Oregon maple, red alder, silver birch	mass, OC, EC, organic species including levoglucosan
<i>Fine et al.</i> [2001] ¹	maple, oak, birch, white pine, hemlock, fir	mass, OC, EC, ionic species, elements incl. K, organic species incl. levoglucosan
<i>Fine et al.</i> [2002] ¹	poplar, ash, sweetgum, hickory, loblolly pine, slash pine	mass, OC, EC, ionic species, elements incl. K, organic species incl. levoglucosan
<i>Hays et al.</i> [2002]	loblolly pine, ponderosa pine, hemlock, hardwood forest litter, slash pine/palmetto, wiregrass/long leaf pine	size distributions, mass, OC, EC, ionic species, elements incl. K, organic species incl. levoglucosan
<i>Hedberg et al.</i> [2002] ²	birch	mass, size distributions, elemental species including K, organic species, PAH
<i>Sheesley et al.</i> [2003] ²	coconut leaves, rice straw, jackfruit branches	OC, EC, ionic species, elemental species including K, organic species including levoglucosan
<i>Christian et al.</i> [2003]	dambo grass, miombo, alang-alang, Canadian soil duff, cottonwood, shredded aspen, fir, ponderosa pine, rice straw, Indonesian peat, semak	mass, OC, EC, Cl, K, S
<i>Fine et al.</i> [2004] ¹	white oak, maple, black oak, beech, cherry, white spruce, fir, ponderosa pine, pinyon pine, aspen	mass, OC, EC, ionic species, elemental species incl. K, organic species including levoglucosan
<i>Chand et al.</i> [2005]	Indonesian peat, German peat, spruce, beech	mass, light scattering (545, 550 nm), $f(\text{RH})$, light absorption (532 nm), growth factor, morphology, $f(\text{RH})$
<i>Oros et al.</i> [2006]	tundra grass, cotton grass, ryegrass, pampas grass, bamboo, sugarcane	mass, OC, EC, organic species including levoglucosan
<i>Wardoyo et al.</i> [2006]	spotted gum, blue gum, bloodwood, iron bark, stringybark	mass, number, size distributions
<i>Keshtkar and Ashbaugh</i> [2007]	rice straw, almond pruning	size-resolved mass, OC, EC, PAH
<i>Dhammapala et al.</i> [2007]	wheat, Kentucky bluegrass stubble	mass, OC, EC, PAH, methoxyphenols, levoglucosan
<i>Mazzoleni et al.</i> [2007]	ponderosa pine, white pine, shredded aspen, sagebrush, Zambia grass, Montana grass, Alaska duff	mass, OC, EC, organic compounds including levoglucosan
<i>Linuma et al.</i> [2007]	pine, spruce, savannah grass, musasa, Indonesian peat, German peat	size-resolved mass, OC, EC, WSOC, ionic species, organic species including levoglucosan
<i>Schmidl et al.</i> [2008] ²	spruce, larch, beech, oak	mass, ionic species, cellulose, OC, EC, carbonate carbon, HULIS, elemental species including K, organic species including levoglucosan
<i>Freeborn et al.</i> [2008]	ponderosa pine, fir, Zambian grass, shredded aspen, sagebrush, white pine needles	mass, light scattering (450, 550, 700 nm)

Study	Fuels burned	Reported properties
FLAME pilot study		
<i>Chen et al.</i> [2006]	white pine needles, ponderosa pine wood	mass, light scattering (450, 550, 700 nm), light absorption (532, 1047 nm), light extinction (532 nm)
<i>Chen et al.</i> [2007]	ponderosa pine, white pine, sagebrush, shredded aspen, Dambo grass, Montana grass, duff	mass, OC, EC, elemental species inc. K, light scattering (450, 550, 700 nm), light absorption (532, 1047 nm), light extinction (532 nm)
<i>Chakrabarty et al.</i> [2006]	sagebrush, poplar, ponderosa pine, white pine, Montana grass, Dambo grass, duff	size, morphology
FLAME		
<i>Hopkins et al.</i> [2007]	see Table 3.1	carbon-to-oxygen atomic ratios, sp ² hybridization, elemental composition, morphology by scanning tunneling X-ray microscopy
<i>Obrist et al.</i> [2008]	see Table 3.1	gas- and particle-phase Hg emissions
<i>Lewis et al.</i> [in review]	see Table 3.1	light scattering (450, 550, 700 nm), light absorption (405, 532, 870 nm), humidification effects on absorption
<i>Sullivan et al.</i> [in review]	see Table 3.1	anhydrous sugars, potassium, OC and EC

¹fireplace emission test, ²wood stove emission test

This chapter presents aerosol composition and optical property measurements made during FLAME and demonstrates their dependence on combustion conditions and plant species and components. It gives emission factors for aerosol species and optical cross sections as a function of combustion efficiency and discusses why emission factors for EC are related to combustion efficiency and why emission factors for inorganic species are not. Many of the emission factors are reported for fuels not previously examined in laboratory combustion studies, but serve as major fuel sources for wildland fires in populated areas, such as California chaparral species. Finally, I discuss the relationships between trace organic gas and particle-phase emissions from the perspective of total observed organic carbon (TOOC) [*Heald et al., 2008*] to assess the influences of atmospheric aging processes and gas-particle partitioning on the significance of these results.

4.1 Aerosol measurements

4.1.1 Filter samples

Several filter samplers collected aerosol during FLAME, but I limit my discussion in this chapter to the Thermo Anderson high volume (Hi-Vol) sampler and URG annular denuder sampling system. During stack burns, the Hi-Vol and URG samplers were located on the platform ~15 m above the fuel bed and connected to stack sampling ports using sampling ports designed by FSL. Their approximate locations are shown in Figure 4.1. During chamber burns, the filter samplers were located on the chamber floor and they sampled smoke that was mixed throughout the chamber. The Hi-vol samplers were placed on tables to keep the inlets of all the filter samplers at a uniform height (~3 m). The Hi-vol sampler and URG sampler were separated by ~5 m on the chamber floor.

Sullivan et al. [submitted] and *Engling et al.* [2006b] described the high-volume sampler we used during FLAME in detail. The Hi-Vol sampler had a nominal flow rate of $1.13 \text{ m}^3 \text{ min}^{-1}$ (1130 L min^{-1}). An assembly of two quartz-fiber filters collected particles divided into two size classes: those with aerodynamic diameters (D_{ae}) $> 2.5 \text{ }\mu\text{m}$ (coarse mode) and those with $D_{ae} < 2.5 \text{ }\mu\text{m}$ (fine mode). I only present results from the analysis of the fine mode filter—equivalent to particulate matter with $D_{ae} < 2.5 \text{ }\mu\text{m}$ or $\text{PM}_{2.5}$ —because the total aerosol mass was dominated by particles in this size range. The quartz filters were wrapped in aluminum foil and baked in an oven at temperatures $> 600^\circ \text{ C}$ for 36 hours prior to sampling to remove organic contaminants. Each filter remained in its foil envelope until it was loaded on the sampler prior to the start of the burn. Following the experiments, the filter samples were shipped and stored frozen before being

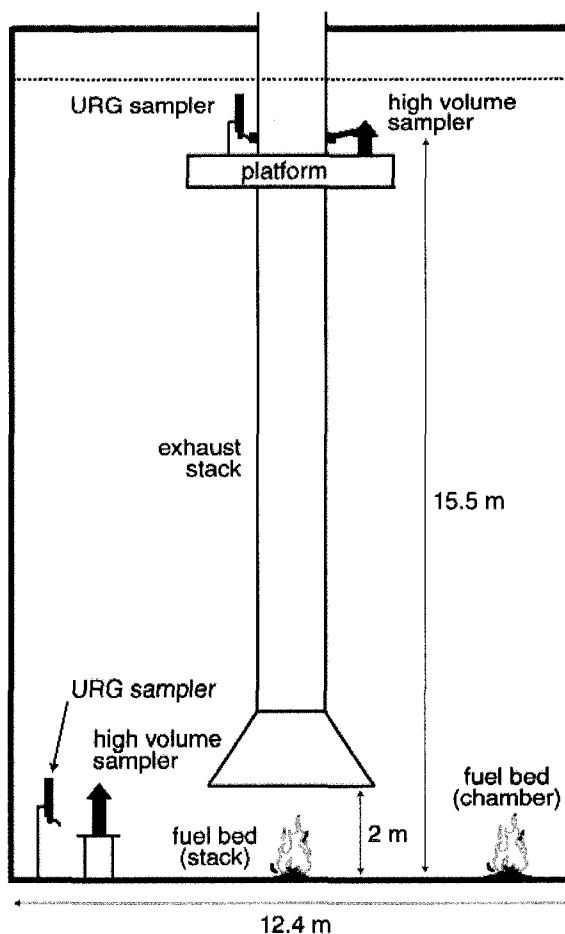


Figure 4.1 The combustion chamber at the USFS Fire Sciences Laboratory in Missoula, Montana. The locations of the high volume and URG samplers and the fuel beds during chamber and stack experiments are indicated.

analyzed.

The URG sampling system consisted of three annular denuders and a filter pack arranged in series, which collected sample for inorganic analysis [Lee *et al.*, 2004]. The sample flow was nominally $0.01 \text{ m}^3 \text{ min}^{-1}$ (10 L min^{-1}). Air and smoke drawn through the URG system first passed through a $2.5 \text{ }\mu\text{m}$ size cut cyclone to remove large particles. Sample then passed through two denuders coated with solutions of sodium carbonate and phosphoric acid in methanol and deionized water. The denuders collected gas-phase ammonia (NH_3), nitric acid (HNO_3) and sulfur dioxide (SO_2). Sample then passed through a nylon filter (Gelman

Nylasorb, 1.0 μm pore size) to collect particles. A backup, citric acid-coated cellulose filter collected NH_3 lost from particles collected on the nylon filter.

During stack burns, the filter sampler pumps were turned on 30 seconds prior to ignition and turned off when the fire was considered extinguished based on visual observations. A single set of filters and denuders collected emissions from multiple replicate burns to ensure adequate concentrations for detection of trace species. During chamber burns, the filter sampler pumps were started approximately four minutes after ignition to allow time for the chamber to become well mixed. Filter sample times were typically two hours, but the filter sample pumps were turned off anywhere from 30 minutes to 10–14 hours (usually overnight) after ignition during experiments that examined potential effects on composition from dilution or chamber aging.

The URG nylon filters were extracted using 6 mL of deionized water by CSU research staff. Extracts were analyzed for inorganic species (Cl^- , SO_4^{2-} , NO_3^- , Na^+ , NH_4^+ , K^+ , Mg^{2+} , and Ca^{2+}) using two Dionex DX-500 series ion chromatography (IC) systems. The cation IC featured an IP 20 isocratic pump, CD 20 conductivity detector, CG12A guard column CS12A separation column and a CSRS-ULTRA1 suppressor. The anion IC featured a GP 40 gradient pump, CD 20 conductivity detector, AG4A-SC guard column, AS4A-SC separation column, and an ASRS-ULTRA suppressor. The ICs were calibrated by injection of aqueous standards prepared in the CSU aerosol composition laboratory.

CSU research staff measured organic carbon (OC) and elemental carbon (EC) concentrations on punches taken from the Hi-Vol quartz fiber filters using a Sunset Labs OC/EC analyzer. The instrument quantified OC and EC carbon mass by thermal optical transmission [Birch and Cary, 1996] using a modified NIOSH Method 5040 (described in more

detail in Chapter 5. The OC/EC measurements reported here were the average of two 1.4 cm² punches from the same filter to reduce measurement uncertainties associated with sample loading heterogeneity [Gorin *et al.*, 2006]. Filter-based carbonaceous aerosol measurements are prone to artifacts caused by gas-phase adsorption onto filter fibers (positive artifact) and volatilization of the sampled particle phase organic material (negative artifact) [e.g., Kirchstetter *et al.*, 2001; Mader and Pankow, 2001; Turpin *et al.*, 1994]. We could not remove organic gases using a denuder upstream from the Hi-Vol sampler because of its high flow rate. Sullivan *et al.* [submitted] concluded that positive artifacts during FLAME were small based on the good agreement between Hi-Vol filter OC concentrations and OC measured by a semi-continuous OC/EC analyzer that sampled with a denuder upstream.

4.1.2 Optical instruments

Aerosol scattering coefficients (b_{sp}) were measured using a TSI 3563 nephelometer during stack and chamber burns. It measured light scattered by gases and particles between 7° and 170° at three wavelengths ($\lambda = 450, 550, \text{ and } 700 \text{ nm}$). The instrument was calibrated with known concentrations of CO₂ and SUVA gases before and after the study. We corrected the light scattering signal for scattering by gases through daily zero-checks when filtered air was passed through the instrument. Particle light scattering coefficients during most of the burns were several orders of magnitude higher than those predicted for gases at the laboratory ambient pressure ($P \sim 900 \text{ hPa}$). We also corrected b_{sp} for truncation and non-lambertian light source errors, following Anderson and Ogren [1998]. The relative humidity in the nephelometer chamber was less than 30% for every burn.

Aerosol light absorption was measured by two single-wavelength photoacoustic spectrometers (PAS) at $\lambda = 532$ nm [Arnott *et al.*, 1999; Arnott *et al.*, 2005b] and by a dual-wavelength PAS at 405 and 870 nm [Lewis *et al.*, in press]. The instruments measure light absorption by detecting the pressure wave caused by the increase in an aerosol particle's thermal energy after it absorbs light. The amplitude of the pressure wave, determined by a sensitive microphone, is directly related to the light absorption coefficient. Photoacoustic spectrometers are not affected by the multi-light scattering artifacts that complicate filter-based absorption measurements [e.g., Arnott *et al.*, 2003; Bond *et al.*, 1999a; Weingartner *et al.*, 2003]. The relationship between the instrument response and b_{ap} was determined by calibrating each PAS with NO₂ gas at known concentrations [Arnott *et al.*, 2000; Virkkula *et al.*, 2005].

Figure 4.2 shows a schematic depicting the sampling setup for the optical instruments during FLAME 1 and 2 stack and chamber burns. During FLAME 1 stack burns, the nephelometer sample flow rate was 0.0167 m³ min⁻¹ (16.7 L min⁻¹) and it sampled downstream of a 2.5 μ m cyclone. The cyclone was not used during the FLAME 2 stack burns. The nephelometer sample was first diluted with nitrogen gas to keep the instruments below their saturation limits. The dilution level was determined post-experiment by comparing measured CO₂ mixing ratios downstream of the diluter and measured directly from the stack. The PAS instruments were not diluted during either study.

The optical instruments sampled from a stainless steel mixing chamber connected to the combustion chamber by corrugated steel tubing during chamber burns, as shown in Figure 4.2. The instruments could not be operated inside the chamber itself because of the high smoke concentrations. The tubing inlet sampled directly from the chamber, ~3 m above the floor

during FLAME 1; it was connected to a 55-gallon stainless steel drum inside the chamber during FLAME 2. The inlet for the 55-gallon drum was ~3 m above the chamber floor. The sampling drum was used to perform filter tests and introduce test aerosol (ammonium sulfate) to the instruments to verify their performance. We used conductive sample lines to minimize losses from electrophoresis. The lengths of sampling lines and the number and severity of bends in them were minimized to reduce diffusive and inertial losses.

4.2 Aerosol composition

4.2.1 Bulk aerosol composition

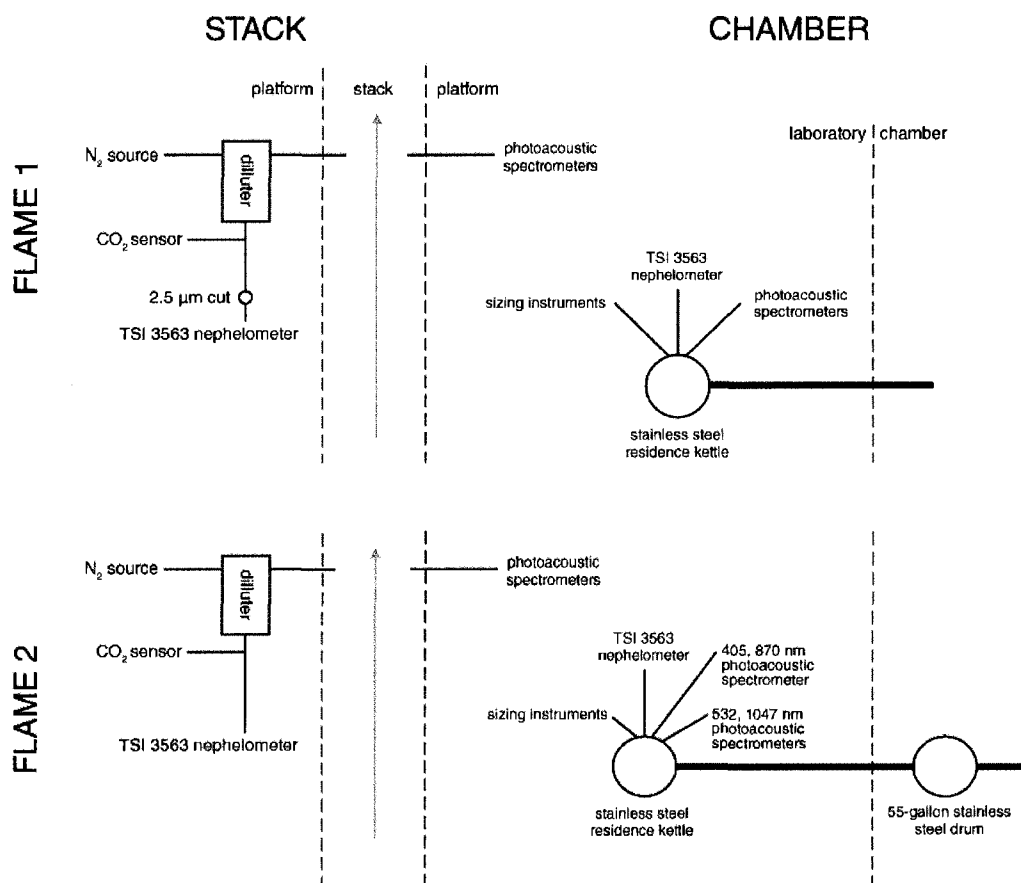


Figure 4.2 Schematic showing locations of optical instruments during FLAME stack (left) and chamber (right) burns. The layout for FLAME 1 is shown on the top half of the figure and the layout for FLAME 2 is shown in the bottom half.

Carbonaceous material was the dominant aerosol species during FLAME. Averaged over all burns performed during the study, TC made up $83 \pm 14\%$ (mean ± 1 standard deviation) of the reconstructed mass of particulate matter smaller than $2.5 \mu\text{m}$ in aerodynamic diameter. Only four of the 145 filters analyzed had TC fractions of reconstructed $\text{PM}_{2.5}$ less than 50%: three different rice straw emissions samples and one palmetto leaves emissions sample. Roughly one-third of the filters had TC mass fractions greater than 90%. My calculations of reconstructed $\text{PM}_{2.5}$ mass concentrations did not include a factor to account for non-carbon species associated with OC, so they are lower than gravimetric $\text{PM}_{2.5}$ mass concentrations. If I included this material—by multiplying measured OC by a fairly conservative factor of 1.5 to estimate POM [Reid *et al.*, 2005b; Turpin and Lim, 2001]—then the EC + POM fraction of reconstructed $\text{PM}_{2.5}$ was 87% on average. Gravimetric $\text{PM}_{2.5}$ mass measurements were only available for chamber burns. In this chapter, my focus is characterizing aerosol composition for the entire study, so I reserve the comparison between reconstructed and gravimetric $\text{PM}_{2.5}$ mass during chamber burns until Chapter 5.

The TC fractions I observed agreed with those found by previous laboratory-based biomass combustion studies. Chen *et al.* [2007] measured TC mass fractions of $\text{PM}_{2.5}$ ranging from 64–100% for fuels burned at the FSL, including several plant species we tested. Hays *et al.* [2002] observed TC mass fractions (of gravimetric $\text{PM}_{2.5}$) in the range of 70–80% for several North American plant species, including ponderosa pine (*Pinus ponderosa*). Carbonaceous material was over 90% of reconstructed mass of particles less than $3.5 \mu\text{m}$ in aerodynamic diameter emitted from the laboratory combustion of several European, African and peat fuels [Iinuma *et al.*, 2007].

Table 4.2 Filter-integrated combustion properties and aerosol emission factors during FLAME. TOOC = total observed organic carbon (see Section 4.4). ΣIN = sum of observed, water-soluble inorganic ions. RFM = sum of all speciated mass. See Appendix A for more emission factors.

ID	Sample	Emission factors (g kg ⁻¹ dry fuel)													
		MCE	CE	EC/JC	TOOC	OC	EC	Cl	K	Na	SO ₄	NH ₃	ΣIN	RFM	PM _{2.5}
FLAME 1 stack															
1	Cellulose filter (plain)	-	-	0	-	-	-	-	-	-	-	-	-	-	-
2	Cellulose filter (K doped 1)	-	-	0	-	-	-	-	-	-	-	-	-	-	-
3	Cellulose filter (K doped 2)	-	-	0	-	-	-	-	-	-	-	-	-	-	-
4	Cellulose powder	-	-	0	-	-	-	-	-	-	-	-	-	-	-
5	Mt. Grass (dry)	-	-	0.047	-	-	-	-	-	-	-	-	-	-	-
6	Mt. Grass (fresh)	-	-	0	-	-	-	-	-	-	-	-	-	-	-
7	Rice Straw	0.874	0.833	0	13.2	7.5	0	1.33	0.54	0.09	0.08	1	2.4	10	13.8
8	PP Duff	-	-	0.013	-	-	-	-	-	-	-	-	-	-	-
9	PP Needle Litter	0.922	-	0.019	-	11.1	0.2	0.13	0.04	0.05	0.04	1.5	0.5	11.8	17.3
10	PP Needle Litter	0.911	0.855	0.001	28.1	22.8	0	0.08	0.04	0.09	0.06	1	0.5	23.3	34.7
11	PP Needle Litter	0.933	-	0.022	-	8.9	0.2	0.09	0.03	0.06	0.04	0.9	0.5	9.5	14
12	PP Needle Litter	-	-	0.005	-	-	-	-	-	-	-	-	-	-	-
13	PP Needle Litter	0.92	-	0.007	-	12.7	0.1	0.14	0.03	0.1	0.04	1.3	0.5	13.3	19.7
14	PP Branches (dead, sm)	0.946	0.914	0.45	12.9	3.6	2.9	0.07	0	0.26	0.03	1.1	0.7	7.2	9
15	PP Branches (dead, large)	0.954	0.941	0.433	4.2	1.9	1.5	0.07	0	0.09	0.04	0.5	0.3	3.8	4.7
16	PP Branches (fresh, small)	0.924	-	0.007	-	-	-	-	-	-	-	-	-	-	-
17	PP Needles (fresh)	0.87	0.79	0.003	45.8	37.7	0.1	0.2	0.15	0.12	0.11	3.6	0.7	38.5	57.4
18	PP Branches (fresh, large)	-	-	0.005	-	-	-	-	-	-	-	-	-	-	-
19	LP Needle Litter	-	-	0.057	-	-	-	-	-	-	-	-	-	-	-
20	LP Needles (fresh)	0.868	0.777	0.005	50.9	33.8	0.2	0.19	0.4	0.17	0.17	3.3	1.3	35.3	52.2
21	LP Branches (dead, small)	0.946	0.936	0.51	3.1	1.5	1.5	0.09	0.02	0.07	0.03	0.2	0.5	3.5	4.2
22	LP Needle Duff	0.932	0.881	0	18	7.6	0	0.23	0.04	0.18	0.09	0.9	0.8	8.4	12.2
23	Rice Straw	0.917	-	0.052	-	4.7	0.3	1.23	0.48	0.14	0.09	0.3	2.2	7.1	9.5
24	Rice Straw	-	-	-	-	-	-	-	-	-	-	-	-	-	-
25	Rice Straw	0.91	-	-	-	6.4	-	-	-	-	-	-	-	-	-
26	Palmetto Leaf (dry)	0.916	-	0.242	-	1.5	0.5	2.24	1.34	0.25	0.31	0.4	4.4	6.4	7.1
27	Chamise Leaf (dry)	0.893	0.866	0.016	10	6.8	0.1	0.3	0.58	0.13	0.26	1.8	1.6	8.4	11.8

ID	Sample	Emission factors (g kg ⁻¹ dry fuel)													
		MCE	CE	EC/TC	TOOC	OC	EC	Cl	K	Na	SO ₄	NH ₃	ΣIN	RFM	PM _{2.5}
28	Chamise Branches (dry)	0.909	0.89	0	7.6	4.1	0	0.13	0.07	0.16	0.1	1.3	0.7	4.8	6.8
29	Chamise Leaf (fresh)	0.866	-	0	-	-	-	-	-	-	-	-	-	-	-
30	Chamise Branches (fresh)	0.926	0.902	0.003	8.9	3.5	0	0.07	0.09	0.17	0.06	1.6	0.7	4.3	6
31	Manzanita Leaves (fresh)	-	-	0	-	-	-	-	-	-	-	-	-	-	-
32	Manzanita Branches (fresh)	0.886	0.855	0	14.2	10.7	0	0.19	0.18	0.33	0.1	0.3	1.2	11.9	17.3
33	Manzanita leaves (dry)	0.87	0.763	0.005	52.7	40	0.2	0.2	0.29	0.13	0.13	4.4	1.1	41.2	61.2
34	Chamise Branches and Leaves (dry)	0.935	0.924	0.324	3.8	1.5	0.7	0.15	0.31	0.12	0.17	0.5	0.9	3.2	3.9
FLAME 1 chamber															
35	PP Pine Complex (dried needles, sticks)	0.972	0.89	0.036	34	2.4	0.1	0.04	0	0.01	0.01	0.7	0.1	2.6	3.7
36	S. CA Chamise Complex	0.949	0.935	0.678	6	0.3	0.7	0.15	0.38	0.02	0.14	0.4	0.7	1.8	1.9
37	PP Pine Complex (dried needles, sticks)	0.942	0.916	0.08	11.3	7.4	0.6	0.05	0.01	0.02	0.03	0.5	0.2	8.3	12
38	S. CA Chamise Complex	0.952	0.938	0.219	6.2	2.4	0.7	0.16	0.35	0.05	0.16	0.5	0.8	3.8	5
39	S. CA Chamise Complex	-	-	-	-	-	-	-	-	-	-	-	-	-	-
40	Taiwanese Rice Straw	0.945	0.935	0	3.6	1.5	0	1.23	0.42	0.03	0.05	0.3	2.2	3.6	4.3
41	PP Pine Duff	0.93	0.91	0	8.6	5	0	0.05	0.02	0.04	0.05	0.9	0.3	5.3	7.8
42	Alaskan Duff (feather moss)	0.901	0.871	0	10	3.6	0	0.04	0.02	0.04	0.04	0.9	0.2	3.8	5.5
43	S. CA Manzanita	0.972	0.962	0.523	3.8	0.7	0.7	0.06	0.16	0.02	0.09	0.5	0.3	1.7	2
44	Utah Juniper Foliage/Sticks	0.959	0.951	0.797	1.3	0.7	2.7	0.11	0.2	0.02	0.08	0.5	0.4	3.8	4.2
45	Utah Rabbitbrush/Sage foliage/sticks	0.942	0.93	0.722	3.7	0.5	1.4	0.28	0.67	0.03	0.18	0.8	1.2	3.1	3.4
46	Lignin	0.977	0.926	0.234	22.1	3.5	1.1	0.07	0.01	0.05	0.03	1.2	0.2	4.8	6.6
47	LP needles/branches, dried (equal mass)	0.97	0.923	0.028	21.4	2.3	0.1	0.01	0	0.03	0.03	0.6	0.2	2.6	3.7
48	Puerto Rico fern, dried foliage	0.952	0.937	0.055	6	2.2	0.1	0.01	0.06	0.01	0.04	0.7	0.4	2.8	3.9
49	S. CA Chamise (dry)	0.949	0.937	0.585	4.2	0.8	1.1	0.15	0.28	0.02	0.19	0.6	0.7	2.5	2.9
50	SE Wax Myrtle, foliage/sticks	0.928	0.897	0.085	14.3	4.5	0.4	1.13	0.58	0.29	0.17	1.7	2.3	7.2	9.4
51	Southern Pine needle, dried	0.962	0.9	0.064	31.5	18.6	1.3	0.4	0.1	0.11	0.15	1.6	1.2	21.1	30.4
52	Puerto Rico mixed wood/dry sticks	0.954	-	0.109	-	-	-	-	-	-	-	-	-	-	-
53	SE Palmetto leaves	0.952	0.945	0.217	1.8	1.3	0.3	-	-	-	-	-	-	-	-
54	S. CA Ceanothus	0.925	0.911	0.036	6.1	3.9	0.1	0.29	0.31	0.03	0.17	1.1	0.8	4.9	6.9
FLAME 2 stack															
55	PP Needles	-	-	-	-	-	-	-	-	-	-	-	-	-	-
56	Ethanol	0.984	-	-	-	-	-	-	-	6.01	0	9	-	-	-

ID	Sample	Emission factors (g kg ⁻¹ dry fuel)													
		MCE	CE	EC/TC	TOOC	OC	EC	Cl	K	Na	SO ₄	NH ₃	ΣIN	RFM	PM _{2.5}
57	Propane Torch	0.995	-	-	-	-	-	-	4.15	0	5.6	-	-	-	-
58	PP Needles	-	-	0.001	-	-	-	-	-	-	-	-	-	-	-
59	MS Palmetto	0.938	0.921	0.06	7.6	6	0.4	0.99	0.28	0.16	0	0.4	1.7	8	11
60	FL inland Palmetto	-	-	0.132	-	-	-	-	-	-	-	-	-	-	-
61	FL coastal Palmetto	0.944	0.925	0.106	7.8	5.3	0.6	1.21	0.43	0.23	0.31	0.9	2.8	8.7	11.4
62	MS Gallberry	0.947	0.913	0.534	10	7.1	8.1	0.16	0.61	0.16	0.45	1.9	1.8	17	20.5
63	MS Longleaf Pine Needles	0.926	0.878	0.041	21.8	18.6	0.8	0.88	0.33	0.23	0	2	1.9	21.3	30.6
64	NC Oak Leaves	0.941	0.912	0.037	13.6	10.6	0.4	0.23	0.54	0.28	0.4	3.8	1.9	12.9	18.2
65	NC Hickory Leaves	0.933	0.908	0.041	10	7.1	0.3	0.23	0.46	0.24	0	3.5	1.6	9	12.5
66	MS Wiregrass	0.961	0.951	0.089	4.2	3.5	0.3	0.18	0.19	0.17	0	0.6	0.8	4.7	6.4
67	FL Titi	-	-	0.255	-	-	-	-	-	-	-	-	-	-	-
68	LA Phragmites	0.957	0.91	0.019	22.8	19.7	0.4	2.54	1.08	0.98	0	1.7	6.3	26.4	36.2
69	MS Wax Myrtle	0.91	0.884	0.037	11.3	8.1	0.3	0.77	0.66	0.28	0.36	2.6	2.5	11	15
70	GA Kudzu	0.857	0.73	0	57.4	44.2	0	0.39	1.06	0.65	0.99	18.5	4.1	48.3	70.5
71	MS Palmetto and Gallberry	0.914	0.866	0	24	19.1	0	1.56	0.49	0.16	0.2	2.5	3	22.1	31.7
72	MS Longleaf Pine Needles and Wiregrass	0.927	-	0.004	-	-	-	-	-	-	-	-	-	-	-
73	Oak and Hickory	-	-	0	-	-	-	-	-	-	-	-	-	-	-
74	PP Needles 25g	-	-	0.033	-	-	-	-	-	-	-	-	-	-	-
75	PP Needles 250g	0.907	0.808	0.001	51.8	45.6	0.1	0.22	0.3	0.23	0	1.2	1.2	46.9	69.7
76	PP Needles 2460g	0.935	-	0.09	-	-	-	-	-	-	-	-	-	-	-
77	PP Needles 80g	0.903	0.786	0	61	52	0	0.52	0.99	1	0	3.2	4.2	56.1	82.1
78	PP Needles 500g	0.939	0.891	0.028	22	17.8	0.5	0.11	0.17	0.11	0.23	0.7	0.8	19.2	28.1
79	AK Black Spruce dried	0.952	0.928	0.08	10.3	8.5	0.7	0.16	0.25	0.12	0	0.7	0.7	10	14.2
80	AK Black Spruce fresh	0.954	0.932	0.01	9.3	6.9	0.1	0.13	0.16	0.12	0	0.7	0.6	7.6	11.1
81	MT Fir Needles fresh	0.852	0.74	0	61.3	49.6	0	0.11	0.31	0.2	0.29	3.7	1.6	51.2	76
82	MT Fir Branches fresh	0.927	-	0.062	33.7	25.2	1.7	1.03	3.09	2.95	0	5.1	11.7	38.6	51.2
83	MT Fir Needles and Branches dried	0.926	0.85	0	37.4	18.8	0	0.15	0.34	0.29	0	3.9	1.3	20.1	29.4
84	MT Fir Needles and Branches fresh	0.882	0.805	0.004	41.1	27	0.1	0.11	0.37	0.18	0.36	1.9	1.5	28.6	42.1
85	MT Fir Needles dried	-	-	0	-	-	-	-	-	-	-	-	-	-	-
86	MT Fir Branches dried	0.922	0.896	0	13.6	9.4	0	0.16	0.41	0.35	0	1.7	1.5	10.9	15.6
87	CA Manzanita	0.918	0.889	0.063	12.6	7.7	0.5	0.19	0.46	0.14	0.3	2	1.5	9.8	13.6

ID	Sample	Emission factors (g kg ⁻¹ dry fuel)													
		MCE	CE	EC/TC	TOOC	OC	EC	Cl	K	Na	SO ₄	NH ₃	ΣIN	RFM	PM _{2.5}
88	CA Ceanothus	0.907	0.891	0.136	6.8	3.8	0.6	0.47	0.88	0.16	0.45	2	2.4	6.8	8.6
89	PP sticks small	0.967	0.957	0.652	2.5	1.6	3.1	0.06	0.16	0.12	0	0.4	0.5	5.2	6.1
90	PP sticks medium	0.965	0.953	0.47	3	2.5	2.2	0.1	0.23	0.23	0	0.7	1.1	5.9	7.1
91	PP sticks large	0.957	0.949	0.347	2.7	2.1	1.1	0.08	0.14	0.14	0.12	0.6	0.8	4	5.1
92	UT Sage	0.905	0.87	0.017	16.6	14.6	0.3	1.87	1.16	0.64	0	3.2	4.5	19.4	26.8
93	UT Sage washed	0.892	0.844	0.069	21	14.5	1.1	2.88	2.5	0.81	0	6	7.6	23.2	30.5
94	CA Chamise	-	-	0.206	-	-	-	-	-	-	-	-	-	-	-
95	CA Chamise washed	0.908	0.888	0.151	9.1	6.5	1.2	0.52	0.96	0.73	0.27	1.9	2.9	10.5	13.8
96	PP Needles Flaming	0.993	-	0.501	-	2.5	2.5	0.11	0.16	0.25	0.03	0.1	0.7	5.6	6.9
97	PP Needles Flaming feeding	0.983	0.97	0.404	4.6	3.9	2.6	-	-	-	-	-	-	-	-
98	PP Needles smoldering	0.8	-	0	-	45.3	0	0.18	0.14	0.5	0	1.9	0.9	46.1	68.8
99	PP Needles smoldering feeding	0.725	-	0	-	21.2	0	-	-	-	-	-	-	-	-
100	Rice Straw flaming	0.977	-	0	-	3.4	0	1.15	0.78	0.14	0.2	0.1	2.5	5.9	7.6
101	Rice Straw smoldering	-	-	0	-	-	-	-	-	-	-	-	-	-	-
102	PP Needles heading	0.939	0.887	0.047	22.9	20.7	1	0.27	0.31	0.32	0.13	0.9	1.3	23	33.3
103	PP Needles backing	0.946	0.928	0.36	5.6	2.9	1.6	0.25	0.23	0.43	0.07	0.8	1	5.5	7
104	MT Sage heading	0.86	0.778	0.032	39.8	24.9	0.8	1.02	2.94	0.44	0.65	6.7	6.2	32	44.5
105	MT Sage backing	0.881	0.833	0.075	21	12.5	1	1.09	2.96	0.47	0.75	5.5	5.8	19.3	25.5
106	MT Sage Ammonium Sulfate coated	0.898	0.859	0.048	17.1	10.7	0.5	0.99	1.65	0.57	0.42	3.6	4.1	15.3	20.6
107	CA Chamise Ammonium Sulfate coated	0.925	0.908	0.318	5.9	4.2	1.9	0.58	1.11	0.76	0.36	1.7	3.4	9.5	11.6
108	MT Sage KCl coated	0.878	0.838	0.033	18.8	12.1	0.4	1.11	1.74	0.56	0.48	3.6	4.4	16.9	22.9
109	CA Chamise coated	0.93	0.915	0.347	6.2	3.2	1.7	0.54	0.68	0.87	0	1.2	2.2	7.2	8.8
110	MT Sage	0.853	0.789	0.028	28.1	16.7	0.5	0.72	1.84	0.37	0.43	3.7	4.1	21.2	29.6
111	Rice Straw	0.922	0.887	0	14.2	11	0	0.98	0.83	0.32	0.24	1.7	3	14.1	19.6
112	NC Turkey Oak	0.886	0.811	0.043	39.5	32.5	1.4	0.33	1.01	0.37	0.23	5.3	2	35.9	52.2
113	NC Black Needle Rush and Salt Marsh Grass	0.891	0.845	0.016	21.8	18.3	0.3	4.73	3.19	2.06	0.49	1.8	10.6	29.2	38.4
114	LA Saw Grass	0.901	0.872	0.111	11.5	9.2	1.1	3.87	4.69	0.68	0.35	2.5	9.6	20	24.6
115	AK Duff Core	0.811	-	0	-	25	0	0.46	0.43	1.13	0	3.2	2.1	27.2	39.7
116	US Charcoal	0.811	-	-	-	-	-	-	-	0.41	0	6.9	-	-	-
117	Asian Charcoal	0.841	-	-	-	-	-	-	-	1.12	0	3.1	-	-	-

FLAME 2 chamber

ID	Sample	Emission factors (g kg ⁻¹ dry fuel)													
		MCE	CE	EC/TC	TOOC	OC	EC	Cl	K	Na	SO ₄	NH ₃	ΣIN	RFM	PM _{2.5}
118	PP Needles	-	-	0.04	-	-	-	-	-	-	-	-	-	-	-
119	Longleaf Pine Needles and Wiregrass	0.983	-	0.045	-	-	-	-	-	-	-	-	-	-	-
120	Black Needle Rush	-	-	0.088	-	-	-	-	-	-	-	-	-	-	-
121	NC Hickory and Oak Leaves	0.964	-	0.084	-	-	-	-	-	-	-	-	-	-	-
122	MT Fir Needles & Branches (fresh)	0.95	-	0.325	-	-	-	-	-	-	-	-	-	-	-
123	MT Fir Needles & Branches (dry)	-	-	0.006	-	-	-	-	-	-	-	-	-	-	-
124	FL Palmetto Leaves (coastal)	0.966	0.959	0.573	1.9	0.8	1.1	0.93	0.16	0.11	0.12	0.9	1.5	3.4	3.8
125	MS Palmetto Leaves	0.963	0.956	0.25	2.3	1.2	0.4	0.72	0.12	0.03	0.05	0.8	1.2	2.9	3.5
126	Burn 119 continued overnight	-	-	-	-	-	-	-	-	-	-	-	-	-	-
127	Rice Straw	0.953	-	0.026	-	-	-	-	-	-	-	-	-	-	-
128	AK Duff Core	0.933	0.91	0.007	7.3	5.4	0	0.03	0.07	0.04	0.05	1.8	0.3	5.8	8.5
129	NC Rhododendron	0.967	0.957	0.091	3.8	2.1	0.2	0.08	0.08	0.03	0.04	2.1	0.3	2.6	3.7
130	AK Black Spruce	0.982	0.968	0.238	6	3.1	1	0.02	0.05	0.04	0.04	1.8	0.2	4.3	5.8
131	MT Fir Needles & Branches (dry-50g)	0.953	-	0	-	-	-	-	-	-	-	-	-	-	-
132	AK Duff Core (40g)	0.942	0.916	0	7.8	6.8	0	0.02	0.09	0.09	0	3.2	0.3	7.2	10.6
133	FL Wiregrass	0.977	-	0.062	-	-	-	-	-	-	-	-	-	-	-
134	CA Chamise	0.95	-	0.502	-	-	-	-	-	-	-	-	-	-	-
135	FL Black Needlerush	-	-	0.038	-	-	-	-	-	-	-	-	-	-	-
136	MT Sage- Undiluted	0.946	-	0.377	-	-	-	-	-	-	-	-	-	-	-
137	MT Sage- Dilution #1	-	-	-	-	-	-	-	-	-	-	-	-	-	-
138	MT Sage- Dilution #2	-	-	-	-	-	-	-	-	-	-	-	-	-	-
139	MS Longleaf Pine Needles- Undiluted	0.956	0.887	0.021	36.9	34.1	0.7	1.27	0.28	0.14	0.14	3.1	2.2	36.9	54
140	MS Longleaf Pine Needles- Dilution #1	-	-	-	-	-	-	-	-	-	-	-	-	-	-
141	MS Longleaf Pine Needles- Dilution #2	-	-	-	-	-	-	-	-	-	-	-	-	-	-
142	MS Longleaf Pine Needles- Dilution #3	-	-	-	-	-	-	-	-	-	-	-	-	-	-
143	MS Gallberry	-	-	0.497	-	-	-	-	-	-	-	-	-	-	-
144	China Sugar Cane	0.981	-	0.105	-	-	-	-	-	-	-	-	-	-	-
145	AK White Spruce	0.979	0.966	0	5.1	3.5	0	0.31	0.16	0.08	0	2.5	0.7	4.2	5.9

The form of the particle-phase carbon emitted by fires—OC or EC—affects the climate and visibility impacts of the smoke produced. Organic carbon primarily scatters visible light and increases the fraction of incoming solar radiation scattered back to space, which causes a negative climate forcing. Elemental carbon absorbs visible light and causes a positive climate forcing [e.g., *Bond and Bergstrom, 2006; Jacobson, 2001; Schulz et al., 2006*]. The mass extinction efficiency (α_e) of EC assumed by the IMPROVE (Interagency Monitoring of Protected Visual Environments) visibility reconstruction formula is over twice that assigned to OC, so EC has a

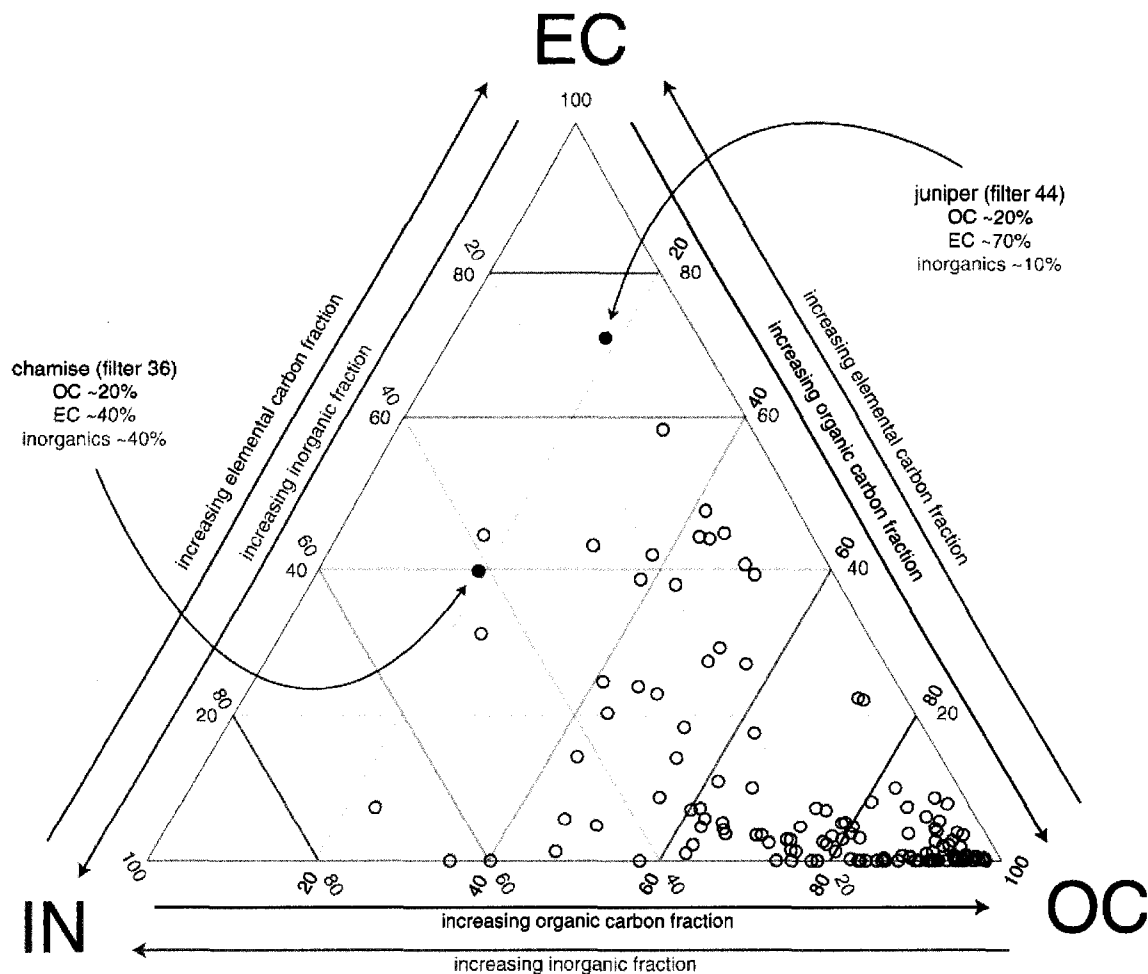


Figure 4.3 Ternary plot comparing mass fractions of elemental carbon (EC), organic carbon (OC) and major inorganic species (K^+ , Na^+ , NH_4^+ , Mg , Ca , Cl^- , SO_4^{2-} , NO_3^-).

stronger visibility impact than OC for a given amount of mass [*Hand and Malm, 2007*]. The OC and EC mass fractions of reconstructed $PM_{2.5}$ during FLAME were a function of the fuel burned and combustion conditions. In general, OC dominated EC, making up $88 \pm 18\%$ of TC. For several fuels, however, the EC mass fraction was bigger; Utah juniper emissions had the largest EC fraction of TC (78%).

Inorganic species—defined here as only the water-soluble ionic species—made up the remainder of reconstructed $PM_{2.5}$. Figure 4.3 shows the contributions from OC, EC and soluble inorganics to reconstructed $PM_{2.5}$ mass in the form of a ternary plot. Most of the samples lie in the OC-dominated region of the plot, reflecting the major contribution by OC to reconstructed mass during the study. Samples with high EC mass fractions often had relatively large inorganic mass fractions. The highest OC content fuels were needles and needle litter from ponderosa, lodgepole and longleaf pines and fuels which burned with a low MCE, including duff core samples and high moisture content fuels. Fuels from the southeastern United States generally had higher inorganic composition compared to the other fuels tested during the study. This may be due to their proximity to polluted and marine regions in the southeastern United States, soils, or from physiological differences in plant composition independent of local environment. Chaparral fuels (e.g., chamise, manzanita and ceanothus) and desert shrubs (e.g., sagebrush, juniper and rabbitbrush) had roughly equal OC, EC and inorganic concentrations. Ponderosa pine fuel components displayed a considerable range between EC and OC fractions, but relatively constant and low inorganic mass fractions (10–20%).

4.2.2 Elemental and organic carbon composition

Elemental carbon emissions are associated with flaming-phase combustion, in agreement with flame-dependent soot formation mechanisms, but measurements of EC and OC are often not presented in the context of MCE or other representations of combustion behavior to describe this relationship. Figure 4.4 illustrates the relationship between fire-integrated MCE and EC/TC for emissions from two fuel classes during FLAME: ponderosa pine (Figure 4.4a) and several chaparral and desert shrub fuels, including sagebrush, chamise, and manzanita (Figure 4.4b). EC/TC ratios were less than 10% for MCE values less than ~0.93 before increasing strongly with MCE for both fuel classes. Total carbon emissions were dominated by OC at low MCE and by EC at high MCE. I observed a consistent relationship for filter samples containing emissions from only the flaming or the smoldering phases of ponderosa pine needle combustion. These filter samples were collected by turning on the sampler pumps during specific phases of combustion. The EC/TC ratio was 0 (measured EC was not above the detection limit) for smoldering phase emissions (MCE = 0.80) and 0.5 for flaming phase emissions (MCE = 0.99).

Figure 4.4 also shows EC/TC ratios measured in previous laboratory-based biomass burning experiments that tested similar fuels: *Chen et al.* [2007] for ponderosa pine needles and wood, *Hays et al.* [2002] for ponderosa pine needles only, *Inuma et al.* [2007] for a 'pine' fuel from western Germany, and the global average for temperate forests given by *Andreae and Merlet* [2001]. The comparison between these studies is not straightforward. *Hays et al.* [2002] did not report fire-integrated MCE, so we estimated MCE based on their reported timeseries of $\Delta[\text{CO}_2]$ and $\Delta[\text{CO}]$ mixing ratios. The FLAME, *Chen et al.* [2007] and *Hays et al.* [2002] EC

measurements were based on the NIOSH/STN thermal-optical analysis (TOA) method. *Iinuma et al.* [2007] used the C-mat 5500 thermographic method to determine apparent EC and reported the median values of $\Delta[\text{CO}]$ and $\Delta[\text{CO}_2]$, which could differ from the burn integrated values. *Christian et al.* [2003] did not give their EC/TC analysis method and *Andreae and Merlet* [2001] recommended a value for black carbon (BC), which I assumed was equivalent to EC for the comparison. I am aware of only one other study that reported EC/TC ratios in the context of MCE for chaparral and desert fuels, *Chen et al.* [2007], who burned sagebrush at the FSL during the FLAME pilot study.

When interpreted through MCE, the FLAME measurements were in agreement with previous results despite the differences in laboratory setups, fuels, and analytical techniques. The wide range of EC/TC ratios in emissions from a single plant species, e.g., ponderosa pine, makes reporting a single value describing the emissions difficult. The results shown in Figure 4.4 underscore the need to interpret OC and EC measurements through a measure of combustion behavior, such as MCE. For example, the EC/TC ratio of ~ 0.3 reported by *Iinuma et al.* [2007] was higher than we observed for burns with MCE below ~ 0.94 , but in good agreement with EC/TC ratios we observed at higher MCE.

Several fuels produced little or no EC when burned, despite featuring a significant amount of flaming combustion and high MCE. These fuels—rice straw in particular—produced particles with some of the highest inorganic mass fractions of reconstructed $\text{PM}_{2.5}$ we observed. These are not the first observations of high inorganic mass fractions in rice straw emissions. *Keshtkar and Ashbaugh* [2007] found carbon accounted for only 28% of the accumulation mode ($0.1 < D_{ac} < 1.8 \mu\text{m}$) aerosol mass emitted by burning rice straw, suggesting a high contribution

by inorganic species. Their results are lower than the observed carbon fractions of 45–80% for rice straw emissions observed during FLAME, but their data were compared to gravimetric $PM_{2.5}$ while we compared to reconstructed mass. *Ryu et al.* [2004] observed high inorganic mass fractions in Korea during the post-harvest rice straw burning season. *Christian et al.* [2003] observed relatively high chlorine emissions from rice straw compared to other fuels, but did not measure EC or OC concentrations for this fuel, so mass fractions could not be determined.

Mazzoleni et al. [2007] examined emissions from rice straw burned in a commercial wood stove. They observed a significant EC fraction of TC (~15%) and observed higher TC mass than gravimetrically determined $PM_{2.5}$. They attributed the TC mass being higher than gravimetric mass to positive sampling artifacts. The large TC fraction suggested a low contribution by inorganic species to total mass. *Mazzoleni et al.* [2007] did not report MCE for the burns, so it is difficult to compare the results directly, but they noted that rice straw ‘tended toward smoldering’ combustion, while the rice straw we burned was dominated by flaming-phase combustion. But if the rice straw tested by *Mazzoleni et al.* [2007] was dominated by smoldering-phase combustion, then their high EC/TC ratios were unusual. From Figure 4.4 we expect smoldering-phase dominated burns to produce less, not more, EC. I suspect the different TOA methods implemented in this work (NIOSH/STN, thermal optical reflectance) and by *Mazzoleni et al.* [2007] (IMPROVE, thermal optical transmittance) explain the different EC/TC ratios. Rice straw emissions collected with an IMPROVE sampler during FLAME 1 had an EC/TC ratio of 7% determined by the IMPROVE protocol compared to 2% for emissions collected on Hi-Vol filters and determined by the NIOSH/STN protocol. I compare carbon analysis methods in much more detail in Chapter 5.

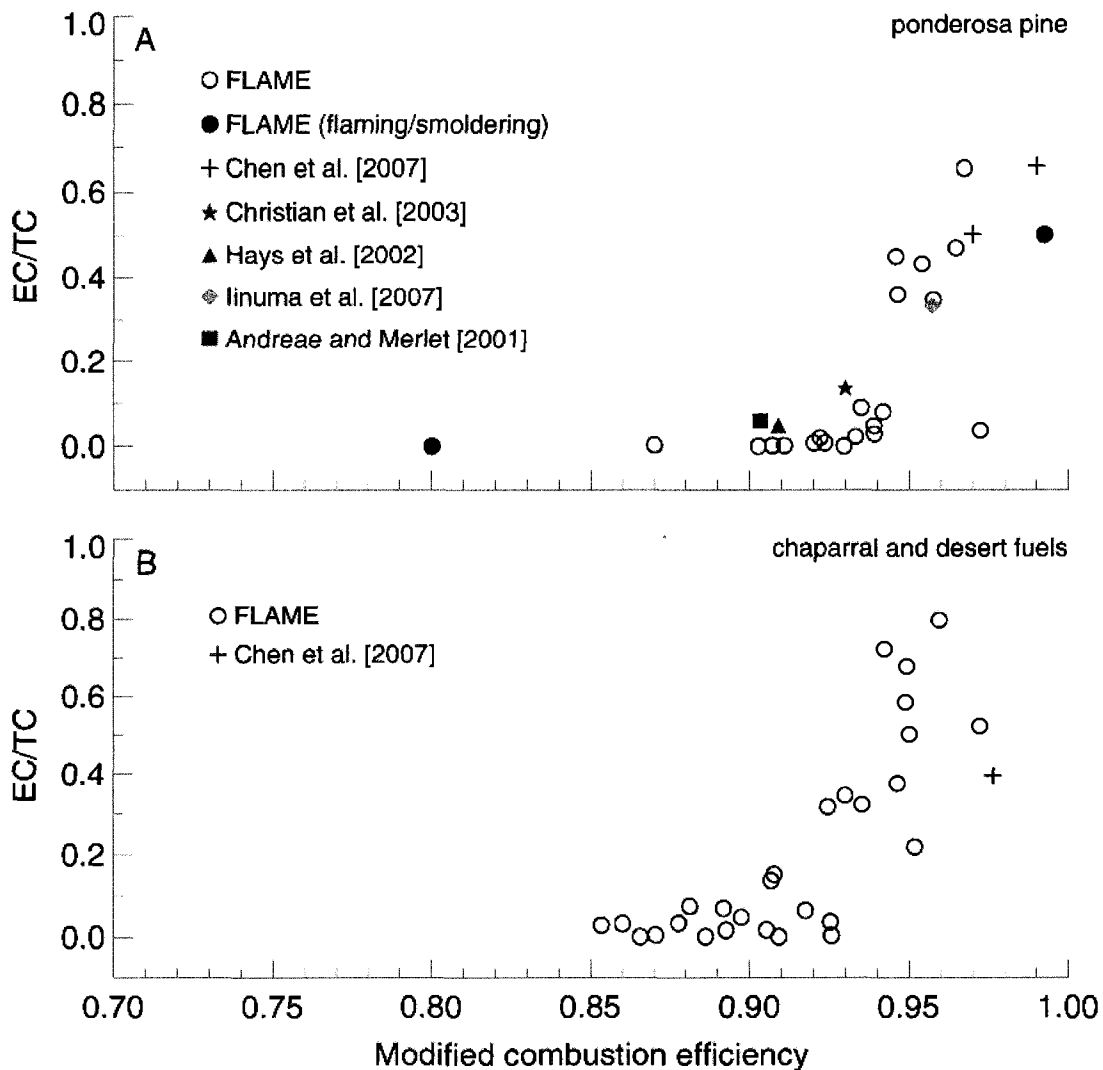


Figure 4.4 Elemental-to-total carbon (EC/TC) ratios observed for emissions from (a) ponderosa pine and (b) chaparral/desert shrub fuels versus fire-integrated modified combustion efficiency (MCE). Ponderosa pine data include needle, branch, needles and branches, needle litter and duff burns. Samples collected during only flaming (high MCE) and smoldering (low MCE) combustion of ponderosa pine needles are indicated by the filled circles. Results reported by several laboratory-based biomass burning emissions studies listed in Table 4.1 are shown for comparison

I was surprised rice straw produced very little EC because it burned primarily by flaming phase combustion during FLAME. The EC concentrations were below the detection limit for rice straw burns although the average of the fire-integrated MCE values was 0.98. EC measured on filters could have oxidized through catalytic reactions with certain inorganic species and been erroneously classified as OC during the TOA analysis, but we do not believe this explains the

lack of EC in the rice straw emissions. Many of the desert and chaparral shrub species we burned emitted large EC mass fractions and large inorganic aerosol mass fractions; the latter comparable to those emitted by rice straw. Rice straw aerosol emissions were dominated by scattering rather than absorption—similar to particles dominated by OC—so the concentrations of light-absorbing EC must have been low.

I hypothesize the mechanism responsible for soot formation in flaming-dominated burns may have been weakened during rice straw burns (and several other fuels), resulting in lower EC concentrations. *Hopkins et al.* [2007] speculated high inorganic salt contents and other fuel properties could influence the amount of EC produced by fires. According to the ‘ionic’ hypothesis [*Mitchell and Miller, 1989*], soot formation begins with pyrolysis of the fuel to produce small radicals and ions, which react to generate large molecular species called soot precursors, e.g., polycyclic aromatic hydrocarbons (PAHs). They act as nuclei for surface growth processes that form particles that agglomerate with each other forming large-chain soot agglomerates [*Mitchell and Miller, 1989*]. Inorganic additives, such as K and Na, are effective soot inhibitors believed to neutralize flame ions and inhibit rapid formation of soot precursors [*Mitchell and Miller, 1989*]. The high concentrations of inorganic species, including K and Na, emitted during rice straw combustion could inhibit soot formation through this mechanism, resulting in lower EC concentrations. Other fuels, however, also emitted large concentrations of inorganic species. In fact, EC was never observed in the absence of inorganic species, but we observed high mass fractions of inorganics, but little EC for several grass and southeastern shrub fuels (see Figure 4.3).

An alternative theory for soot-formation links precursor concentrations to the

availability of double and triple bonded hydrocarbons in the fuel [Frenklach, 2002]. I do not know if rice straw contains fewer of these compounds compared to the other fuels we tested, but since most plant species are dominated by cellulose, hemicellulose and lignin, it is unlikely that there were large differences in the hydrocarbon composition of the fuels we burned during FLAME. Combustion temperature may also play a role, as higher combustion temperatures are needed to volatilize the soot precursor species, but I did not observe any relationship between the thermal energy release rate and EC formation. The thermal energy release rate calculation, however, was only a crude estimate of combustion intensity. Infrared camera measurements may provide some insight into this puzzle, but were awaiting processing at the time of writing.

4.2.3 Inorganic species

Chloride

Chloride was the most abundant inorganic species on average, accounting for $5.4 \pm 7.0\%$ of the speciated $PM_{2.5}$ mass (i.e., mass reconstructed from OC (no multiplier), EC and soluble inorganics) and $26 \pm 16\%$ of the soluble inorganic mass. The observations agreed with Reid *et al.* [2005b], who concluded chloride made up 2–5% of fine particle mass based on observations reported by several studies that examined fresh biomass burning emissions. Chen *et al.* [2007] found chloride accounted for 0.1–9.6% of gravimetric $PM_{2.5}$ for several of the same fuels we burned. Emissions from several southeastern fuels contained high mass fractions of chloride relative to other inorganic species. For example, chloride was ~60 % of the inorganic $PM_{2.5}$ emissions for a palmetto leaf (*Serenoa repens*) burn.

Christian *et al.* [2003] observed a loose correlation between chlorine emission factors

and fuel chlorine content. Several studies showed that roughly one-third of fuel chlorine was emitted in the form of particulate matter for tropical and savannah fuels [Christian *et al.*, 2003; Keene *et al.*, 2006; Yokelson *et al.*, 2008]. We did not measure the chlorine content in our fuels, so we cannot verify this observation, but chloride mass fractions of total inorganics within fuel classes were relatively constant, indicating fuel type, and presumably fuel chlorine content, was the major driver of chloride mass fractions. Hays *et al.* [2002] speculated the high chlorine and sodium concentrations emitted by burning western hemlock (*Tsuga heterophylla*) were due to their proximity to a coastal environment, i.e., sea salt. A similar phenomenon could explain the higher chloride concentrations I observed in the emissions from southeastern fuels. Sodium concentrations emitted by these fuels were lower than for non-coastal plants, however, so the marine influence may be less important than plant physiology.

Potassium

Potassium was the second-most abundant inorganic species during FLAME, making up $4.8 \pm 5.0\%$ of reconstructed fine mass and $24 \pm 13\%$ of the inorganic mass. Several studies have noted higher potassium mass fractions of aerosol fine mass in flaming-dominated combustion emissions. Echalar *et al.* [1995] observed higher potassium content in emissions (3.2–4.4%) from savannah fires—which tend to feature more flaming phase combustion—compared to emissions from more smoldering-dominated tropical forest fires ($0.3 \pm 0.1\%$). Ward and Hardy [1991] observed similar differences between potassium content for flaming and smoldering emissions from logging slash fires in the western U.S. I observed differences in potassium mass fractions for emissions from flaming (2.8%) and smoldering (0.3%) ponderosa pine needles, but potassium mass fractions were higher for rice straw emissions during both flaming (13.3%) and

smoldering (19.9%) combustion phases. The potassium mass fractions for all sagebrush burns were $11.2 \pm 4.0\%$ and for all chamise burns were $8.9 \pm 4.6\%$, but were only $0.24 \pm 0.07\%$ for ponderosa pine needle litter burns. These burns all had fire-integrated MCE values within 0.03, so combustion phase was less important than plant type, and presumably composition, in determining potassium mass fractions of fine mode aerosol. The correlation between MCE and potassium mass fraction for the entire study was poor ($r^2 = 0.04$).

Posfai et al. [2003] suggested potassium and chloride take the form KCl in the core of smoke particles with BC. In our study, the relationship between potassium and chloride strongly depended on fuel type. Chaparral and rangeland shrub fuels produced particles with chloride/potassium molar ratios significantly less than one ($0.39 \text{ mol Cl mol}^{-1} \text{ K}$; $r^2 = 0.78$). *Chen et al.* [2007] observed a similar potassium-chloride ratio of $0.44 \text{ mol Cl mol}^{-1} \text{ K}$ for sagebrush. Other fuels, including palmetto leaves and rice straw, produced aerosol with potassium-chloride ratios greater than one. The relationship between potassium and chloride in these fuels was consistent despite variations in combustion behavior, fuel mass, or experiment type (stack or chamber). I believe they reflect similar relationships between fuel K and Cl content. The distinction in potassium-chloride ratios in emissions from these fuels may prove useful in distinguishing biomass burning emissions from different regions.

Other inorganic species

Sodium was $2.5 \pm 3.1\%$ of reconstructed fine mass on average, followed by sulfate ($1.6 \pm 1.7\%$), ammonium ($0.9 \pm 1.5\%$) and nitrate ($0.6 \pm 0.9\%$). Sodium mass fractions were relatively independent of fuel type and were usually high for fuels with low inorganic mass fractions. Sulfate mass fractions were highest for desert shrubs and chaparral fuels, ranging from 10–20%

of the inorganic mass. Ammonium mass fractions were largest in rice straw emissions (~10%), possibly from high fuel ammonium content resulting from fertilization of the crop. Calcium, magnesium and nitrite made up the remainder of the analyzed inorganic species in the emissions.

4.3 Particulate emission factors

To calculate emission factors for each aerosol species, I determined m_i by multiplying the mass concentration of i on the filter by the total volume of air passing through the stack during the stack burn sampled. We usually sampled three replicate burns on a single filter during FLAME 1 and two replicate burns on a single filter during FLAME 2. I calculated m_i during chamber burns by multiplying filter concentrations by the total volume of the chamber (~3000 m³). We obtained filter-integrated emission factors for gas phase species and filter-integrated MCE values that corresponded to the filter sampling periods using the same methods.

Figure 4.5 shows emission factors as a function of MCE for OC (no multiplier applied), EC, TC, K⁺, Cl⁻, total analyzed inorganics, reconstructed/speciated fine mass (OC + EC + inorganics) and PM_{2.5} (OC x 1.5 + EC + inorganics). Organic carbon emission factors (no multiplier applied) were negatively correlated with MCE ($r^2 = 0.36$), meaning OC emissions were higher for burns featuring relatively more smoldering-phase combustion (Figure 4.5a). Emission factors ranged from ~0.5 g C kg⁻¹ fuel at high MCE values to ~50 g C kg⁻¹ fuel at lower MCE values, with a study average of 11.6 g C kg⁻¹ fuel. The study average was slightly higher than the literature-averaged OC emission factor for extratropical forest fires (8.6–9.7 g kg⁻¹ fuel) reported by *Andreae and Merlet* [2001], but I again stress that the results were highly sensitive to

combustion conditions. *Christian et al.* [2003] observed OC emission factors ranging from 0.99–15.7 g kg⁻¹ fuel for several savannah and Indonesian fuels burned at the FSL. They observed OC emission factors as high as 122.4 g kg⁻¹ fuel for spot measurements that did not represent the fire-integrated values.

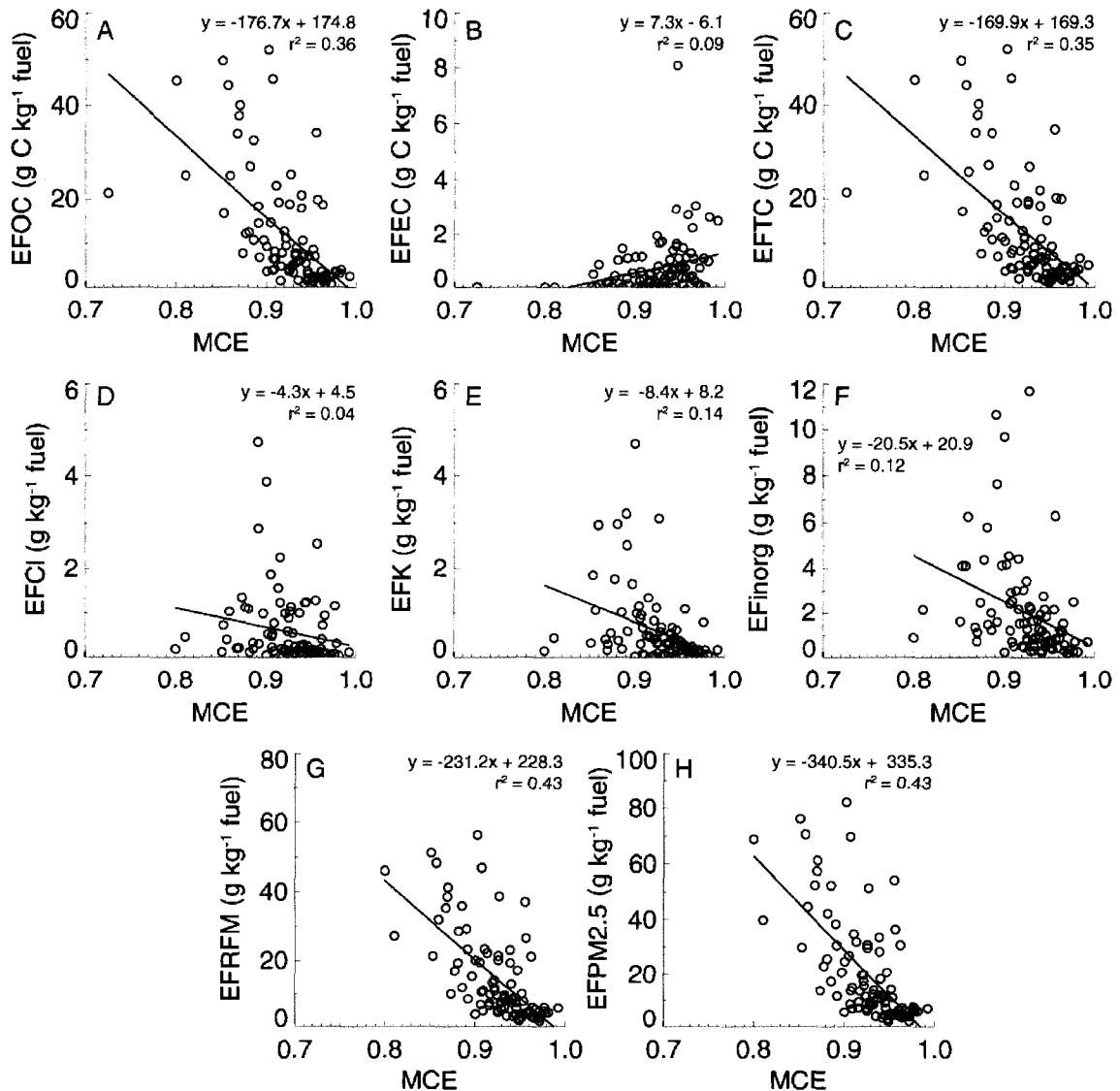


Figure 4.5 Emission factors as a function of modified combustion efficiency for: a) organic carbon (OC); b) elemental carbon (EC); c) total carbon (TC); d) chloride; e) potassium; f) total inorganics; g) reconstructed fine mass; and h) reconstructed fine mass including species associated with OC.

Elemental carbon emission factors ranged from 0.0–8 g C kg⁻¹ fuel (Figure 4.5b). The significance of the relationship between EC and MCE was weaker ($r^2 = 0.11$) than that between

OC and MCE. Elemental carbon emission factors tended to be higher for fuels featuring more flaming-phase combustion and higher MCE, but many fuels had high MCE and did not produce EC, such as rice straw. Other burns had low EC emission factors despite featuring a strong flaming-phase of combustion and high MCE, including lodgepole pine and ponderosa pine chamber burns, rhododendron. The study-average EC emission factor was $0.7 \pm 1.1 \text{ g C kg}^{-1}$ fuel, slightly higher than the literature-average of 0.56 ± 0.19 reported by *Andreae and Merlet* [2001] for extratropical forests. *Christian et al.* [2003] reported EC emission factors ranging from 0.04–1.52 g kg^{-1} . They found the highest EC emission factors for dambo and miombo fires that burned with a high MCE (0.97–0.98). Gallberry (*Ilex glabra*) burning with an MCE of 0.95 produced our study maximum EC emission factor of 8.1 g kg^{-1} . We also observed high EC emission factors for burning pine, fir and spruce twigs and sticks. Total carbon emission factors were closely related to OC emission factors because OC emission factors were 2–10 times larger than EC emission factors (Figure 4.5c).

Total inorganic ion emission factors were weakly correlated with MCE ($r^2 = 0.12$), with slightly higher emission factors at lower MCE (see Figure 4.5f). I suspect inorganic emission factors are more closely tied to fuel composition, as noted by several other studies [*Christian et al.*, 2003; *Keene et al.*, 2006]. Chloride emission factors (Figure 4.5d) were not a function of MCE ($r^2 = 0.04$). Chloride emission factors ranged from 0.01–4.7 g kg^{-1} fuel with a study average of $0.6 \pm 0.8 \text{ g kg}^{-1}$ fuel. *Keene et al.* [2006] observed chloride emission factors ranging from ~0–3.2 g kg^{-1} fuel and *Christian et al.* [2003] observed emission factors ranging from 0.01–1.8 g kg^{-1} fuel.

Potassium was slightly more dependent on MCE ($r^2 = 0.14$) than chloride. Potassium

emission factors ranged from 0.0–4.7 g kg⁻¹ fuel, with a study average of 0.6 ± 0.8 g kg⁻¹ fuel (Figure 4.5e). *Christian et al.* [2003] reported potassium emission factors ranging from 0.02–1.29 g kg⁻¹ fuel and *Andreae and Merlet* [2001] provide literature-average values ranging from 0.08–0.41 g kg⁻¹ fuel for extratropical forests. *Yokelson et al.* [2008] found an average potassium emission factor of 0.62 ± 0.35 g kg⁻¹ fuel at an average MCE of 0.95 and asserted that potassium emissions increase for burns with greater proportions of flaming combustion. Our data disagree with this finding. Potassium emissions decreased with increasing MCE during FLAME. Higher potassium mass fractions of aerosol fine mass at high MCE—such as those observed by *Ward and Hardy* [1991]—are due to less OC emissions at high MCE, not more potassium emissions. Potassium emission factors were a stronger function of the fuel and presumably potassium content, e.g., plant species, component, or fuel condition. For example, EFK was 0.4 ± 0.4 g kg⁻¹ fuel for all ‘fresh’ ponderosa pine needle burn emissions, but only 0.03 ± 0.01 g kg⁻¹ fuel for ponderosa pine litter emissions, about a factor of 10 less. This difference was much larger than that observed between the flaming and smoldering ponderosa pine needle emissions (0.16 g kg⁻¹ fuel for flaming versus 0.14 g kg⁻¹ fuel for smoldering).

I calculated emission factors for two different estimates of particle mass. In Figure 4.5, reconstructed fine mass refers to the sum of OC, EC and measured inorganics and PM_{2.5} refers to the sum of EC, inorganics and total organic matter estimated by multiplying OC by a factor of 1.5 to account for non-carbon species in the organic material. Emission factors for both were strongly driven by the OC emission factors because OC was the dominant species during the study. Reconstructed/speciated mass emission factors ranged from 1.7–56.1 g kg⁻¹ fuel with an average of 14.4 ± 13.2 g kg⁻¹ fuel. PM_{2.5} (OC x 1.5 + EC + inorganics) emission factors ranged

from 1.9–82.1 g kg⁻¹ fuel with an average of 20.3 ± 19.5 g kg⁻¹ fuel. The latter depended strongly on the factor assumed to convert measured OC to total particulate organic matter.

Both reconstructed fine mass ($r^2 = 0.4$) and PM_{2.5} ($r^2 = 0.32$) were strong functions of MCE. They increased by ~15–20 g kg⁻¹ fuel for a 0.1 decrease in MCE. Wide ranges in observed aerosol mass emission factors are common in the literature for this reason. *Reid et al.* [2005b] give particle emission factors of ~9 g kg⁻¹ fuel based on flaming combustion measurements—which they define as MCE > 0.9—and ~34 g kg⁻¹ fuel for smoldering combustion measurements (MCE < 0.9). *Ward and Hardy* [1991] reported PM_{2.5} emission factors ranging from roughly 2–35 g kg⁻¹ fuel and *Christian et al.* [2003] report PM_{2.5} emission factors ranging from 2.9–61.6 g kg⁻¹ fuel. *Andreae and Merlet* [2001] report a literature-average PM_{2.5} emission factor of 13.0 ± 7.0 for extratropical forests.

4.4 Carbon mass budgets and total observed organic carbon emissions

The mass of dry biomass consumed (m_{consumed}), assuming the residual ash contains no water, was given by:

$$m_{\text{consumed}} = \frac{m_{\text{fuel}}}{1 + FM} - m_{\text{ash}} \quad 4.1$$

where FM is the fuel moisture fraction, m_{fuel} is the initial (wet) fuel mass and m_{ash} is the mass of the ash remaining following the burn. The assumption of zero ash water content was not valid for high moisture content fuels that do not completely burn, so I did not calculate m_{consumed} for fuels with $FM > 0.4$. The carbon consumed (C_{consumed}) during each burn was calculated by multiplying m_{consumed} by the fraction of carbon in each fuel. I assumed a carbon content of 0.45 in the absence of measured carbon concentration to be consistent with the value assumed by

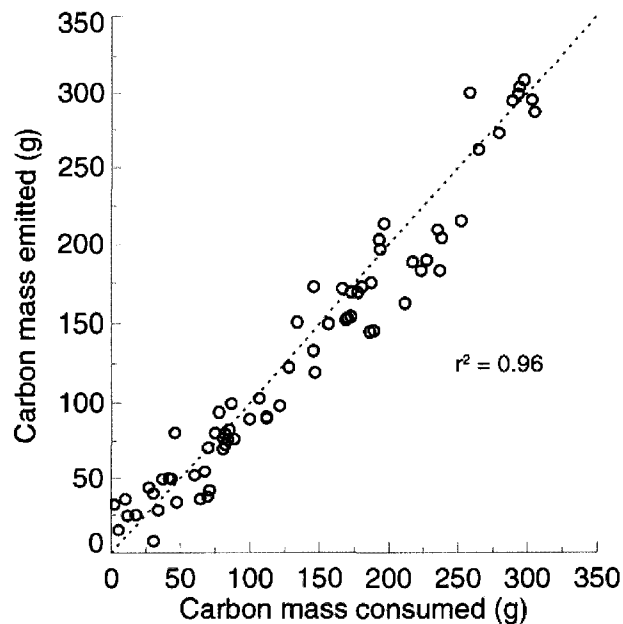


Figure 4.6 Carbon mass consumed versus carbon mass emitted during FLAME.

Andreae and Merlet [2001]. I calculated the mass of carbon emitted (C_{emitted}) during each burn by adding together carbon emitted in the form of CO_2 , CO, C_{1-4} hydrocarbons, and particle phase OC and EC. The gas data were integrated over multiple burns that corresponded to the filter collection periods. Figure 4.6 compares C_{consumed} to C_{emitted} . The mass of carbon emitted and consumed during the stack burns were highly correlated ($r^2 = 0.96$) and in agreement with the 1:1 line, indicating that emissions were effectively captured by the stack.

I combined gas-phase and particle-phase carbon species measurements to examine the fate of carbon combusted during the FLAME burns. On average, $89 \pm 5.7\%$ of the carbon was emitted in the form of CO_2 , followed by CO ($6.9 \pm 3.0\%$), $\text{PM}_{2.5}$ OC ($2.3 \pm 2.5\%$), $\text{C}_2\text{-C}_4$ hydrocarbons ($1.3 \pm 1.9\%$), CH_4 ($0.5 \pm 0.4\%$) and $\text{PM}_{2.5}$ EC ($0.2 \pm 0.2\%$).

The particle-phase carbon measurements allowed me to compare MCE to CE, which is defined as the fraction of total carbon emitted in the form of CO_2 . Unlike MCE, CE depends on gas-phase hydrocarbon and aerosol carbon emissions. As illustrated in Figure 4.7, CE is

consistent with MCE for high MCE, or flaming-dominated burns. A few burns had high MCE, but low CE. Most of these were chamber burns (shown in red) that had unusually high hydrocarbon gas concentrations. The large hydrocarbon gas concentrations may have been more uncertain due to the relatively large background concentrations in the chamber during the early portion of the experiments. The two measures of combustion disagree more at low MCE when smoldering-phase combustion becomes important, because more non-CO and non-CO₂ species are emitted by these fires.

Fires dominated by smoldering combustion produced more OC emissions, so I also plotted the emission factors from Figure 4.5 against CE rather than MCE in Figure 4.8. The correlation between CE and OC was much higher ($r^2 = 0.71$) than between MCE and OC because CE accounts for carbon emitted in the form of OC. Many of the burns with high OC

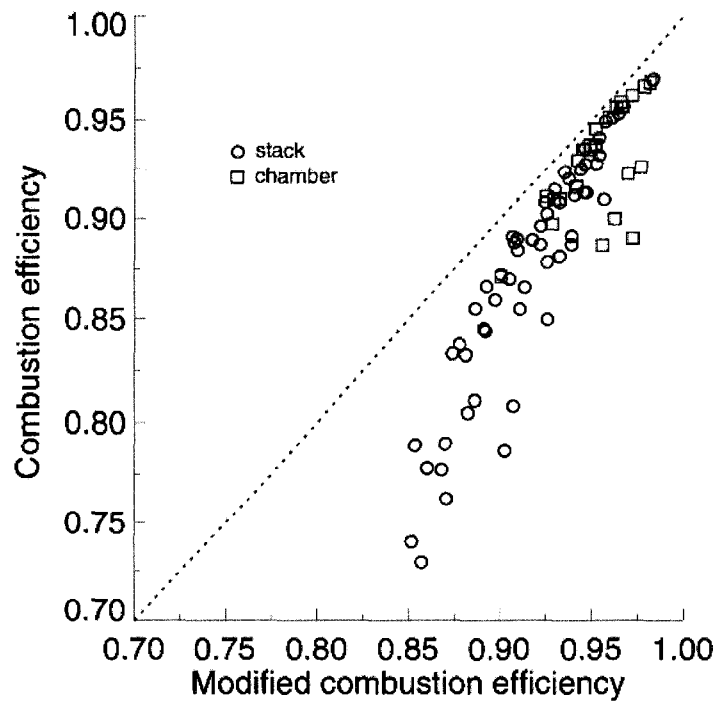


Figure 4.7 Combustion efficiency (CE) versus modified combustion efficiency (MCE) during FLAME.

emission factors that lie far from the regression line in Figure 4.5a had larger MCE than CE because they emitted a large amount of OC that was not captured by MCE. The relationship between CE and TC, reconstructed/speciated fine mass, and estimated total PM_{2.5} were stronger because OC was the dominant aerosol component. The relationship between CE and inorganic species was similar to that between MCE and inorganic species, so both measures of combustion behavior indicated that inorganic emissions were relatively independent of combustion conditions.

I continue to use MCE as the primary measure of combustion behavior during FLAME because MCE only requires measurements of CO and CO₂, so it is more easily measured and has been more commonly reported. We also measured CO and CO₂ at high time resolution, so I can calculate MCE as a function of burn time, which I cannot for CE.

Heald et al. [2008] introduced the concept of total organic carbon (TOC) to examine carbonaceous aerosol and gases observed over North America during several field campaigns. TOC includes organic species present in the atmosphere in either gas- or particle-phases. Total observed organic carbon (TOOC) is defined as the fraction of TOC that can be identified with current measurement capabilities. TOC is analogous to NO_x in the atmosphere. Nitrogen oxides rapidly cycle between NO and NO₂ and organic species can oxidize, condense and re-volatilize between the gas- and particle-phase. Emission factors for TOOC provide a measure of the total hydrocarbon emissions (excluding CH₄) emitted by a process, such as biomass burning.

I determined TOOC emission factors during FLAME by adding emission factors for OC and C₂₋₄ hydrocarbon measurements together to calculate TOOC emitted by fires and examined its relationship to varying combustion conditions (Figure 4.9). TOOC emission

factors were negatively correlated to CE ($r^2 = 0.75$), and showed a similar relationship with MCE. The relationship with MCE was weaker because, by definition, MCE under-predicts the smoldering-phase combustion contribution to fires that produce more OC and hydrocarbons. Flaming-dominated fires produce much less TOOC than smoldering-dominated fires. Emission factors at the lower range of MCE and CE observed during FLAME were on the order of 60 g C kg⁻¹ fuel compared to ~5 g C kg⁻¹ fuel at the upper range of MCE and CE.

TOC emission factors give the upper limit for particulate OC that can eventually be

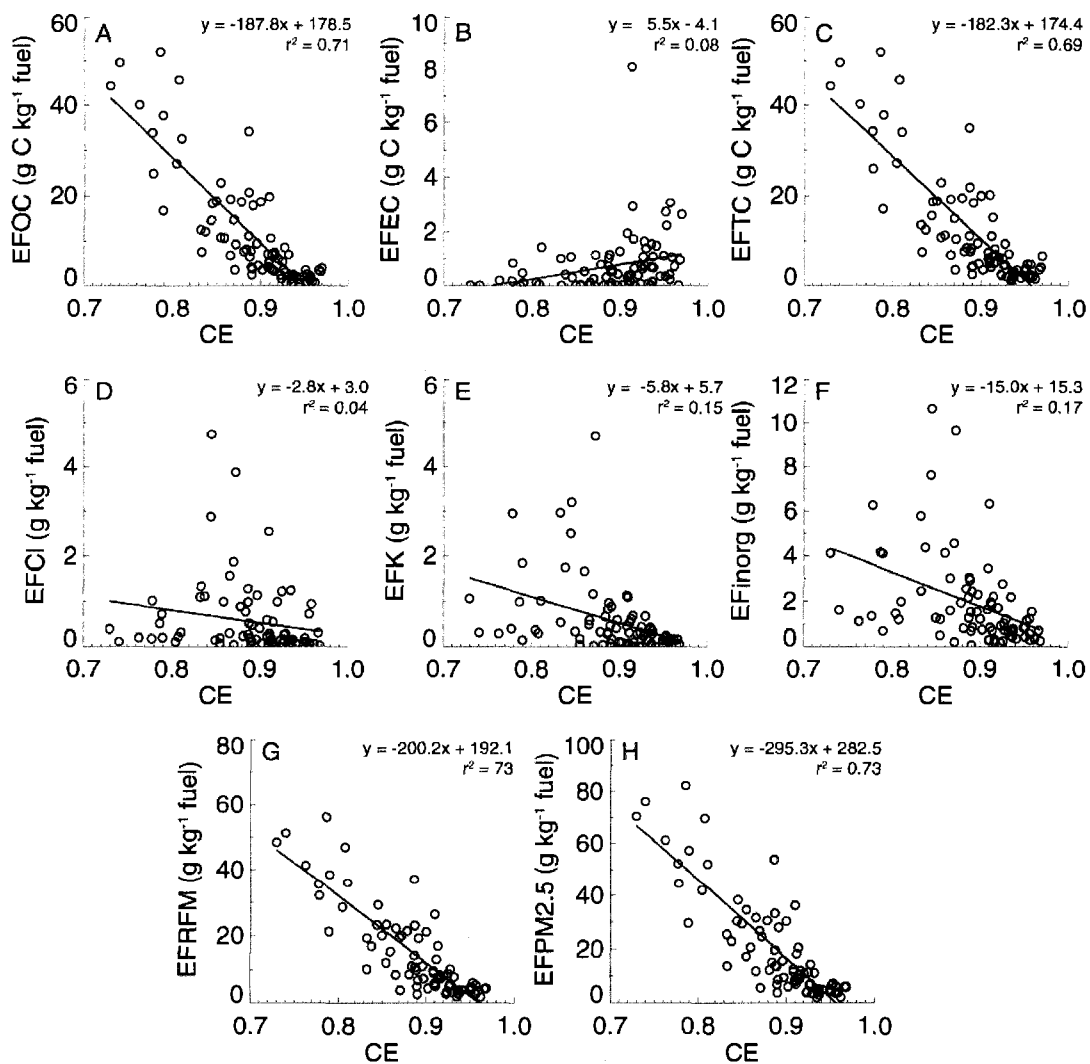


Figure 4.8 Particulate emission factors as a function of combustion efficiency (CE) following Figure 4.5.

formed from all fire emissions through subsequent atmospheric aging processes in the atmosphere, assuming all gas-phase hydrocarbon species are eventually oxidized to lower volatility species that can nucleate new particles or condense onto preexisting particles. Unfortunately, TOOC underestimates TOC because all of the hydrocarbon species in the particle and gas phase cannot yet be measured. For example, during FLAME, we only measured C₁₋₄ hydrocarbon species. Measurements made using open path and aircraft-based Fourier-transform infrared spectrometry (FTIR) have shown that oxygenated volatile organic compounds (OVOCs) can comprise a large fraction (~70–80%) of non-methane organic compounds emitted by fires [Christian *et al.*, 2003; Yokelson *et al.*, 2007a]. OVOC emissions are strongly correlated with CO and C₁₋₄ hydrocarbon emissions. If we assume C₁₋₄ hydrocarbons make up the remaining 20–30% of non-methane organic compounds emitted by fires, then TOOC emission factors—recalculated using the higher gas-phase emissions—increase by roughly a factor of two. Simultaneous measurements of OVOCs and aerosol organic carbon could confirm these estimates.

The partitioning of TOC between the gas and aerosol phases depends on the organic aerosol concentration [Donahue *et al.*, 2006; Robinson *et al.*, 2007]. Lipsky and Robinson [2006] showed that particulate matter emission rates of wood smoke decreased with increasing levels of dilution, which they attributed to changes in partitioning. Following this reasoning, emission rates for gas-phase compounds should increase with dilution, though the magnitude of this increase will depend on the fraction of gas-phase organics made up by semi-volatile species. Aerosol concentrations typically found in laboratory emission studies are much higher than in the atmosphere, particularly in regions distant from sources. The mean OC concentration

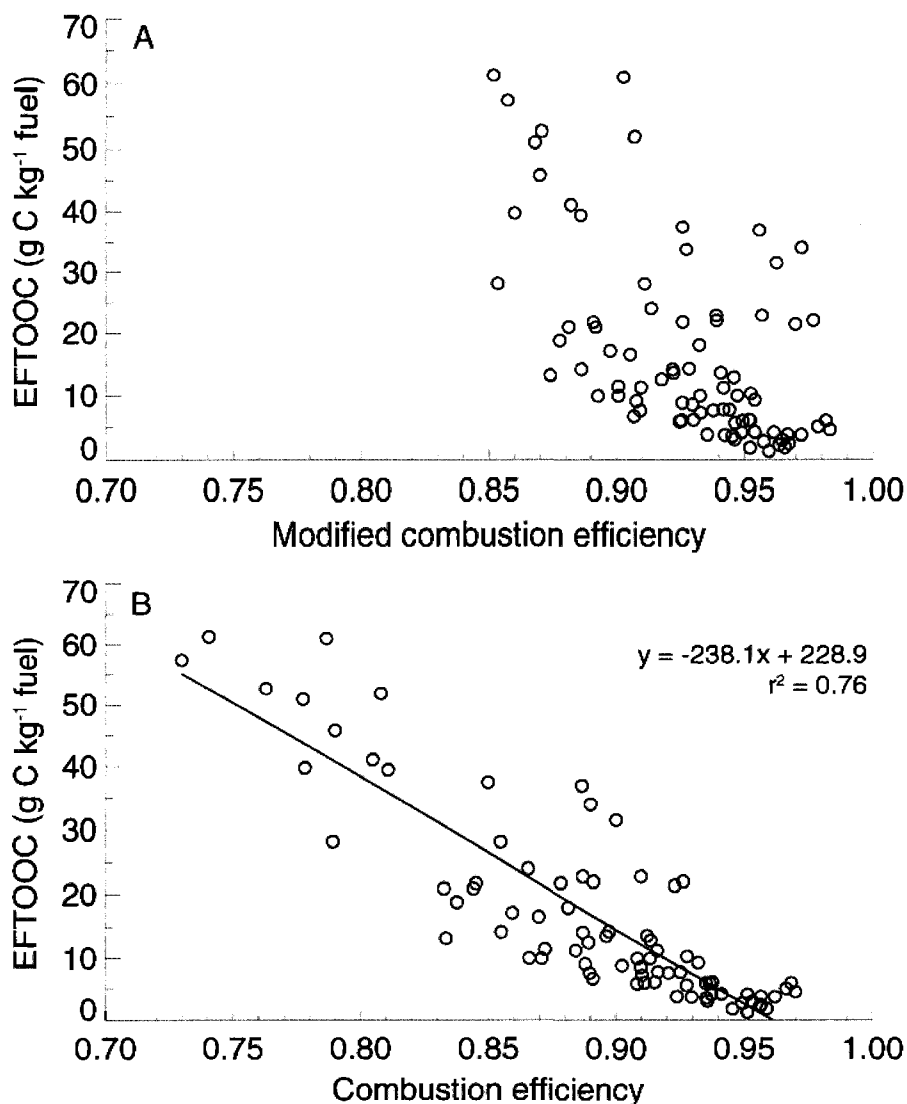


Figure 4.9 Total observed organic carbon (TOOC) emission factors during FLAME as a function of a) modified combustion efficiency and b) combustion efficiency.

during FLAME was $320 \pm 460 \mu\text{g m}^{-3}$, much higher than OC concentrations of $\sim 10 \mu\text{g m}^{-3}$ observed at Yosemite NP during fire-impacted periods [Engling *et al.*, 2006b]. We observed a weak relationship between the aerosol fraction of TOOC and OC mass concentrations (Figure 4.10). It is difficult to link the variations in the OC fraction of TOOC directly to partitioning effects. As stated earlier, we only measured a fraction of the gas-phase species, which limited our ability to detect possible changes in partitioning. I discuss the partitioning issue in more detail in Chapter 5.

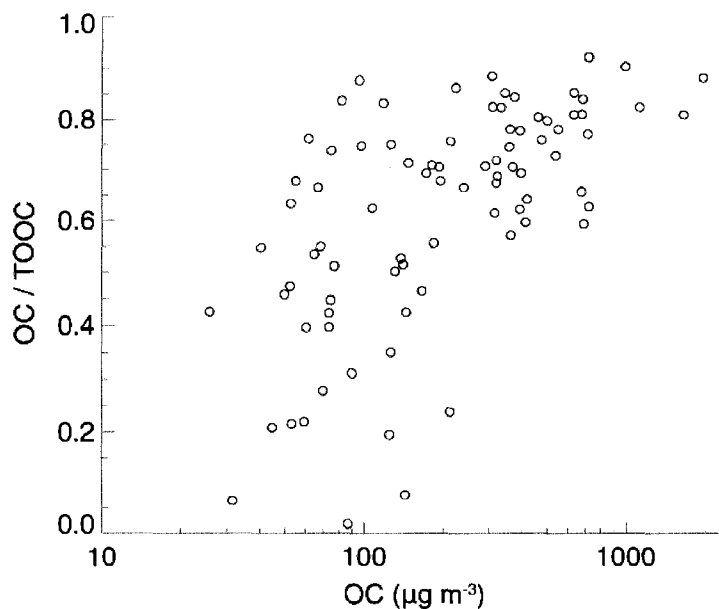


Figure 4.10 Semi-log scatter plot showing organic carbon (OC) fractions of total observed organic carbon (TOOC) as a function of OC mass concentrations during FLAME.

4.5 Aerosol optical properties

The TSI nephelometer b_{sp} measurements do not accurately capture the true scattering coefficient because of truncation and non-lambertian errors [Anderson and Ogren, 1998]. Non-lambertian errors are due to the non-cosine weighted intensity distribution of the nephelometer light source. Truncation errors result from the instrument not capturing the full 0–180° scattering phase function due to geometric obstructions inside the cavity; it collects light between 7–170°. Aerosols scatter more light than calibration gases in the forward direction not captured by the instrument, so measured scattering coefficients underestimate the true total scattering coefficients. The magnitude of the error depends on the phase function, which itself depends on particle size, shape and refractive index.

I corrected the TSI nephelometer data for these effects using the sub- μm log-normal size distribution parameters given by Anderson and Ogren [1998]. I used the sub- μm parameters

because size distributions were dominated by particles in this size range and there was a 2.5 μm sizecut for the TSI nephelometer during FLAME 1. *Anderson and Ogren* [1998] accounted for the size-dependence of the correction factors by including scattering Ångström exponents in their formulation. The scattering Ångström exponents (\mathring{A}_s) were calculated using:

$$\mathring{A}_s = - \frac{\log \frac{b_{sp1}}{b_{sp2}}}{\log \frac{\lambda_1}{\lambda_2}} \quad 4.2$$

where b_{sp1} and b_{sp2} were the uncorrected scattering coefficients measured at wavelengths λ_1 and λ_2 . We calculated \mathring{A}_s at the three wavelength pairs—450 and 700 nm, 450 and 550 nm, and 550 and 700 nm—to determine correction factors using Table 4b in *Anderson and Ogren* [1998]. I refer to these as $\mathring{A}_s(450/700)$, $\mathring{A}_s(450/550)$ and $\mathring{A}_s(550/700)$. I took $\mathring{A}_s(450/700)$ to be the ‘standard’ \mathring{A}_s because it covered the widest wavelength range. It ranged from 0.8–3.1, with a study mean value of 1.9 ± 0.6 . The wavelength dependence of scattering was larger at longer wavelengths. Ångström exponents calculated at 450/550 were roughly 12% lower than $\mathring{A}_s(450/700)$ and $\mathring{A}_s(550/700)$ were roughly 10% higher. I assumed the uncertainty in corrected scattering coefficients was $\pm 10\%$ and was associated with uncertainties in the instrument calibration and with deviations from the aerosol properties assumed in performing the truncation and non-lambertian light source corrections [*Anderson et al.*, 1996]. The largest deviations from the *Anderson and Ogren* [1998] assumed conditions were the high imaginary refractive indices (k) of particles that were emitted during many burns, because *Anderson and Ogren* [1998] developed their corrections assuming k ranged from 0.00–0.01.

The PAS instruments also measured b_{sp} (at 405, 532, and 870 nm) using reciprocal

nephelometry [Mulholland and Bryner, 1994]. The laser beam in the PAS provided a parallel light source and a cosine-weighted sensor coupled to a photomultiplier tube (PMT), which detected light scattered by particles in the center of the sample cavity. The scattering coefficient was calculated from the magnitude of the Fourier transformed functions of the PMT signal (P_{PMT}) and laser power (P_L) at the resonance frequency [Lewis *et al.*, in press]. The calibration method is described by Lewis *et al.* [in press]. The scattering background—scattering from gases—was determined periodically by sampling filtered, particle-free air into the instrument. I removed the background scattering signal from the raw data. Abu-Rahmah *et al.* [2006] discuss the uncertainties involved in reciprocal nephelometry and characterize the behavior of an instrument similar to the PAS used during FLAME.

Figure 4.11 gives timeseries for b_{sp} measured at four wavelengths ($\lambda = 450, 532, 550,$ and 700 nm) measured by the $3\text{-}\lambda$ integrating nephelometer (uncorrected) and the PAS reciprocal nephelometer and b_{ap} at 532 nm measured by the PAS as a function of time during six example stack burns. Modified combustion efficiency is also shown as a function of time. Flaming combustion dominated the early portions of most burns, indicated by the MCE near 1.0 during the first few minutes of the example burns shown in Figure 4.11 for the pine needle litter and palmetto leaves burns. It also increased for a brief period during the ponderosa pine duff burn after an initial smoldering-dominated period (when the fuel was being ignited). The absorption coefficient increased during the periods of high MCE because of the emission of light absorbing particles from the flaming fuel bed. Scattering coefficients at all wavelengths also increased during this time, but they increased dramatically following the transition from flaming-phase dominated combustion to smoldering-phase dominated combustion. Absorption coefficients

always decreased following the transition to smoldering-phase combustion to near-zero values, i.e, particles emitted during these phases of the fire had low absorption coefficients.

4.5.1 Fire-integrated emission factors and single-scattering albedo

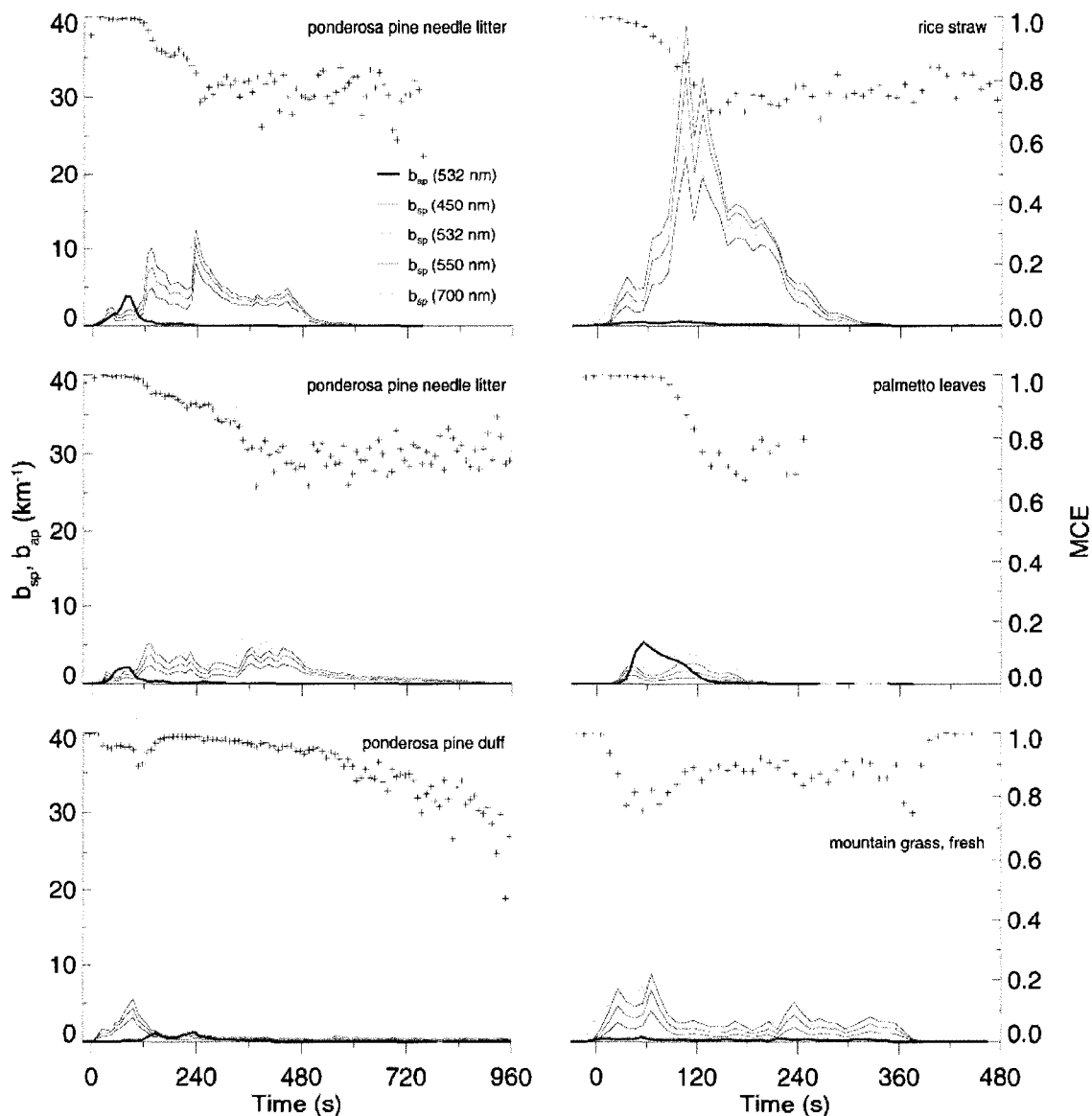


Figure 4.11 Timeseries for uncorrected aerosol scattering coefficients measured at 450, 550, and 700 nm using a TSI 3- λ nephelometer and at 532 nm using a reciprocal nephelometer (colored lines). Aerosol light absorption at 532 nm measured using a photoacoustic spectrometer is shown by the thick black line. All optical data are plotted against the left-hand side axis. The black crosses indicate the real-time modified combustion efficiency, plotted against the right-hand side axis. The vertical gray line indicates the transition from flaming to smoldering combustion determined from visual observations of the fire.

I calculated the fire-integrated optical properties for stack burns by integrating scattering and absorption coefficients multiplied by the stack volume fluxes and dividing by the total volume flux for the entire burn. For chamber burns, we calculated mean values of each parameter during the filter collection periods. All fire-integrated TSI nephelometer measurements were corrected for truncation and non-lambertian light source error. I adjusted b_{sp} measured by the TSI nephelometer at 550 nm to 532 nm using $\hat{A}_s(450/700)$ to match the PAS wavelength. Fire-integrated b_{sp} measured with the PAS and TSI nephelometers agreed well for burns with relatively low b_{sp} , including chamber burns, but PAS measurements for burns with high b_{sp} were roughly 15% higher than the TSI nephelometer-measured values. The highly absorbing aerosol observed during FLAME may play a role in the disagreement between the nephelometers. *Moosmüller and Arnott* [2003] showed that highly-absorbing particles were more affected by truncation error than mostly scattering particles. I did not observe a stronger disagreement between the nephelometers for more strongly absorbing aerosol, however, which suggests this is not the dominant cause of the nephelometer disagreement.

I calculated emission factors for aerosol scattering (σ_s) and absorption (σ_a) cross-sections at $\lambda = 532$ following the method used to determine gas and aerosol mass emission factors, but substituting the fire-integrated b_{sp} and b_{ap} for m_i . PAS-measured scattering emission factors at 532 nm ranged from 4–500 $\text{m}^2 \text{kg}^{-1}$ with a FLAME 1 mean of $95 \pm 130 \text{ m}^2 \text{kg}^{-1}$ (± 1 standard deviation) fuel. There was a large range in scattering emission factors because scattering depends on particle size, concentration, and composition, and these all varied considerably from burn to burn. If more carbon was emitted in the particle phase during a specific burn, if the mean particle size is large, or if the refractive index is high, then the scattering

emission factor will be large. If more carbon is emitted in the form of gases, if particle size is smaller, or if refractive index lower, then the scattering emission factor is small. *Chen et al.* [2007] reported fire-integrated light scattering emission factors ranging from 5.5–33.1 m² kg⁻¹ fuel at 550 nm, but also observed larger values—as high as 125.1 m² kg⁻¹ fuel—during the smoldering phase of combustion.

Light absorption cross section emission factors were lower than scattering cross section emission factors, ranging from 0.4–27.2 m² kg⁻¹ fuel. The FLAME 1 mean was 8.4 ± 5.2 m² kg⁻¹ fuel. This agrees well with the absorption emission factors reported by *Chen et al.* [2007] for similar fuels that ranged from 0.9–19.8 m² kg⁻¹. Total extinction cross section emission factors at 532 nm—the sum of scattering and absorption at 532 nm—ranged from 10.9–530 m² kg⁻¹ fuel. The minimum value for extinction was higher than that for scattering or absorption because burns with the lowest scattering emission factors often had higher absorption emission factors and vice versa.

Fire-integrated ω_0 ranged from 0.27–0.99, with a study mean of 0.81 ± 0.20 . Field-averaged measurements of ω_0 for fresh smoke range from 0.6–0.97 for a range of ecosystems [*Reid et al.*, 2005a]. Our study mean is within this range, but our lowest ω_0 values are substantially lower than the lower end of this range. Individual samples collected during fires, however, can have ω_0 as low as our observed values. *Reid and Hobbs* [1998] reported ω_0 on the order of 0.3 to 0.5 for a mixed grass/slash fire and *Radke et al.* [1991] and *Martins et al.* [1996] have found high mass absorption efficiencies during the earliest stages of fires. *Reid et al.* [2005a] suggested these low ω_0 events can occur during the late ignition and early flaming stages of real fires. *Roden et al.* [2006] observed ω_0 as low as 0.1 for particles emitted during flaming phase

wood combustion in a cook stove. Burning chamise branches dominated by flaming phase combustion produced particles with the lowest fire-integrated ω_0 . This burn featured very little smoldering combustion, so the fire-integrated ω_0 more closely reflects values typically observed during intense, flaming events.

4.5.2 Relationship with aerosols

The mass scattering (α_s) and absorption (α_a) efficiencies relate the scattering and absorption coefficients to aerosol mass. They depend on the particle size distribution and composition, which determines particle refractive index ($n + ik$) and density (ρ). Fine-mode aerosol species, such as sulfates, typically have α_s on the order of 3–4 m² g⁻¹; for fresh smoke at visible wavelengths α_s has been reported to range from 2.8–4.2 m² g⁻¹ [Reid *et al.*, 2005a]. I calculated α_s by dividing nephelometer- and PAS-measured b_{sp} by aerosol PM_{2.5} mass, assuming a particulate organic mass (POM)-to-OC ratio of 1.5. Scattering coefficients were measured without a 2.5 μ m sizecut during FLAME 1, so α_s could be overestimated if super-2.5 μ m particles contributed significantly to light scattering. Mass scattering efficiencies during FLAME ranged from approximately 2–8 m² g⁻¹, with a study-average value of 3.9 ± 1.9 m² g⁻¹. Fuels that produced particles with high α_s included manzanita and chamise leaves whereas fuels that produced particles with low α_s included palmetto leaves and manzanita and chamise branches. I observed a large range in α_s because of the wide range of combustion conditions during the study. Figure 4.12 gives α_s as a function MCE and CE, which shows that α_s generally decreased with increasing MCE and CE during FLAME. Flaming combustion emissions (high MCE/CE) tend to have lower α_s than smoldering combustion emissions (low MCE/CE) because flaming

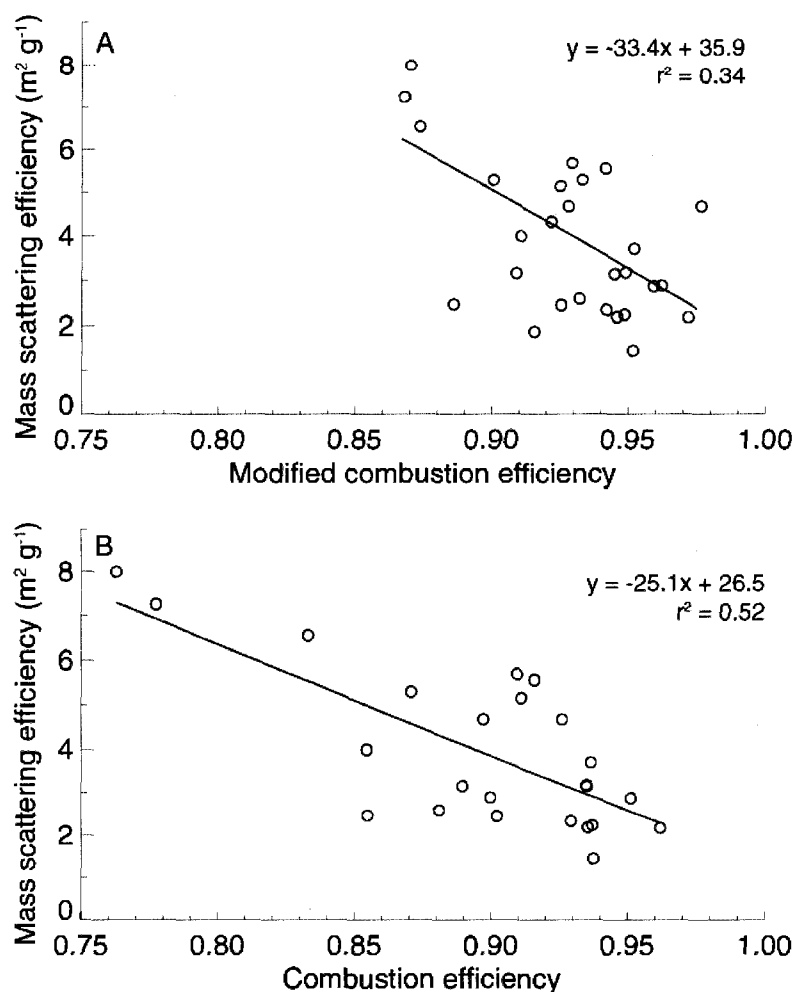


Figure 4.12 Mass scattering efficiency ($\lambda = 532$ nm) as a function of modified combustion efficiency for filter-integrated burns during FLAME 1.

combustion emits smaller particles [Reid *et al.*, 2005a]. This relationship is also seen for particles emitted by fires in the field. Reid and Hobbs [1998] reported a mean a_s of $3.6 \text{ m}^2 \text{ g}^{-1}$ for smoldering fires in Brazil, but a mean a_s of only $2.8 \text{ m}^2 \text{ g}^{-1}$ for flaming fires. Chen *et al.* [2006] observed $a_s \sim 5 \text{ m}^2 \text{ g}^{-1}$ for smoldering white pine needles (*pinus monticola*).

I used the Ångström exponent calculated from scattering measured at 450 and 700 nm as a proxy for particle size to explore the relationship between a_s and particle size (Figure 4.13). The a_s values tended to have a maximum at intermediate Å_s , near 1.5–2, with lower a_s values at the upper and lower extremes in Å_s (0.7 and 2.5). This pattern occurs because as Å_s becomes

small (very large particles), scattering scales with D_p^2 , while mass scales with D_p^3 , so scattering efficiency scales with D^{-1} and decreases for smaller \dot{A}_s . At the other extreme (large \dot{A}_s or smaller particle sizes approaching the Rayleigh regime), the scattering scales with D_p^4 , so the scattering term drops faster than the mass term for decreasing D_p .

Emissions with low \dot{A}_s were dominated by organic carbon. The strong increase in a_s with decreasing \dot{A}_s (and increasing particle size) has implications for particle aging. Field-based measurements of aged plumes [Reid and Hobbs, 1998] and regional hazes [Haywood *et al.*, 2003; McMeeking *et al.*, 2005; Reid *et al.*, 1998] have found higher a_s compared to field-based measurements of fresh smoke. This increase results from particle growth through coagulation and condensation. Reductions in \dot{A}_s for aged smoke plumes to values as low as one support this hypothesis [Eck *et al.*, 1999; Eck *et al.*, 2001; O'Neill *et al.*, 2002b]. Our short-duration chamber burns did not capture true atmospheric aging effects because aging during our chamber burns was affected only by coagulation effects on particle size and possibly dark chemistry. The lack of sunlight prevented photochemistry that may occur during real plume aging, so the formation of lower volatility material by the oxidation of fresh emissions was inhibited, which prevented multi-generation organic aerosol formation and condensation. Field-based measurements of \dot{A}_s range from 2–2.5 [Reid *et al.*, 2005a], a narrower range than we observed during FLAME (~2–4). I attribute this to the extremely fresh particles observed during the stack burns leading to a larger range in particle size distributions. Reid *et al.* [1998] found aging increased \dot{A}_s by ~20%, so the estimates should be considered lower bounds.

The hemispherical backscatter ratio (β)—defined as the ratio of backscattered light to total scattered light—was measured with the 3- λ nephelometer. The backscatter ratio decreases

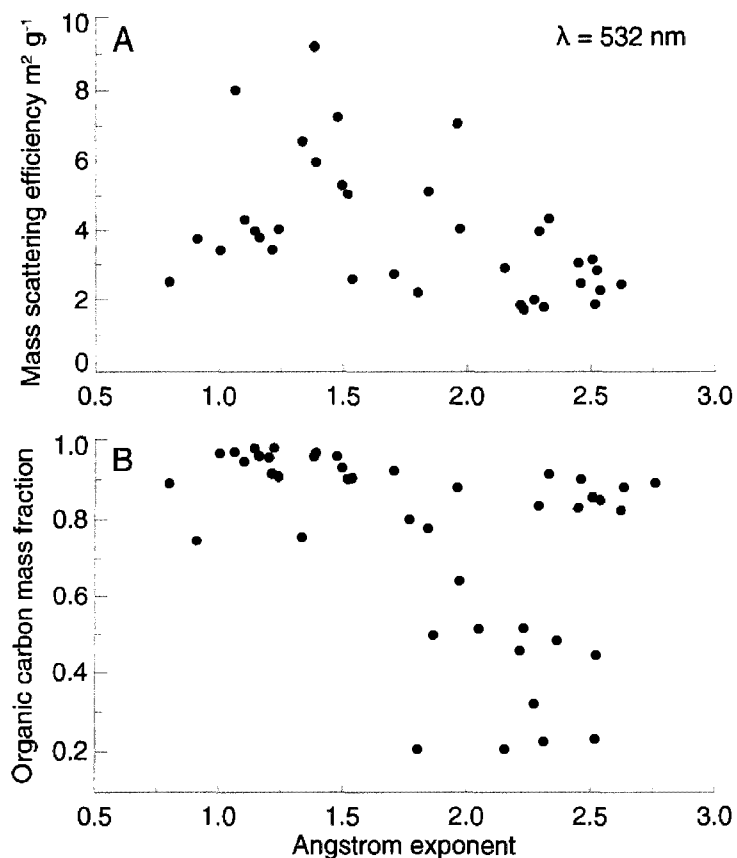


Figure 4.13 a) Mass scattering efficiency ($\lambda = 532 \text{ nm}$) and b) total carbon mass fraction as a function of Ångström exponent calculated from scattering measured at $\lambda = 450$ and 700 nm during FLAME 1.

with increasing particle size as more light is scattered in the forward direction [Bohren and Huffman, 1983]. I found similar β ($\lambda = 550 \text{ nm}$) to those observed in fresh smoke plumes, with a range of 0.12–0.22 and a study average value of 0.16 ± 0.03 . The backscatter ratio was highly and positively correlated with Å_s ($r^2 = 0.70$). For comparison, the backscatter ratio was roughly 0.18 at $\lambda = 550 \text{ nm}$ for fresh smoke plumes in Brazil and over savannah in Africa [Reid and Hobbs, 1998]. The backscatter ratio was lowest for fuels dominated by smoldering combustion, with low MCE, consistent with the relationship observed between MCE and Å_s .

Mass absorption efficiency during FLAME 1 ranged from 0.05–5.7 $\text{m}^2 \text{g}^{-1}$, with a study mean value of $1.2 \pm 1.5 \text{ m}^2 \text{g}^{-1}$. Larger contributions by smoldering combustion, which emitted weakly or non-absorbing material but not strongly light-absorbing black carbon (BC), resulted

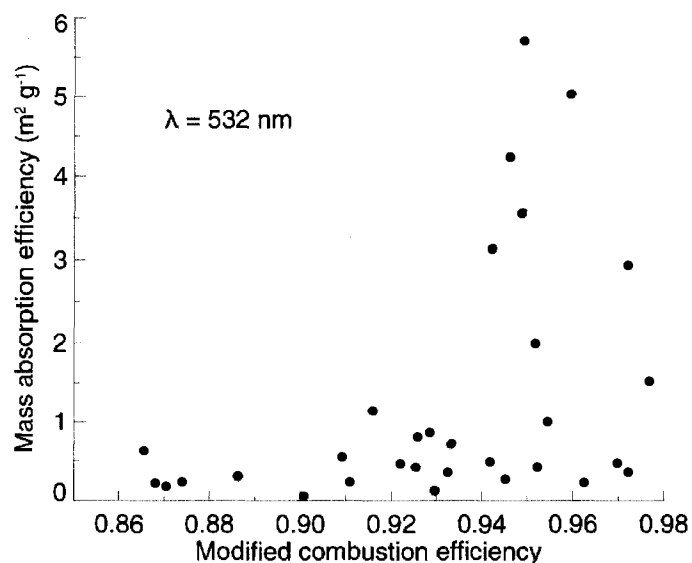


Figure 4.14 Mass absorption efficiency ($\lambda = 532 \text{ nm}$) as a function of modified combustion efficiency during FLAME 1.

in lower α_a . Figure 4.14 illustrates this by comparing MCE to α_a , showing that α_a was always low for burns with MCE < 0.94. Mass absorption efficiency was higher at high MCE, but several burns produced little EC despite featuring a strong flaming phase, and these burns also produced particles with low α_a . Field measurements of α_a for fresh smoke range from values < 0.3 $\text{m}^2 \text{g}^{-1}$ for purely smoldering combustion to 1–1.4 $\text{m}^2 \text{g}^{-1}$ for flaming combustion and as high as $\sim 3 \text{ m}^2 \text{g}^{-1}$ for intense fires [Reid *et al.*, 2005a], consistent with my results. I observed somewhat higher maximum values of α_a than have been observed in the field, but I also observed higher mass fractions of EC, as discussed earlier.

4.5.3 Relationships between optical properties and aerosol composition (OC/EC)

The composition of particles, especially the fraction made up by light-absorbing EC, had a strong impact on their optical properties. I showed that the OC and EC emissions from fires during FLAME were a function of combustion conditions, but also noted that several fuels, particularly grass-like fuels, produced little EC, despite featuring a strong flaming combustion

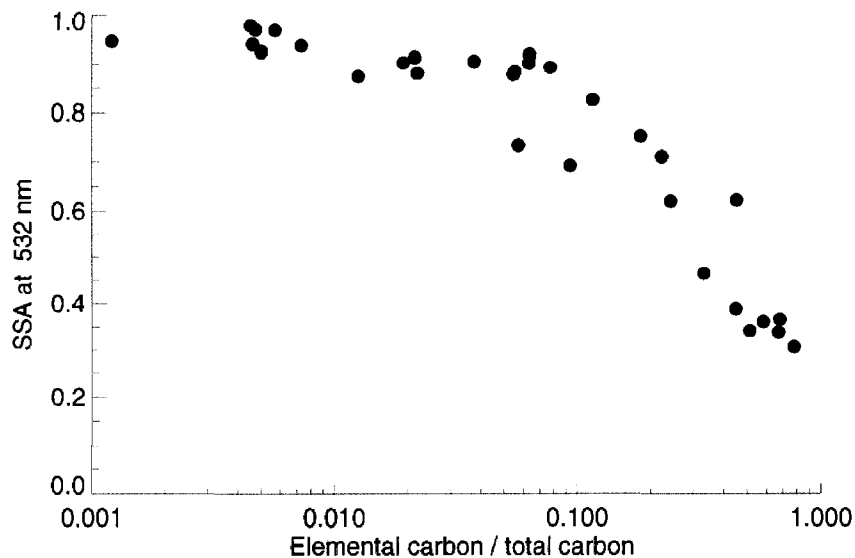


Figure 4.15 Single scattering albedo at $\lambda = 532$ nm as a function of elemental carbon-to-total carbon ratios. This added to the scatter in the relationships between optical properties and MCE.

Single scattering albedo at $\lambda = 532$ nm was a function of the EC mass fraction, as shown in Figure 4.15. Single-scattering albedo was a weak function of EC/TC ratios for EC/TC ratios below ~ 0.1 , but then decreased sharply from 0.9 to 0.3 for higher EC/TC ratios. This reflects the strong light-absorption efficiency of EC. Recent work has shown that OC contributes to aerosol light absorption by biomass burning emissions, particularly at near-UV wavelengths [Kirchstetter *et al.*, 2004], but its contribution is thought to be small compared to that from EC at 532 nm. The high values of ω_0 for OC-dominated aerosol during FLAME confirm this. I discuss these issues in much more detail in the following chapters.

4.6 Summary

I have reported aerosol composition, optical properties, and species-resolved emission factors based on observations of over 250 laboratory burns of ~ 40 different plant species. Combustion conditions control the relative abundance of OC and EC in the aerosol and

determine the importance of light absorption and scattering for most fuels. In several cases, however, the production of EC by flaming phase combustion was inhibited, possibly by high, simultaneous emissions of inorganic salts, flame temperature, or unique attributes of the fuel. This has major implications for combustion-behavior based estimates of EC emissions for certain fuels, such as rice straw.

Optical properties, such as the single scattering albedo, were closely related to EC/TC ratios. Emissions of inorganic material were not a strong function of combustion conditions, and instead depended more strongly on fuel type, which I assume was related to fuel composition. Inorganic emissions were dominated by chloride and potassium, but in some cases sulfate, sodium, and ammonium made up substantial fractions of the inorganic mass. Reconstructed particle mass was usually dominated by OC, but in many cases EC and analyzed inorganics contributed significantly to reconstructed mass. Emission factors for reconstructed particle mass were a function of MCE, with roughly 40% of the variability explained by variations in modified combustion efficiency. Mass scattering and absorption efficiencies showed weaker relationships with combustion behavior than chemical properties due to the complications introduced by variations in particle size.

Modeling efforts focused on predicting aerosol optical properties must accurately predict smoke EC content, which depended on combustion behavior and fuel type. This requires either a) a detailed inventory of global fire behavior as a function of location and season, or b) accurate prediction of fire behavior from fuel conditions and meteorology. Unfortunately the lack of EC formation at high MCE by a significant fraction of the fuels tested in our study adds additional complications to these efforts. Modeling efforts focused on prediction of aerosol

hygroscopic properties, which were a stronger function of inorganic content, require detailed knowledge of fuel composition in addition to fire behavior. The inorganic emissions from many fuels we tested were large. For example, many western desert and chaparral fuels produced large concentrations of inorganic species, which contributed as much as half of the identified aerosol mass.

The strong dependence of $PM_{2.5}$ emission factors on fire combustion behavior is a challenge to efforts to predict fire emission impacts on air quality, visibility, and climate. The most popular approach for dealing with this has been to determine a representative MCE for different fire-types within ecosystems and assign emission factors based on this [Andreae and Merlet, 2001]. Ideally emission factors could be linked directly to MCE observations, but MCE is difficult to measure from space because it requires separation of the relatively small fire CO_2 signal from the larger ambient CO_2 signal. Sophisticated fire behavior models could predict MCE or CE based on fuel type and conditions and then determine emissions based on the predicted MCE or CE values. Freeborn *et al.* [2008] showed that emissions of carbon dioxide were strongly related to fire radiative energy, which can be related to fire radiative power. If a similar relationship exists for aerosol emissions, then satellite based measurements of fire radiative power could provide a better estimate of biomass burning particulate emissions.

A major limitation of our study and other laboratory combustion studies is that we are unable to observe smoke aging processes. We must also assume emissions from our small scale laboratory fires are applicable to larger fires in the field. I attempted to address the latter by presenting our results in the context of MCE (and in some cases CE). Trace gas emissions from biomass burning in Brazil agree with trace gas emissions from laboratory fires when MCE is

accounted for [Yokelson *et al.*, 2008]. The similarities between these results and observations from field fires at similar MCE suggests this is also true for aerosol emissions. I found significant variability in aerosol emissions and optical properties, even after accounting for combustion behavior. These variations may arise from differences in fire behavior that are not captured by combustion efficiency, such as combustion temperature, which can also affect emissions. Fuel type is also important for inorganic emissions, so care must be taken when applying the inorganic emission factors presented here for real fires to ensure fuel components are accurately represented in the emissions model. Including fire radiative power measurements, such as those described by *Freeborn et al.* [2008], in our analysis may help us discover other controls on emissions.

To estimate potential increases in aerosol mass with aging, I also presented emission factors for TOOC. More work is needed to determine what fraction of the gas-phase TOOC emissions is eventually converted to the particle phase following oxidation and aging in the atmosphere. I found that the particle-phase fraction of TOOC is higher for increasing OC concentrations, which might reflect changes in gas-particle partitioning with OC concentration, or a greater production of OC relative to trace gas emissions at lower combustion efficiencies.

Smoldering-dominated combustion produces roughly four times as much particulate matter than flaming-dominated combustion, primarily because much more aerosol OC is emitted at lower combustion efficiencies. Smoldering-dominated combustion also produces much higher emissions of gas-phase hydrocarbons relative to flaming-dominated combustion. An unknown fraction of these gases can be converted to the aerosol phase with atmospheric aging. The aerosol emissions by smoldering-dominated combustion when this conversion

process is accounted for are therefore likely to be even higher. The organic-dominated aerosol emitted through smoldering-combustion tends to be larger in size relative to aerosol emitted during flaming-dominated combustion, leading to higher mass scattering efficiencies. The higher mass scattering efficiencies of these particles combined with their much higher emission rates means that smoldering-dominated combustion is responsible for a much greater fraction of light scattering compared to flaming-dominated combustion. The contributions from smoldering combustion are underestimated in emission inventories [*Bertschi et al.*, 2003; *Christian et al.*, 2007; *Yokelson et al.*, 2007a], mainly because it is difficult to capture the full emissions cycle—from ignition through extinction—in the field. The large emissions of highly efficient light scattering particles by smoldering-dominated combustion during FLAME stress the need to include these emissions in model-based calculations of radiative forcing and visibility impairment.

Chapter 5 A comparison of organic and elemental carbon measurement techniques

In the previous chapter I discussed measurements of aerosol organic carbon (OC) and elemental carbon (EC) measured on high volume filter punches using a Sunset semi-continuous analyzer operating in an off-line mode (see *Sullivan and Weber [2006]*). Organic and elemental carbon made up a large fraction of the $PM_{2.5}$ aerosol mass during FLAME. Measurements of OC and EC are affected by the choice of analytical protocol used to measure them and by a number of sampling biases. The measurement issues affect the interpretation of relationships between aerosol composition and optical properties, so this chapter compares several sets of carbon measurements to estimate uncertainties and potential biases in the composition data.

5.1 Methods for measuring organic and elemental carbon

Aerosol organic carbon is composed of hundreds, if not thousands, of different organic compounds, which have not been fully identified [*Brown et al., 2002; Heald et al., 2008; Rogge et al., 1993; Simoneit, 2002; Yamasoe et al., 2000*]. Measurements of total OC, in lieu of detailed chemical composition, and EC are often used to describe overall aerosol composition and to predict the aerosol effects on climate and visibility [*Chung and Seinfeld, 2002; Malm et al., 1994; Malm et al., 2004*]. The distinction between OC and EC is notable in this regard. EC is the primary visible light absorbing component of atmospheric aerosols whereas OC primarily scatters visible light. Accurate classification of the carbonaceous aerosol material at least into these two categories is therefore important.

Concentrations of OC and EC can be measured using thermal optical analysis (TOA) techniques that heat the sample under controlled atmospheric conditions and measure the total carbon concentration in evolved gases. These thermal evolution techniques typically involve a two-stage procedure, first heating the sample in an oxygen-free atmosphere to volatilize OC, then adding oxygen to combust EC. The separation of total carbon into OC and EC is not always straightforward because some OC can pyrolyze or 'char' in the initial oxygen-free heating step. The pyrolyzed OC (POC) can evolve in the oxygen-containing atmosphere during the second stage of the analysis and be incorrectly identified as EC. POC absorbs light, so the filter darkens when it forms. Light transmittance through [Birch and Cary, 1996] or reflectance from [Chow *et al.*, 1993; Chow *et al.*, 2004] the filter is monitored during heating to correct for POC. Carbon evolving before the filter returns to its initial transmittance or reflectance value is treated as POC by the TOA protocols.

Several TOA methods exist and a number of studies, recently summarized by Watson *et al.* [2005], have shown that different TOA measurements usually agree for total carbon (TC). They report considerable disagreement between measurements of OC and EC in rural and biomass burning samples that typically have low EC/TC ratios. These studies report measurements of EC that vary by as much as a factor of seven. This large discrepancy is primarily due to the different heating protocols, time spent at each temperature stage, analysis atmospheres and techniques used to correct for the pyrolysis of OC. Other factors leading to disagreement include non-uniform sample deposits on filters, organic vapor adsorption, samples that are optically saturated, catalytic oxidation of EC when certain inorganic species are present in the sample, and changes in optical properties during thermal evolution [Watson *et al.*, 2005].

Further differences can arise from the volatilization of semi-volatile material and adsorption of organic vapors during sampling, transport and storage of filters [Chow *et al.*, 2001].

Many carbon measurement comparison studies have focused on urban, diesel or laboratory generated soot aerosols [Chow *et al.*, 2005; Japar *et al.*, 1984; Lim *et al.*, 2003; Park *et al.*, 2006; Schmid *et al.*, 2001; e.g., Venkatachari *et al.*, 2006]. Few studies have specifically compared OC and EC measurement techniques for biomass burning samples, and those that did only examined a small number of samples [Birch, 1998; Countess, 1990; Fung, 1990]. The previous chapters showed that aerosol composition varies with fuel and combustion conditions, so a more complete comparison of TOA protocols for aerosol emitted from biomass burning through a range of combustion behaviors is needed.

5.2 Description of the filter samplers

Four filter samplers, in addition to the high volume sampler introduced in Chapter 3, collected particulate matter during each burn experiment. Details of each configuration are provided in Table 5.1. Aerosol was collected by two IMPROVE samplers, which were similar to those used to collect particulate matter concentrations in national parks and wilderness areas as part of the IMPROVE program. The standard IMPROVE sampler has four independent modules (A–D), each with its own inlet, filter pack and pump assembly [Malm *et al.*, 2004]. Module A collects particles on a Teflon filter, which is analyzed for gravimetric mass and elemental composition by X-ray analysis. Module B collects particles on a Nylasorb substrate for analysis by ion chromatography. Module C collects particles onto a 25 mm quartz filter for carbon analysis by thermal optical reflectance. Modules A, B, and C operate with a 2.5 μm

Table 5.1 Configurations of the filter sampling systems that measured aerosol carbon composition during FLAME 1 chamber burns.

Name	Sampler	TOA protocol	Filter medium(s)	Flow rate (LPM)	Size cut (μm)	Location	Face velocity (cm s^{-1})
IMPROVE PM _{2.5}	IMPROVE	IMPROVE_A	quartz-quartz	22	2.5	chamber	74.7
IMPROVE PM ₁₀	IMPROVE	IMPROVE_A	quartz-quartz	17	10	chamber	57.7
DRI	-	IMPROVE_A	quartz	25	-	laboratory	-
Sunset 'A'	high volume	NIOSH/STN	quartz	~1000	2.5	chamber	52.0
Sunset 'B'	high volume	NIOSH/STN	quartz	~1000	2.5	chamber	41.6
Sunset semi-continuous	Sunset	NIOSH/STN	denuder- quartz	3	2.5	laboratory	35.7

cyclone to remove larger particles. Module D has a 10 μm inlet and collects particles on a Teflon filter, which is analyzed for gravimetric mass and elemental composition.

The IMPROVE samplers that ran during FLAME were distinct from the basic IMPROVE samplers in three important ways. First, Module D was replaced by a second sampler that had its own Modules A, B, and C, but with 10 μm inlets as opposed to 2.5 μm . This provided more composition information for PM₁₀ aerosol than normally provided by module D in the basic IMPROVE sampler. Second, Module C for both PM_{2.5} and PM₁₀ samplers operated with two quartz filters as opposed to one. They were positioned in series to characterize potential sampling artifacts, such as the adsorption of gases onto the filters. The primary filter collected particles and gases and the secondary filter collected gases. The back-to-back quartz filter setup is also used in select IMPROVE sites for the same purpose. Finally, the program that controls filter collection times—samplers collect ~24 hour samples every third day at IMPROVE sites—was modified to run for shorter intervals and multiple times per day. The IMPROVE sample inlets were approximately 3 m above the floor of the chamber. The PM_{2.5} samples were collected at a nominal flow rate of 22 L min⁻¹ and the PM₁₀ samples were collected at a nominal flow rate of 17 L min⁻¹. The exposed areas of the filters were 3.53 cm².

Two high-volume samplers collected PM_{2.5} from ~2.5 m above the chamber floor on 20 x 25 cm quartz filters (exposed area = 400.5 cm²). One high-volume sampler, referred to as the 'A' sampler, sampled PM_{2.5} using an inlet with impactor nozzles (Thermo Fisher Scientific GMW PM_{2.5}, Waltham, MA). The 'A' sampler ran at a nominal flow rate of ~1250 L min⁻¹. The second, 'B' sampler operated with a two-stage impaction grating, described in Chapter 4 and in detail by *Engling et al.* [2006b]. It ran at a nominal flow rate of ~1100 L min⁻¹. The OC and EC data presented in Chapter 4 are from the analysis of the 'B' high volume filters. I considered the carbon measured by this sampler to be the 'standard' OC and EC measurements because the same sampler ran during both stack and chamber burns.

A semi-continuous TOA carbon analyzer (Sunset Laboratory Inc., Forest Grove, Oregon), referred to as the semi-continuous Sunset analyzer, was located in a room adjacent to the chamber. It drew sample from the ~50 L mixing chamber from which the optical instruments discussed in Chapter 3 pulled flow, which in turn was filled from the smoke-filled chamber (see description in Chapter 4). The semi-continuous carbon analyzer operated with an activated-carbon denuder upstream of the instrument inlet to remove organic gases. The analyzer operated in two modes: collection and analysis. During collection mode, the Sunset analyzer collected sample on a 1.4 cm² quartz filter punch at a flow rate of 3.0 L min⁻¹ for ~18 minutes. The instrument switched to analysis mode when the collection period ended and measured OC and EC in the sample using the modified NIOSH/Sunset protocol. The analysis period was approximately 12 min. The two-part cycle repeated continuously over the duration of the chamber burns, collecting a new sample every 30 minutes. The individual measurements were averaged over the high volume collection times to obtain a single value for each filter that

could be compared with the other filter measurements. The instrument operated during both studies, but only results from FLAME 1 are examined here.

The high-volume and DRI samplers began sampling immediately following ignition and collected particles over the same time window within five minutes during each experiment. During a few FLAME 1 burns, the IMPROVE modules operated for a longer time interval than the other samplers and in some cases they started significantly earlier or later (~20-25 min) than the other samplers. The timing issues resulted from problems we encountered in modifying the basic IMPROVE sampling programs. For burns when the IMPROVE samples started too early or ran for too long, a known volume of room air was sampled through the PM_{2.5} and PM₁₀ filters. To account for this background room contamination, I adjusted the IMPROVE carbon measurements using Equation 5.1:

$$x_s = \frac{t_f x_f - t_r x_r}{t_f - t_r} \quad 5.1$$

where x_s is the adjusted sample concentration, x_f is the original measured filter concentration, x_r is the assumed room concentration, t_f is the total filter sample time and t_r is the time the sampler operated before or after the chamber experiment. I estimated a constant background room concentration in FLAME 1 of 12 $\mu\text{g C m}^{-3}$ for OC and 3 $\mu\text{g C m}^{-3}$ for EC based on dynamic chamber blank samples collected between burns. The adjustment increased the sample concentration from 0–21% depending on the amount of time room air was sampled and on the sample concentration of carbon in the sample. The average increase was ~8% compared to the original, unadjusted values. No corrections were needed for the FLAME 2 samples because the IMPROVE sampler programs ran as planned.

Samples were collected on quartz-fiber filters that were pre-baked for at least 6 hours at temperatures $> 550^{\circ}\text{C}$ to remove residual organic impurities prior to sampling. After each experiment the filters were taken from the samplers, packed in clean aluminum foil and frozen to minimize volatilization of organic species from the sample. IMPROVE filter samples were stored at temperatures below -4°C and shipped to Desert Research Institute in Reno, Nevada for analysis. High-volume filter samples were stored at temperatures at or below 0°C and punches from these filters were analyzed with the Sunset analyzer in 'off-line' mode at Colorado State University in Fort Collins, Colorado. To analyze high volume filters with the Sunset analyzer in off-line mode, a punch from the filter was inserted into the instrument's analysis chamber in place of the punch used to collect aerosol when the analyzer is used in semi-continuous or 'on-line' mode [Sullivan and Weber, 2006]. The collection time was set to zero seconds in the instrument software, so the analyzer immediately begins analyzing the punch without first collecting sample.

5.3 Organic and elemental carbon analysis protocols

5.3.1 *The IMPROVE_A protocol*

In the IMPROVE_A analysis protocol [Chow *et al.*, 2007], the sample is heated to four temperature plateaus (140, 280, 480 and 580°C) in pure helium followed by three temperature plateaus (580, 740 and 840°C) in 98% helium and 2% oxygen. Carbon measured during each of these temperature steps is classified as one of four OC fractions (OC1, OC2, OC3, OC4) and one of three EC fractions (EC1, EC2, EC3). The evolved carbon is oxidized to carbon dioxide using a heated MnO_2 catalyst. Carbon dioxide is reduced to methane using a methanator (H-

enriched nickel catalyst). The methane is quantified using a flame ionization detector (FID). The temperature is ramped to the next level when the FID response returns to its baseline or remains constant for more than 30 seconds. A known quantity of methane gas is injected into the analyzer at the end of each analysis run to calibrate the FID. A replicate analysis, selected randomly, is performed once every ten samples. The uncertainty (δC_i) for each carbon fraction (C_i) is given by:

$$\delta C_i = \sqrt{(CV \times C_i)^2 + MDL} \quad 5.2$$

where CV is the coefficient of variation of the replicate analyses and MDL is the minimum detection limit, which is equal to three times the standard deviation of 100 laboratory blank samples [Chow *et al.*, 2007].

POC is determined by continuously measuring laser light ($\lambda = 632 \text{ nm}$) reflectance or transmittance from the filter. The filter darkens as POC is formed, causing reduced light reflectance from the surface of the filter and reduced light transmittance through the filter. POC is assumed to be the material that evolves during the EC heating steps before the reflectance from or transmission through the filter returns to its initial value. Optical corrections assume the light extinction per unit mass of POC produced equals the light extinction per unit mass of carbon removed to the point when reflectance or transmittance reaches its initial value. The IMPROVE_A protocol reports OC and EC values that have been corrected for POC determined by both reflectance (IMPROVE_A thermal optical reflectance or TOR) and by transmittance (IMPROVE_A thermal optical transmittance or TOT). Historically, the IMPROVE protocol reported only TOR-based OC and EC measurements, and these are the

values considered to be the standard measures in the IMPROVE historical record. I will discuss both TOR- and TOT-based measures of OC and EC throughout the remainder of this chapter. Only filters collected by the two IMPROVE samplers were analyzed following this protocol.

5.3.2 The modified NIOSH 5040 / Sunset analyzer protocol

Analysis of samples using the Sunset analyzer (high volume 'B', and semi-continuous/on-line samples) followed a modification of the NIOSH 5040 protocol [Bae *et al.*, 2004; Birch and Cary, 1996]. The sample punch is heated in pure helium to 600 °C in 80 seconds and then to 840 °C in 90 seconds. The sample is cooled for 35 seconds and then oxygen is added to the analysis atmosphere (98% He, 2% O₂). Punches were then heated to 550 °C in 30 seconds, 650 °C in 45 seconds, and 850 °C in 90 seconds. Evolved carbon is converted to CO₂ using an MnO₂ catalyst and the CO₂ is quantified by a non-dispersive infrared (NDIR) detector. A methane standard is injected at the end of each analysis run to calibrate the NDIR detector for 100 seconds. The method corrects for POC using light transmittance ($\lambda = 660$ nm) rather than reflectance. EC is taken to be the carbon that evolves after the laser transmittance returns to its original values. Carbon that evolves in the He-O₂ environment before the transmittance returns to its original value is classified as POC. The high volume results reported here are the averages of two 1.4 cm² punches taken from the same filter. Average values are reported to reduce measurement uncertainties [Gorin *et al.*, 2006]. The levels of detection were ~6 µg m⁻³ for OC and ~1 µg C m⁻³ for EC [Sullivan *et al.*, submitted].

5.4 Organic gas adsorption artifacts

Chapter 4 discussed sampling artifacts resulting from the adsorption of gas-phase

compounds by the quartz filter fibers—often called the positive artifact—and the evaporation of semi-volatile species during sampling—often called the negative artifact. The sampling artifacts affect OC measurements [e.g., *Kirchstetter et al.*, 2001; *Subramanian et al.*, 2004; *Turpin et al.*, 2000]. OC is overestimated if the positive artifact dominates and underestimated if the negative artifact dominates. EC measurements are thought to be unaffected by these sampling artifacts because EC is non-volatile. If adsorbed gases pyrolyze to form char during analysis and are incorrectly identified as EC, however, EC measurements can be affected by the adsorption artifact.

During FLAME, the IMPROVE PM_{2.5} and IMPROVE PM₁₀ samplers collected aerosol using two quartz filters arranged in series: a front, or primary, quartz filter and a back, or secondary, quartz filter located behind the first. The primary filter collected particles from the sample stream; gases are adsorbed by both the primary and secondary filters. Ideally, the OC (adsorbed gases) measured on the secondary filter equal the fraction of OC measured on the primary filter resulting from adsorbed gases. Figure 5.1 shows OC and EC measured on the IMPROVE PM_{2.5} primary and secondary filters using the IMPROVE-TOR protocol during the FLAME 1 and FLAME 2 chamber experiments. The majority of carbon on the secondary filters was identified as OC. This material was likely POC, formed from the pyrolysis of the adsorbed organic vapors, that was identified erroneously as EC by the IMPROVE_A TOR protocol.

Secondary filter OC was related to primary filter OC, suggesting most OC was semi-volatile and that the filters were not at equilibrium with the sample stream, e.g., as OC concentrations increased (and presumably gas-phase concentrations increased) there was more adsorbed carbon on the secondary filter. If the filter was saturated with respect to adsorbed

gases, then the mass of carbon on the secondary filters should level off as OC concentrations increased. One sample had an unusually high secondary OC concentration relative to the primary filter OC concentration, but this sample was collected for only 10 minutes, while all other samples were collected for at least 60 minutes, and more often 90–120 minutes.

The low fractions of OC and EC on the backup filters show that adsorption artifacts during FLAME were relatively small. They were lower than positive adsorption artifacts, on the order of 20–50% of levels found during other biomass burning aerosol emissions studies [*Fine et al.*, 2001; *Lipsky and Robinson*, 2005; 2006]. In these studies, the aerosol samples were diluted to lower concentrations than we observed during FLAME, which may have altered the partitioning behavior of semivolatile species. The high concentrations of OC in the chamber probably drove more semi-volatile material into the particle phase than during the earlier, diluted aerosol

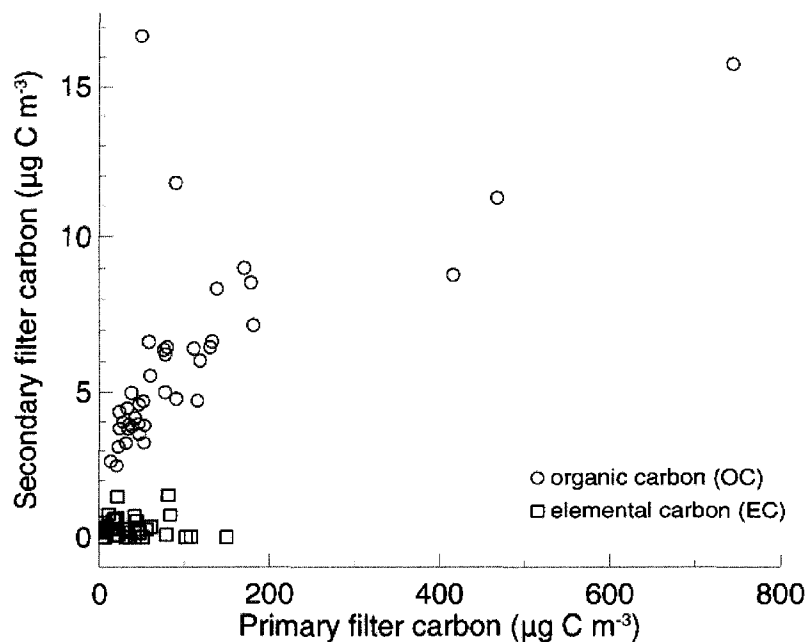


Figure 5.1 Carbon mass concentrations ($\mu\text{g C m}^{-3}$) measured on the primary and secondary IMPROVE $\text{PM}_{2.5}$ filters during FLAME 1 and 2. Organic carbon (OC) concentrations are shown by red circles and elemental carbon (EC) concentrations are shown by black squares.

studies. The fraction of OC that was observed on the secondary filter relative to the primary filter decreased at higher OC concentrations (Figure 5.2). At high OC concentrations ($> 100 \mu\text{g m}^{-3}$), when presumably more semi-volatile material was in the particle phase, secondary filter OC was ~2–5% of the primary filter OC. At lower OC concentrations ($< 50 \mu\text{g m}^{-3}$), when more semi-volatile material was in the gas phase, secondary filter OC approached 20% of the primary filter OC, closer to the values reported by *Fine et al.* [2001] and *Lipsky and Robinson* [2005; 2006]. The outlier sample with the short collection time had a much higher secondary fraction of OC (~35%) compared to other samples with similar primary filter OC concentrations.

5.5 Total carbon, gravimetric and inorganic mass measurements

Figure 5.3 compares TC concentration measurements for the IMPROVE $\text{PM}_{2.5}$, IMPROVE PM_{10} , semi-continuous Sunset and 'B' high-volume filter samples collected during FLAME. IMPROVE filters were analyzed using the IMPROVE_A protocol; Hi-vol filters were analyzed using the modified NIOSH 5040/Sunset protocol. The data have not been adjusted to account for gas-phase adsorption artifacts because the high volume filters were not sampled with backup filters. The IMPROVE and Hi-vol 'B' data include samples collected during FLAME 1 and 2, but the semi-continuous data contain samples from FLAME 1 only. The semi-continuous Sunset measurements were averaged over the high-volume filter collection times, but the collection times do not match exactly because of gaps when the instrument switched over to analysis mode during the burns. Each scatter plot compares data from different samplers and/or TOA methods. The linear least-squares regression and r^2 values for each data pair are also shown. The TC measurements were highly correlated in general, with r^2 values on the order of

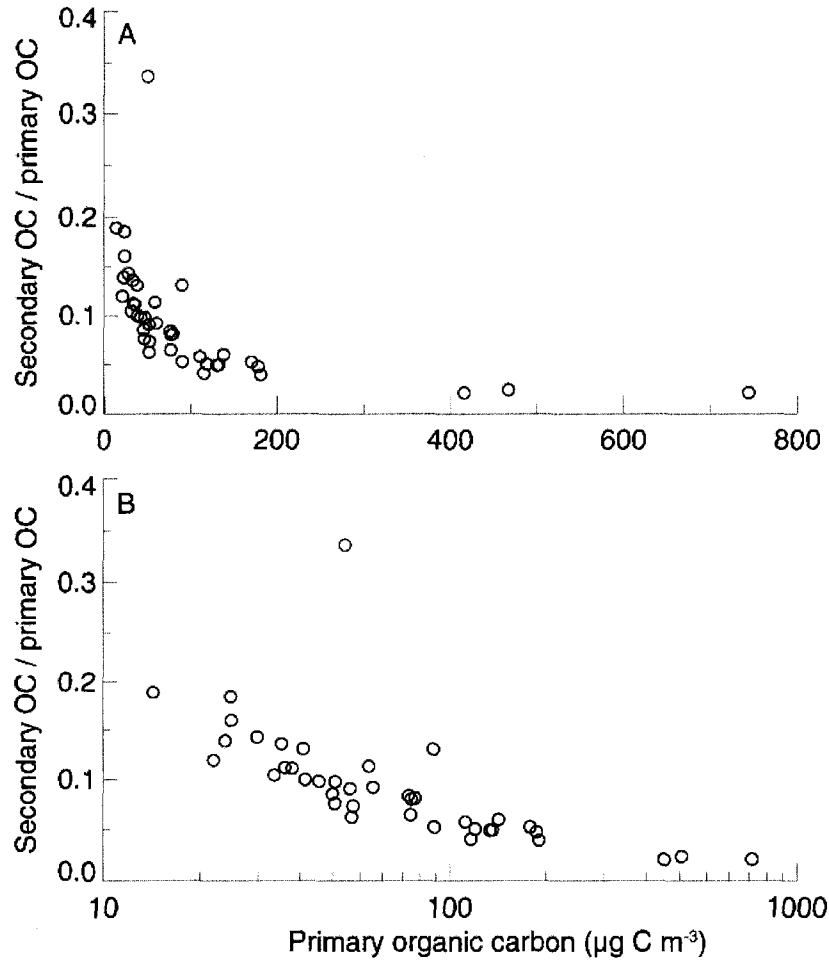


Figure 5.2 Organic carbon (OC) measured on secondary (backup) IMPROVE filters normalized by OC measured on primary (front) IMPROVE filters as a function of the primary OC mass concentration during the FLAME 1 and FLAME 2 chamber burns. The sample with the unusually short collection time is highlighted in red.

0.88–0.99. The strength of the correlation was partly due to the good agreement between the highest TC measurements. I also correlated TC measurements restricted to values below $300 \mu\text{g m}^{-3}$, which resulted in weaker correlations ($r^2 \sim 0.5\text{--}0.95$).

The regression coefficient for TC measured on the 'B' high volume $\text{PM}_{2.5}$ filter samples using the modified NIOSH 5040 protocol against TC measured on the IMPROVE $\text{PM}_{2.5}$ filter samples using the IMPROVE_A protocol was 0.87, with an $r^2 = 0.94$, but these were analyzed for different filters. The agreement between the semi-continuous analyzer and the 'B' Hi-vol TC measurements was worse, with a regression coefficient of 0.71 and $r^2 = 0.88$. The agreement

between the various TC measurements made during FLAME was weaker than found by previous intercomparison studies. For example, *Chow et al.* [2001] observed a regression coefficient of 1.00 ± 0.01 between TC measurements made with the same analyzer and punches from the same filter using the IMPROVE and NIOSH 5040 protocols, but this study was designed to minimize differences due to sampling. A number of factors could be responsible for the observed differences in TC including: the use of different aerodynamic particle sizing techniques, sampler locations and differences in sampling lines, the magnitude of gas phase adsorption (positive artifact), and the magnitude of volatilization of material from the particulate matter on the filters (negative artifact), the latter two depending on flow rate and substrate.

TC concentrations were on average 10–15% higher on the IMPROVE PM₁₀ samples compared to IMPROVE PM_{2.5} samples (Figure 5.3a). The PM₁₀ TC mass was dominated by particles with $D_{ae} < 2.5 \mu\text{m}$, which made up $91 \pm 8\%$ of PM₁₀ TC mass. The main exceptions to this general result were emissions from the burning duff fuels, Alaskan duff (tested in FLAME 1 and 2) and ponderosa pine duff (tested in FLAME 1 only). PM_{2.5} TC was between 65–80% of the PM₁₀ TC mass for these burns, reflecting a larger contribution by particles with $2.5 < D_{ae} <$

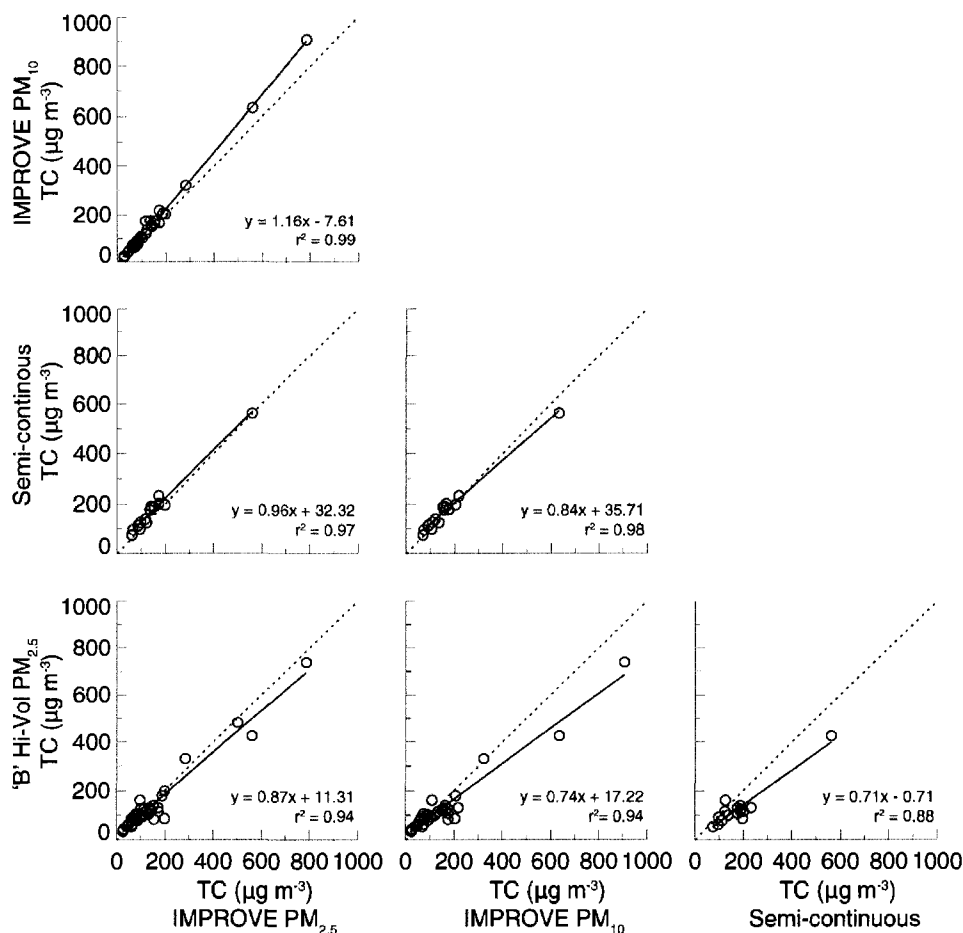


Figure 5.3 Scatter plots showing total carbon (TC) in $\mu\text{g C m}^{-3}$ for each measurement technique and/or filter sampler during FLAME. Each scatter plot shares axes with the corresponding plots in its row or column. To find the comparison between any two measurements, locate the column and row for each technique. For example, plot C compares TC measured on IMPROVE PM₁₀ samples using the IMPROVE_A protocol to TC measured by the semi-continuous Sunset analyzer using the modified NIOSH 5040 protocol. The least-squares linear regression and coefficient of determination (r^2) is given for each data pair. The dashed black line is the 1:1 line.

10 μm to PM_{10} mass, also seen in particle sizing data [E. Levin, personal communication]. The duff fuels were a mixture of decomposing plant material and soil, which may have been lofted into the chamber during the burn.

Gravimetric mass was measured by DRI following the standard procedure used to measure gravimetric mass in samples collected over the IMPROVE network. Relative humidity in the weighing laboratory is maintained between 20–40% [L. Ashbaugh, personal communication]. The gravimetric mass data also show that PM_{10} mass concentrations were dominated by $\text{PM}_{2.5}$ mass concentrations (Figure 5.4). The dominance of $\text{PM}_{2.5}$ has been observed previously for many types of biomass burning aerosol [Reid *et al.*, 2005b]. The relatively higher PM_{10} mass in the duff emissions was also reflected in the gravimetric mass data shown in Figure 5.4. A few burns other than duffs had relatively larger PM_{10} mass compared to $\text{PM}_{2.5}$ mass, including white spruce, sugar cane, and one ponderosa pine burn.

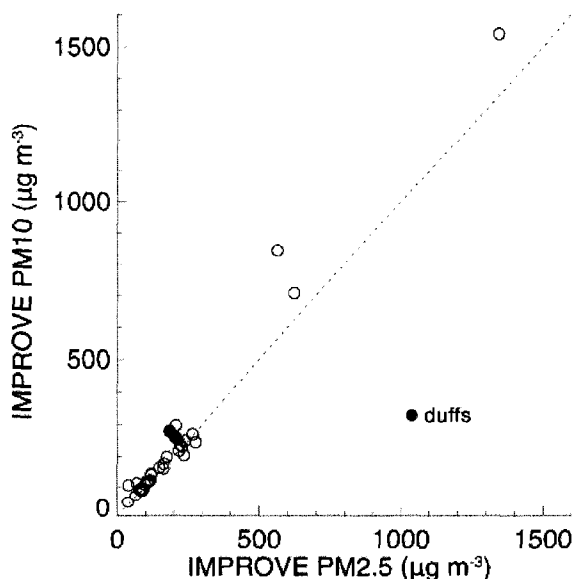


Figure 5.4 Gravimetric mass of particles with aerodynamic diameters less than 10 μm (PM_{10}) compared to gravimetric mass of particles with diameters less than 2.5 μm ($\text{PM}_{2.5}$) for IMPROVE filter samples during FLAME 1 and 2 chamber burns. Data for the duff emissions are highlighted by filled blue circles (see text for details).

Inorganic species were measured independently by ion chromatography on IMPROVE filter samples and for samples from filters collected by the URG sampling system described in Chapter 4. Figure 5.5 shows a strong correlation ($r^2 = 0.98$) between total sub-2.5 μm inorganic ions (defined as the sum of K^+ , Na^+ , NH_4^+ , Ca^{2+} , Mg^{2+} , Cl^- , SO_4^{2-} , and NO_3^-) measured on each set of filters. The regression was not performed through one outlier, which had nearly twice the URG chloride concentration compared to that measured on the IMPROVE filter. Inorganic aerosol measurements are less prone to the carbonaceous aerosol sampling artifacts related to gas-phase adsorption and loss of semi-volatile material, so the inorganic data agree better than the TC. The filter samplers were also located in closer proximity. The good agreement between inorganic ionic species measured on the different filters using independent analytical techniques indicates that the chamber was well mixed on the scale of the separation samplers, which were a few meters apart.

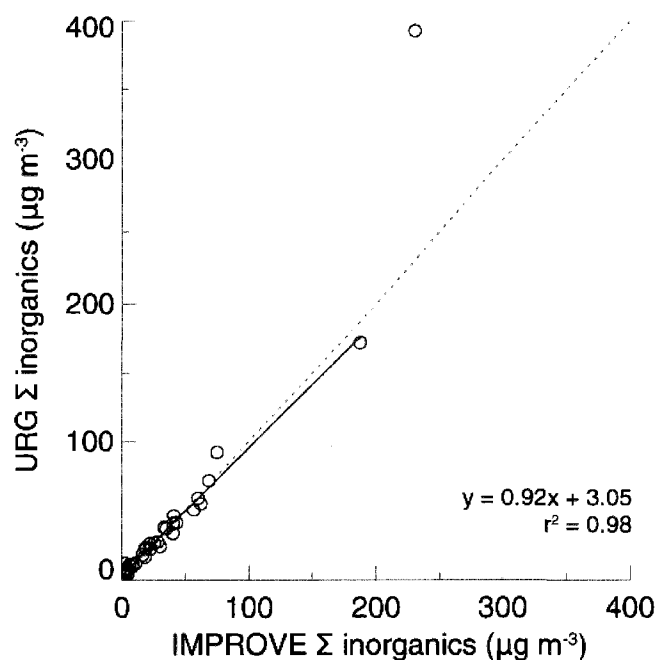


Figure 5.5 The sum of $\text{PM}_{2.5}$ inorganic species measured on IMPROVE versus URG filter samples during FLAME 1 and 2.

I presented emission factors for $PM_{2.5}$ mass reconstructed from inorganic and TC measurements in Chapter 4, which assumed an organic matter-to-OC conversion factor of 1.5. Figure 5.6 compares $PM_{2.5}$ gravimetric mass with mass reconstructed from the Hi-vol carbon measurements and the URG inorganic measurements presented in Chapter 3 and mass reconstructed from the IMPROVE carbon and inorganic species data. An organic mass-to-organic carbon multiplier of 1.5 has been applied to both sets of OC measurements. The two sets of reconstructed masses had similar relationships to gravimetric mass, with regression coefficients of 0.94 for the Hi-vol/URG species versus gravimetric mass and 0.97 for the IMPROVE species versus gravimetric mass. They were also both strongly correlated with gravimetric mass ($r^2 = 0.92$ and 0.95 , respectively). Note that I did not perform a rigorous analysis to determine the 'best' organic mass-to-OC multiplier and only suggest that 1.5 is a

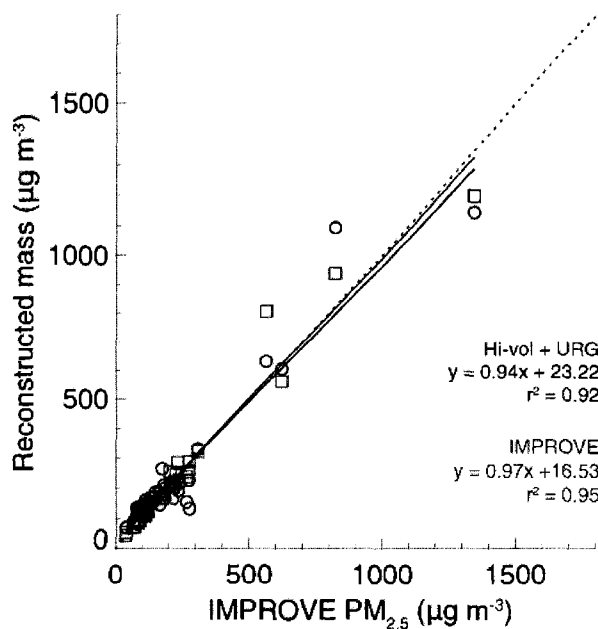


Figure 5.6 $PM_{2.5}$ mass reconstructed from Hi-vol carbon measurements and URG inorganic species (black circles) and $PM_{2.5}$ mass reconstructed from IMPROVE carbon and inorganic species (red squares) versus gravimetric mass measured on IMPROVE $2.5 \mu\text{m}$ samples during FLAME 1 and 2. Organic carbon concentrations have been multiplied by a factor of 1.5 to account for non-carbon species present in the organic aerosol.

reasonable average guess of the true value.

5.6 Measured organic and elemental carbon fractions

We normalized EC by TC for each measurement to remove the biases in Figure 5.3, allowing me to examine differences in assigned EC due to TOA method (Figure 5.7). The good agreement between EC/TC ratios found for the IMPROVE PM₁₀ and PM_{2.5} samples ($r^2 = 0.95$, regression coefficient = 0.98) shows that the EC fraction of TC in super-2.5 μm aerosol was similar to that in sub-2.5 μm aerosol. EC/TC ratios obtained by the same TOA protocol were strongly correlated. Figure 5.7f shows that EC/TC measured by the Sunset analyzer on the 'B' Hi-vol filter samples in off-line mode were slightly higher than the semi-continuous measurements made in on-line mode ($r^2 = 0.96$, regression coefficient = 1.15).

There were large disagreements in EC/TC ratios measured using different TOA protocols. Figure 5.7a, b, c, and d compare EC/TC ratios measured by the IMPROVE_A protocol with EC/TC ratios measured using the modified NIOSH 5040 (Sunset) protocol. IMPROVE_A EC/TC ratios were consistently a factor of two or more higher than the Sunset EC/TC ratios for samples with IMPROVE EC/TC ratios below about 0.5. The agreement improved for samples with greater contributions by EC to TC. The higher IMPROVE_A EC/TC ratios indicate that a greater fraction of the carbonaceous aerosol present in the filters was identified as EC rather than OC. In some cases, the IMPROVE_A protocol measured significant fractions of the emitted TC as EC (~ 0.15), but the modified NIOSH 5040 (Sunset) protocol identified it all as TC, i.e., zero EC. The approximately factor of two differences observed during FLAME were similar to those found in previous carbon measurement

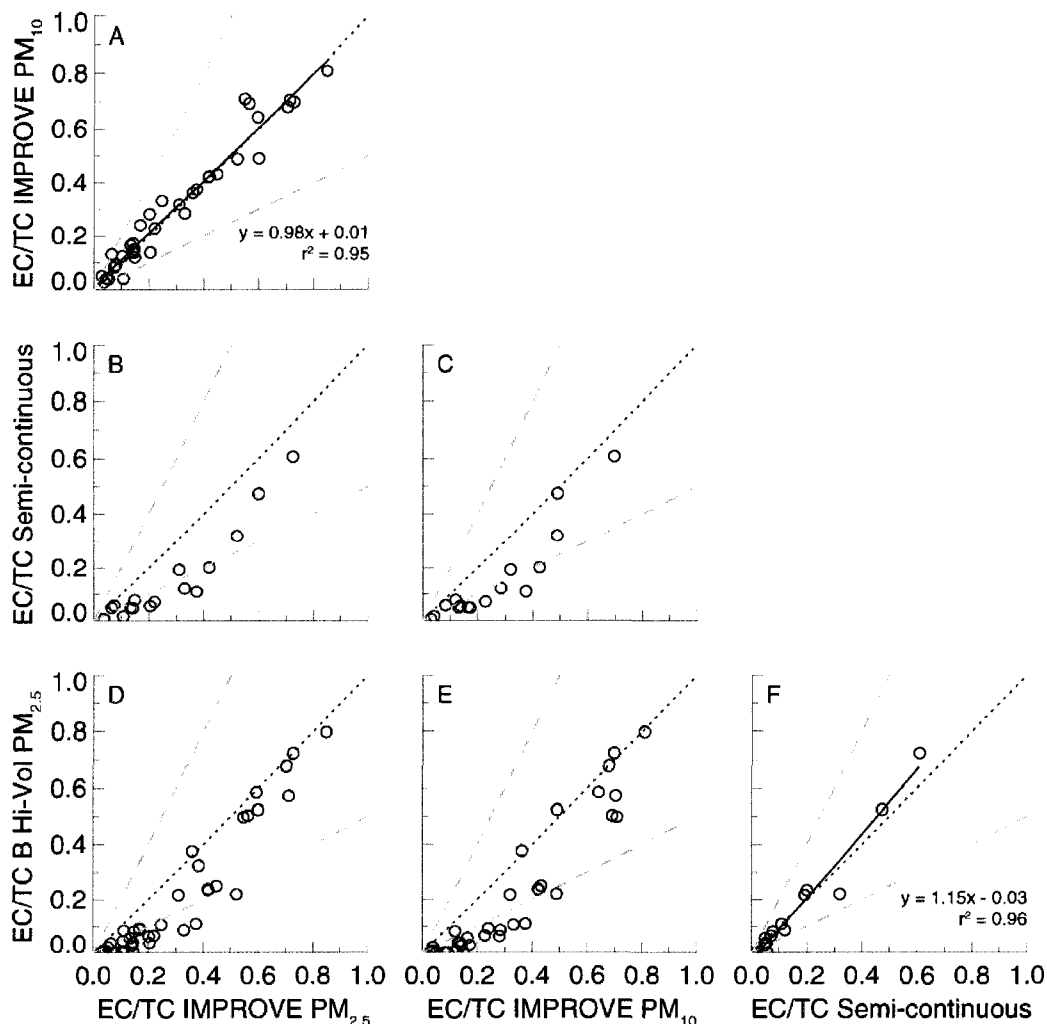


Figure 5.7 Scatter plot showing elemental carbon (EC) divided by total carbon (TC) for each measurement technique and/or filter sampler during FLAME. The short, dashed black line gives the 1:1 line and the two dashed gray lines show points where one measurement is double the magnitude of the other.

comparison studies for biomass burning samples [Watson *et al.*, 2005].

One major difference between the TOA protocols is how each corrects EC measured during the He-O₂ heating steps (referred to here as ‘apparent EC’ or EC_A) for POC formed during the prior oxygen-free heating steps. The NIOSH 5040/Sunset analyzer protocol used light transmittance only and the IMPROVE_A protocol measured light reflectance and light transmittance to determine two values of POC. If the transmittance and reflectance methods determine different amounts of POC, the correction to EC_A will be different, causing different

EC measurements. Measurements of EC_A can also vary due to differences in the temperature levels, heating rates, and times spent at each analysis temperature [Chow *et al.*, 2004]. EC measurements were more sensitive to the identification of POC when its concentration was similar to EC concentrations. Figure 5.8 shows reflectance-based POC (R-POC) normalized by EC_A measured for the IMPROVE $PM_{2.5}$ filters (measured using the IMPROVE_A protocol) as a function of EC_A/TC . R-POC was a significant fraction of EC_A for samples with low concentrations of EC_A relative to OC, i.e., a lower EC_A/TC ratios. R-POC made up over half of the EC_A for several OC-dominated samples. In other cases, usually samples with higher fractions of EC_A , no R-POC was detected. Small differences in the determination of POC led to large differences in EC/TC for samples dominated by OC, because a large fraction of the thermally-measured EC in the FLAME samples was really POC. This may be the source of the disagreement between samples with low EC/TC seen in Figure 5.7. Conversely, samples with high concentrations of EC contain relatively less POC, so EC measurements were not as sensitive to the POC correction and there is better agreement between the different TOA methods in Figure 5.7.

I examined the IMPROVE_A R-POC and transmittance-based POC (T-POC) measurements to check if the optical correction method alone is responsible for the large disagreement in EC/TC measurements. Figure 5.9 compares IMPROVE R-POC and T-POC for the IMPROVE $PM_{2.5}$ samples. T-POC was higher than R-POC for all but one sample, and were of similar magnitude for several samples in which no POC was detected by either method. R-POC was zero and T-POC was non-zero for about a quarter of the samples, but in other cases R-POC and T-POC agreed within a factor of 1-2. I did not find any relationship between fuel

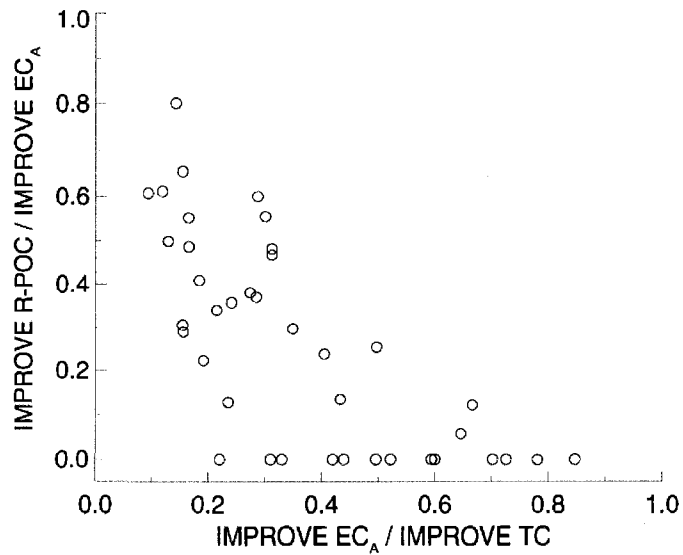


Figure 5.8 Reflectance-based pyrolyzed organic carbon (POC) versus elemental carbon (EC) measured on the IMPROVE PM_{2.5} filter samples during FLAME. Each value is normalized by the corresponding total carbon (TC) concentration measured on the filter.

type or combustion phase and the agreement between R-POC and T-POC.

The IMPROVE EC concentrations reported thus far have been the ‘apparent’ EC (EC_A) concentrations—carbon measured during the He/O₂-stages of the thermal analysis—corrected for POC using reflectance, which I denote as EC_R . An alternate EC value was calculated by subtracting POC measured using transmittance from EC_A , which I denote as EC_T . Differences between EC_R and EC_T were due only to differences in the optical correction method. Figure 5.10 shows the comparison of EC_T and EC_R for the FLAME 1 and 2 filter samples. The reflectance corrected values are higher than the transmittance corrected values ($EC_R > EC_T$) because the R-POC was generally lower than T-POC (Figure 5.9). The agreement between EC_R and EC_T fractions of TC was better than that observed between the Hi-Vol NIOSH 5040/Sunset analyzer EC and IMPROVE EC_R fractions of TC shown in Figure 5.7d. The optical correction method alone cannot explain the differences between the two TOA protocol measurements. Other factors, such as differences in heating rates and analysis temperatures [Subramanian *et al.*,

2006], must have also contributed to the differences in EC/TC ratios observed here .

The light transmittance through a filter is a function of the filter properties, the collected aerosol, and the charring adsorbed gases throughout the filter depth, but light reflectance from the filter surface is a stronger function of the filter properties, collected aerosol, and adsorbed gases at the filter surface [Chen *et al.*, 2004; Chow *et al.*, 2004]. If we assume charred gas-phase species adsorb uniformly throughout the depth of the filter, then T-POC must be more affected by the pyrolysis of the adsorbed gases compared to R-POC because R-POC measurements are more sensitive to the pyrolysis of particulate and gas-phase material at the filter surface [Chow *et al.*, 2004]. In other words, the R-POC correction did not ‘see’ the darkening of the inner portion of the filter caused by the charring of adsorbed organic gases, so it determined a lower amount of POC compared to the T-POC measurement. Subramanian *et al.* [2007] have suggested that just as gases are adsorbed within the filter, OC liquid particles deposit throughout the filter as

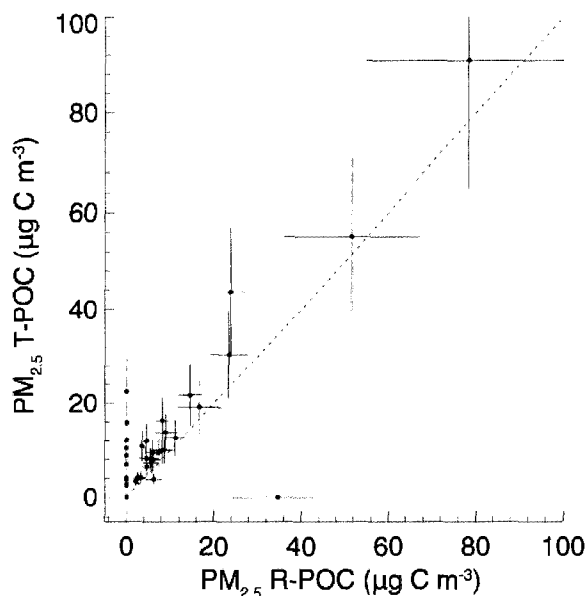


Figure 5.9 Transmittance- and reflectance-based pyrolyzed organic carbon (TPOC, RPOC) concentrations ($\mu\text{g C m}^{-3}$) measured on the IMPROVE PM_{2.5} filter samples using the IMPROVE-A protocol. The solid line shows the 1:1 line. Error bars indicate the uncertainty in each measurement calculated from Equation 5.2.

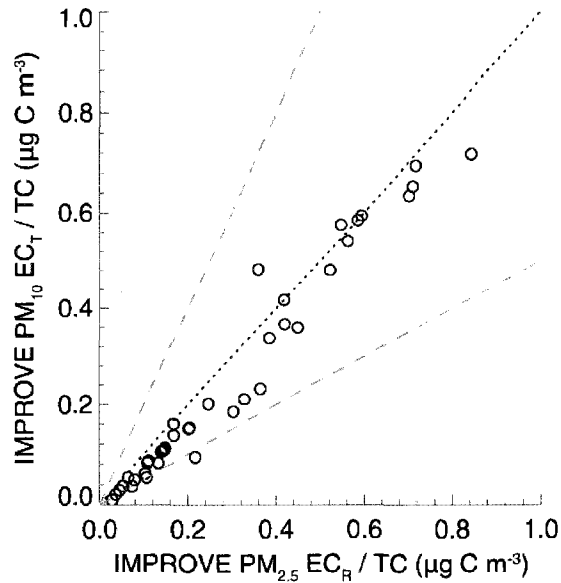


Figure 5.10 Elemental carbon (EC) fractions of total carbon (TC) measured on IMPROVE PM_{2.5} filters. EC was corrected for pyrolyzed organic carbon using reflectance (EC_R) and transmittance (EC_T). The short dashed line indicates the 1:1 line and the long dashed lines show regions where one measurement disagreed with the other by a factor of two.

organic films and 'beads', rather than on the surface with solid OC and EC particles. Just like the gases, the OC deposits can also char. The reflectance correction for POC would also be 'blind' to the darkening of the filter associated with the liquid films and beads. The magnitude of this effect depends on the relative masses of EC and adsorbed gases and organic films.

The IMPROVE PM_{2.5} secondary filters provide more information about the potential impacts of charred adsorbed gasses. Figure 5.11 shows T-POC and R-POC concentrations measured on the IMPROVE PM_{2.5} secondary filters versus EC_A concentrations measured on the same samples. There should not be any EC in the secondary filter because EC is non-volatile (so is not expected to penetrate past the first filter), assuming the filter efficiency is high. EC_A measured on the secondary filters must be POC. The T-POC concentrations matched EC_A concentrations for the majority of the samples, confirming that all of the EC_A on these filters was char. The reflectance method failed to detect any charred material on 30 of the 43 samples and

underestimated EC_A/T -POC concentrations for those cases when some R-POC was measured. Only 5–15% of the OC detected on the secondary filters formed POC, however, and the fraction of OC on the secondary filters was between 2–20% of the OC on the primary filter. Roughly 10–20% of the OC on the primary filter charred, so charred organic gases were small compared to the charring of particles or liquid films/beads sampled on the primary filter.

I could not determine if liquid films or beads were present in the filters or made important contributions to POC formation. Some type of microscopy, e.g. scanning emission microscopy or transmission electron microscopy, would need to be performed on the filter samples to determine if organic films/beads were present in the filter matrices. I did notice evidence of liquid-like substance emitted from the smoldering combustion of cellulose fibers

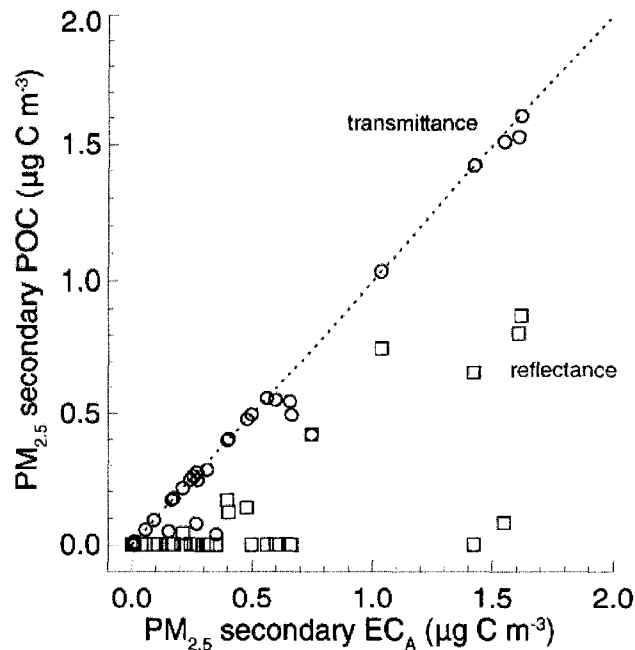


Figure 5.11 Transmittance- and reflectance-based pyrolyzed organic carbon (TPOC, RPOC) concentrations ($\mu\text{g C m}^{-3}$) versus apparent elemental carbon (EC_A) concentrations measured on the IMPROVE $PM_{2.5}$ secondary filters. EC_A is defined as the carbon evolving at the three EC temperature plateaus and is not corrected for RPOC. TPOC is shown by the black circles and RPOC is given by the red squares. The solid line gives the 1:1 line.

during several experiments carried out at LBNL. Burns that featured stronger contributions by smoldering combustion emitted relatively more OC compared to EC and produced OC-dominated filter samples with the large disagreements in EC/TC between TOA protocols. *Subramanian et al.* [2007] pointed out that while gas-phase adsorption can be limited to the availability of adsorption sites on the filter, the amount of liquid coating is not, so the concentrations of liquid films and beads could be high. Unlike gasses, their concentrations may not be affected by the aerosol-phase OC concentration. Finally, the organic films/beads have a yellow color [*Subramanian et al.*, 2007], which means they have a strong light absorption wavelength dependence, so they may contribute to the spectral optical properties observed on these samples discussed in Chapter 6.

5.7 Summary and conclusions

This chapter discussed two major sources of uncertainty in the carbonaceous aerosol measurements made during FLAME: adsorption of gas-phase organic species (related to gas-particle partitioning) and disagreement in OC and EC determined by different TOA protocols. I estimated gas-phase adsorption artifacts by comparing OC measured on the IMPROVE PM_{2.5} primary and secondary (backup) quartz filters, and found that ~2–20% of the primary filter OC was adsorbed organic gasses, depending on OC concentrations. Approximately 25% of the samples had gas-phase adsorption artifacts of at least 10% due to lower OC concentrations.

I investigated differences in carbonaceous aerosol mass concentrations measured by two TOA protocols, IMPROVE_A and modified NIOSH 5040/Sunset. Though TC measured on different filters by different TOA protocols showed little systematic bias, EC measured by the

IMPROVE_A protocol was roughly 2–4 times higher than EC measured by the modified NIOSH 5040/Sunset protocol for samples dominated by OC. Some of this disagreement could be explained by differences in the amount of POC identified through light reflectance and transmittance measurements. The transmittance measurements determined a higher concentration of POC than the reflectance measurements, so the corrected EC values were lower for transmittance compared to reflectance. Differences in POC alone, however, could not account for the disagreement in EC measured by the two protocols, so differences in heating rates and temperature plateaus must have also played a role. For example, *Subramanian et al.* [2006] suggested that IMPROVE/TOR-based protocols measured more EC compared to NIOSH/TOT-based protocols because non-light absorbing carbon evolves from the filter in the oxidizing mode together with EC in the former. The reflectance-based POC measurements underestimate charred organic gases, but these species do not make up a large enough fraction of the material on the filter to account for all of the disagreement between the methods.

The purpose of this chapter was not to determine the ‘best’ TOA protocol, or exhaustively investigate the sources of disagreement between them. A thorough investigation of the sources of disagreement between TOA protocols requires the analysis of punches from the same filter by different analyzers, which eliminates sources of disagreement due to sampling artifacts, and modification of the heating rates and analysis times to determine their impact on POC formation and the timing of EC and OC evolution [*Chow et al.*, 2004; *Subramanian et al.*, 2006]. These are important issues, but the focus here is to assess the magnitudes of the uncertainty in the OC and EC measurements because these are used in the analysis of the spectral optical properties in Chapter 7. Table A.3 summarizes the findings discussed in this

chapter.

It is difficult to assign a single number to the uncertainty in OC concentrations caused by gas-phase adsorption, because it was a strong function of OC concentration, but 10% is probably a fair estimate for the range of OC concentrations during FLAME. Ideally, the artifact could be subtracted from each sample, but no backup filters were available for stack burn measurements. The disagreement between TOA methods was also a function of the EC/OC fractions of TC. Disagreements were minimal for EC/TC ratios > 0.4 . OC fractions of TC disagree by about 15% for samples with EC/TC ratios < 0.4 and EC fractions of TC disagree by about 100–200% for samples with EC/TC fractions < 0.4 .

Chapter 6 Wavelength dependence of aerosol light attenuation

This chapter discusses aerosol light attenuation (ATN) measured as a function of wavelength (λ) on filter samples collected during FLAME. I begin with a description of the experimental methods and a discussion of the appropriate methods for quantifying the wavelength-dependence of ATN. After presenting the bulk aerosol results, I compare them to results of previous measurements of ATN and to ATN measured during several major field campaigns. Finally, I describe the results of some simple techniques used to distinguish the material responsible for the wavelength-dependent light absorption behavior from EC and/or black carbon (BC).

6.1 Method

6.1.1 *Filter samples and preparation*

Wavelength-dependent ATN measurements were performed on high-volume filter samples collected during FLAME 1 and 2 in 2006 and 2007. FLAME 1 Hi-vol sample filters were divided into eight equally-sized pieces and stored separately in aluminum foil. The entire high-volume FLAME 2 filters were stored in foil before being cut for the measurements presented here. Roughly 4 x 6 cm rectangular pieces from the selected filters were packed (and cut if necessary) and shipped in a cooler with chemical ice packs to Lawrence Berkeley National Laboratory (LBNL) for analysis. All filter handling apparatus was cleaned thoroughly with acetone before the next filter was processed to minimize cross contamination of the samples.

All FLAME 1 chamber samples were analyzed at LBNL in the fall of 2006, but no stack samples were examined. Selected FLAME 2 stack and chamber samples were analyzed at LBNL in the fall of 2007. At LBNL the samples were kept in a freezer except during brief periods when 1.14 cm² circular filter punches were collected for immediate analysis in the spectrometer or carbon analyzer.

6.1.2 *Optical system*

A diffraction grating spectrometer (Model S2000, Ocean Optics, Dunedin, Florida) measured the intensity of light transmitted through filter punches over the UV, visible and near-infrared (NIR) range of the electromagnetic spectrum. The spectrometer was sensitive over the range $\lambda = 200\text{-}1100$ nm with $\sim 0.3\text{-}10$ nm resolution depending on the diffraction grating used. During these experiments the resolution was ~ 2 nm. The spectrometer was sensitive to as low as 86 photon/count at 1-second time resolution. The spectrometer integration time was adjusted to maximize signal strength while still avoiding detector saturation, but was typically between 30-50 ms. The instrument software reported spectra as the mean of 50 individual spectra smoothed with a 40-element boxcar average.

Filter punches were placed in an anodized aluminum punch-holder that slid into a specially-built dark box containing the light source [Kirchstetter *et al.*, 2004]. A bundle of light emitting diodes (LEDs) served as the light source. Light from the LEDs traveled through a quartz rod that terminated adjacent to the sample. A second quartz rod fed the light transmitted through the sample to a fiber-optic cable, through which light traveled to the spectrometer aperture. An example spectrum of the light source is shown in Figure 6.1. Light emitted by the

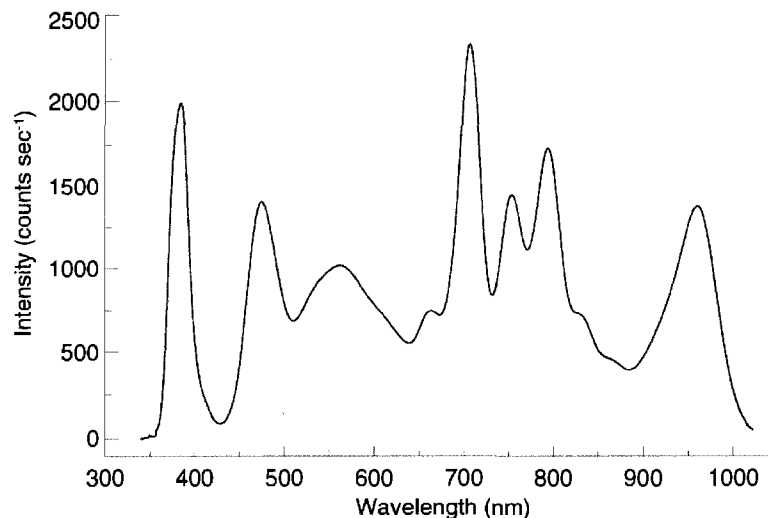


Figure 6.1 Spectrum of light intensity (counts second⁻¹) emitted by the light emitting diode (LED) bundle that served as the light source during the FLAME 2 sample attenuation measurements.

LED bundle peaked at several wavelengths, each associated with a specific LED. Transmission data were considered valid in regions of the spectrum with photon counts above 250 s⁻¹, which resulted in an effective range of $365 < \lambda < 1000$ nm.

6.1.3 Filter treatments

Attenuation was measured for bulk samples, samples treated with three different solvents (acetone, hexane and de-ionized water), and through the front and back halves of selected filter punches. The solvent treatment technique was based on the method described by *Kirchstetter et al.* [2004] but I expanded it to include hexane and DI water in addition to acetone. Filters were placed in 20 ml baths of acetone, hexane and DI water and left to soak for one hour. Ideally only soluble material dissolved from the filter matrix during the soak, but there was visible evidence of mechanical separation, particularly for heavily loaded samples. For example, the surface of the filter brightened following solvent treatments, which could result from particles being removed more selectively from the surfaces of the samples, or relocating to deeper within the filter. The wavelength-dependence of attenuation of the treated samples was

measured following the same procedure used for bulk, or untreated, samples.

Selected filter punches were cut into front- and back-filter halves by slicing them horizontally approximately half-way through the filter depth. *Engling et al.* [2006b] used a similar technique to investigate the contribution of adsorbed gas-phase species to OC and EC at Yosemite National Park during smoke-impacted periods. Slicing was performed using a specially-built polycarbonate filter-punch holder with a razor-blade cleaned with acetone. The filter punches had a natural cleavage point between the front- and back-halves of the filter, so filters were cut in a relatively consistent matter. There was no visual evidence of aerosol loading on the back-halves of the filter punches.

6.1.4 Filter samples from field measurements

I examined several laboratory-generated aerosol species and filter samples collected in the field for comparing to FLAME results. Field samples included several quartz-behind-quartz filter samples collected in Houston, Texas during the 2006 Texas Air Quality Field Study II-Gulf of Mexico Atmospheric Composition and Climate Study (TexAQS-GoMACCS) for comparison with the FLAME samples (more information regarding the field study can be found in *Quinn et al.* [2008]; more information regarding the filter sampling method can be found in *Ziamba et al.* [2007]). The filter sampler was located on the roof of the 18-story North Moody Tower on the University of Houston campus, approximately 5 km southeast of downtown Houston. The TexAQS-GoMACCS filter samples were collected and provided by Luke Ziamba and Rob Griffin from the University of New Hampshire. The filter sample flow rate was 15 L min⁻¹.

I also examined quartz filter samples collected at the Blodgett Forest Research Station (BFRS), a ponderosa pine-dominated field site located about 100 km east of Sacramento, California in the Sierra Nevada foothills [Lamanna and Goldstein, 1999; Lunden *et al.*, 2006; Schade and Goldstein, 2001]. Samples were collected in September and October of 2003 during the daytime (~0830 to 1830 local time) and nighttime (~1700 to 0800 local time).

6.2 Attenuation measurements

The transmission (Tr) of light through an aerosol-laden filter was defined as:

$$Tr(\lambda) = \frac{I(\lambda)}{I_0(\lambda)} \quad 6.1$$

where $I(\lambda)$ was the intensity of light transmitted through the loaded filter and $I_0(\lambda)$ was the intensity of light transmitted through the 'clean' filter. Aerosols and/or gases present within the filter punch were volatilized/oxidized from the filter by heating it to ~700° C in pure oxygen (FLAME 1 samples) or air (FLAME 2 samples). The intensity of light transmitted through the punch increased following the removal of material during the heating step, due in part to the removal of light absorbing material from the sample. Any light-absorbing mineral dust present in the sample was not removed by heating because it does not evaporate, decompose or combust at temperatures below 700° C, so any increase in light transmission through filters after heating was due to the removal of OC and EC only [Kirchstetter *et al.*, 2004].

Equation 6.1 was adjusted to account for variations in the light source strength over the duration of the experiments using:

$$Tr(\lambda) = \frac{I(\lambda)/I_r(\lambda)}{I_0(\lambda)/I_{r,0}(\lambda)} \quad 6.2$$

where $I_{r,0}(\lambda)$ was light intensity transmitted through a reference filter punch at the time of the 'blank' or $I_0(\lambda)$ measurement and $I_r(\lambda)$ was the light intensity transmitted through the same reference filter at the time of the initial loaded $I(\lambda)$ measurement. Note that if the reference filter transmission is identical at both measurement times ($I_r = I_{r,0}$) then Tr is simply the ratio of the loaded-to-blank intensities. Light attenuation as a function of wavelength, $ATN(\lambda)$, was calculated from $Tr(\lambda)$:

$$ATN(\lambda) = -100 \ln Tr(\lambda) \quad 6.3$$

The light attenuation coefficient (b_{ATN}) was calculated from:

$$b_{atn}(\lambda) = \frac{A_f}{Q t_s} \frac{ATN(\lambda)}{100} \quad 6.4$$

where A_f was the area of a high volume sample filter (400.5 cm²), Q was the high volume sampler flow rate, which was on the order of 1100 lpm (1 m³ s⁻¹), and t_s was the sample time.

I examined variability in the light attenuation measurements during the analysis of FLAME 1 samples by analyzing multiple filter punches from the selected samples and examining multiple spectra observed for each punch. Figure 6.2 shows five spectra observed for two different punches both taken from the FLAME 1 longleaf pine needle chamber burn filter sample (burn 115, filter 51). Replicate spectra collected for either punch agreed within 0.5%

over all valid wavelengths. I only performed one spectral measurement per punch when analyzing the FLAME 2 samples because of the high reproducibility observed for the FLAME 1 samples. For simplicity, the results presented in this chapter are based on the first spectrum collected for each sample. The punch-to-punch differences were larger than the variations in the spectrometer response, but remained within $\pm 3\%$ over all wavelengths for the different punches plotted in Figure 6.2.

The limited amounts of filter samples and of laboratory time prevented a thorough (i.e., a higher number of filter punches) investigation of the uncertainty in the attenuation measurements due to heterogeneity in the filter deposits. My estimate of the punch-to-punch variability in attenuation is probably underestimated because the punches were taken from a single 'octant' of the original high-volume filter. Punches collected from different portions of the original filter may have displayed larger $ATN(\lambda)$ differences.

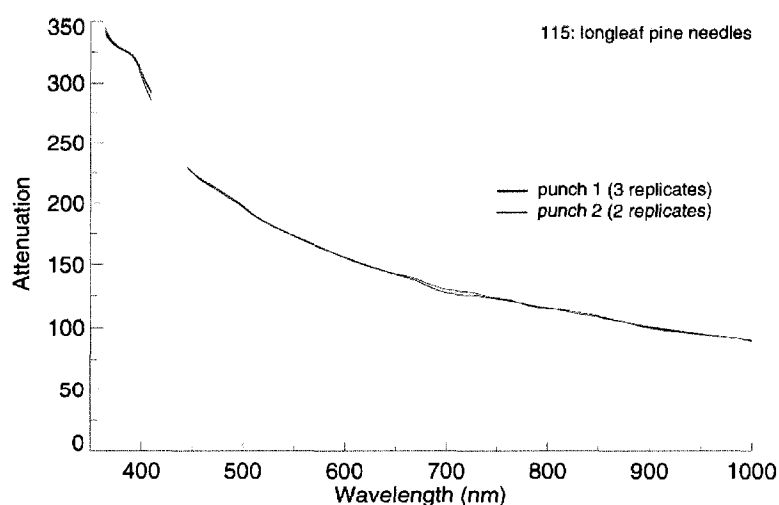


Figure 6.2 Attenuation plotted as a function of wavelength (nm) for two punch samples taken from the FLAME 1 longleaf pine needle chamber burn (burn 115, filter S1). There are actually five spectra plotted, but individual replicates from single punches are indistinguishable.

6.3 Quantifying the wavelength dependence of attenuation

The Ångström exponent for scattering was introduced in Chapter 4. Here I introduce a related concept, the Ångström exponent for attenuation, which describes the wavelength dependence of light attenuation. Rayleigh theory predicts that the light absorption efficiency (Q_a), which relates a particle's optical cross section to its physical cross section, has a $1/\lambda$ wavelength dependence ($\dot{A}_{\text{ATN}} = 1$) for particles with $D_p \ll \lambda$, assuming the real and imaginary components of the refractive index, $n(\lambda)$ and $k(\lambda)$, are constant [Bohren and Huffman, 1983]. In this case, the light scattering efficiency (Q_s) has a $1/\lambda^4$ dependence. Q_s and Q_a can be calculated for larger particles with diameters comparable to the wavelength, which make up the majority of aerosol described here, using Lorenz-Mie theory [Bohren and Huffman, 1983].

Bond [2001] used Lorenz-Mie theory to calculate \dot{A}_A for log-normal distributions of particles with constant real refractive index ($n[\lambda] = 1.55$) and geometric standard deviation ($\sigma_g = 1.5$), but varied count median diameters (CMD) and $k(\lambda)$. Figure 6.3 originally published by Bond [2001], illustrates several key features of \dot{A}_a behavior predicted by Mie theory. Absorption Ångström exponents are near unity for CMD smaller than ~ 90 nm over a wide range of k , consistent with Rayleigh theory predictions. For strongly absorbing particles ($k > \sim 0.2$), \dot{A}_a decreases with increasing D_p above ~ 100 nm. Finally, there is a range of CMD (between ~ 0.8 and $1 \mu\text{m}$) where \dot{A}_a is greater than 1.0, but only for material with complex refractive indices ranging from $0.001 < k < 0.1$.

As mentioned earlier, the traditional definition of \dot{A} requires optical measurements at two arbitrary wavelengths (Equation 4.2). This definition is particularly suited to measurements at a few discrete wavelengths, including those measured by AERONET sun photometers

Table 6.1 Discrete measurement wavelengths of the optical instruments sampling during FLAME.

Instrument	Wavelengths (nm)	Description	Reference
AE-22 Aethalometer	370, 880	filter-based attenuation	Hansen et al. [1984]
AE-31 Aethalometer	370, 470, 520, 590, 660, 880, 950	filter-based attenuation	Schmid et al. [2006]
TSI 3563	450, 550, 700	integrating nephelometer	Anderson and Ogren [1998]
PAS	405, 532, 870	multiple PAS instruments	Lewis et al. [in review]

[Holben et al., 1998], the TSI 3563 3- λ integrating nephelometer [Anderson and Ogren, 1998], the two- and seven-wavelength Aethalometers [Hansen et al., 1984; Schmid et al., 2006], and multiple-wavelength photoacoustic spectrometers (PAS) [Lewis, et al., submitted]. The measurement wavelengths for these instruments are given in Table 6.1. The spectrometer provided information at far more wavelengths, so to take advantage of the additional information, \hat{A}_{ATN} values were also determined by regressing $\ln(\text{ATN})$ against $\ln(\lambda)$ over the entire spectral range of the measurements, referred to here as the linear regression approach [Kirchstetter et al., 2004]. For clarity, $\hat{A}_{\text{ATN-L}}$ refers to Ångström exponents determined this way, while $\hat{A}_{\text{ATN}}(\lambda_{n1}, \lambda_{n2})$ refers to exponents determined from Equation 4.2 at wavelengths λ_{n1} and λ_{n2} .

Figure 6.4 gives an example of the linear-regression approach for determining $\hat{A}_{\text{ATN-L}}$ for ceanothus emissions (burn 118, filter 54). The bottom half of the figure shows the relationship between ATN and λ and the top half of the figure shows $\ln(\text{ATN})$ versus $\ln(\lambda)$. The red lines indicate the linear least squares regression through the log-transformed data plotted in both coordinate systems. The slope of the line is equivalent to $\hat{A}_{\text{ATN-L}}$, but opposite in sign, and in this case is 2.00 ± 0.005 (95% confidence interval, CI). The confidence interval was determined by multiplying the standard error of the regression by the Students t -statistic for a two-tailed distribution at 95% confidence and >1000 degrees of freedom ($t_{\alpha(2),0.05} = 1.962$). The coefficient of determination (r^2) for this example was 0.99, indicating that the power-law relationship was a

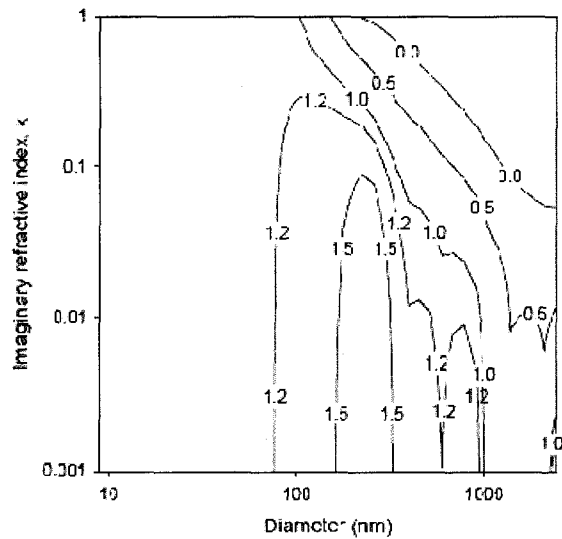


Figure 6.3 Values of the Angstrom absorption exponent (\hat{A}_a) predicted by Mie theory for size distributions of varying count median diameter (nm) for a range of imaginary refractive indices. The real part of the refractive index is fixed at 1.55 and the geometric standard deviation of the size distribution is 1.5. Reprinted with permission from Bond [2001].

good fit to the $ATN(\lambda)$ data for this case. This is qualitatively shown by the good agreement between the data and the power-law expression shown in red in the bottom half of the figure.

Kirchstetter *et al.* [2004] reported that the power law relationships predicted by \hat{A}_{ATN-L} underestimated the spectral dependence of absorption in samples with strong spectral dependence, which included biomass smoke samples. The FLAME samples also displayed a similar behavior. For example, emissions from burning Alaskan duff (burn 106, filter 42) had a high spectral dependence of ATN (Figure 6.5) that was not completely described by the \hat{A}_{ATN-L} determined for this sample. Unlike cyanobacteria emissions, the ATN curve for Alaska duff emissions does not fall on a single line in the log-transformed coordinates, meaning a single power-law fit fails to accurately describe the features of the data.

Standard linear regression, such as that used to determine \hat{A}_{ATN-L} , seeks to minimize the residual error between the model prediction (in this case $ATN_{\text{predicted}} = \hat{A}_{ATN-L} \lambda + C_1$, where C_1 is

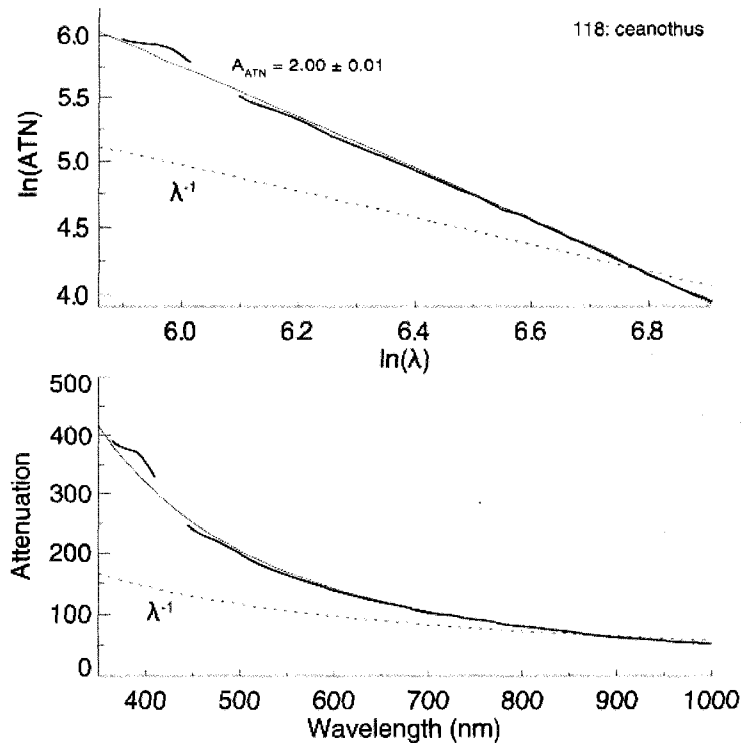


Figure 6.4 Attenuation as a function of wavelength (bottom) and $\ln(ATN)$ as function of $\ln(\lambda)$ (top) measured for a ceanothus emissions sample (burn 118, filter 54). The solid red line indicates the linear least-squares regression to the log-transformed data in both coordinate systems. The regression coefficient (A_{ATN}) and 95% confidence limits are indicated. The dashed line indicates ATN predicted for $1/\lambda$ relationship extended from the measured $ATN(\lambda_r = 880 \text{ nm})$.

the y-intercept of the regression line) and the data (ATN) to determine the best fit to the data.

Equal weight is given to the residuals regardless of the magnitude of the independent variable, which in this case is λ . The linear regression of the log-transformed data shown in Figure 6.5 returned a line that featured relatively large residuals at both the lower and upper extremes of the wavelength range. When the data and fit were plotted in normal coordinates, the residuals became very large at low wavelengths, and the fit underestimated ATN at low wavelengths by nearly 50%. The log-transformation of ATN gave more weight to the low ATN values at the upper-end of the wavelength range, and less weight to the high ATN values at the lower-end of the wavelength range. As a result, the total error, quantified as the sum of the residuals, of the fit in normal coordinates is unnecessarily large.

Non-linear regression provided an alternative approach to fitting the power law that best described the ATN data from a least-squares error minimization standpoint. I used a gradient-expansion algorithm (the CURVEFIT routine in the Industrial Design Language data analysis application) to compute a non-linear least squares regression to the FLAME ATN observations. The model function fit to the data was $y = A_0 x^{A_1}$, where A_0 was a constant and A_1 was $-1 \times \dot{A}_{\text{ATN}}$. The routine iterated over values of A_0 and A_1 until the χ^2 goodness-of-fit statistic remained within 0.1% of its previous value or 20 iterations were performed without convergence. The parameters returned from the linear regression of the log-transformed data provided the initial estimates of A_0 and A_1 .

The results of the non-linear regressions performed over the entire observed wavelength range and only the UV-visible portions of the spectrum (370 nm – 750 nm) are also shown in Figure 6.5. The non-linear regression fits were both significantly closer in magnitude to the low-wavelength ATN data, but the errors at longer wavelengths were larger than observed using the linear-regression approach. These data were given less weight in the fit because ATN decreased with increasing λ for the samples analyzed here. Unfortunately, the errors at longer λ make extrapolating ATN measurements made at a single, longer wavelength, e.g., the 880 nm Aethalometer measurement, problematic. This is because the predicted values are very sensitive to errors in the fit at these values. For example, the \dot{A}_{ATN} returned by the non-linear regression fit to the Alaskan duff data (~ 4.3) and the measured ATN for this sample at $\lambda = 880$ nm (8.2) predict an ATN (at $\lambda = 370$ nm) of ~ 265 compared to the measured value of ~ 200 , an error of more than 25%.

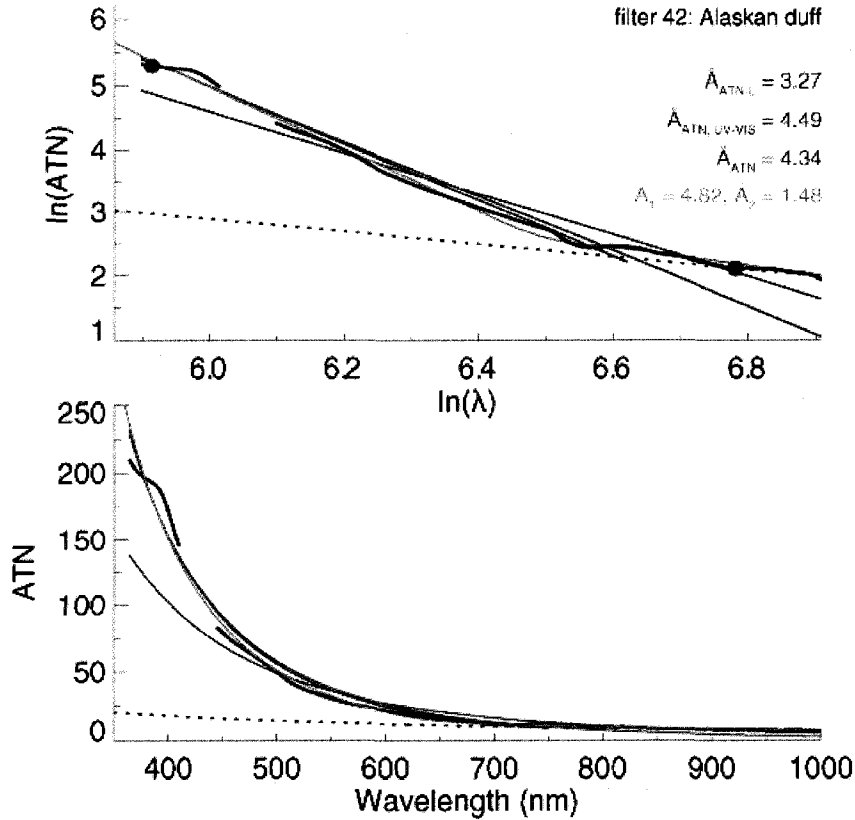


Figure 6.5 Attenuation as a function of wavelength (bottom) and $\ln(\text{ATN})$ as function of $\ln(\lambda)$ (top) measured for an Alaskan duff emissions sample (burn 106, filter 42). The red line indicates the linear least-squares regression to the log-transformed data for $360 < \lambda < 1000$ nm in both coordinate systems. The green line shows the fit given by a non-linear regression to the data assuming a power-law functionality. The blue line indicates is a non-linear regression fit, but restricted to the UV-visible (UV-VIS) wavelength range: $360 < \lambda < 750$ nm. The orange line is the fit provided by the weighted sum of two power laws fit to different regions of the spectrum (see text for details). The dashed line indicates ATN predicted for $1/\lambda$ relationship extended from the measured $\text{ATN}(\lambda_i = 880 \text{ nm})$. The solid circles indicate $\ln(\text{ATN})$ values at $\lambda = 370$ and 880 nm.

The poor predictive value of the power-law fit to the Alaskan duff emission spectra results from the fact that the ATN data are not adequately described by a single power law. This is obvious from the sudden change in slope that occurs at $\ln(\lambda) \sim 6.55$ in Figure 6.5. A simple, four-parameter model based on the weighted average of two power laws was developed in collaboration with Dr. Markus Petters to better describe the ATN data, given by:

$$\ln \text{ATN}(\ln \lambda) = (1 - \gamma)(C_1 + \hat{A}_1 \ln \lambda) + \gamma(C_2 + \hat{A}_2 \ln \lambda) \quad 6.5$$

where γ is the weighting function:

$$\gamma = \frac{\text{erf}[10(\ln \lambda - \ln \lambda_c)]}{2} + 0.5 \quad 6.6$$

and λ_c is the transition wavelength between the two power laws and $\text{erf}()$ is the error function. The transition wavelength is determined from the intersection of the two lines (in log-space) described by the power laws, given by:

$$\ln \lambda_c = \frac{C_1 - C_2}{\hat{A}_2 - \hat{A}_1} \quad 6.7$$

Equation 6.5 is simply the sum of two lines in log-space, weighted such that for $\lambda < \lambda_c$ ($\gamma \approx 0$) the predicted ATN is governed primarily by the values of C_1 and \hat{A}_1 (line 1) and for $\lambda > \lambda_c$ ($\gamma \approx 1$) the predicted ATN is described mainly by the values of C_2 and \hat{A}_2 (line 2). Physically, \hat{A}_1 is essentially the Ångström attenuation exponent valid in the UV-VIS ($\lambda < 750$ nm) region of the spectrum and \hat{A}_2 is the Ångström exponent valid in the near-infrared (NIR) region of the spectrum. Samples with weak spectral-dependence were in good agreement with a simple, single power law fit, so C_2 and \hat{A}_2 were fixed at zero when $\lambda_c > 850$ nm.

I performed the non-linear regression described above, but with Equation 6.5 as the model function to obtain best estimates of \hat{A}_1 and \hat{A}_2 . The resulting predicted value is shown by the orange curve in Figure 6.5. In log-transformed coordinates, the weighted, two power law fit resembles two lines intersecting at the kink in the data near $\ln(\lambda) = 6.55$. The predicted values match the data equally well in the low- and high-wavelength spectral regions. Note that in the UV-VIS region, \hat{A}_1 is slightly higher than $\hat{A}_{\text{ATN, UV-VIS}}$ and \hat{A}_{ATN} because it is not influenced by the weaker ATN- λ relationship at longer wavelengths.

The results of the various curve fitting procedures described above are shown for the untreated FLAME samples in Figure 6.6. Ångström attenuation exponents returned by the

different fitting routines are in good agreement for samples with weak ATN spectral dependence ($\dot{A}_{\text{ATN}} < 2$). There are larger differences when spectral dependence becomes stronger between Ångström exponents determined from the linear regression of the log-transformed data and non-linear regression of the original data (Figure 6.6a) and between exponents calculated from Equation 4.2 and those determined by non-linear regression (Figure 6.6c). There was good agreement (slope = 0.98, $r^2 = 0.97$) between \dot{A}_{ATN} obtained using non-linear regression over the UV-VIS and entire measured portions of the spectrum (Figure 6.6b), showing the relatively weak dependence of the non-linear regression technique on ATN at longer wavelengths.

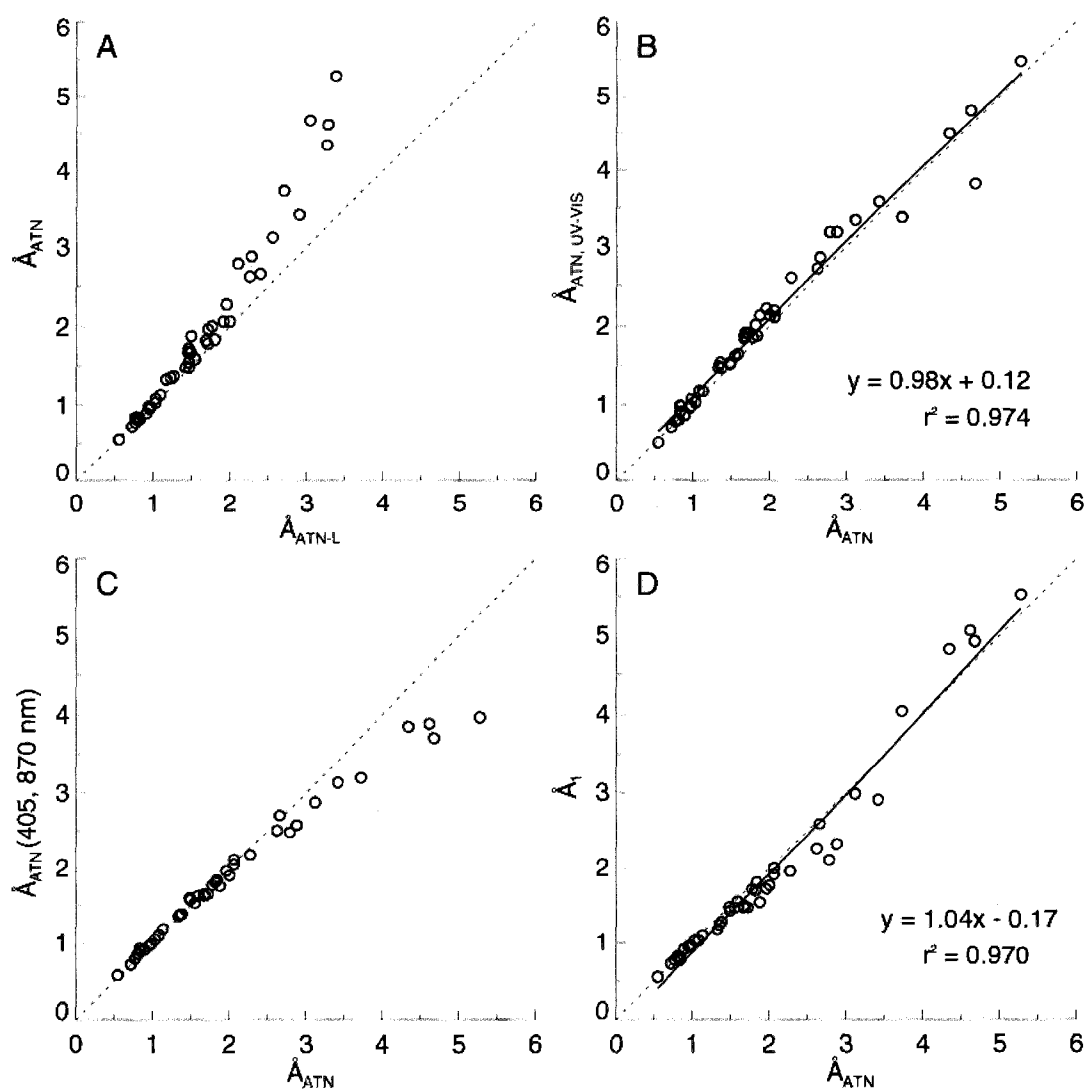


Figure 6.6 Scatter plots comparing Ångström attenuation exponents obtained from a) linear regression of log-transformed attenuation (ATN) as a function of log-transformed wavelength (\hat{A}_{ATN-L}) and non-linear regression of $ATN(\lambda)$ assuming a power-law functionality (\hat{A}_{ATN}), b) non-linear regression over the UV-VIS and entire measurement spectra, c) non-linear regression and \hat{A}_{ATN} calculated from Equation 4.2 at $\lambda = 405$ and 870 nm, and d) non-linear regression and the low-wavelength exponent (\hat{A}_1) obtained from non-linear regression assuming ATN is a function of weighted power laws (see text for details).

Ångström attenuation exponents determined for the lower portion of the spectrum using the weighted power law model were similar to those obtained by a single power law (Figure 6.6d). This indicates that the Ångström exponent governing the single power law fit to the data represents the wavelength dependence well. The utility of the weighted power law model stems from its ability to predict ATN at longer wavelengths as well as at shorter

wavelengths. For most of this chapter, we are concerned with quantifying \dot{A}_{ATN} to enable comparisons of the spectral dependence of attenuation with other parameters, so the \dot{A}_{ATN} obtained from the simpler single power law regression will be used as the standard representation of the Ångström exponent.

6.4 Results for untreated samples

FLAME biomass burning filter samples featured a large range of ATN-wavelength relationships. Though a qualitative measure, the range in filter sample color was a preliminary indicator that biomass burning produces aerosols with strongly varying optical properties. A filter's color is a manifestation of the wavelength-dependence of its attenuation. Figure 6.7 shows the wavelength dependence of attenuation measured for three samples: ponderosa pine duff (burn 105, filter 41), lodgepole pine needles and litter (burn 111, filter 47), and chamise (burn 113, filter 49). A photograph of each filter taken with a digital camera is included in the figure.

The dashed line indicates a $1/\lambda$ attenuation dependence, normalized to the sample attenuation at a reference wavelength, λ_r , of 880 nm. The choice of λ_r is somewhat arbitrary, as it is only a reference point for interpreting the strength of the wavelength dependence. I chose λ_r to equal 880 nm because it is the same wavelength that the Aethalometer uses to determine BC [Hansen *et al.*, 1984]. The $1/\lambda$ relationship between wavelength and ATN will be shown in a number of the figures in this chapter. This line can be thought of as representing the ATN expected at all wavelengths based on a measurement of BC ($\dot{A}_{\text{ATN}} = 1$) at the Aethalometer measurement wavelength, $\lambda = 880$ nm.

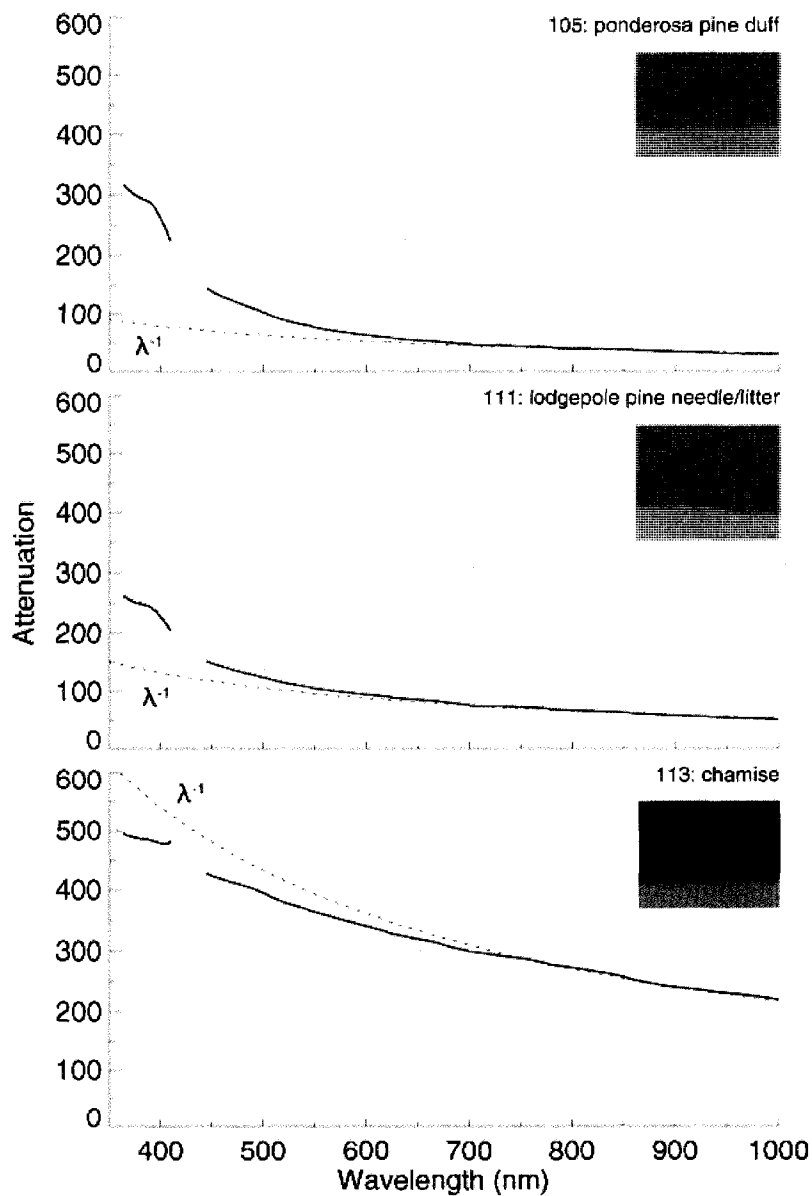


Figure 6.7 Attenuation coefficients (ATN) as a function of wavelength for three biomass burning aerosol samples collected during FLAME: ponderosa pine duff (top), lodgepole pine needle and litter (middle) and chamise (bottom). Dashed lines give the attenuation coefficient predicted from a $1/\lambda$ attenuation dependence on wavelength normalized to ATN at a reference wavelength of 880 nm. Inset photographs are pictures of each filter sample taken in the laboratory with a digital camera

The samples shown in Figure 6.7 represent the range of attenuation-wavelength relationships I observed for FLAME samples. At one extreme, chamise emissions, the filter appeared black to the naked eye, featured high attenuation from ~400 to 1000 nm, and exhibited a relatively weak attenuation wavelength dependence, with \hat{A}_{ATN} close to one, implying large

particles with high k (Figure 6.3). At the other extreme, ponderosa pine duff emissions, the filter had a light yellow/brown color, featured low attenuation values at larger wavelengths, but had a strong wavelength dependence, with ATN at $\lambda = 400$ nm about a factor of 10 higher than that predicted by the $1/\lambda$ relationship extended from λ_r . The filter with lodgepole pine needle and litter emissions fell in between these two extremes, both in terms of visible color and attenuation as a function of wavelength.

Each filter sample was fit with a power law using the non-linear regression method described in Section 6.3 to obtain values of \hat{A}_{ATN} . Figure 6.8 summarizes the untreated FLAME filter sample results in order of increasing \hat{A}_{ATN} . Emissions from Alaskan duff, smoldering ponderosa pine needles, phragmites and kudzu had the largest \hat{A}_{ATN} values, all greater than 3.0. The lowest \hat{A}_{ATN} were observed for juniper, chamise, black spruce and manzanita emissions, all less than 1. Overall, \hat{A}_{ATN} observed for FLAME samples ranged from 0.54 to 5.27, with a mean of 1.9 ± 1.15 (± 1 standard deviation). The distribution of \hat{A}_{ATN} was skewed towards lower values, with about 2/3 of the samples having \hat{A}_{ATN} values less than 2. The median \hat{A}_{ATN} of the FLAME samples was ~ 1.6 . Note that the study averages partially reflect the choice of fuels and the number of times they were burned during the study.

I examine relationships between \hat{A}_{ATN} , combustion conditions, and aerosol properties in more detail in the following chapter, but make some brief qualitative observations regarding the untreated filter data here. Smoldering ponderosa pine needle emissions had $\hat{A}_{ATN} \sim 4.5$ compared

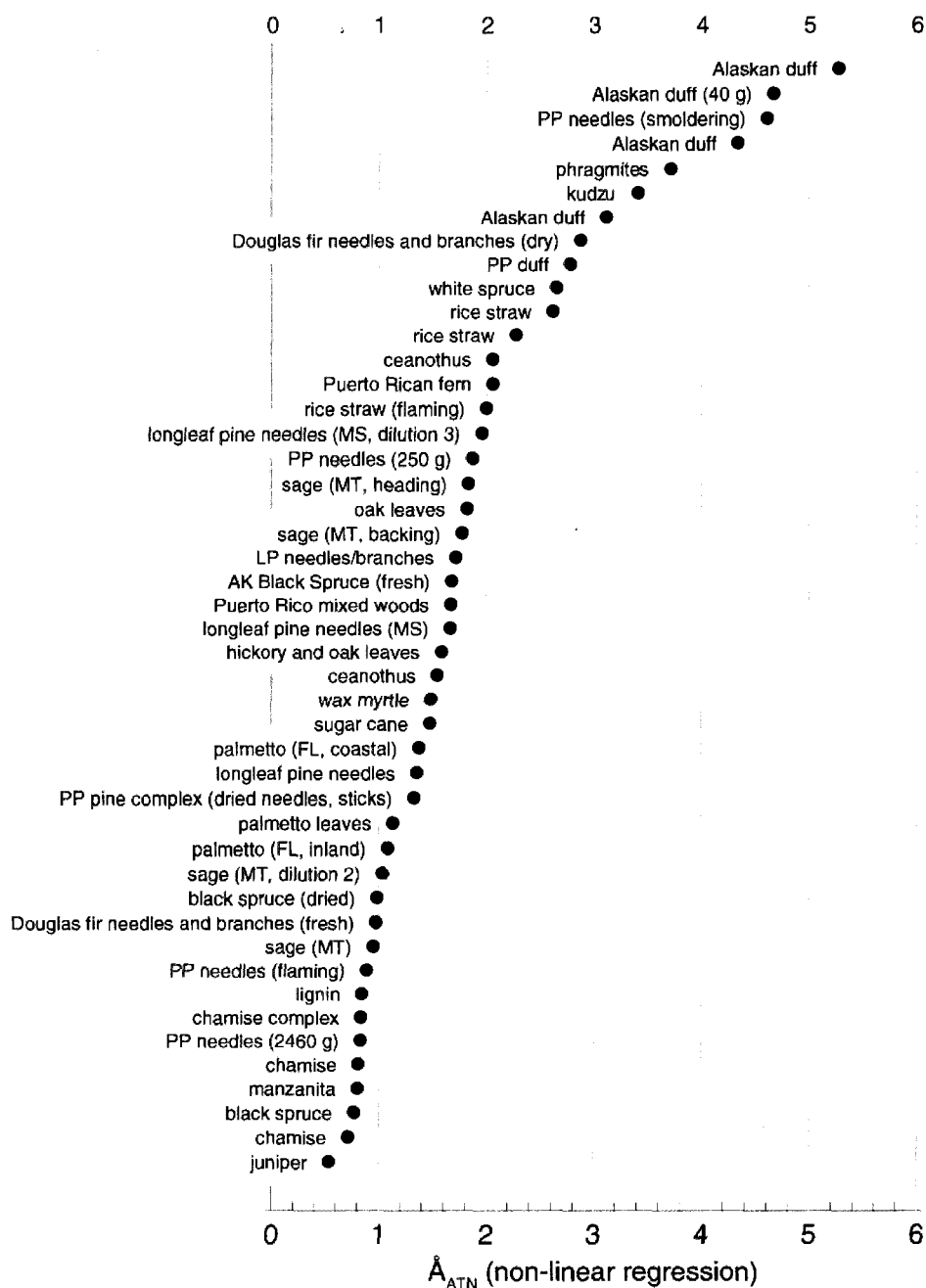


Figure 6.8 Attenuation Ångström exponents (\hat{A}_{ATN}) observed for untreated, bulk filter samples of biomass burning emissions. Attenuation as a function of wavelength data for each sample were fit to a power-law using non-linear regression to obtain values of \hat{A}_{ATN} . See Chapter 3 for a complete description of the fuels. Data are ranked in order of increasing \hat{A}_{ATN} .

to ~0.9 for flaming ponderosa pine needle emissions, suggesting that combustion conditions play an important role in determining \dot{A}_{ATN} for biomass burning emissions. Emissions from separate burns of the same fuel species had similar \dot{A}_{ATN} , but only if the fuel conditions and components were similar, indicating a fairly high degree of repeatability in the experiments. For example, the chamise and Alaskan duff samples were closely grouped at the low and upper ranges of \dot{A}_{ATN} . That said, increasing the fuel mass over several ponderosa pine needle burns resulted in lower \dot{A}_{ATN} values, likely the consequence of increased contributions by flaming combustion as the fuel mass increased. Fuel species at the low-range of \dot{A}_{ATN} values tended to be dominated by chaparral and desert shrubs, while fuel types at the upper-range of \dot{A}_{ATN} values featured leafy fuels, such as kudzu, ceanothus, and Puerto Rican fern, as well as dense fuels (duffs).

The comparison of FLAME results with previous observations is complicated by the variety of instrumental and analytical methods that have been used to characterize the spectral optical properties of combustion aerosol, which are summarized in Table 6.2. Few studies have focused specifically on the spectral absorption properties of laboratory fire aerosol emissions [Kirchstetter *et al.*, 2004; Lewis *et al.*, in press; Patterson and McMahon, 1984; Roden *et al.*, 2006; Schnaiter *et al.*, 2005]. Other work has examined biomass burning-influenced samples collected in the field [Chand *et al.*, 2006; Clarke *et al.*, 2007; Hoffer *et al.*, 2006; Kirchstetter *et al.*, 2004; Sandradewi *et al.*, 2008]. Different techniques have been used to determine \dot{A}_{ATN} and \dot{A}_a from ATN and absorption measurements (e.g., linear regression, Equation 4.2). Reported LAOC optical properties show considerable variation, partly due to the differences in methods described above, and partly due to natural variability within the broad range of organic species

Table 6.2 Optical properties of LAOC produced by combustion sources. Discrete wavelengths or wavelength ranges are indicated by italic text. OC or mixed refers to the bulk classification of the carbonaceous material. PSAP = particle soot absorption photometer.

Reference	\hat{A}_A $\lambda_1 - \lambda_2$ nm	\hat{A}_S $\lambda_1 - \lambda_2$ (nm)	ω_0 λ_0 (nm)	α_a (m ² g ⁻¹) λ_0 (nm)	technique	OC or mixed?
<i>Biomass burning</i>						
Foot and Kilsby [1989]	1.6 <i>500-900</i>	-	-	-	integrating plate	-
Kirchstetter et al. [2004]	1.8-2.2 <i>330-1000</i>	-	-	0.6 [†] <i>550</i>	filter-based spectrometer	OC
Schnaiter et al. [2005]	1.5-1.9 <i>450, 700</i>	-	0.74 <i>550</i>	-	LOPES [‡] , 3- λ nephelometer	mixed
Roden et al. [2006]	1-5 <i>467, 660</i>	-	0.2-1.0 <i>530</i>	6.5-0.4 -	3- λ PSAP, nephelometer	mixed [‡]
Chand et al. [2006]	2 <i>450, 615</i>	~2 <i>450, 700</i>	0.92 \pm 0.02 <i>545</i>	0.33 <i>545</i>	aethalometer, PSAP, nephelometer	mixed [‡]
Clarke et al. [2007]	2.1 <i>470, 660</i>	1.2-2 <i>450, 700</i>	0.87-0.97 <i>530</i>	0.09 <i>530</i>	3- λ nephelometer, 3- λ PSAP	'refractory OC'
Sandradewi et al. [2007]	2.7 \pm 0.4 <i>370, 520</i>	-	-	-	7- λ aethalometer	mixed [‡]
Lewis et al. [in press]	1.5-3.5 <i>510, 840</i>	-	-	-	PAS, 3- λ nephelometer	mixed [‡]
<i>Other combustion</i>						
Bond et al. [1999]	0.8-3.0 4- λ regression	-	-	0.32 \pm 0.09 <i>550</i>	Integrating plate, PSAP	mixed
Bond et al. [2002]	1-2.8 4- λ regression	-	0.4, 0.98 <i>550</i>	4.1, 0.2 <i>525</i>	integrating plate, PSAP, neph.	mixed [§]
Schnaiter et al. [2003]	2.1 <i>450-700</i>	0.9 <i>450, 700</i>	0.25 \pm 0.04 <i>550</i>	2.9 \pm 0.4 <i>550</i>	Multiple	'Palas soot'
Schnaiter et al. [2006]	2.2-3.5 <i>450, 700</i>	2.2-2.8 <i>450, 700</i>	0.5-0.76 <i>550</i>	1.4-2.1 <i>550</i>	LOPES [‡] , 3- λ nephelometer	mixed

[†] Absorption efficiency determined by dividing average attenuation by a factor of 2.

[‡] LOPES is an extinction spectrometer operating from 200 to 1015 nm with 2.5 nm resolution, but absorption is determined using the difference method ($b_a = b_e - b_s$), where b_s is measured by a nephelometer at 450, 550 and 700 nm.

[‡] The first number refers to the flaming-dominated combustion, the second value to smoldering-dominated combustion.

[‡] Values refer to study averages during the burning season, except for \hat{A}_a , which is reported for 'high pollution events'.

[‡] Average value between 2200–0200 during winter in a wood-smoke dominated mountain valley.

[‡] Highest \hat{A}_a and ω_0 observed for OC-dominated samples.

[§] The first number refers to observations for bituminous coal, the second to lignite. \hat{A}_a was determined by regressing absorption measured at 435, 525, 660 and 800 nm against wavelength.

present in LAOC.

Table 6.2 lists studies that reported \hat{A}_A for biomass burning aerosol. Most reported \hat{A}_A values on the order of 2, but Roden et al. [2006] and Lewis et al. [in review] found \hat{A}_A as large as 3-5 for certain fuels and burning conditions. They found the largest values of \hat{A}_A corresponded to

fuels dominated by smoldering combustion or during periods of smoldering combustion. The mean value for FLAME samples was in good agreement with those reported previously, but as mentioned earlier, the study average reflects the selection of filters analyzed, and does not carry a great deal of meaning. These studies used different methods to fit the spectral dependence of absorption, which can change the resulting estimates of \dot{A}_A by as much as 50% (Figure 6.6). For example, *Kirchstetter et al.* [2004] fit data using linear regression but *Roden et al.* [2006] used Equation 4.2. This issue is discussed further in Section 6.7, which compares FLAME filter- and PAS-based measurements.

The range of \dot{A}_{ATN} observed during FLAME was also in good agreement with values reported in Table 6.2. For example, *Roden et al.* [2006] reported \dot{A}_a ranging from ~0.6 to 5 for wood burning stove emissions based on real-time measurements of absorption. Given the wide variety of fuels burned during FLAME and the agreement with the range of previously reported values, the spectral dependence of absorption for biomass burning emissions is probably bound by these lower- and upper-limits. Several studies listed in Table 6.2 noted that \dot{A}_A was strongly influenced by combustion conditions. *Bond et al.* [1999b] noted an increase in \dot{A}_A when the operating load on the lignite combustion facility decreased. *Schnaiter et al.* [2006] linked changes in \dot{A}_A to different C/O ratios in the propane/air fuel mixture fed into the combustion flame, and *Roden et al.* [2006] saw increases in \dot{A}_A when CO/CO₂ ratios indicated smoldering combustion of wood fuel during cook stove experiments.

6.5 Results for front- and back-filter halves and treated filters

6.5.1 *Front- and back-filter halves*

I measured ATN as a function of wavelength on several pairs of front- and back-filter halves to estimate the contribution of adsorbed gases to ATN for selected FLAME samples. The number of samples analyzed in this way was limited due to the increased labor required to prepare and analyze the samples. The samples analyzed in this fashion were collected during FLAME 1 only. The magnitude of adsorbed gas artifacts were similar between the studies (Chapter 5), so the adsorbed gases contribution to ATN was probably similar during the two phases of the study as well. I picked eight burns to represent the range of aerosol properties I observed when analyzing the unmodified filter spectra: two ‘intermediate’ samples (ponderosa pine complex and lodgepole pine complex), five strongly spectrally dependent samples (rice straw, ponderosa pine duff, Alaskan duff, Puerto Rican fern, and ceanothus), and one weakly spectrally dependent sample (chamise).

Sampling artifacts associated with the adsorption of gas-phase organic species onto quartz filter fibers are often divided into two categories. The ‘positive artifact’ describes the spurious increase in aerosol loading resulting from the adsorption of organic gases onto the quartz filter fibers. The ‘negative artifact’ expresses the loss, or evaporation, of semi-volatile organic material originally sampled as particles. Numerous studies have attempted to quantify and distinguish between the effects of these two processes using combinations of denuders and filter media for various aerosol types [e.g., *Kirchstetter et al.*, 2001; *Lipsky and Robinson*, 2006; *Mader and Pankow*, 2001; *Subramanian et al.*, 2004; *Turpin et al.*, 1994]. I examine gas-phase

adsorption artifacts more closely in Chapter 5, which is focused on OC and EC measurements and their uncertainties during FLAME. In this chapter, I only investigate the contribution of adsorbed gas-phase species to the filter-based ATN measurements.

Attenuation measured on whole, front- and back-half filter samples of rice straw emissions (burn 104, filter 40) are shown in Figure 6.9. The sum of the front- and back-half ATN was 10-15% lower than ATN measured through the whole filter sample. The quartz fibers in the back-half of the filter acted as a mirror, scattering light back towards the more heavily loaded front filter half. Removing these fibers by cutting the filter in half reduced the amount of multiply-scattered light absorbed by the particles loaded on the front half of the filter. Light attenuation through the back filter half was about a factor of 10 lower than ATN measured on the front half of the filter for this sample.

I made a crude estimate of the ATN due to particles and adsorbed gases by assuming: a) gases were adsorbed equally throughout the filter depth, b) the back filter half contained only adsorbed gases, c) the filters were cut exactly in half, and d) the mass-normalized attenuation efficiency (a_{ATN}) was constant throughout the filter depth. Under these assumptions, the attenuation due to adsorbed gases (ATN_g) was simply twice the back- filter half ATN value. The particle contribution to ATN was the front half of the filter ATN minus the back half ATN. The particle contribution to ATN is shown in blue in Figure 6.9. Particles were the major contributor to light ATN for this sample. They had a much stronger wavelength dependence of ATN than the $1/\lambda$ functional dependence predicted from the ATN value at $\lambda = 880$ nm. If gases were solely responsible for the increased wavelength dependence of ATN in this sample, the particle contribution to ATN curve should fall close to this line.

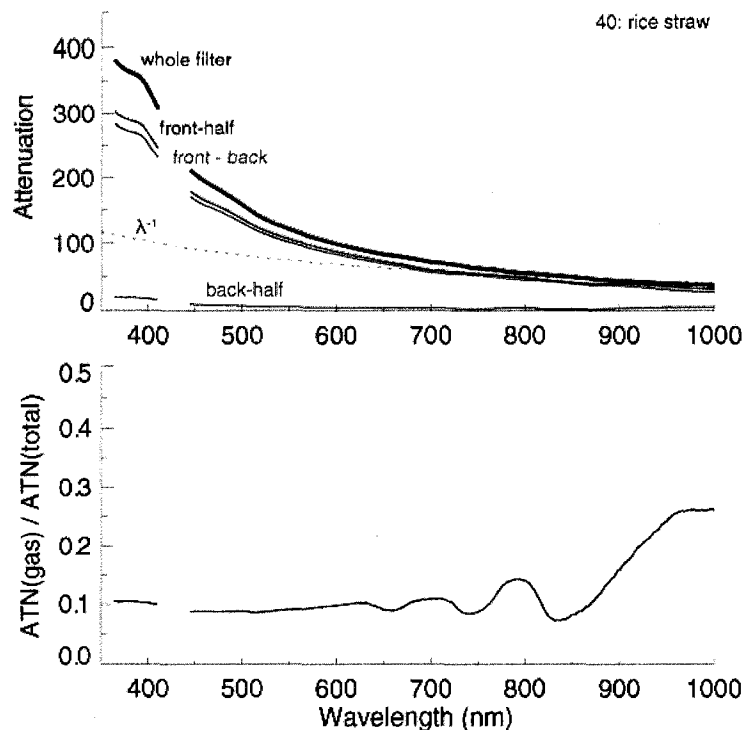


Figure 6.9 (top) Light attenuation measured as a function of wavelength on whole (thick black), front-half (thin black) and back-half (red) filter samples of burning rice straw emissions (burn 104, filter 40). The blue line gives the difference between ATN measured on the front- and back-filter halves, which an estimate of the ATN due to particles (see text for details). The dashed line shows the ATN predicted by a $1/\lambda$ dependence based on ATN measured at $\lambda = 880$ nm on the front-filter half. (bottom) Fraction of total ATN attributable to an estimate of ATN by gas-phase species plotted as a function of wavelength for the same sample shown in (a).

Figure 6.10 shows the front- and back-half filter ATN data plotted in a similar fashion to Figure 6.9, but for all eight front/back filter samples. The magnitude of ATN measured on back-filter halves relative to front-filter halves was similar to that observed for rice straw emissions for samples with high \dot{A}_{ATN} (ponderosa pine duff, Alaskan duff, Puerto Rican fern, and ceanothus). In these cases the back-half filter ATN was about a factor of 10 lower than ATN measured on the intact filter. The back-half filter contribution to ATN was also very small for chamise emissions, which had high ATN and low \dot{A}_{ATN} . The gas-phase contribution to ATN appeared to be significant for intermediate samples (ponderosa and lodgepole pine complexes), which had higher ATN at longer wavelengths than the high \dot{A}_{ATN} samples, but a stronger ATN-wavelength

dependence than the chamise emissions. The particle contribution to ATN estimated for ponderosa pine emissions was slightly less than those expected from the $1/\lambda$ relationship, indicating that gas-phase species were responsible for the increased ATN at shorter wavelengths for this sample. Unfortunately the spectrometer performance during the analysis of the front-half filter samples for this burn was questionable, as indicated by the strange drops in ATN in the $380 < \lambda < 400$ nm and $690 < \lambda < 720$ nm ranges of the spectra in Figure 6.10a. The particle-contribution to ATN is stronger for lodgepole pine emissions (Figure 6.10e), a sample analyzed when the spectrometer measurements were more reliable.

The ATN_g fraction of whole filter ATN is plotted in Figure 6.9b and indicated that for rice straw emissions, roughly 10% of ATN was due to gases, independent of wavelength. This value was in agreement with *Kirchstetter et al.* [2004], who measured the light attenuation of firewood smoke sampled by two quartz filters collected in series. They found that the impact of ATN_g on \dot{A}_{ATN} was too small, $< 10\%$, to explain differences observed between filter samples containing smoke and urban emissions. *Roden et al.* [2006] observed similar \dot{A}_{ATN} to those reported here for fresh wood smoke aerosol using a particle soot absorption photometer (PSAP), which is not affected by gaseous absorption.

6.5.2 Solvent-treatment results

Kirchstetter et al. [2004] treated filter samples collected over southern Africa during the Southern African Regional Science Initiative (SAFARI) with acetone to examine the contribution by OC to the spectral dependence of light attenuation. They used a TOA technique to show that acetone removed a large fraction of the OC, while leaving behind the

bulk of black carbon. The spectral dependence of attenuation also decreased following acetone treatment, so *Kirchstetter et al.* [2004] attributed the enhancement of ATN at shorter wavelengths in the SAFARI samples to acetone-soluble OC.

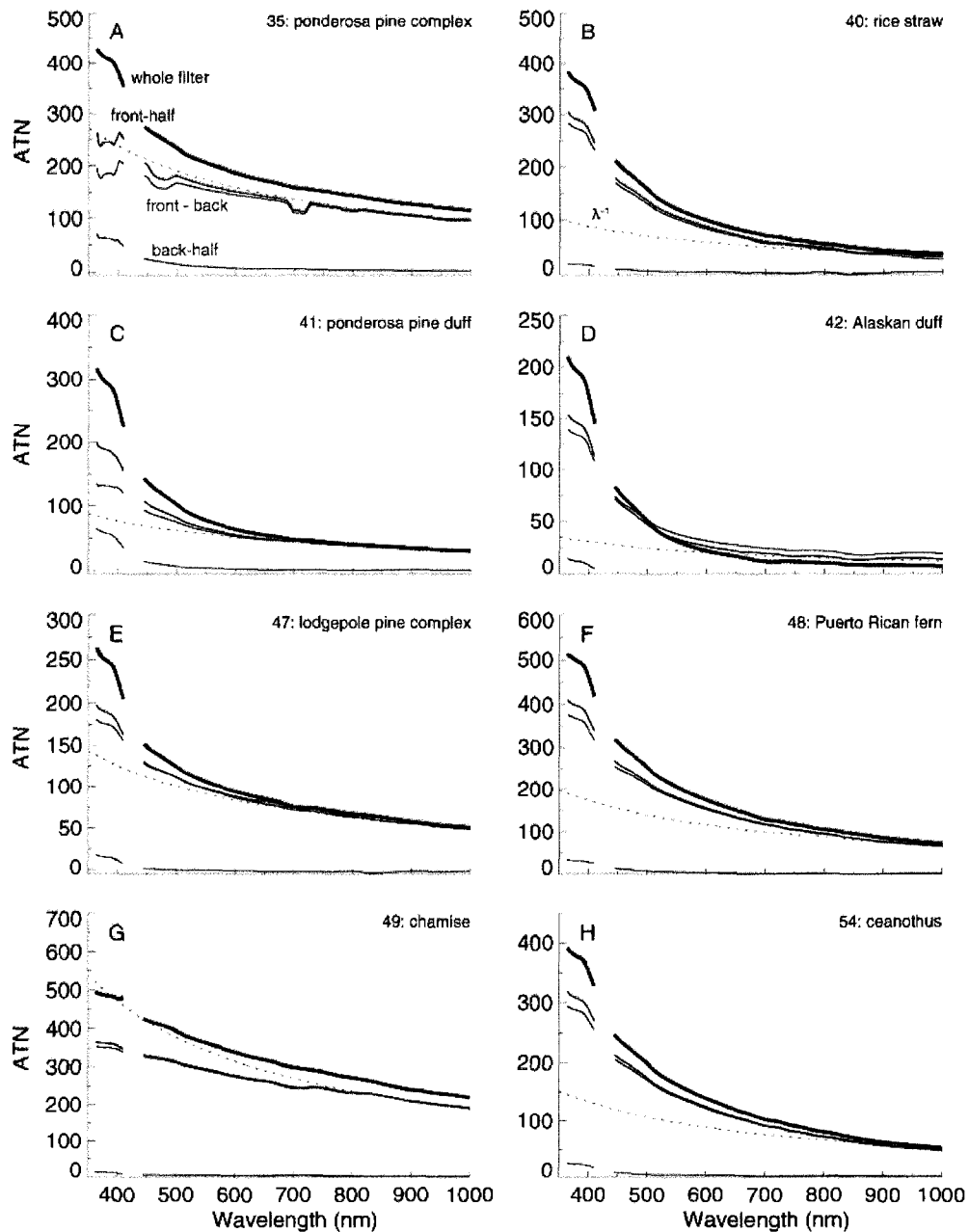


Figure 6.10 Attenuation (ATN) versus wavelength for whole filters (thick black line) and the front- (thin black line) and back-halves (red line) of filters for eight different fuels burned during FLAME. The difference between the front and back filter ATN measurements is shown by the blue line. The dashed line indicates the ATN expected from a $1/\lambda$ relationship extended from ATN measured on the front filter half at 880 nm.

I repeated the acetone treatment experiments *Kirchstetter et al.* [2004] carried out, but for FLAME samples and also tested two new solvents, hexane and DI water. Hexane is a non-polar organic solvent that I expected to remove other non-polar species from the sample, such as alkanes. Water is highly polar, and should have removed other polar compounds and inorganic salts from the samples. The organic compounds soluble in water are termed water-soluble organic carbon (WSOC). They include humic-like substances (HULIS), which are highly colored, polymeric materials that have been identified in biomass burning emissions [*Hoffer et al.*, 2006].

Figure 6.11 illustrates the effects of the different filter treatments on ATN for rice straw emissions. Treatment with hexane only caused a small reduction in ATN, about 5%, which was evenly spread over all wavelengths. Water treatment caused an approximately 20% reduction in ATN, but this was also independent of wavelength. Acetone treatment, however, resulted in a maximum ATN reduction from 50 to 70% at $\lambda = 400$ nm, but only caused a 10 to 20% reduction in ATN, similar to that observed for hexane and water treatments, at near-IR wavelengths. The ATN spectrum following acetone treatment was similar to that expected for BC based on the ATN measured for the untreated sample at $\lambda = 880$ nm, indicated by the dashed black line in Figure 6.11a. The reduction in ATN from acetone treatment was similar in magnitude to that resulting from hexane and water treatments above $\lambda \sim 700$ nm.

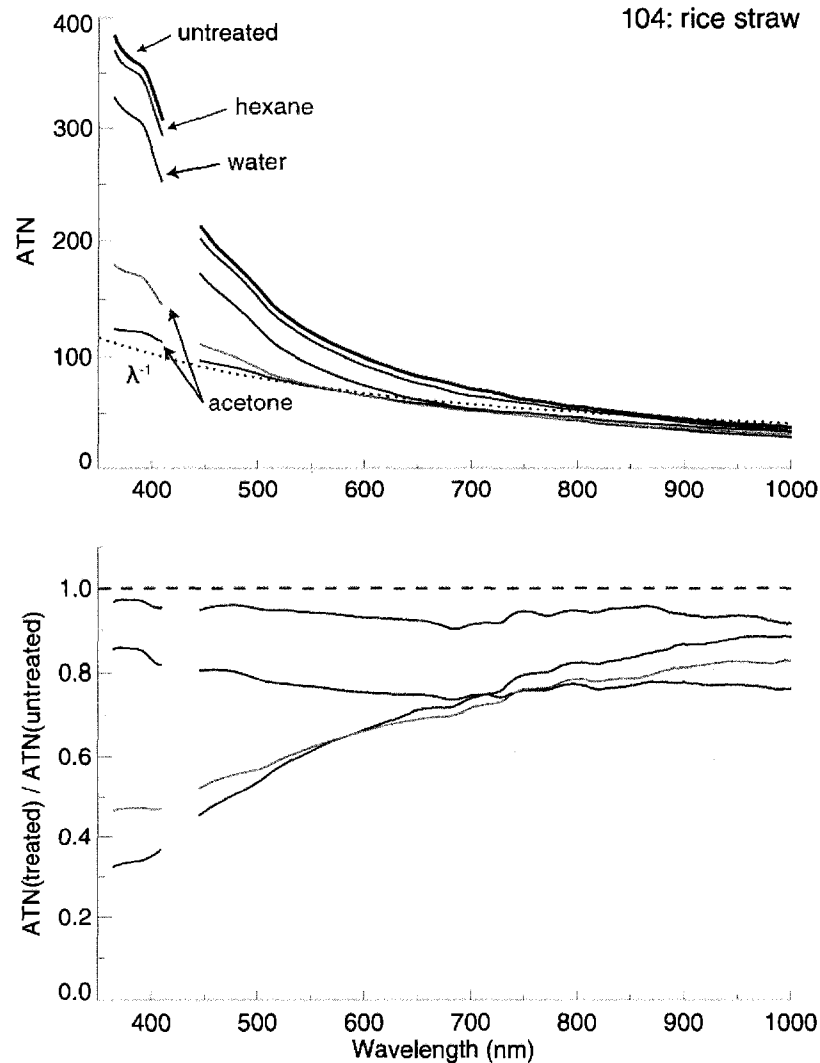


Figure 6.11 Attenuation (ATN) versus wavelength (a) for the untreated rice straw emissions sample (black line) and samples treated with acetone (red and orange lines), hexane (green line), and de-ionized water (blue line). The dashed line in (a) indicates ATN predicted from a $1/\lambda$ relationship from ATN measured at $\lambda = 880$ nm on the untreated sample. ATN normalized by the untreated ATN values is also plotted as a function of wavelength (b), with the same color scheme.

The results indicate that hexane and water treatments did not selectively remove material responsible for enhancements in ATN at shorter wavelengths for this sample, while acetone treatments did. *Kirchstetter et al.* [2004] showed that this material was OC using thermal optical analysis, as expected because BC is insoluble in acetone. A portion of the suspended particles were lost during these treatments, which is reflected by the uniform decrease in ATN over all wavelengths observed for the hexane and water treatments. The larger reduction in ATN

following water treatment compared to hexane probably resulted from the reduction of the filter/particle multiple scattering artifact caused by dissolution of inorganic salts and water-soluble organic carbon (WSOC) in the water [Arnott *et al.*, 2005a].

Acetone treatment caused a reduction in ATN at short wavelengths for five of the other six emission samples tested using the procedure: ponderosa pine (Figure 6.12a), Alaskan duff (Figure 6.12d), lodgepole pine (Figure 6.12e), Puerto Rican fern (Figure 6.12f), and ceanothus (Figure 6.12h). ATN following acetone treatment was within 10% of that expected for BC based on ATN measured at $\lambda = 880$ nm (indicated by the dashed line in each plot in Figure 6.12. The post-acetone ATN values did not drop as low as those expected for BC for Alaskan duff and ceanothus, but still decreased by 50 to 60%. I did not perform an acetone treatment for the ponderosa pine duff emissions (Figure 6.12c).

The ATN results for the chamise emission acetone treatment (Figure 6.12g) are puzzling. As opposed to the other seven samples, ATN increased following treatment. The increase was independent of wavelength, suggesting the higher ATN may be due to mechanical disturbance of the BC in the sample. For example, BC could have been re-suspended to deeper within the filter matrix, where the multiple-scattering effects could be greater. This was also the most heavily loaded of the filter samples I tested using the various solvent treatment techniques and was the most difficult to handle without causing disturbances.

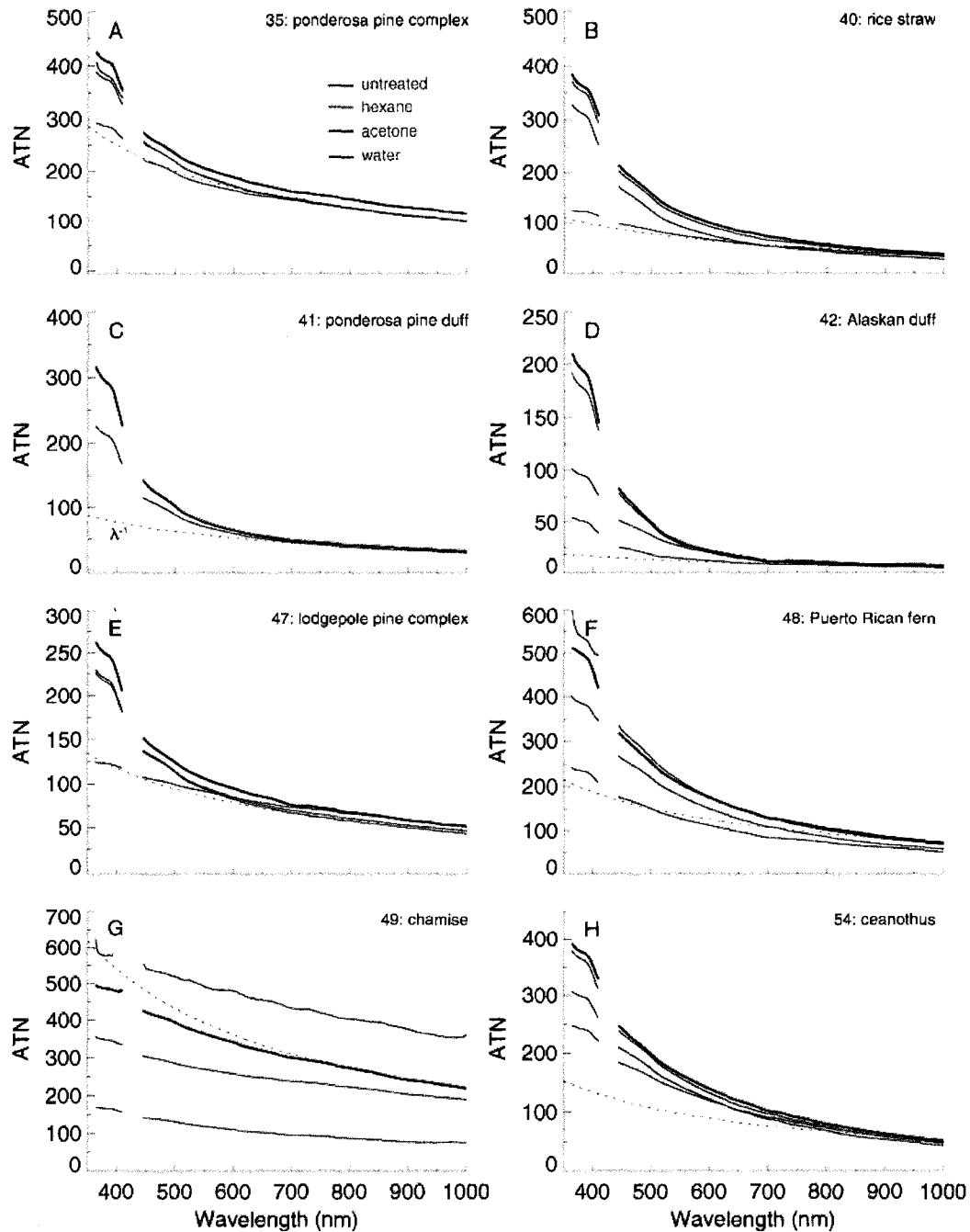


Figure 6.12 Attenuation (ATN) versus wavelength for untreated (black line) and filter samples treated with acetone (red line), hexane (green line) and de-ionized water (blue line). The dashed line indicates the ATN expected from a $1/\lambda$ relationship extended from ATN measured on the untreated filter at 880 nm.

The results of the water treatments were less consistent than observed for acetone treatments. Water treatment typically resulted in a reduction in ATN between 20 to 30% over all observed wavelengths, similar to the results for rice straw emissions discussed earlier. The

Alaskan duff emissions, and to a lesser degree the ponderosa pine duff emissions, displayed a much larger effect from water treatment. At $\lambda = 400$ nm, ATN decreased from ~200 to ~50 following water treatment for this sample. Unlike the other emissions samples, the ATN decrease for Alaskan duff following water treatment was a strong function of wavelength, though this was amplified by very low ATN at longer wavelengths for this sample. The ATN decrease following water treatment observed for the chamise samples was large, but independent of wavelength, indicating mechanical changes, rather than chemical changes, following the treatment were responsible for the decrease. The removal of water-soluble inorganic salts, which reduced the filter scattering artifact, was the likely culprit. As noted earlier, this sample was heavily loaded and prone to mechanical disturbances during handling. There was visible removal of black material from the filter during the treatment procedure, so an overall loss of aerosol from the filter bed during water-treatment also contributed to reduced ATN following treatment.

Hexane had a generally weak impact on ATN for all tested samples. It caused a small (5-10%) decrease in ATN that was independent of wavelength. The largest decrease occurred on the chamise sample, but as noted earlier this filter was prone to mechanical disturbance during treatment, and I have less confidence in these results. ATN on the Puerto Rican fern sample showed a small increase (5-10%) following hexane treatment.

Kirchstetter et al. [2004] found a similar decrease in ATN after extraction with acetone at shorter wavelengths to those presented here for savannah fire emissions sampled during SAFARI. They did not observe changes in the spectral dependence of wavelength for samples dominated by vehicle emissions or collected in an urban area (Berkeley, California). Based on

these findings, *Kirchstetter et al.* [2004] suggested two distinct aerosol components were responsible for light ATN: acetone-soluble OC and BC. The FLAME results confirm this hypothesis for other biomass burning fuels including several common to North America. The acetone-soluble OC fraction can be responsible for as much as half of the light ATN at wavelengths below 500 nm. Measurements of absorption at a single wavelength that are extrapolated to shorter wavelengths assuming a $1/\lambda$ dependence will greatly underestimate the true light absorption for samples with large OC fractions.

6.6 Comparison of FLAME results with field measurements

I compared ATN spectra measured on FLAME filters with those measured for filters collected in Houston, Texas in 2006 during TexAQS-GoMACCS and at Blodgett Forest Research Station (BFRS) in 2003. I also compared \dot{A}_{ATN} measured during FLAME with Aethalometer measurements of ATN at $\lambda = 370$ and 880 nm for aerosol sampled at Yosemite National Park and BFRS during 2002 [*McMeeking et al.*, 2006]. The Houston and BFRS filters were analyzed using the same procedure and spectrometer as the FLAME filter samples.

Two examples of ATN spectra observed for Houston filter samples collected during the day of 19 September 2006 and the night of 20 August 2006 are shown in Figure 6.13. The sample times were 10.5 and 11.17 hours, respectively. Both samples had a wavelength dependence of ATN near 1, that expected for BC, with no evidence of enhanced ATN at shorter wavelengths. ATN was larger at all wavelengths for the nighttime filter sample, which indicated a higher BC loading, assuming filter-based artifacts are the same for these samples. The higher BC concentrations at night were probably due to the lower height of the nocturnal boundary layer,

which trapped emissions near the surface. The boundary layer was higher during daytime, so emissions were diluted by a greater volume of air and surface concentrations were smaller.

I analyzed approximately 20 filter samples collected from various times during TexAQS – GoMACCS to determine if ATN or \hat{A}_{ATN} displayed significant variations with time. No filters from the period 25 August to 15 September were sent to LBNL, so I was unable to analyze any filters from this time period. I determined \hat{A}_{ATN} by performing a non-linear regression and determined $\text{ATN}(\lambda = 880)$ for each Houston sample; results are shown in Figure 6.13. The wavelength dependence of ATN was slightly weaker than the $1/\lambda$ relationship often assumed for BC, with the exception of one sample collected in mid-September. \hat{A}_{ATN} values ranged from 0.7 to 0.9 during August and mid-September and showed a slight increase ($\hat{A}_{\text{ATN}} \sim 1$) near the end of September (Figure 6.13a). Interestingly, there was some evidence of smoke transport from fires burning near Los Angeles, California to eastern Texas at this time [Brioude *et al.*, 2007].

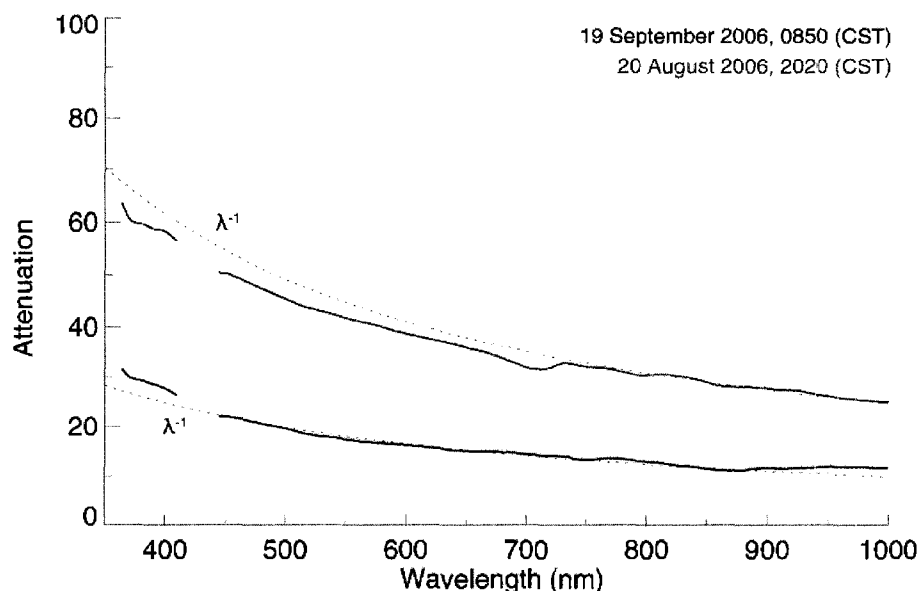


Figure 6.13 Attenuation (ATN) plotted as a function of wavelength for two filter samples collected in Houston, Texas on 19 September 2006 (black) and 20 August 2006 (red). The start times for each filter collection period are indicated. The dashed lines give ATN predicted from ATN at 880 nm with a $1/\lambda$ wavelength dependence.

The low \dot{A}_{ATN} observed over the duration of the study indicated that ATN in Houston during this period was dominated by BC, as could be expected for an urban aerosol dominated by vehicular emissions. *Kirchstetter et al.* [2004] reported similar values for particles sampled inside a highway tunnel in the San Francisco Bay Area. \dot{A}_{ATN} was not a strong function of $\text{ATN}(\lambda = 880 \text{ nm})$ during the study (Figure 6.14b), with similar values observed during relatively clean (24-26 August) and relatively polluted (21-23 August) periods of the study.

Aerosol samples collected on filters at BFRS did show slightly enhanced light ATN at

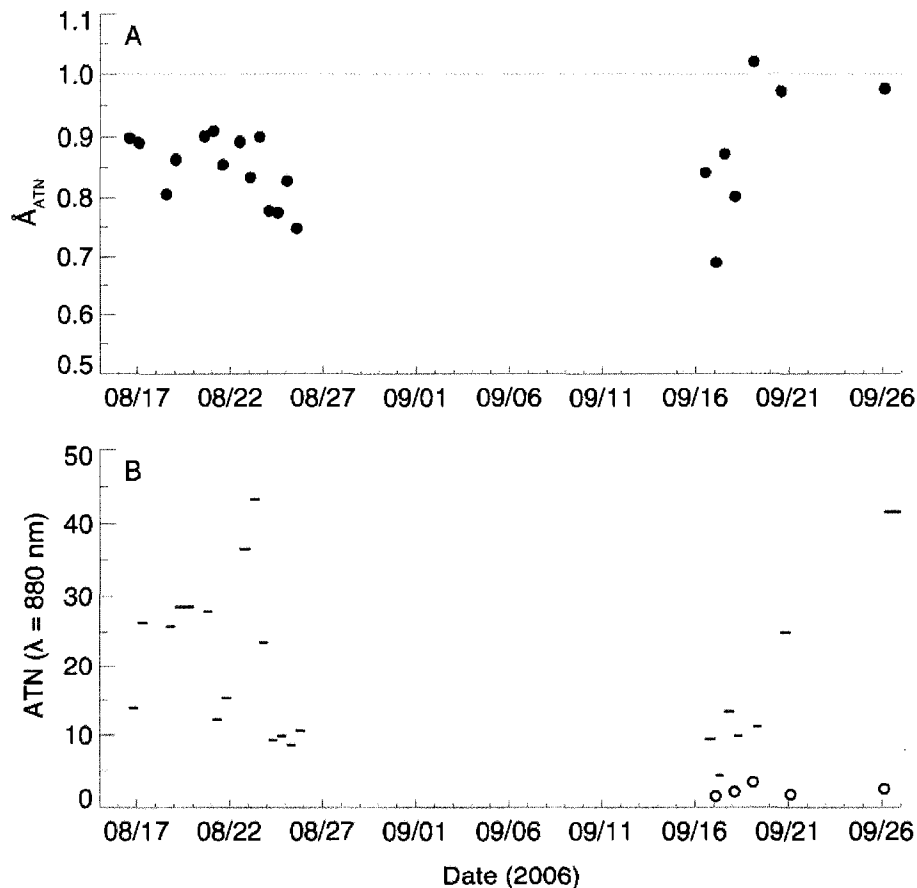


Figure 6.14 Ångström attenuation exponents (\dot{A}_{ATN}) determined by non-linear regression (a) and attenuation (ATN) measured at 880 nm versus time for filter samples collected during TexAQS – GoMACCS. The dashed line indicates $\dot{A}_{\text{ATN}} = 1$, the values expected for pure black carbon. ATN data are plotted as horizontal lines matching the start and end sample collection times. The two samples shown in Figure 6.13 are highlighted in red. The empty blue circles indicate ATN observed for field blanks collected during the study. Filter samples from the period 27 August to 15 September were not available.

shorter wavelengths. Figure 6.15 shows ATN versus wavelength for two filter samples collected at BFRS on 10 September and 16 October 2003. The September sample had a higher ATN below ~500 nm than that expected from a $1/\lambda$ relationship extended from the ATN measurement at 880 nm. For the October sample, the wavelength dependence was closer to the $1/\lambda$ relationship expected for BC, as observed in Houston (Figure 6.13) and other urban areas [Kirchstetter *et al.*, 2004]. The BFRS site is frequently impacted by pollution from the Sacramento area [Dillon *et al.*, 2002], smoke from wildfires and prescribed burns [McMeeking *et al.*, 2006], and SOA formed from anthropogenic and biogenic precursors [Lunden *et al.*, 2006]. The result is that carbonaceous aerosol sampled at BFRS at various times represent a wide range of carbonaceous aerosol types in the atmosphere.

For my M.S. work I examined aerosol properties observed at Yosemite National Park during the late-summer of 2002. Smoke-impacted and carbon-dominated aerosol were frequently observed at the site. When I later compared the Yosemite results to aerosol properties measured by Dr. Melissa Lunden during the same period at BFRS, we found evidence that both sites were impacted by similar aerosols. We concluded that wildfires burning in the west, particularly those in Oregon, were responsible for increased aerosol concentrations throughout California, Oregon and Washington [McMeeking *et al.*, 2006].

Part of the previous analysis compared BC measured with $2\text{-}\lambda$ Aethalometers at both sites. For this study, I reexamined the Aethalometer data to compare with FLAME observations by calculating \hat{A}_{ATN} from the raw ATN measurements at $\lambda = 370$ and 880 nm using Equation 4.2 (Figure 6.16). McMeeking *et al.* [2006] identified smoke-impacted periods in late-July and mid-August at both sites using carbonaceous aerosol measurements and back-trajectory calculations.

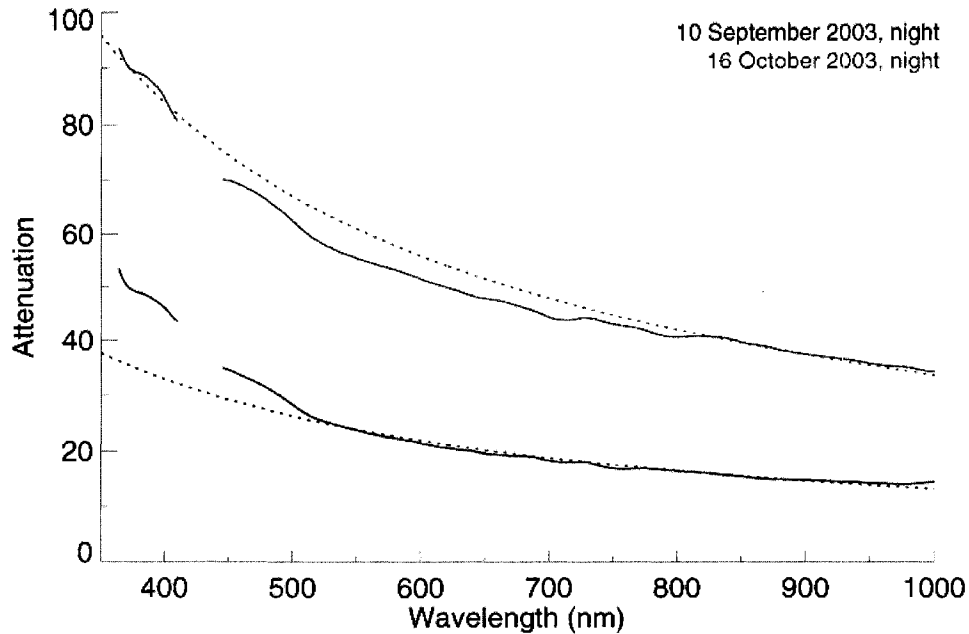


Figure 6.15 Attenuation plotted against wavelength for two filter samples collected at Blodgett Forest Research Station.

These times are associated with high \dot{A}_{ATN} compared to other periods. For example, \dot{A}_{ATN} at Yosemite NP was ~ 1.2 from 29 July to 5 August and varied between 1.2 and 2 from 5 to 31 August. \dot{A}_{ATN} values also increased at BFRS during these periods. These values agree with the majority of the \dot{A}_{ATN} values given in Figure 6.8 and those reported previously for biomass fuels [e.g., Kirchstetter *et al.*, 2004; Roden *et al.*, 2006; Schmid *et al.*, 2006]. There were relatively smoke-free periods at the beginning and end of the time series shown in Figure 6.16 when SOA and aged pollution from the San Joaquin Valley were probably the dominant source of carbonaceous aerosol—little fire activity was reported in the region—and $\dot{A}_{\text{ATN}} \sim 1$ during these periods.

The strong diurnal pattern evident in Figure 6.16 from 27 August to 5 September arose from the thermally driven mountain-valley wind pattern, which featured up-valley, or westerly, winds during the day and down-valley, or easterly, winds at night. Several small fires were

burning in the park during this time, so the high \dot{A}_{ATN} at night reflected the transport of smoke past the observation site, which was located on the western edge of the park. During the day, air from the polluted San Joaquin Valley was transported to the park, and \dot{A}_{ATN} decreased to values near unity. The \dot{A}_{ATN} values near two are similar to those found for many of the FLAME fuels, including several found at Yosemite NP, even though the smoke measured at Yosemite was 2-3 days old [McMeeking *et al.*, 2006].

Attenuation Ångström exponents during FLAME displayed a wider range, from about 0.7 to 5.0, compared to those observed in the field at an urban site (Houston) and two rural sites (BFRS and Yosemite NP). The wavelength dependence of ATN in Houston during late-

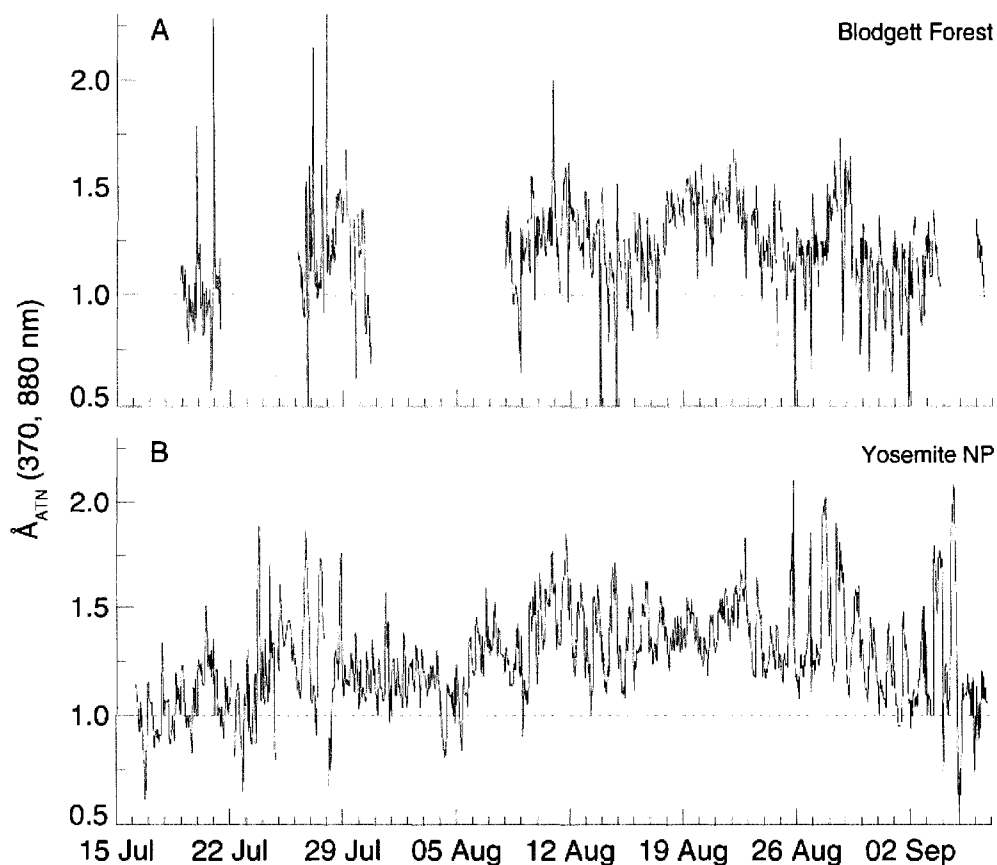


Figure 6.16 Aethalometer measured \dot{A}_{ATN} ($\lambda = 370, 880 \text{ nm}$) observed at Blodgett Forest Research Station (a) and Yosemite National Park (b) in 2002. The dashed line indicates $\dot{A}_{\text{ATN}} = 1$, equivalent to a $1/\lambda$ dependence of ATN.

summer was almost always less than unity, indicating that BC was the dominant source of light absorption during this time. Similar values were observed at BFRS and Yosemite NP when the sites were not impacted by biomass burning, but \dot{A}_{ATN} values approached 2.0 when smoke-impacted aerosol was present. This suggests that SOA from biogenic and anthropogenic sources, which probably dominated the carbonaceous aerosol budget at these locations during 'clean' periods, were not significant contributors to light absorption. Increases in \dot{A}_{ATN} were closely linked to the transport of smoke-impacted aerosol from other regions, particularly the northwestern U.S., or periods of significant fire activity near the sites. The transport time from the most likely smoke source regions in Oregon and Washington during some periods with higher \dot{A}_{ATN} was on the order of 1-3 days [McMeeking *et al.*, 2006]. This suggests the optical properties of aged smoke, from an \dot{A}_{ATN} perspective, are similar to those observed for the fresh biomass burning emissions collected during FLAME.

6.7 Comparisons with photoacoustic spectrometer measurements during FLAME

The bulk of light attenuation measured by filter-based transmission techniques is primarily due to light absorption [Rosen and Novakov, 1983], but several factors must be accounted for in order to convert ATN coefficients into aerosol absorption coefficients (b_{ap}). Filter-based ATN measurements exaggerate aerosol light absorption because embedded particles absorb light scattered by the highly reflective quartz fibers in the filter matrix in addition to absorbing light emitted directly from the source. Comparisons involving Aethalometer measurements (a filter-based technique) and other absorption measurement methods (e.g., extinction cells, photoacoustic spectrometers) suggest the filter-related

enhancement is on the order of two [Bond *et al.*, 1999a; Weingartner *et al.*, 2003]. Non-absorbing particles embedded in the filter may also enhance light absorption by increasing light scattering, but this effect is less clear. While Lindberg *et al.* [1999], Horvath *et al.* [1997], Bond *et al.* [1999a], and Arnott *et al.* [2005] have shown enhanced absorption in low-BC content aerosol samples, Weingartner *et al.* [2003] found that this enhancement did not extend beyond the factor of ~2 already accounted for by the filter fiber effect, at least for the case of the Aethalometer.

Subramanian *et al.* [2007] hypothesized that liquid aerosol particles deform during collection and take on a different geometry that more efficiently absorbs light compared to its original, spherical shape, and therefore enhances light absorption. Organic vapors can condense on filter fibers and absorb light, though this effect can be examined through measurements on backup filters. Magnitudes of the artifacts listed above partially depend on amount and composition of material loaded on the filter, which complicates correction efforts. Arnott *et al.* [2005] and Weingartner *et al.* [2003] noted that Aethalometer measurements overestimated the light absorption (and BC) when particle mass loadings were relatively low.

Several studies have compared PAS absorption measurements to ATN measured using the 2- λ and 7- λ Aethalometers to develop procedures for converting filter-based b_{ATN} to b_a [Arnott *et al.*, 2005a; Schmid *et al.*, 2006; Weingartner *et al.*, 2003]. Weingartner *et al.* [2003], referred to as W2003, suggested that b_{aeth} , the ‘true’ absorption coefficient measured by the Aethalometer, could be given by:

$$b_{\text{aeth}} = \frac{b_{\text{ATN}}}{C R(\text{ATN})} \quad 6.8$$

where C is the correction factor that accounts for the increase in the optical path from multiple

light scattering by filter fibers and $R(ATN)$ describes the reduction in the optical path due to light ATN by embedded particles, often called the ‘shadowing’ effect. The loading factor can be expressed as [Arnett *et al.*, 2005a]:

$$R(ATN) = \left(\frac{1}{f} - 1\right) \frac{\ln ATN - \ln 10}{\ln 50 - \ln 10} + 1 \quad 6.9$$

where f is the shadowing factor that depends on the type of aerosol sampled. For $f > 1$, then $R(ATN) < 1$, so the addition of aerosol to the filter reduces the multiple scattering of light within the filter matrix.

W2003 found that C was not affected by light scattered by sampled particles. This is in contrast to Arnett *et al.* [2005], referred to as A2005, who found that embedded particles did affect C . Schmid *et al.* [2006] introduce C^* , based on the work of A2005, which includes the particle effect on C :

$$C^* = \frac{C(b_{ATN} - m_s b_{sp})}{b_{ATN}} \quad 6.10$$

where m_s is the fraction of light scattered by particles erroneously reported as absorption and b_{sp} is the light scattering coefficient. Substituting the single scattering albedo for b_{sp} and neglecting the loading factor, $R(ATN)$, yields [Schmid *et al.*, 2006]:

$$C^* \approx C \left[1 - \frac{m_s \omega_0}{C(1 - \omega_0)} \right] \quad 6.11$$

The aerosol scattering effect on the optical path length in the filter is large when the sampled particles have high single scattering albedo and the filter-matrix effect (C) is small.

The preceding discussions illustrate that the magnitude of the correction applied to filter-based absorption measurements depends on the filter properties (C) and the properties of

the sampled aerosol (ω_0 and f). Schmid *et al.* [2006] used Equations 6.8-6.11 and PAS measurements of b_a and nephelometer measurements of b_s to determine $C^* \sim 5$ and $f \sim 1.2$ for smoke-impacted aerosol sampled in Brazil, but these values are unique to their samples and the instrument they used. The correction factors were designed for aethalometer measurements. Though this measurement is similar to spectrometer measurements I performed, differences between the structure of the high volume filters and the quartz filter tape in the aethalometer, and differences in the light sources used by either technique, will cause differences in the magnitude of C . The correction procedure determines the magnitude of C by examining ATN measurements when the filter loading is low ($ATN < 10$) so that the shadowing parameter can be neglected. These periods occur just after every filter-tape advances to a new filter spot during aethalometer measurements, but no FLAME samples had low enough sample loading to achieve something similar. The time-integrated filter samples I analyzed do not allow for time-resolved ATN measurements, so determining C in this fashion is not possible.

Figure 6.17 presents \hat{A}_{ATN} and \hat{A}_a determined from ATN and b_a measured at two different pairs of wavelengths (405 and 870 nm; 532 and 870 nm) using Equation 4.2. PAS-based \hat{A}_a (405, 870 nm) was usually higher than filter-based \hat{A}_{ATN} (405, 870 nm), by about 0.3, meaning the wavelength-dependence of ATN is weaker than the wavelength dependence of absorption. This relationship is less clear from the comparison between \hat{A}_{ATN} and \hat{A}_a determined from measurements at 532 and 870 nm. The offset between the techniques is still about 0.3 for some samples, but in other cases there is good agreement between the \hat{A} values. The filter-based method also returns a higher \hat{A}_{ATN} than the PAS for the most strongly-wavelength dependent sample. The low bias for \hat{A}_{ATN} suggests that ATN overestimates absorption at longer

wavelengths and/or underestimates it at shorter wavelengths, resulting in a reduced wavelength dependence of ATN compared to absorption.

Schmid et al. [2006] examined the spectral dependence of C^* (filter scattering) and $R(\text{ATN})$ on wavelength. They found that C^* increased with wavelength depending on ω_0 , \hat{A}_s (the scattering Ångström exponent) and \hat{A}_a while $R(\text{ATN})$ decreased with wavelength because ATN decreased with wavelength. The smoke-impacted aerosol examined by *Schmid et al.* [2006] featured a mean $\omega_0 = 0.92$ and \hat{A}_s , for which they found C^* increased or decreased from its reference value at $\lambda = 521$ nm by $\pm 25\%$. *Schmid et al.* [2006] do not explicitly report the wavelength sensitivity for $R(\text{ATN})$, but I calculated $R(\text{ATN})$ for their reported f of 1.2 using

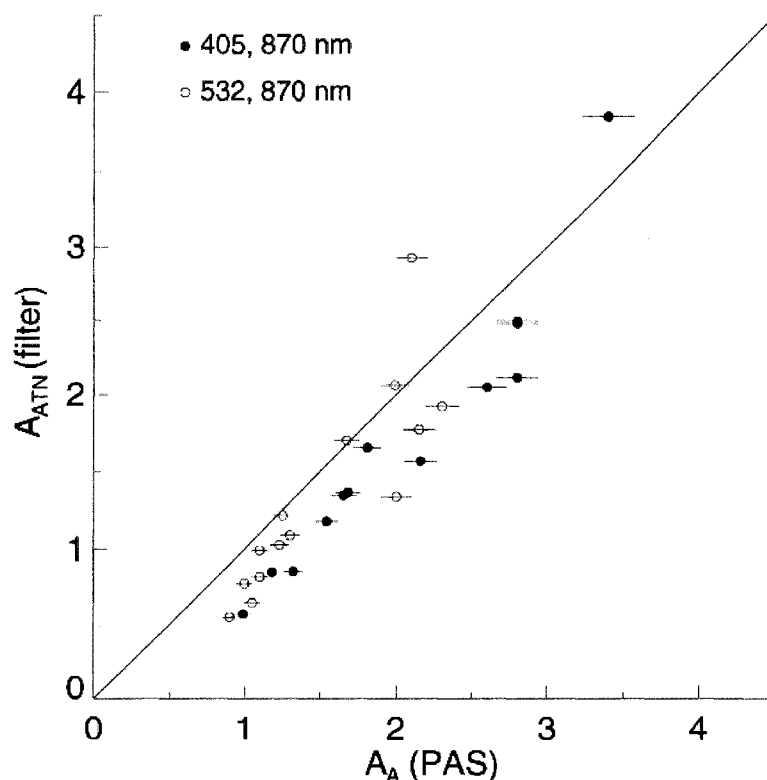


Figure 6.17 Ångström exponents from attenuation measured on filters (\hat{A}_{ATN}) and absorption measured *in situ* using photoacoustic spectrometers (\hat{A}_A). Exponents were calculated using Equation 4.2 for ATN/absorption measured at wavelengths of 405 and 870 nm (filled circles) and 532 and 870 nm (hollow circles). Error bars represent $\pm 5\%$ uncertainty, reported by *Lewis et al.* [in press]. The 1:1 line is also indicated.

Equation 6.9 (Figure 6.18), assuming it could be extrapolated to ATN values greater than those observed by the Aethalometer (the filter spot changes when $ATN > 75$). The filter shading correction is large ($>20\%$) for ATN values larger than ~ 100 , and the corrected ATN is nearly double the uncorrected value at $ATN = 1000$. The optical path length is substantially reduced due to the high particle loading in the filter at high ATN. The large value of C^* (~ 5), however, indicates that the filter-scattering effect was more important for the aerosol sampled by *Schmid et al.* [2006], even at these high ATN values. If the filter-scattering factor reported by A2005 and W2003 is used then C^* and $R(ATN)$ are equally important at high ATN. FLAME filter samples frequently had ATN values > 100 over all wavelengths, suggesting the shadowing factor is probably significant for these samples.

If the Aethalometer corrections developed by W2003, A2005 and *Schmid et al.* [2006] are valid for the filter method presented here, then I can make several qualitative statements about the potential impacts of the filter artifacts on the results presented in this chapter. First, if the value of C^* is ~ 5 , then the filter-scattering correction factor dominates $R(ATN)$, especially at low ATN values. Since C^* increases with wavelength, ATN corrected for filter-scattering at large λ is proportionally *lower* than the corrected ATN at small λ . This has the net effect of increasing the wavelength dependence of the corrected ATN values compared to the uncorrected values. If C^* is small relative to $R(ATN)$, the correction is also larger at shorter wavelengths (where ATN is higher) compared to at lower wavelengths (where ATN is lower). It has the net effect of increasing the wavelength dependence of ATN. For example, *Schmid et al.* [2006] used an iterative procedure to correct their Aethalometer-based measurement of \hat{A}_{ATN} with spectrally dependent values of C^* and $R(ATN)$ and found that an \hat{A}_{ATN} of ~ 1.5 increased to ~ 1.95

following this correction. The higher values of \dot{A}_A compared to \dot{A}_{ATN} shown in Figure 6.17 can also be explained by this reasoning. Differences in the magnitudes of f , C^* , ω_0 , \dot{A}_s and \dot{A}_a , which in turn determine the importance of the $R(ATN)$ and C^* terms in the filter corrections, are responsible for the variability in the relationship.

Another interesting relationship shown in Figure 6.17 is that between Ångström exponents calculated for different wavelength pairs, i.e., 405 and 870 nm versus 532 and 870 nm. The filter and PAS data both give a higher \dot{A} when it is calculated from 405 and 870 nm measurements versus 532 and 870 nm measurements. *Lewis et al.* [in press] attributed the difference to increased wavelength dependence at shorter wavelengths. This hypothesis agrees with the deviations from the power-law fit discussed in Section 6.3 and illustrated in Figure 6.5, both of which show an increased wavelength dependence at shorter wavelengths for samples with a strong spectral dependence of ATN, e.g., Alaskan duff emissions.

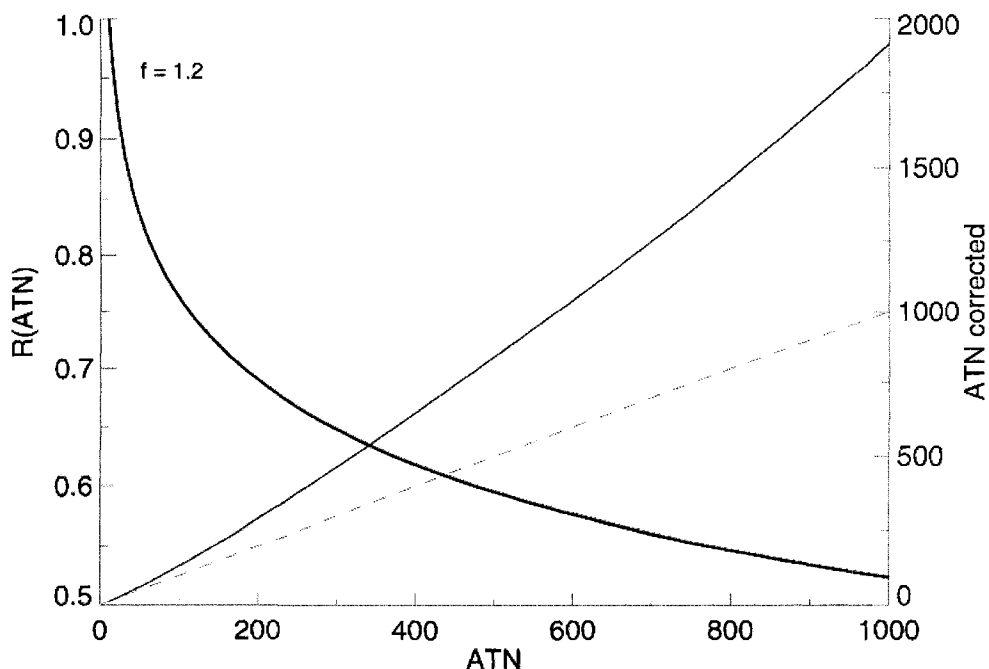


Figure 6.18 Values of the particle loading factor ($R(ATN)$) for correcting Aethalometer ATN coefficients to absorption coefficients, assuming a 'shading factor', $f = 1.2$ as a function of ATN (black line). Corrected ATN is shown in red on the right axis, assuming the filter scattering correction factor (C^*) is equal to one. The dashed red line indicates the values where $ATN = ATN_{corrected}$, i.e. $R(ATN) = 1$.

Figure 6.19 compares Ångström exponents calculated with ATN data from several wavelength pairs using Equation 4.2. The exponents calculated at $\lambda = 405$ and 870 nm (PAS) were not statistically different from those calculated at $\lambda = 370$ and 880 nm ($2-\lambda$ Aethalometer), meaning \hat{A}_{ATN} was not strongly sensitive to small changes in λ . A similar relationship was observed for \hat{A}_{ATN} calculated at $\lambda = 450$ and 700 nm and at the photoacoustic wavelengths $\lambda = 405$ and 870 nm (Figure 6.19c). Picking wavelengths from different regions of the spectrum, however, results in large differences in \hat{A}_{ATN} , as shown in Figure 6.19b. Exponents calculated in the green to near-UV region of the spectrum were much higher than those calculated in the red and near-IR region of the spectrum, reflecting the deviations from the power-law fit at shorter wavelengths discussed previously. The spectral dependence calculated from 532 and 870 nm was about 70% of that calculated at 405 and 870 nm for measurements of ATN and absorption,

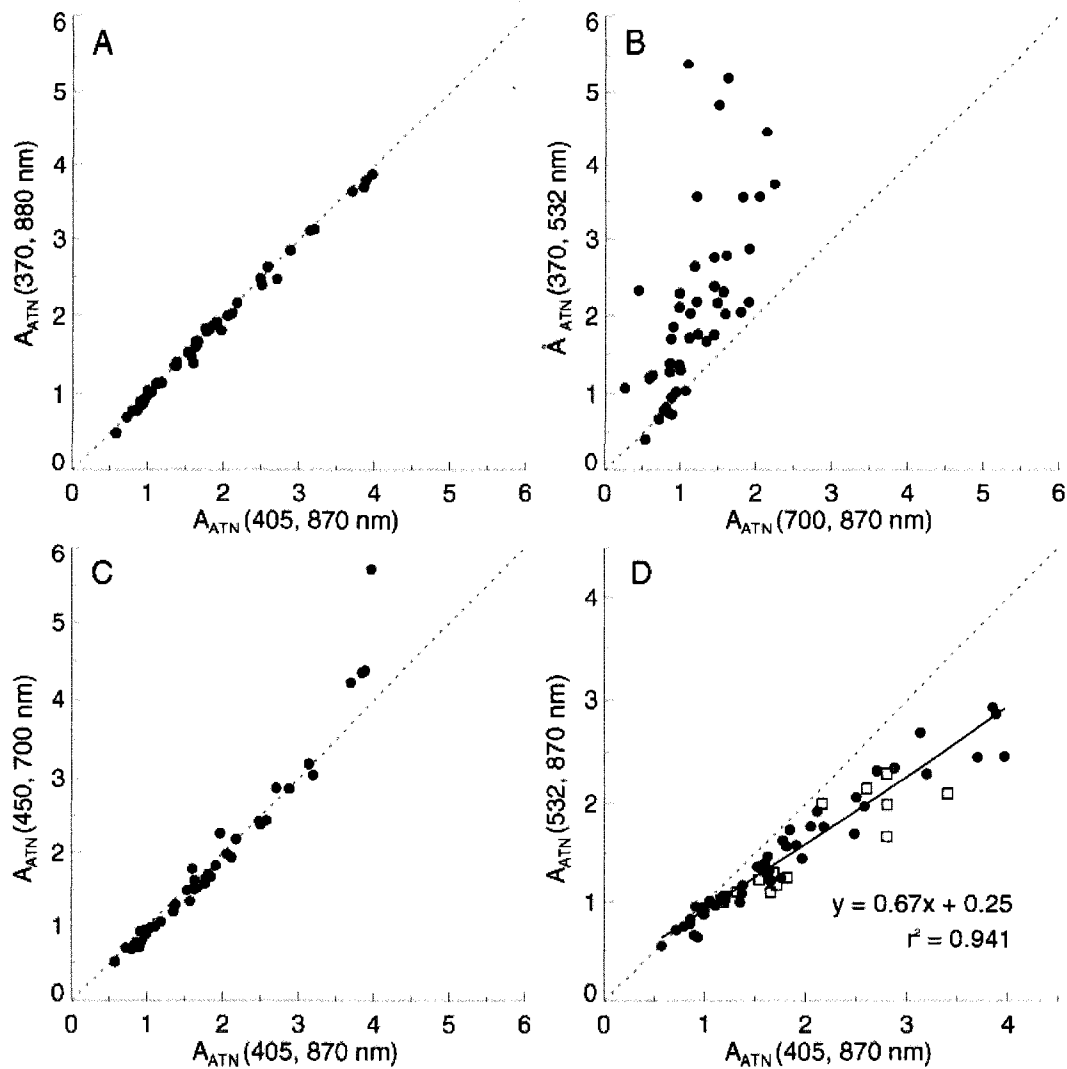


Figure 6.19 Scatter plots comparing attenuation (ATN) Angström exponents (\hat{A}_{ATN}) calculated from measured ATN on untreated FLAME bulk filter samples using Equation 4.2 at the wavelength pairs indicated in the axis labels. The wavelength pairs correspond to the measurement wavelengths of: a) photoacoustic spectrometer and 2- λ Aethalometer, b) short and long wavelength regions of the spectrum, c) photoacoustic and TSI integrating nephelometer, and d) two sets of photoacoustic measurements. Absorption Angström exponents determined from photoacoustic measurements (as opposed to ATN at the same wavelengths) are also shown in d) as red squares. The 1:1 relationships are indicated by a dashed lines.

as shown in Figure 6.19d. These findings agree with previous work that has found a stronger spectral dependence of attenuation for λ below ~ 600 nm [Kirchstetter *et al.*, 2004; Sandradewi *et al.*, 2008].

The differences between \hat{A}_{ATN} determined from the regression and discrete-wavelength

methods have important implications for how light absorption measurements are interpreted. The Aethalometer and photoacoustic instruments measure light attenuation or absorption at discrete wavelengths, e.g., 370, 405, 532, 870 and 880 nm. If these measurements are used to calculate \dot{A}_{ATN} following Equation 4.2, the predicted absorption or attenuation will be over- or underestimated compared to the true absorption or attenuation at other wavelengths depending on the portion of the spectrum that is of interest.

6.8 Summary

Aerosol emitted by biomass burning combustion during FLAME had wavelength dependences of absorption that varied between the extremes in previously observed values. I quantified the strength of the absorption/attenuation dependence using the Ångström exponent. Emissions from some fuels had weakly wavelength dependent spectra, similar to those found in urban and vehicle-dominated regions, such as Houston, Texas. Others had a much stronger wavelength dependence, with \dot{A}_{ATN} approaching 5.0. I showed that the method used to calculate \dot{A}_{ATN} had a large impact on the estimated wavelength dependences, with higher \dot{A}_{ATN} values obtained at shorter wavelengths. Non-linear regression was able to find a better fit to most continuous spectra because it weighted higher ATN measurements appropriately.

I showed that gas-phase adsorption artifacts likely played a limited role in determining the wavelength dependence of attenuation for the FLAME samples by comparing spectra measured for front- and back-halves of filter samples. Treating the filter samples with acetone to remove OC resulted in wavelength dependences of attenuation closer or approximately equal to those expected for pure EC ($\dot{A}_{\text{ATN}} \sim 1.0$). Treatment with hexane had no effect on the spectra,

but treatment with DI water resulted in a reduction of the wavelength dependence for one sample, Alaskan duff emissions.

The majority of \dot{A}_{ATN} values observed for FLAME samples were between 1–2, matching observations from fire-impacted sites in California during a severe fire season in the western United States (Blodgett Forest and Yosemite National Park). Most of the samples were also similar in magnitude to \dot{A}_{ATN} measured in a mountain valley at night in the winter, when the contribution by wood smoke to the ambient aerosol was expected to be high [Sandradewi *et al.*, 2008]. Samples collected in Houston, Texas (an urban site) and at Blodgett Forest during a period with little evidence of fire activity had \dot{A}_{ATN} near that found for other urban regions and for motor-vehicle dominated emissions previously [Kirchstetter *et al.*, 2004].

I compared filter-based measurements to photoacoustic spectrometer measurements of absorption at 405, 532, and 870 nm to assess the impact of filter-based artifacts on calculations of \dot{A}_{ATN} . I observed a constant offset of ~ 0.15 , with filter-measurements generally lower than PAS measurements. Filter-based and PAS-based estimates of \dot{A}_{ATN} and \dot{A}_{A} were highly correlated with no apparent bias other than this offset, indicating that the filter-based artifact was not a strong function of the value of \dot{A}_{A} itself. As a result, relative differences in \dot{A}_{ATN} between different burns were similar to those observed in \dot{A}_{A} .

Chapter 7 Linking aerosol optical properties, composition and fire combustion behavior

Kirchstetter et al. [2004] proposed that the absorption spectra of aerosols could be separated into BC and OC components. Assuming the BC spectral properties are constant and well known, spectra for mixed aerosol can be used to determine biomass burning-emitted OC light absorption properties as a function of wavelength. This enables the assessment of the role of LAOC on atmospheric radiative processes [*Andreae and Gelencser, 2006*]. *Andreae and Gelencser* [2006] state that the two component approach should be validated with a larger data set. *Kirchstetter et al.* [2004] stressed the need to determine the variability in spectral absorption for different aerosol types, "...especially as a function of combustion efficiency." The FLAME data set provides an excellent opportunity to examine the magnitude and variability of biomass burning-emitted OC spectral absorption for a wide range of combustion conditions and fuel species.

In this chapter, I examine the relationships between the spectral absorption/attenuation properties described in Chapter 6 with the aerosol composition data and other aerosol property measurements reported in Chapter 4. I show that a two-component model featuring strongly absorbing EC with a weak spectral dependence of absorption and weakly absorbing OC with a strong spectral dependence of absorption explains the bulk aerosol attenuation spectra. I recommend mass-normalized absorption/attenuation efficiencies for OC emitted by biomass burning at multiple-wavelengths for use in radiative transfer models and satellite retrievals.

Finally, I briefly discuss a possible theoretical basis for the spectral behavior of carbonaceous aerosols introduced by [Bond, 2001] and [Sun *et al.*, 2007].

7.1 Angstrom exponent and aerosol composition

Treating filters by extracting material with acetone, and in a few cases water, reduced the Angstrom attenuation exponent ($\mathring{A}_{\text{ATN}}$) to near that expected for BC. This finding agreed with the observations of *Kirchstetter et al.* [2004], who attributed the decrease in $\mathring{A}_{\text{ATN}}$ to the removal of light absorbing OC by acetone. They concluded that OC was responsible for enhanced light absorption at shorter wavelengths and led to a higher $\mathring{A}_{\text{ATN}}$ than that expected for BC. To confirm this, I compared $\mathring{A}_{\text{ATN}}$ measured on the filter samples to EC/TC ratios for aerosol sampled on the same filter. Figure 7.1 compares $\mathring{A}_{\text{ATN}}$ to EC/TC measured on the Hi-Vol filters using the modified NIOSH 5040/Sunset analyzer TOA protocol. The EC-dominated samples (high EC/TC ratios) had a weak spectral dependence, with $\mathring{A}_{\text{ATN}} \sim 1$, matching that expected for pure BC. As I discussed in Chapter 1, BC is not equivalent to EC [Andreae and Gelencser, 2006; Bond and Bergstrom, 2006]. Black carbon has an unclear definition, and is conventionally assumed to share optical properties and composition similar to soot carbon [Andreae and Gelencser, 2006]. BC is associated with filter-based optical measurements, which assume a constant absorption per unit mass value [Bond and Bergstrom, 2006]. Elemental carbon refers to the fraction of carbon oxidized above a certain, operationally-defined temperature threshold in an oxidizing atmosphere that has been corrected for charred organic species formed during the analysis. Even though the composition and optical properties of EC and BC are not necessarily identical, Figure 7.1 indicates that they have similar, weak spectral dependences of attenuation,

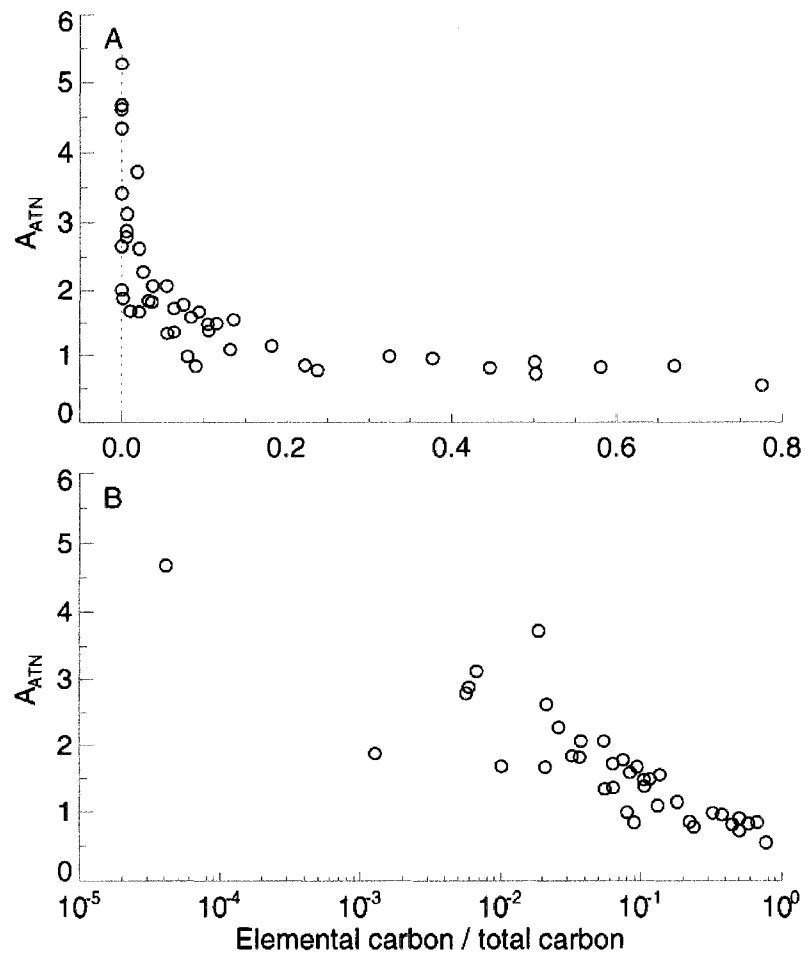


Figure 7.1 Angstrom attenuation exponents (A_{ATN}) for bulk FLAME samples versus elemental-to-total carbon (EC/TC) ratios (measured using the NIOSH 5040/Sunset analyzer protocol) on a) normal coordinates and b) semi-log coordinates. The dashed line in a) indicates an EC/TC ratio of zero, i.e., no EC above detection limits.

at least for biomass burning aerosol.

Figure 7.1 shows that A_{ATN} increased as the EC fraction of TC decreased or the OC fraction of TC increased, confirming that OC was responsible for the enhanced light attenuation at shorter wavelengths. A_{ATN} for samples with EC/TC ratios above 0.2 was ~ 1 , but for samples with no detectable EC it ranged from 2–5.5. The relationship between EC/TC ratios and A_{ATN} plotted in regular and semi-log coordinates (Figure 7.1b) indicated a consistent relationship between the contributions of OC and EC to TC and the strength of the spectral dependence, quantified through A_{ATN} .

The strength of the spectral dependence of attenuation was not related to the inorganic fraction because compounds composed of the major aerosol inorganic species emitted during FLAME (e.g., K^+ , Cl^-) do not absorb a significant amount of light at visible wavelengths. Mineral dust can have a strong spectral dependence of light absorption and absorb visible light [Foot and Kilsby, 1989], but I expect very little mineral dust in the samples because they were collected in a laboratory setting. Even if mineral dust was present in the background chamber air and was sampled on the filters, it cannot be responsible for the spectral dependence of light attenuation I observed. It would remain on the filter after heating and appear to be part of the background filter attenuation signal used to calculate the filter transmission and attenuation (see Chapter 6 for details). The attenuation measured on the FLAME samples was only due to material that evolved from the filter at temperatures below 650 °C [Kirchstetter *et al.*, 2004].

Chapter 5 discussed differences in EC/TC measured using two different TOA protocols, the IMPROVE_A protocol, which used light reflectance to correct for POC, and a modified NIOSH 5040/Sunset analyzer protocol, which used light transmittance to correct for POC. I found EC/TC ratios could differ by more than a factor of two for samples dominated by OC, so the relationship between the bulk aerosol A_{ATN} and EC/TC ratio depends on the choice of TOA protocol. Figure 7.2 shows A_{ATN} as a function of EC/TC ratio in the same manner as Figure 7.1, but for EC/TC ratios measured on the IMPROVE $PM_{2.5}$ filters by the IMPROVE_A protocol. The pattern of higher A_{ATN} with lower EC/TC was the same as observed for the modified NIOSH/Sunset EC/TC ratios, but because the IMPROVE_A protocol measured more EC on the OC-dominated filters, A_{ATN} was higher at larger IMPROVE_A EC/TC ratios compared to the Sunset EC/TC ratios. A_{ATN} increased from ~1 at IMPROVE EC/TC ratios of

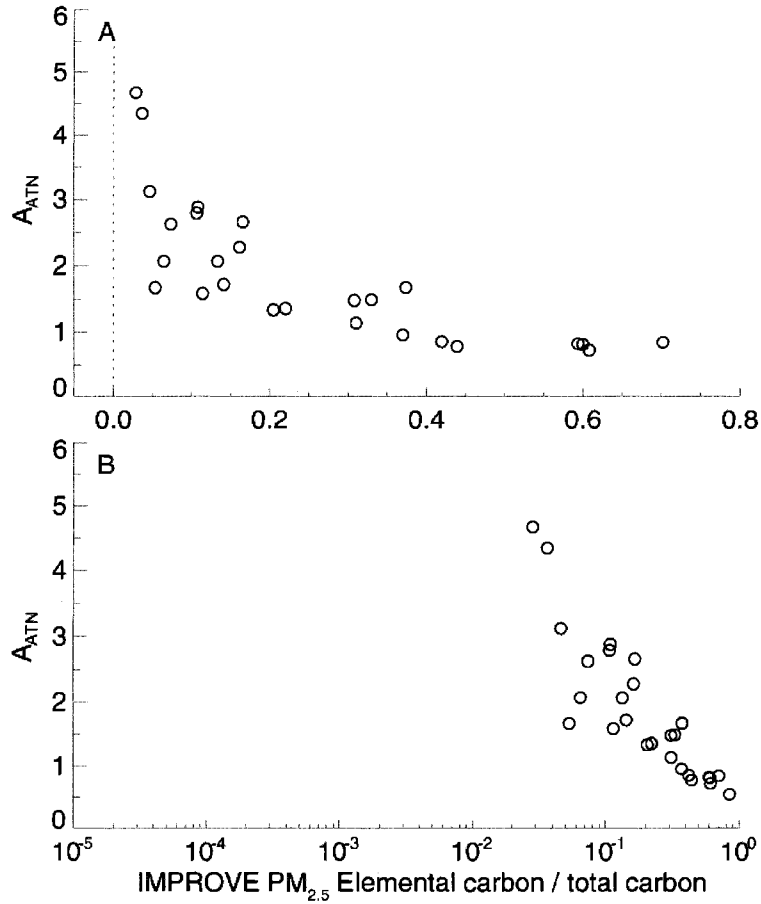


Figure 7.2 Elemental-to-total carbon (EC/TC) ratios measured on IMPROVE PM_{2.5} filters using the IMPROVE_A thermal optical analysis protocol versus Angstrom attenuation exponent (A_{ATN}). Data are plotted on the same axes as Figure 7.2.

0.4 compared to 0.2 for the Sunset EC/TC ratios.

7.2 A simple, two-component model of Angstrom exponent behavior

Let us assume that the light attenuation by the mixed aerosol (ATN) at a given λ can be represented by the sum of light attenuation by OC (ATN_{OC}) and EC (ATN_{EC}) at that λ :

$$ATN(\lambda) = ATN_{EC}(\lambda) + ATN_{OC}(\lambda) \tag{7.1}$$

Equation 7.1 is valid if OC and EC are the only species contributing to the light attenuation through the filter and the process is additive. Organic coatings can enhance light attenuation [Bond et al., 2006; Fuller et al., 1999; Subramanian et al., 2007], so the simple additive

assumption may not hold. Many filter-based artifacts can enhance light absorption by the embedded particles, which complicates the conversion of ATN to absorption, as I discussed in Chapter 6. These impacts appear less problematic for measurements of the spectral dependency of absorption compared to measurements of the absolute values of aerosol light absorption or of mass efficiencies.

ATN_{EC} and ATN_{OC} can be calculated by multiplying the mass attenuation efficiency for each by the mass of OC and EC (m_{OC} , m_{EC}) measured in the sample:

$$ATN_{OC}(\lambda) = m_{OC} \alpha_{ATN,OC}(\lambda) \quad 7.2$$

$$ATN_{EC}(\lambda) = m_{EC} \alpha_{ATN,EC}(\lambda) \quad 7.3$$

where $\alpha_{ATN,OC}(\lambda)$ and $\alpha_{ATN,EC}(\lambda)$ are the mass attenuation efficiencies for OC and EC, respectively. The mass attenuation efficiency is a function of wavelength, and can be approximated for any λ from $\alpha_{ATN}(\lambda_0)$ (for OC or EC) at reference wavelength (λ_0) using the Angstrom attenuation exponent for each species (e.g., $A_{ATN,OC}$):

$$\alpha_{ATN,OC}(\lambda) = \alpha_{ATN,OC}(\lambda_0) \left(\frac{\lambda_0}{\lambda} \right)^{A_{ATN,OC}} \quad 7.4$$

Equation 7.4 is also valid for EC and assumes the attenuation spectra of OC and EC can be represented by power-laws. Figure 7.3 gives example $\alpha_{ATN,OC}$ and $\alpha_{ATN,EC}$ spectra calculated from Equation 7.4 assuming $A_{ATN,OC}$ is 5.0, $A_{ATN,EC}$ is 0.75, $\alpha_{ATN,OC}$ at 550 nm is $0.1 \text{ m}^2 \text{ g}^{-1}$ and $\alpha_{ATN,EC}$ at 550 nm is $10 \text{ m}^2 \text{ g}^{-1}$. Based on these parameters, EC has a weaker ATN spectral dependence than OC, but attenuates more light at all λ than OC for the same amount of mass. The mass-normalized EC ATN efficiency dominates the OC ATN efficiency at wavelengths above ~ 600 nm, but the OC ATN efficiency increases rapidly to values approaching the EC efficiency below

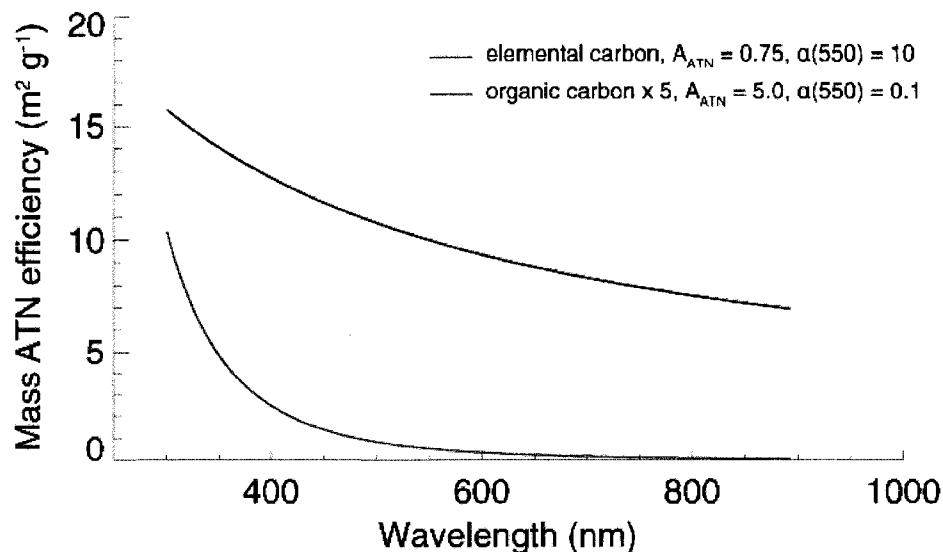


Figure 7.3 Mass attenuation efficiency (α_{ATN}) spectra for organic carbon (OC) and elemental carbon (EC) calculated assuming Angstrom attenuation exponents of 5.0 for OC and 0.75 for EC and α_{ATN} for OC is 0.1 $\text{m}^2 \text{g}^{-1}$ and for EC is 10 $\text{m}^2 \text{g}^{-1}$ at 550 nm.

~400 nm.

The curves shown in Figure 7.3 can be multiplied by OC and EC masses and combined with Equation 7.1 to predict the ATN spectra for mixed aerosol containing a range of OC and EC fractions of TC. I refer to these as the modeled bulk aerosol spectra. Figure 7.4 gives an example of the ATN spectra calculated by this method for a mixture containing OC and EC in a 9:1 ratio (or an EC/TC ratio of 0.1). Light attenuation at longer wavelengths is dominated by EC, which makes up over 90% of the total ATN above $\lambda \sim 550$ nm for this hypothetical mixture of EC and OC. OC contributes < 5% of the total ATN above 800 nm (dashed green line in Figure 7.4). The fraction of ATN due to OC, however, becomes important at shorter wavelengths because of the strong spectral dependence of ATN by OC and its large mass fraction compared to EC. It is responsible for about one-third of the total ATN at 350 nm. I focus on the implications of these relationships in the following sections.

The spectral dependence of the modeled bulk mixtures can be quantified through A_{ATN}

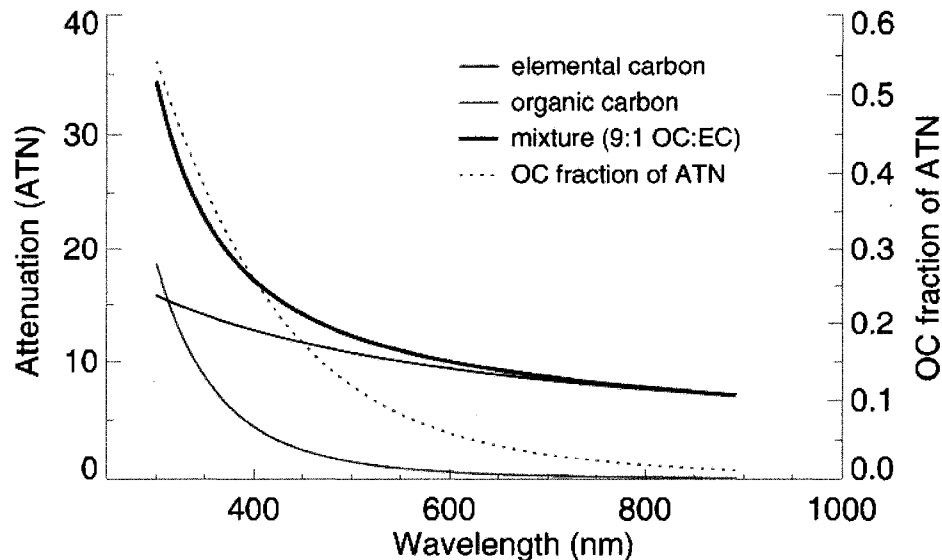


Figure 7.4 Attenuation as a function wavelength calculated from Equation 7.1 for a two-component aerosol consisting of organic (OC) and elemental carbon (EC) in a 9:1 ratio (elemental-to-total carbon ratio of 0.1). The attenuation for the two-component mixture is shown by the thick red line, the attenuation from EC in the mixture is shown by the thin black line, and the attenuation from OC in the mixture is shown by the thin green line. The fraction of the total ATN due to ATN by OC is shown by the dashed green line and plotted on the right-hand side axis.

in the same way as the measured data. The modeled spectra do not agree perfectly with a single power law, following the trend observed for the measured data, because the sum of two power laws is not a power law itself. I calculated A_{ATN} for modeled bulk mixtures with EC/TC ratios ranging from 0–1 by performing a non-linear regression on the modeled spectra, the same method used to determine A_{ATN} for the measured spectra. A_{ATN} for the modeled bulk mixture depended on three parameters: the ratio of the attenuation efficiencies for EC and OC at the reference wavelength ($\lambda = 550 \text{ nm}$), $A_{\text{ATN, OC}}$ and $A_{\text{ATN, EC}}$. Fixing each of these parameters resulted in a single function that described the relationship between A_{ATN} of the modeled bulk sample and the EC/TC ratio. The parameters were obtained by performing a second non-linear regression between the two-component model predicted A_{ATN} and measured A_{ATN} for each EC/TC measurement.

Figure 7.5 shows measured A_{ATN} (from Figure 7.1) and modeled A_{ATN} as a function of EC/TC ratio (from Hi-Vol NIOSH/Sunset measurements because more of these data were available) with $A_{ATN,OC} = 3.3$, $A_{ATN,EC} = 0.8$, and $a_{ATN,EC}/a_{ATN,OC} \sim 60$ (according to the best fit, 1 g of EC is 60 times more absorbing at 550 nm than 1 g of OC). For OC-dominated samples, the modeled A_{ATN} values asymptote to $A_{ATN,OC}$ and for EC-dominated samples the modeled A_{ATN}

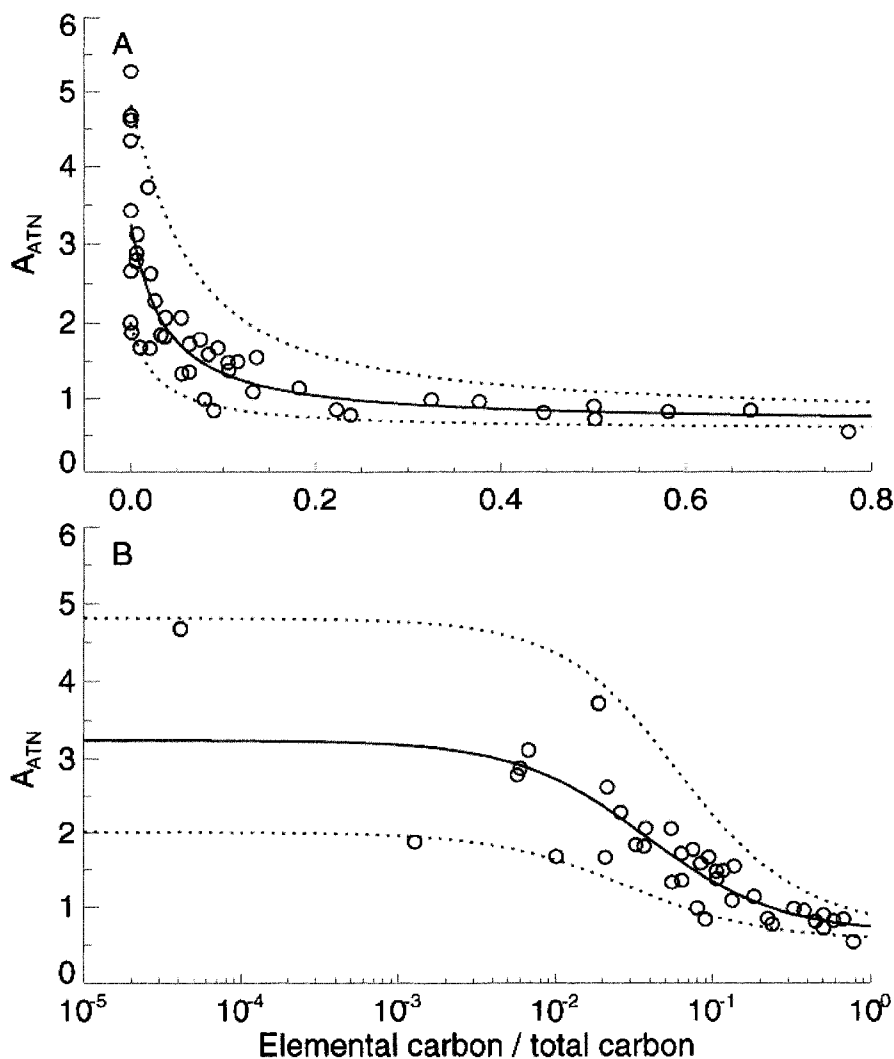


Figure 7.5 Measured (symbols) and modeled attenuation Angstrom exponents (A_{ATN}) as a function of elemental carbon / total carbon ratios measured on FLAME Hi-vol samples using a modified NIOSH/Sunset analyzer thermal optical analysis protocol. The solid blue line gives the modeled A_{ATN} values for the best-fit parameters to the data (see text). The dashed blue lines represent upper and lower extremes.

values asymptote to $A_{\text{ATN, EC}}$. This is more clearly seen in Figure 7.5b, which plots the data in semi-log-transformed space. The modeled A_{ATN} transition from one extreme to the other for EC/TC ratios between ~ 0.2 and 0.001. The transition region was weighted towards lower EC/TC fractions because EC had a much higher attenuation efficiency than OC.

The modeled A_{ATN} show a similar relationship to EC/TC ratios as the measured data. The two dashed lines in Figure 7.5 represent reasonable upper and lower bounds for the fit to the data and are based on two additional sets of model parameters, but the same EC/OC mass absorption efficiency ratio at 550 nm. I fixed the ratio of absorption efficiencies to examine the sensitivity to A_{ATN} . The upper bound was calculated assuming $A_{\text{ATN,OC}} = 4.8$ and $A_{\text{ATN,EC}} = 0.9$ and the lower bound $A_{\text{ATN,OC}} = 2.0$ and $A_{\text{ATN,EC}} = 0.6$. The uncertainty in the fit and the scatter in the measured A_{ATN} were much larger for OC-dominated samples than for EC-dominated samples. Two main factors were probably responsible for the larger variability for OC-dominated samples: a) EC had a more consistent attenuation spectral dependence than OC and b) measurements of EC and the EC/TC ratio were more uncertain for OC-dominated samples compared to EC-dominated samples. The two-component model is also consistent with the results from the solvent-extraction procedures, i.e., removal of the OC (component 1) by acetone resulted in an attenuation spectrum that matched that expected for EC (component 2).

7.3 Recommended optical properties for light absorbing organic carbon

7.3.1 Light attenuation

I combined measurements of OC, EC and $\text{ATN}(\lambda)$ to determine optical constants for OC and EC emitted by biomass burning. The previous section identified the best fit A_{ATN} for

OC and EC by assuming they were the only species responsible for light attenuation in the sample. This two-component model only provides information about the spectral dependence of each species and their *relative* absorption efficiencies, but not their absolute magnitudes. To estimate the absorption efficiencies for OC and EC sampled during FLAME, I followed the approach of *Kirchstetter et al.* [2004], who estimated $\alpha_{\text{ATN, EC}}$ and $\alpha_{\text{ATN, OC}}$ for several aerosol types from filter-based ATN and OC/BC measurements.

An example of the procedure applied to the bulk ATN spectra measured for ponderosa pine needle emissions (FLAME 1, filter 35) is illustrated in Figure 7.6. I calculated $\alpha_{\text{ATN, EC}}$ by dividing $b_{\text{ATN}}(\lambda = 870)$ by the EC concentration. This assumed all of the light attenuation at $\lambda = 870$ nm was due to EC and was supported by the large ratio between $\alpha_{\text{ATN, EC}}$ and $\alpha_{\text{ATN, OC}}$ at longer wavelengths, estimated in the previous section. The mass attenuation efficiency for EC was extrapolated to other wavelengths using an EC $A_{\text{ATN}} = 0.8$, obtained from the best fit from the two-component model approach described in the previous section (shown by the dashed

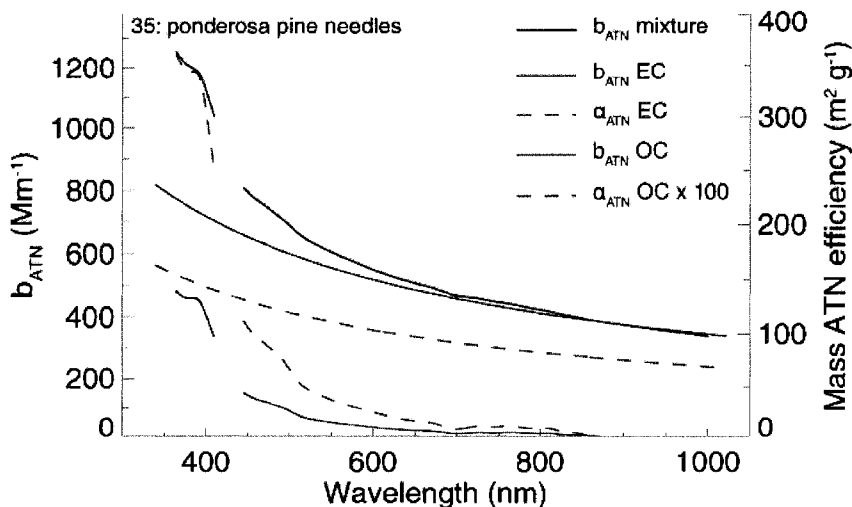


Figure 7.6 Measured light attenuation coefficients (b_{ATN}) for the bulk sample (black line) and estimates of the OC and EC b_{ATN} (solid red and blue lines, respectively) and mass attenuation efficiencies (α_{ATN} , dashed red and blue lines, respectively) as functions of wavelength for ponderosa pine needle emissions (filter 35) during FLAME 1.

red line plotted against the right-hand side axis). I estimated $b_{\text{ATN}}(\lambda)$ due to EC alone by multiplying the EC concentration by $\alpha_{\text{ATN,EC}}(\lambda)$ for each sample (shown in Figure 7.6 by the solid red line). I assumed that the entire difference between the measured $\text{ATN}(\lambda)$ and the EC estimated contribution was due to light attenuation by OC (the solid blue line in Figure 7.6). I divided the ‘residual’ or OC attenuation coefficient (at each wavelength) by the OC mass concentration to determine the OC mass-normalized attenuation efficiency as a function of wavelength (the dashed blue line in Figure 7.6). I applied the same procedure to each FLAME filter sample I tested at LBNL.

Mass attenuation efficiencies for EC ranged from 0, when no EC was detected in the sample, to unrealistically high values of $\sim 5000 \text{ m}^2 \text{ g}^{-1}$ at 870 nm. The maximum value was observed for a sample with very low measured EC ($0.004 \mu\text{g m}^{-3}$), so this value should be considered extremely uncertain. By including only samples with EC concentrations greater than $5 \mu\text{g m}^{-3}$, the range in observed $\alpha_{\text{ATN,EC}}$ at $\lambda = 870 \text{ nm}$ was reduced to 0–84 $\text{m}^2 \text{ g}^{-1}$, and yielded a ‘study’ (for the subset of filters I tested) mean of $12 \pm 20 \text{ m}^2 \text{ g}^{-1}$. Mass attenuation efficiencies for OC, calculated using the method described above, ranged from 0 (no enhancement in ATN at shorter wavelengths was observed) to 19 $\text{m}^2 \text{ g}^{-1}$, with a study mean of $6.5 \pm 4.2 \text{ m}^2 \text{ g}^{-1}$. The magnitude of $\alpha_{\text{ATN,OC}}$ was independent of MCE or CE, suggesting that the optical properties of emitted OC were not a function of combustion behavior. *Kirchstetter et al.* [2004] found an α_{ATN} of 10 $\text{m}^2 \text{ g}^{-1}$ at 350 nm for acetone-soluble OC in wood smoke and savannah fire emissions samples, and α_{ATN} of 22 $\text{m}^2 \text{ g}^{-1}$ at 700 nm for BC (determined by evolved gas analysis, another TOA technique [*Kirchstetter and Novakov, 2007*]) in motor vehicle and urban samples. Their technique differed from the method used here in that they did not attempt

to separate the contributions of OC and EC to bulk attenuation in biomass burning samples. Instead, *Kirchstetter et al.* [2004] calculated the differences in ATN and OC mass before and after acetone treatments to determine $\alpha_{\text{ATN,OC}}$ and they calculated $\alpha_{\text{ATN,EC}}$ for motor vehicle emissions dominated samples that did have a strong spectral dependence. The FLAME results are similar to those found by *Kirchstetter et al.* [2004] despite these differences in the experimental approach.

Kirchstetter et al. [2004] converted their attenuation-based optical property calculations to absorption-based values by dividing the filter-measured b_{ATN} by two to account for enhancements due to filter-based artifacts. Applying this correction to the FLAME results produced mass absorption efficiencies (α_A) of $6 \pm 10 \text{ m}^2 \text{ g}^{-1}$ for EC at 870 nm and $3.3 \pm 2.1 \text{ m}^2 \text{ g}^{-1}$ for OC at 370 nm. *Kirchstetter et al.* [2004] also estimated the imaginary part of the complex refractive index (k) using [*Bohren and Huffman, 1983*]:

$$k = \frac{\rho \alpha_A \lambda}{4\pi} \quad 7.5$$

where ρ is the density (assumed to equal 1.2 g cm^{-3} for OC and EC). I used Equation 7.5 to calculate a FLAME-average k_{OC} of 0.12 ± 0.07 at 370 nm and k_{EC} of 0.49 ± 0.41 at 870 nm. *Kirchstetter et al.* [2004] reported a k_{OC} of 0.17 at 350 nm and k_{BC} of 0.75 at 870 nm. These estimates of optical properties are highly uncertain because they require many assumptions.

7.3.2 Light absorption

I repeated the above exercise using the DRI photoacoustic spectrometer (PAS) measurements of b_A at 405, 532 and 870 nm instead of the attenuation data to examine filter-related artifacts on calculated optical properties. Section 6.7 compared PAS-based

measurements of \dot{A}_A and filter-based A_{ATN} , but this section focuses on the attenuation/absorption coefficients themselves and mass absorption/attenuation efficiencies, rather than on their wavelength-dependence. PAS data were only available for FLAME 1 burns at the time of writing, so the analysis presented here is only valid for FLAME 1.

Figure 7.7 compares b_{ATN} measured at 405, 532 and 870 nm on FLAME 1 filter samples with b_A measured by two PAS instruments and averaged over the filter collection periods. The filter-based attenuation coefficients were about a factor of five higher than the PAS-based absorption coefficients for burns with $b_A < 400 \text{ Mm}^{-1}$. The agreement improved to within a factor of ~ 2 for higher b_A , and to within a factor of ~ 1 for the highest b_A burns. On average, filter-

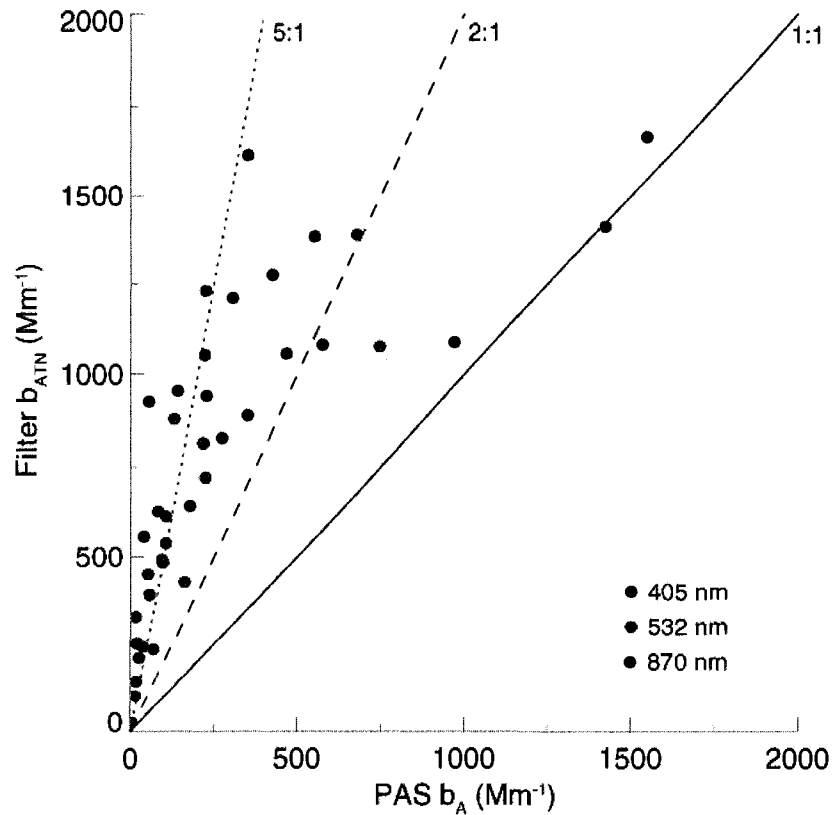


Figure 7.7 Light attenuation coefficients (b_{ATN}) measured on FLAME 1 filter samples versus light absorption coefficients (b_A) measured by two photoacoustic spectrometers at 405, 532 and 870 nm. The solid, dashed, and dotted lines indicate $b_{ATN}:b_A$ ratios of 1:1, 2:1 and 5:1, respectively.

based attenuation measurements were 4.9 ± 3.4 times higher than the absorption measurements. The disagreement between the techniques was only a weak function of wavelength, as expected by the consistent A_{ATN} values obtained from the filter and PAS spectra shown in Figure 6.17.

I discussed a method for correcting filter-based measurements of light absorption in Section 6.7 [Weingartner *et al.*, 2003], but from the perspective of the spectral dependence of the correction rather than its absolute magnitude. The Weingartner *et al.* [2003] (W2003) correction assumes the filter-based artifact consists of two components. The first is the increased optical path in the filter matrix due to multiple scattering, represented by the parameter C . The second is the reduction in the optical path due to the attenuation of light by particles embedded in the filter, referred to as the ‘shadowing effect’ and represented by the parameter $R(\text{ATN})$. The competing effects of the components are evident in Figure 7.7. Note that ATN , on which the shadowing factor depends, and b_{ATN} are not the same. A sample could have a high b_{ATN} , but if the sampling period was short, the ATN measured on the filter would be low. Conversely, a sample could have low b_{ATN} , but if the sample period was long, the ATN measured on the filter would be high. The sampling periods during FLAME were consistent, so b_{ATN} can be used as a proxy for ATN for the purposes of this discussion. For samples with low b_{ATN} (and low ATN), the multiple-scattering parameter, C , dominates the shadowing effect, $R(\text{ATN})$, and the disagreement between b_{A} and b_{ATN} was large. The shadowing parameter became more important for higher b_{ATN} and b_{A} samples, reducing the impact of the multiple-scattering artifact. The factor of ~ 5 difference between b_{ATN} and b_{A} for lower b_{A} samples suggests $C \sim 5$, in agreement with the value determined by Schmid *et al.* [2006] for biomass burning aerosol sampled in Brazil.

Table 7.1 Elemental carbon mass attenuation efficiency (α_A), mass absorption efficiency (α_A) and the imaginary part of the complex refractive index (k) determined from Equation 7.5 at 870 nm. Elemental carbon data was taken from the NIOSH 5040/Sunset analyzer measurements from high volume filter samples (EC) or from the IMPROVE_A measurements from the IMPROVE PM_{2.5} filters (ECI).

Fuel	ID	$\alpha_{ATN, EC}$ (m ² g ⁻¹)	$\alpha_{A, EC}$ (m ² g ⁻¹)	$\alpha_{A, ECI}$ (m ² g ⁻¹)	k_{EC} (ATN)	k_{EC}	k_{ECI}
ponderosa pine	35	77.0	9.9	1.6	6.4	0.82	0.13
chamise	36	14.0	8.1	4.2	1.16	0.67	0.35
ponderosa pine	37	-	-	-	-	-	-
chamise [†]	38	-	5.7	4.0	-	0.48	0.33
rice straw ^{1,2}	40	-	-	3.4	-	-	0.29
ponderosa duff ¹	41	-	-	0.7	-	-	0.05
Alaskan duff ^{1,2}	42	-	-	0.8	-	-	0.07
chamise	49	13.3	-	-	1.11	-	-
wax myrtle	50	48.8	-	-	4.06	-	-
longleaf pine	51	51.0	2.3	0.6	4.24	0.19	0.05
PR mixed woods	52	43.4	3.2	0.8	3.61	0.26	0.07
palmetto	53	28.9	5.5	3.5	2.40	0.46	0.29
ceanothus ¹	54	51.1	6.4	2.3	4.24	0.53	0.20
<i>Mean ± standard deviation</i>		<i>40.9 ± 21.4</i>	<i>5.9 ± 2.6</i>	<i>2.7 ± 1.5</i>	<i>1.77 ± 2.3</i>	<i>0.49 ± 0.22</i>	<i>0.22 ± 0.12</i>

¹Hi-vol/Sunset EC concentration < 5 µg m⁻³

²IMPROVE EC concentration < 5 µg m⁻³

[†]High volume filters were collected for first 20 minutes of the IMPROVE sampling interval

Table 7.1 summarizes the optical constants derived from filter-based ATN measurements and PAS-based absorption measurements for EC emitted (during FLAME 1 chamber burns only) at 870 nm. Mass absorption efficiencies were calculated for EC mass concentrations determined using the two TOA protocols on separate filter samples. Particles may have been lost in the sampling lines between the chamber and the PAS instruments, whereas filters sampled directly from the smoke-filled chamber, so the mass absorption efficiencies reported in Table 7.1 should be treated as lower limits. The mass absorption efficiencies calculated from the IMPROVE EC measurements are about a factor of two lower than those calculated from the Hi-vol EC measurements because the IMPROVE EC concentrations were about a factor of two higher than the Hi-vol EC concentrations. Mass attenuation efficiencies were about a factor of five higher than the absorption efficiencies, reflecting the factor of five difference observed between b_{ATN} and b_A .

The mean $\alpha_{A,EC}$ at 532 nm (for samples with $EC > 5 \mu\text{g m}^{-3}$) was $12.9 \pm 4.2 \text{ m}^2 \text{ g}^{-1}$ for EC measured on the Hi-vol filters and $6.6 \pm 2.5 \text{ m}^2 \text{ g}^{-1}$ (these are higher than the average values reported in Table 7.1 because they were made at a shorter wavelength. These calculations treated EC as the only absorbing species at 532 nm to compare with the α_{EC} reported by *Chen et al.* [2007] at this wavelength. They treated EC as the only light absorbing species for aerosol emitted by biomass burning during the FLAME pilot study. *Chen et al.* [2007] found a study-average $\alpha_{A,EC}$ of $9.6 \pm 0.8 \text{ m}^2 \text{ g}^{-1}$ for PAS-based b_A measurements and IMPROVE-based EC measurements, but only $7.8 \pm 0.9 \text{ m}^2 \text{ g}^{-1}$ for EC measurements based on the NIOSH 5040 protocol. This implies that NIOSH-based EC measurements were higher than IMPROVE-based measurements during the FLAME pilot study, but data from Table 2 in *Chen et al.* [2007] show that IMPROVE-based EC concentrations were higher than most of the NIOSH-based measurements. *Chen et al.* [2007] calculated $\alpha_{A,EC}$ by regressing absorption cross-section emission factors against EC (measured by each TOA protocol) emission factors. The regression intercepts were large for both measures of EC, which influenced the slopes of the regression.

I calculated the mass absorption efficiency (α_A) for EC by assuming all light absorption at 870 nm was due to EC, following the method used to calculate $\alpha_{ATN,EC}$ from filter measurements discussed in Section 7.3.1. From this, I estimated $\alpha_{A,EC}$ at 405 nm using Equation 4.2 with \hat{A}_A from PAS absorption measurements at 405 and 870 nm. For example, filter 52 (*Puerto Rican mixed woods*) had $b_A = 18.5 \text{ Mm}^{-1}$ at 870 nm measured by the PAS and $5.8 \mu\text{g m}^{-3}$ of EC, giving a $\alpha_{A,EC}$ of $3.2 \text{ m}^2 \text{ g}^{-1}$ at 870 nm. This extrapolates, assuming an $A_{A,EC}$ of 0.8 taken from Figure 7.5, to 4.7 and $5.9 \text{ m}^2 \text{ g}^{-1}$ at 532 and 405 nm, respectively. The total absorption coefficient at 405 nm for this sample was 130 Mm^{-1} , of which 34 Mm^{-1} was due to EC, leaving 96

Table 7.2 Mean optical constants (± 1 standard deviation) for OC and EC measured on high volume filter samples during the FLAME 1 chamber burns. Optical data were taken from filter-based attenuation measurements and two photoacoustic spectrometers. OC mass absorption efficiencies were calculated by extrapolating the absorption from EC using an Angstrom absorption exponent of 0.8. The mass absorption efficiency of EC was calculated by assuming it was the only species responsible for absorption at 870 nm. The imaginary component of the complex refractive index (k) was calculated from Equation 7.5.

wavelength	Filter-based attenuation				PAS-based absorption			
	α_{OC} ($m^2 g^{-1}$)	α_{EC} ($m^2 g^{-1}$)	k_{OC}	k_{EC}	$\alpha_{A, OC}$ ($m^2 g^{-1}$)	$\alpha_{A, EC}$ ($m^2 g^{-1}$)	k_{OC}	k_{EC}
370	5.3 ± 4.6	62.8 ± 56.7	0.18 ± 0.16	2.09 ± 2.01	-	-	-	-
405	4.8 ± 3.8	58.4 ± 52.7	0.18 ± 0.15	2.09 ± 2.01	2.7 ± 2.8	10.4 ± 12.6	0.10 ± 0.11	0.40 ± 0.49
532	1.1 ± 1.5	50.0 ± 42.4	0.06 ± 0.08	2.09 ± 2.01	1.0 ± 3.6	8.4 ± 10.1	0.14 ± 0.18	0.43 ± 0.52
870	0.0	31.7 ± 28.6	0.0	2.48 ± 2.39	0.0	5.6 ± 6.8	0.0	0.47 ± 0.57

Mm^{-1} from (presumably) the $47.6 \mu g m^{-3}$ of OC produced during the burn. This gives a $\alpha_{A, OC}$ of $\sim 2 m^2 g^{-1}$ at 405 nm. The mass attenuation efficiency for OC calculated from filter-based measurements for the same sample was $8.8 m^2 g^{-1}$, consistent with the factor of five difference between ATN and absorption coefficients.

Table 7.2 lists filter- and PAS-derived recommended optical constants for OC and EC measured on the high volume filters using the modified NIOSH 5040/Sunset TOA protocol. The OC absorption/attenuation efficiency at 870 nm was defined to be zero. The OC α_{ATN} at 370 nm ranged from $0 m^2 g^{-1}$ —no attenuation beyond that expected from EC was measured—to $\sim 18 m^2 g^{-1}$, but most of the samples fell between $4\text{--}8 m^2 g^{-1}$. At 405 nm $\alpha_{ATN, OC}$ ranged from $0\text{--}15 m^2 g^{-1}$ and at 532 nm it ranged from $0\text{--}6 m^2 g^{-1}$. The PAS-derived $\alpha_{A, OC}$ at 405 nm ranged from $0\text{--}11 m^2 g^{-1}$ and at 532 nm ranged from $0\text{--}11 m^2 g^{-1}$. The highest $\alpha_{A, OC}$ were observed for samples with a high concentration of EC, so they would be overestimated if the spectral dependence of EC was overestimated by the fitting method described above. These high values had a strong influence on the mean $\alpha_{A, OC}$ values reported in Table 7.2. Samples with lower contributions by EC had $\alpha_{A, OC}$ in the $0.5\text{--}3 m^2 g^{-1}$ range at 405 nm and $0.25\text{--}1.5 m^2 g^{-1}$ range at 532 nm.

The only samples for which filter b_{ATN} and PAS b_A measurements were available were

collected during the FLAME 1 chamber burns. Light attenuation measurements were made for filters collected during FLAME 2, but PAS data for these burns were still being processed by DRI at the time of writing. The average $\alpha_{\text{ATN,OC}}$ at 370 nm for all the FLAME 1 and 2 filters tested was $5.8 \pm 4.5 \text{ m}^2 \text{ g}^{-1}$. *Kirchstetter et al.* [2004] divided their measured $\alpha_{\text{ATN,OC}}$ by a factor of two to account for filter-based measurement artifacts, but my comparisons to photoacoustic data suggested this correction factor should be closer to 5 for the FLAME samples. Dividing $\alpha_{\text{ATN,OC}}$ by 5 yields an estimate of $\alpha_{\text{A,OC}}$ of $1.2 \pm 0.9 \text{ m}^2 \text{ g}^{-1}$, which corresponds to a k_{OC} of 0.042. At 405 nm, the average of all filter measurements of $\alpha_{\text{ATN,OC}}$ (and $\alpha_{\text{A,OC}} = \alpha_{\text{ATN,OC}} / 5$) was $4.8 \pm 3.6 (1.0 \pm 0.7) \text{ m}^2 \text{ g}^{-1}$, which gives a k_{OC} of 0.039.

PAS measurements were made during the FLAME 1 stack burns, but no filter-based ATN measurements were made for these filters. The average of all PAS-based estimates of $\alpha_{\text{A,OC}}$ at 405 nm was $1.8 \pm 2.1 \text{ m}^2 \text{ g}^{-1}$. Even though the PAS-based and filter-based averages were taken for different samples, the mean mass absorption/attenuation efficiencies measured by each technique agreed within the uncertainty, assuming a filter correction factor of five. The factor of five difference is larger than the value ~ 2 typically assumed when correcting filter-based absorption measurements [*Kirchstetter et al.*, 2004], but recent comparisons between PAS- and Aethalometer-measured absorption in the Amazon during smoke-impacted periods have also observed a factor of five correction [*Schmid et al.*, 2006].

7.3.3 *Optical properties of an OC-dominated sample*

The FLAME 1 chamber Alaskan duff burn emitted aerosol dominated by OC. No EC was measured above the detection limit on the Hi-vol filter samples by the modified NIOSH

5040/Sunset protocol, and only $4.9 \mu\text{g m}^{-3}$ of EC was measured on the IMPROVE $\text{PM}_{2.5}$ filters compared to $130.7 \mu\text{g m}^{-3}$ of OC. Light absorption by these emissions was dominated by OC, so the sample provides a check for the mean values reported in Table 7.2. The Alaskan duff a_A calculated from PAS measurements of light absorption and Hi-vol OC concentrations were 0.48, 0.13, and $0.04 \text{ m}^2 \text{ g}^{-1}$ at 405, 532 and 870 nm, respectively. These values were low compared to the mean values reported in Table 7.2. The mean values in Table 7.2 were influenced by outliers in the data, which were associated with burns that featured either very low EC concentrations (making the calculation of absorption due to EC compared to OC uncertain) or high absorption (where the contribution by OC to total absorption was difficult to separate from the contribution by EC). The median $a_{A,OC}$ at 405 nm was $1.8 \text{ m}^2 \text{ g}^{-1}$ for the FLAME 1 chamber burns, but still about 3 times higher than the Alaskan duff values. A lower mean $a_{A,OC}$ ($1.4 \text{ m}^2 \text{ g}^{-1}$) was obtained by assuming the absorption Angstrom exponent was the traditional value of 1.0, rather than 0.8 in Equation 7.5. Mass attenuation coefficients were 4.2, 0.94, and $0.22 \text{ m}^2 \text{ g}^{-1}$ at these wavelengths, higher due to filter artifacts, and possibly because of losses in the sampling lines connecting the PAS instruments to the chamber, which resulted in lower PAS-estimated absorption efficiencies. The lower value of a_{OC} for Alaskan duff emissions compared to the mean values in Table 7.2 may reflect the variability in the OC emitted by different fires. This burn also produced more large OC particles compared to other burns, so the lower mass absorption and attenuation efficiencies could also be lower because the large particles absorbed less light relative to their mass.

7.4 Angstrom absorption exponent and combustion conditions

The strong relationship between the EC/TC ratio—or the relative abundance of OC and EC in the emitted aerosol—and the bulk aerosol \dot{A}_{ATN} suggests there should be a relationship between combustion behavior and \dot{A}_{ATN} . The fire combustion behavior, quantified through MCE, determined how much OC was emitted relative to EC, though there were important exceptions to this, notably rice straw emissions. Sections 7.2 and 7.3 showed that OC emitted during FLAME had similar optical properties, so combustion processes that lead to greater OC production should have also resulted in a greater spectral dependence of attenuation/absorption. This section explores the relationship between combustion conditions and the spectral dependence of absorption.

7.4.1 *Flaming and smoldering pine needle emissions*

The most straight-forward comparison of the spectral properties of aerosol emitted by different combustion phases can be made using the samples of burning ponderosa pine needle emissions that were collected during the flaming and smoldering combustion stages alone. The MCE for the flaming pine needle burn was 0.99 and for smoldering pine needle emissions it was 0.80. Figure 7.8 shows the measured attenuation spectra for these two samples (solid lines), together with the non-linear regression power law fit to the measurements (dashed lines). The optical properties of aerosol emitted by the different combustion stages were strongly related to their OC and EC content. Flaming emissions had a high EC/TC ratio (0.5) compared to most of the FLAME samples, whereas smoldering emissions had an EC/TC ratio of zero, i.e., no detectable EC was produced by the smoldering stage of combustion for this fuel.

The spectra represent the two extremes in attenuation-wavelength relationships discussed in Chapter 4. The light attenuated by flaming emissions had a weak wavelength dependence ($A_{\text{ATN}} = 0.9$) and light attenuated by smoldering emissions had a strong wavelength dependence ($A_{\text{ATN}} = 4.6$). The light attenuation by the flaming emissions was stronger than the light attenuation by smoldering emissions at long wavelengths, but weaker at shorter wavelengths. Roden *et al.* [2006] reported similar differences in the absorption spectral dependence of wood smoke aerosol under varying combustion conditions. They measured \hat{A}_A between 0.9–1.9 during the flaming stage of combustion and \hat{A}_A between 3.5–6.0 during the smoldering phase of combustion.

7.4.2 Fire-integrated MCE

I compared the strength of the spectral dependence of light attenuation with

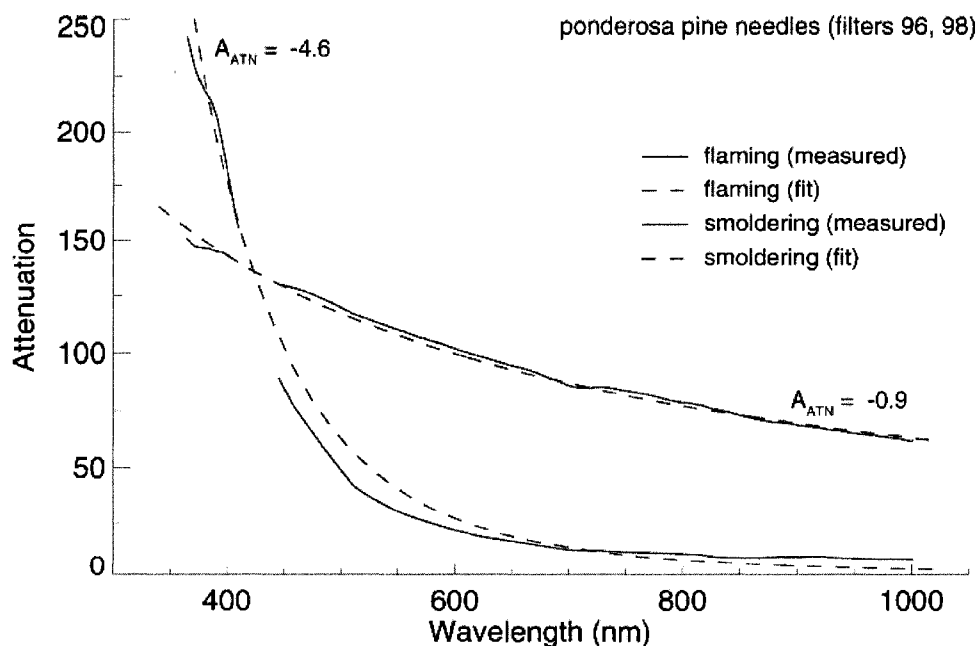


Figure 7.8 Attenuation as a function of wavelength measured on filter samples of ponderosa pine needle flaming combustion emissions (red lines) and smoldering combustion emissions (blue lines). Non-linear regression power law fits to the data are shown by the dashed lines and the attenuation Ångström exponents are also given for each sample.

combustion conditions by plotting A_{ATN} as a function of MCE and CE (Figure 7.9). The attenuation Ångström exponent increased with decreasing MCE, because fires with low MCE tended to produce more OC (with a strong attenuation wavelength dependence) and less EC (with a weak attenuation wavelength dependence). The flaming and smoldering pine needle emissions discussed in the previous section were consistent with the general trend in the data. Several burns had high MCE, but produced little EC, which I discussed in more detail in Chapter 4. These samples were partly responsible for the increased scatter in the relationship between A_{ATN} and MCE. Just as MCE was not a perfect predictor of the EC/TC ratio, it was also not a perfect predictor of A_{ATN} ($r^2 = 0.39$), nor was CE.

7.5 Relationships between Angstrom exponents and single scatter albedo

This chapter has focused on the relationships between aerosol light absorption and attenuation with composition and combustion behavior. Aerosol light scattering, however, plays a major role in the extinction of light at visible wavelengths, and it also has a strong wavelength dependence. As discussed in Chapter 3, scattering Ångström exponents (A_{S}) ranged from $\sim 1-3$, with scattering at shorter wavelengths always higher than scattering at longer wavelengths. There was no correlation between A_{ATN} or A_{A} and A_{S} . A few of the burns that produced the lowest A_{S} also produced some of the highest A_{ATN} , but this relationship was not consistent over the range of A_{S} and A_{ATN} observed during FLAME.

Samples with high \dot{A}_{ATN} were dominated by OC, which had a high mass scattering efficiency, so they also had a relatively high ω_0 . Figure 7.10, based on *Lewis et al.* [in press], shows \dot{A}_A calculated from PAS measurements of light absorption at 870 and 405 nm versus ω_0 calculated from PAS-measured b_A and b_S . Figure 7.10 differs slightly from the plot shown by *Lewis et al.* [in press] by showing results not only from chamber burns during FLAME 1, but from stack burns as well. Both types of burns show a strong increase in \dot{A}_A for $\omega_0 > 0.8$ as the EC

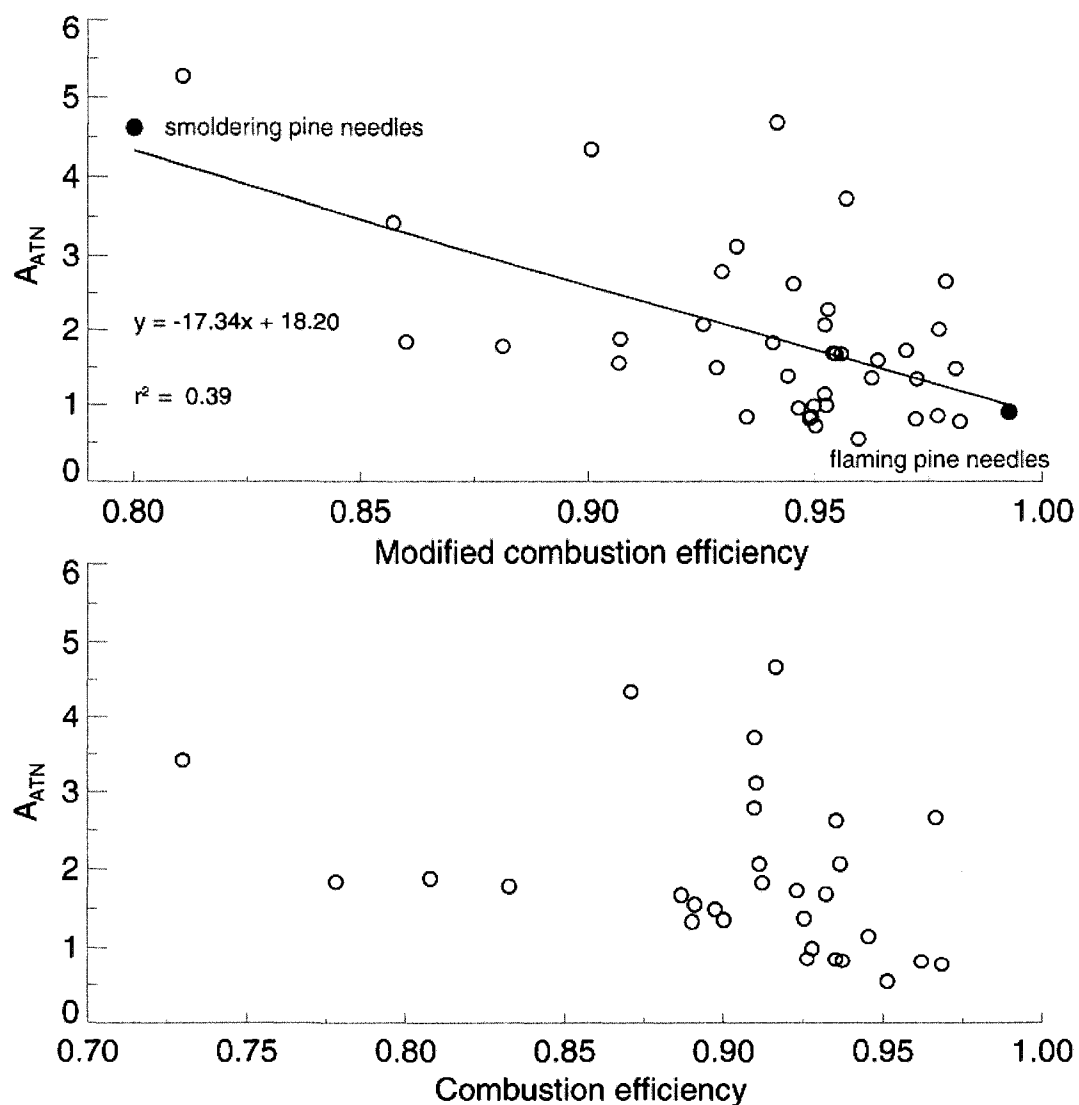


Figure 7.9 Attenuation Angstrom exponent versus fire- and filter-integrated modified combustion efficiency for selected FLAME samples/burns. Solid line indicates the linear least-squares regression to the data.

fraction of aerosol mass decreases. Some of the variability in the relationship was due to concentrations of inorganic material in the aerosol, which increased ω_0 , but did not affect \dot{A}_A .

The light scattered by a particle depends on its refractive index (i.e., composition), its size, and the wavelength of the incident light. At the Rayleigh limit (sufficiently small particles), the absorption efficiency (Q_{abs}) is proportional to $1/\lambda$, whereas the scattering efficiency (Q_{scat}) is proportional to $1/\lambda^4$. Thus, ω_0 increases with decreasing wavelength, because Q_{scat} increases faster than Q_{abs} . OC-dominated aerosol emitted during FLAME, however, had a stronger absorption wavelength dependence than that predicted by Rayleigh theory, and a weaker scattering wavelength dependence. The former was due to variations in the imaginary part of the refractive index with wavelength and the latter to typical aerosol sizes greater than those sufficient for Rayleigh theory. As a result, ω_0 decreased with increasing wavelength for several OC-dominated burns. For example, ω_0 was 0.99 at 870 nm, 0.98 at 532 nm, and 0.95 at 405 nm

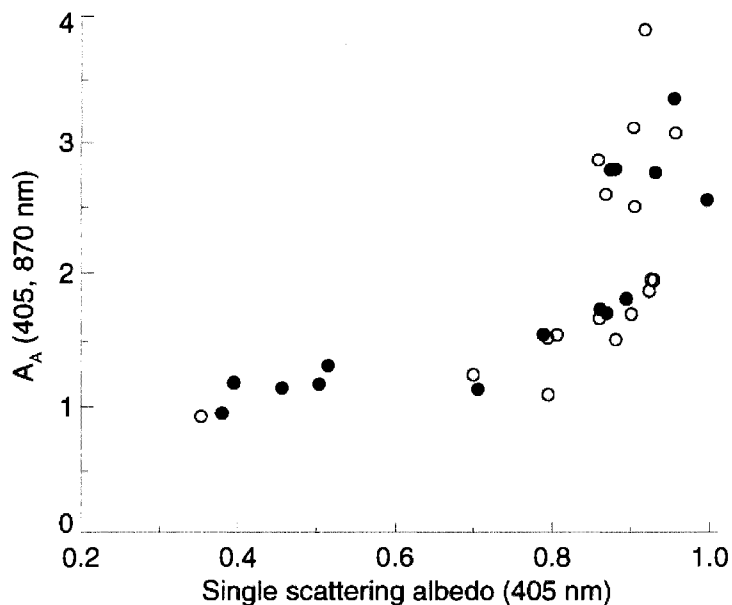


Figure 7.10 Absorption Ångström exponents calculated from absorption measured at 405 and 870 nm as a function of single scattering albedo (ω_0) at 405 nm (adapted from *Lewis et al.* [in press]). Measurements for emissions from the flaming and smoldering-phase combustion of ponderosa pine needles are highlighted.

for aerosol emitted by Alaskan duff burned during the FLAME 1 chamber experiments. These particles had an \dot{A}_{ATN} of 4.3 and a \dot{A}_{S} of 1.0.

Bergstrom et al. [2007] reported that ω_0 decreased with increasing wavelength (see their Figure 3). The relationship between ω_0 and wavelength has been used to differentiate between dust, biomass burning and urban pollution [*Bergstrom et al.*, 2007], so it is important to predict the SSA-wavelength relationship for biomass burning aerosol. It is a function of both particle composition and size. It also has implications for measurements of biomass burning-impacted aerosol light absorption made at a single wavelength, particularly at near-IR wavelengths. An aerosol assumed to be a near-perfect light scatterer at all wavelengths based on measurements at 870 nm could have a significant contribution from absorption at visible and UV wavelengths.

7.6 Physical explanation of absorption spectral dependence – links to composition

The light absorbing properties of EC arise from the high mobility of graphitic carbon electrons. In graphite, three of the valence carbon atoms are bonded by hybrid sp^2 orbitals and the fourth is loosely held in a π orbital normal to the plane of the sp^2 orbitals [*Bond and Bergstrom*, 2006]. Carbonaceous particles with higher fractions of sp^2 -bonded carbon have more of these highly mobile electrons, which can be excited by photons over a wide range of visible and infrared wavelengths [*Bond and Bergstrom*, 2006]. Flame-generated carbonaceous particles contain sp^3 -bonded carbon in addition to sp^2 -bonded carbon, which affects their optical properties [*Bond and Bergstrom*, 2006; *Hopkins et al.*, 2007]. Some organic compounds, such as polycyclic aromatic hydrocarbons (PAHs) contain aromatically bonded carbon. Electrons in these bonds also have a relatively higher mobility than those participating in aliphatic carbon

bonds, and can absorb light, though this tends to be limited to shorter-wavelengths near or in the UV [Jacobson, 1999].

A handful of studies have hypothesized that the light absorbing properties of organic aerosol were due either to nitrated and aromatic compounds (UV) [Jacobson, 1999] or differing levels of aromatization (near-UV, visible) [Bond, 2001]. The composition of HULIS has been examined more closely, with a number of studies [Decesari *et al.*, 2006; Hoffer *et al.*, 2004] noting a large number of humic and fulvic acids present in the aerosol phase. Humic and fulvic acids represent a large number of individual compounds, but they share a number of physical properties, including water-solubility and high-molecular weight. Ideally one could determine the identity of every absorbing compound present in biomass burning emissions, such as those just mentioned, to calculate the bulk absorption spectrum, but this approach is limited by the low fraction of organic material in aerosols we can currently identify [Sun *et al.*, 2007]. Instead, several studies have sought broader theoretical foundations to explain the light absorption behavior of carbon-dominated aerosols [e.g., Bond, 2001; Jacobson, 1999; Sun *et al.*, 2007].

The band gap theory originates from examining the optical properties of amorphous carbon and semiconductors. The band gap or optical gap (E_g) is the energy required to excite an electron from the highest ground state to the lowest excited state. Bond and Bergstrom [2006] explain that the structure of amorphous carbon is known as medium-range order (as opposed to atomic- or crystal-scale order) and is related to the number of adjacent sp^2 -bonded carbon rings. The size of the sp^2 -clusters or the number of aromatic rings in the clusters is inversely related to the optical gap [Sun *et al.*, 2007]. For example, the band gap for benzene (one ring) corresponds to a wavelength of 200 nm, and as more rings are added the band gap decreases and longer-

wavelength light can participate in the absorption. *Bond and Bergstrom* [2006] refer to the transition from sp^3 -bonded carbon to sp^2 -bonded carbon as graphitization. Graphitization is promoted by higher temperatures and it occurs in flames [*Bond and Bergstrom, 2006*]. Non-graphitic precursor aerosol is transformed to a more graphitic substance in the flame, and the longer they remain in the flame the more graphite-like they become. *Bond* [2001] suggested the optical properties of coal combustion emissions were related to varying cluster sizes, ranging from pure coal tar (few adjacent rings) to complete graphitization (infinite cluster size).

Bond [2001] proposed that the optical properties of LAOC could be described using a band gap relationship. *Tauc et al.* [1966] related E_g to the bulk absorption coefficient (β):

$$\sqrt{\beta E} = B(E - E_g) \quad 7.6$$

where B is a constant and E is the photon energy given by $E = hc/\lambda$ where h is Planck's constant (6.63×10^{-34} J s) and c is the speed of light in vacuum (2.998×10^8 m s^{-1}). The absorption efficiency (α) and its spectral dependence depend on the value of E_g . For EC, E_g is essentially 0, and β is proportional to $1/\lambda$. *Sun et al.* [2007] showed that \hat{A}_λ was equal to $(E + E_g)/(E - E_g)$.

Figure 7.11 shows the relationship predicted by the band gap theory for a substance with $E_g = 1.85$ eV (fit to the data) and $B^2 = 57800$ cm^2 g^{-1} eV^{-1} (taken from *Sun et al.* [2007]). The data are plotted in the form of a Tauc plot [*Tauc et al., 1966*], which compares the square-root of the product of β and E with $E - E_g$. The band gap relationship is shown by the solid-black line. *Sun et al.* [2007] showed that the particle mass absorption efficiency a can be expressed in terms of the bulk absorption coefficient (β) by:

$$\alpha = \frac{\beta}{\rho} \xi \quad 7.7$$

where ξ , which describes the particulate effect, was defined as

$$\xi = \frac{9n}{(n^2 - k^2 + 2)^2 + 4n^2k^2} \quad 7.8$$

where n and k are the real and imaginary components of the refractive index, respectively. *Sun et al.* [2007] estimated ξ ranges from 0.69–0.75 for particles with $n = 1.5$ that are small compared to the wavelength. They took an intermediate value of ξ to estimate a_{bulk}/ρ from the mass absorption efficiencies reported by *Kirchstetter et al.* [2004]. For example, *Kirchstetter et al.* [2004] reported a mass absorption efficiency of $1.5 \text{ m}^2 \text{ g}^{-1}$ at 450 nm, which translates to an a_{bulk}/ρ of $\sim 2 \text{ m}^2 \text{ g}^{-1}$. I divided the measured attenuation spectra by the OC mass for emissions that contained no measurable concentration of EC to estimate α_{ATN} . I then divided the result by a factor of two to remain consistent with *Kirchstetter et al.* [2004] and by $\xi = 0.71$ to be consistent with *Sun et al.* [2007]. The absorption spectrum for Alaskan duff emissions, sampled during the FLAME 1 chamber burns, is plotted in Figure 7.11 on the same coordinate system. The spectrum deviates from the band gap relationship as E approaches E_g . This “Urbach tail” occurs because a few energy states exist within the band gap, so absorption spectra do not have a sudden drop off at E_g [*Sun et al.*, 2007]. An entirely empirical relationship describes absorption by:

$$\alpha = \alpha_{cr} \exp\left(\frac{E_{cr} - E}{E_0}\right) \quad 7.9$$

where α_{cr} and E_{cr} are determined from the absorption spectrum and E_0 is a characteristic decay width [*Sun et al.*, 2007]. For the Alaskan duff emissions plotted in Figure 7.11, $\alpha_{cr} = 0.27 \text{ eV}$ and

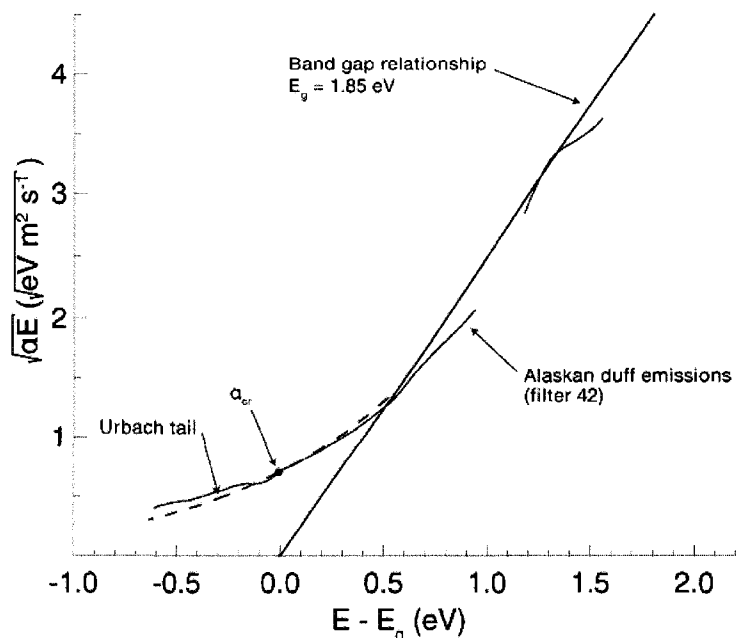


Figure 7.11 Tauc plot illustrating the band gap relationship with $E_g = 1.85$ eV with the measured spectra for Alaskan duff emissions (see text for details).

$$E_{cr} = E_g.$$

Sun et al. [2007] assumed that biomass combustion aerosol and water-soluble OC, e.g., humic like substances, have similar building blocks: organic chromophores—the parts of organic molecules that absorb light. *Sun et al.* [2007] derived an $E_g = 2.5$ eV for the chromophores. They obtained this value by examining the spectra for over 500 organic molecules, with the caveat that many of these were not necessarily found in atmospheric aerosol. They assumed the components of biomass burning aerosol have the same chromophore ‘building blocks’, but contain more clustered, unsaturated bonds. From their examination of individual organic spectra, *Sun et al.* [2007] determined that E_g scaled with unsaturation number. They used mass spectra of wood pyrolysis products to estimate an unsaturation number of 14 for high-temperature pyrolysis products, which yielded $E_g = 1.65$ eV, which they recommend for biomass burning OC. They recommend using $E_g = 2.5$ eV with an Urbach tail to

represent water-soluble, humic-like organic carbon, and $E_g = 1.65$ eV without the tail to represent more polymerized OC and combustion aerosol.

In order to test the validity of this approximation, I compared the filter- and PAS-based absorption measurements estimated in Section 7.3 with the spectrum predicted by an $E_g = 1.65$ eV recommended by *Sun et al.* [2007] for combustion aerosols (Figure 7.12). Aerosol mass-normalized absorption efficiencies for acetone-soluble OC recommended by *Kirchstetter et al.* [2004] are shown in Figure 7.12 and were divided by an intermediate ξ (0.71), following *Sun et al.* [2007]. Also shown are the study mean filter-based attenuation and PAS-based absorption efficiencies measured during FLAME. I divided the filter-based measurements by a factor of two to remain consistent with *Kirchstetter et al.* [2004], even though the comparison with PAS measurements suggested a factor of two correction is too low. I excluded samples in which EC made up over half of the measured TC because the determination of the absorption from OC in these samples was highly uncertain. Figure 7.12 also shows the range of filter-based and PAS-based absorption efficiencies for the FLAME measurements. The error bars associated with the *Kirchstetter et al.* [2004] data represent the uncertainty in ξ when adjusting the particulate absorption efficiencies to the bulk absorption efficiencies needed for the band gap calculations. The FLAME data error bars do not include this uncertainty because I wanted to show the range of observations. The true uncertainty was slightly larger than that illustrated by the error bars due to the uncertainty in ξ . The three red lines give attenuation measured absorption efficiency (divided by a factor of two) for three Alaskan dust emissions samples collected during FLAME 1 and 2. Each of these samples contained no measurable EC, so the light they absorbed should be due to only OC.

Figure 7.12 shows that the band gap theory mimics the wavelength-dependent absorption behavior of biomass burning aerosol emitted over a range of conditions, but the PAS- and filter-based measurements both indicate that an E_g of 1.65 eV may be too low. Figure 7.11 indicated that for Alaskan dust emissions, which contained only OC, E_g is probably closer to 1.85 eV. That said, the filter-based measurements of absorption are highly uncertain due to filter artifacts and the PAS measurements may be affected by particle losses in their long sampling lines that did not affect the filter measurements of OC.

Sun et al. [2007] derived E_g for biomass burning aerosol based on physical reasoning rather than measured values, so its relatively good agreement with the measured values was not due to excessive massaging of the band gap model's parameters. Thus, the FLAME data provide additional support for the band gap approach to modeling the optical properties of biomass burning OC. Mass spectra of aerosol collected during FLAME could provide more information regarding the average unsaturation number for the emitted organics, which could explain why a slightly lower band gap energy fits the FLAME observations more closely than that derived assuming the unsaturation number for wood smoke was 14.

7.7 Summary

Variations in \dot{A}_{ATN} with combustion help explain the large variability in \dot{A}_{ATN} reported by previous studies. Biomass burning samples have been observed to have spectral dependencies ranging from ~ 2 – 5 . Smoldering-dominated combustion produces aerosol with higher mass fractions of OC, which increases the bulk aerosol spectral dependence. Though several authors have noted a relationship between combustion conditions and \dot{A}_{ATN} [e.g., *Lewis et al.*, in press;

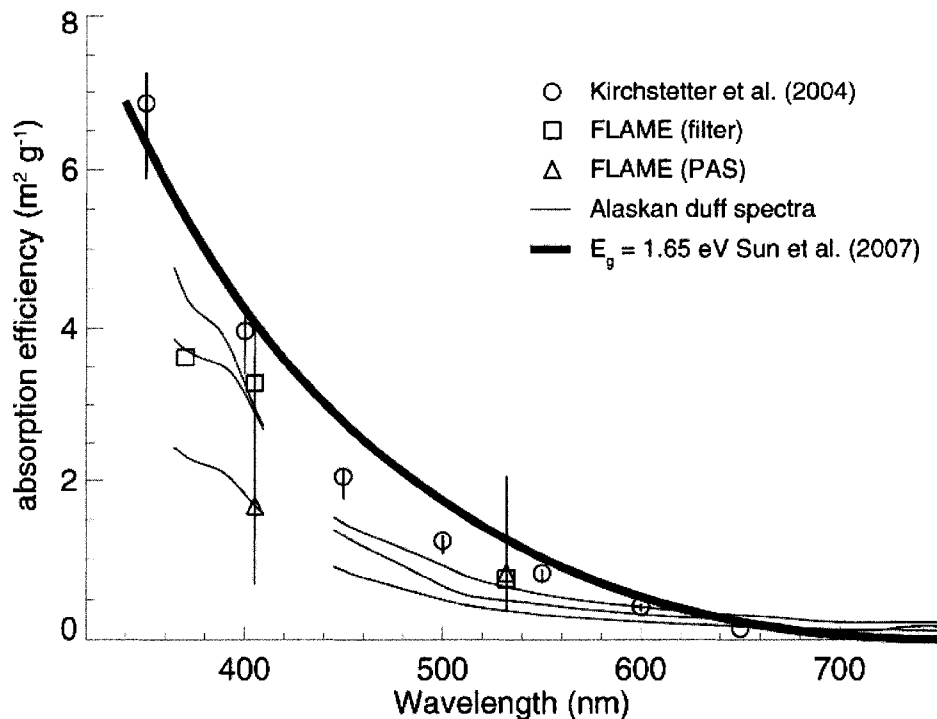


Figure 7.12 Mass-normalized bulk absorption efficiency (β) as a function of wavelength for: a) a band gap, $E_g = 1.65$ eV (recommended by *Sun et al.* [2007], b) filter-based measurements of the acetone-soluble fraction of OC in aerosol collected over savannah fires in Africa, reported by *Kirchstetter et al.* [2004], c) study-averaged FLAME OC absorption efficiency determined from filter measurements, d) study-averaged FLAME OC absorption efficiency determined from photoacoustic spectrometer measurements, and e) three spectra measured for OC-dominated Alaskan duff emissions collected during FLAME 1 and 2.

Roden et al., 2006], this study was the first to quantify this relationship with a measure of combustion behavior, MCE. The results presented in this chapter suggest that the optical properties of the emitted OC are relatively consistent, regardless of combustion conditions. The mixture optical properties depend more on the relative mixture of OC and EC, rather than on varying OC properties. This interpretation is consistent with *Sun et al.* [2007], who proposed that combustion aerosol could be grouped into a single class with a band gap. That biomass burning OC optical properties differ from those attributed to humic like substances is not surprising, considering they are formed and emitted to the atmosphere by different processes.

This was one of the first studies to combine detailed measurements of combustion behavior, OC/EC content, and spectral optical properties determined by both filter- and PAS-

based techniques. *Lewis et al.* [in press] presented spectrally-resolved absorption and scattering data for these burns, and qualitatively linked their observations to OC/EC composition and combustion conditions, but did not attempt to quantify these relationships. Complications were introduced by natural variability in the wavelength-dependence of EC and OC light absorption, variability in the absorption efficiencies of EC and OC, and measurement artifacts related to the measurement of OC, EC, and filter-based attenuation measurements. Yet the FLAME data suggest that OC and EC optical properties are relatively consistent over a range of combustion conditions. They provide upper- and lower- bounds for estimated optical properties, suggesting that the mass absorption efficiency for OC at 405 nm falls between 0.5 and 3 m² g⁻¹. The mean value was between 1.4 and 2.7 m² g⁻¹, depending on the assumed spectral dependence of EC light absorption. The OC absorption efficiency at 400 nm reported by *Kirchstetter et al.* [2004] was 2.9 m² g⁻¹, which agreed well with the range of $\alpha_{A,OC}$ found during FLAME.

Chapter 8 Conclusions and Future Work

8.1 Conclusions

Fires represent an extremely complex combination of physical and chemical processes that result in the conversion of the fuel (primarily carbon, hydrogen and oxygen) into trace gases and particles. The formation of the emitted species depends strongly on conditions within the fuel bed. The supply of oxygen to the combustion region affects the oxidation rate and emitted products, as does the supply of volatile hydrocarbon species from the fuel. The temperature of the fire, which varies throughout the fuel bed, determines the equilibria between the formation and destruction of chemical species in the fuel bed, and their phase (gas or particle) [*Flagan and Seinfeld, 1988*]. Unfortunately, these variables (temperature, oxygen concentration, concentrations and composition of volatile species) are spatially and temporally variable and difficult to measure, even in relatively controlled combustion environments such as those encountered in this study. As a result, we are forced to rely on measurements of the combustion end products and their relationships to each other in order to investigate the processes that govern emissions.

Diagnostic variables, such as the modified combustion efficiency or MCE, only tell part of the story. MCE, for example, provides no information about the temperature within the fuel bed, which plays an important role in determining emissions. Its utility depends on the correlation of other emissions and their properties to the amount of carbon monoxide and

dioxide released during the fire. Despite its drawbacks, the MCE at least provides a succinct and quantitative description of the combustion behavior of the fire. Clearly, our understanding of the processes that govern the emissions of specific aerosol species would benefit from additional measures of the fire combustion behavior, but until these become more readily available, MCE remains our best option as a diagnostic variable.

In this work, I found that MCE was strongly related to the emissions of CO₂, CO, CH₄, C₁₋₄ hydrocarbons, and aerosol EC and OC. Total observed organic carbon (TOOC) emissions were about 4–6 times higher for smoldering-dominated fires compared to flaming-dominated fires, so smoldering-dominated fires have a higher potential of producing additional aerosol mass via secondary organic aerosol formation and condensation mechanisms as plumes age. OC emissions were typically higher at low MCE, and usually larger than EC or inorganic emission factors for the range of MCE observed during FLAME. OC emission factors were the dominant constituent of particulate matter produced by most of the FLAME fuels. Because OC was strongly related to MCE, total aerosol mass was as well. Smoldering fires produced roughly four times as much OC as flaming-dominated fires.

The aerosol optical properties were also strongly dependent on combustion conditions. This was because flaming-dominated combustion could produce EC, but smoldering-dominated combustion did not. The higher mass fractions of EC in aerosol produced by flaming-dominated fires lead to particles with low single scattering albedo (in the mid-visible) and a weak wavelength dependence of absorption. The single scattering albedo in these cases was as low as 0.4, the attenuation Ångström exponent as low as 0.7, and the absorption Ångström exponent was as low as 1.0. Smoldering-dominated combustion produced particles

dominated by OC. Aerosol emitted by smoldering combustion had high single scattering albedo (in the mid-visible) and a strong wavelength dependence of light, with absorption and attenuation Ångström exponents approaching 5.

This study was the first to examine the spectral properties of light absorption for emissions from a large number of plant fuels and combustion conditions. It is the first to report mass-normalized absorption efficiencies for OC as a function of wavelength based on PAS measurements of absorption, which are not affected by filter artifacts. I showed that a simple, additive model of strongly light absorbing elemental carbon and weakly light absorbing, but strongly wavelength dependent organic carbon explained the bulk aerosol spectral absorbance observed during FLAME. Such a mechanism may also account for the relatively large range in attenuation and absorption Ångström exponents reported for various combustion processes.

Predicting the radiative impacts of these particles requires information regarding their abundance and distribution in the atmosphere and their optical properties. Though this study cannot address the former, it represents the largest single tabulation of aerosol absorption and scattering properties as a function of wavelength yet produced. It adds to the growing body of evidence that OC emitted by fires absorbs light. My results suggest that the OC emitted by fires has relatively consistent optical properties that differ from those emitted by other sources and that variations in the bulk aerosol optical properties can be explained by the amount of OC and EC emitted by the fire. This means that if OC and EC emissions can be estimated accurately, the optical properties of the aerosol can also be predicted. Emission inventories and to a limited extent global models, already account for OC and EC emitted by fires, so the optical properties for OC and EC reported in this work could be applied to the existing data to improve estimates

of smoke radiative impacts.

Inorganic emissions were a stronger function of fuel type than of combustion conditions, but the absence of fuel composition measurements of species such as Cl, K, and Na (the major inorganic species identified in biomass burning emissions during FLAME) makes it impossible to link inorganic emissions directly to fuel. Previous studies have shown a relationship between fuel chlorine content and chlorine emissions, so similar relationships probably exist between other fuel inorganic components and their emissions. The relative abundance of inorganic species was related to particle hygroscopicity [*Carrico*, in preparation]. Aerosol hygroscopicity depended more strongly on plant type because the presence of high hygroscopicity inorganic species was needed to overcome the low hygroscopicity of organic carbon. In fact, many flaming-dominated fuels produced high hygroscopicity aerosol [*C. Carrico and M. Petters*, personal communication]. However, if a high inorganic-content fuel produced a large amount of OC, the low ratio of inorganics to low-hygroscopicity OC produced a low bulk aerosol hygroscopicity, so combustion conditions can still play a role in limiting highly hygroscopic aerosol emissions.

Not all flaming-dominated fires emitted EC, probably because of variations in combustion temperatures not captured by the MCE, lower concentration of PAH soot-precursor compounds, the inhibition of soot formation by inorganic ions in the flame region, combustion of soot before it escaped the flame, or some combination of these mechanisms. As a result, there were flaming-dominated fuels that produced high inorganic content/low EC content particles that were both hygroscopic and had a strong wavelength dependence of absorption, such as rice straw emissions.

Efforts to predict aerosol hygroscopic effects, such as CCN activity and indirect effects, of biomass burning aerosol on climate, should focus more on accurate representation of plant type and inorganic composition in emissions models. Efforts to predict aerosol optical properties, however, should focus on accurate classification of combustion conditions, as this mechanism is the primary driver of dry aerosol optical properties, including their wavelength-dependence. Though MCE was related to these properties, MCE may be of limited effectiveness in such efforts, because it fails to account for the lack of EC formation in certain, flaming-phase dominated fuels. Further, MCE is difficult to measure from space because it requires measuring CO₂ increases against a high CO₂ background.

8.2 Future work

The research presented here will be continued through three specific projects. First, the lack of EC formation for certain high MCE fuels, such as rice straw, suggests additional measures of combustion behavior are needed to characterize biomass burning emissions. One candidate is fire radiative power, which can be retrieved from satellites, and has been linked to gas-phase emissions [Freeborn *et al.*, 2008]. We monitored outgoing IR radiation during each burn during FLAME using a thermal imaging system. These data can be used to calculate fire radiative energy and fire radiative power, but have not yet been processed. When available, they will provide an additional diagnostic of combustion that may explain emissions that deviated from the relationships with MCE.

Second, the estimates of OC optical properties presented here could be included in a radiative transfer model (in UV and in visible) to examine the impact of OC on UV and visible

radiation at the surface for varying smoke concentrations and height distributions. The Tropospheric Ultraviolet and Visible (TUV) Radiation Model with aerosol optical properties determined for various FLAME fuels [Madronich, 1993]. Aerosol optical properties based on the observations from FLAME can be assigned to explore the impacts of the emissions from fires of varying MCE. The radiative transfer code will also provide an estimate of the error in predicted UV fluxes and photolysis rates that results from ignoring the light absorbing organic carbon emitted by biomass burning.

Third, the differences in EC and OC measurements obtained by different TOA protocols will be explored further using a newly developed thermal optical analysis method, spectral evolved gas analysis (S-EGA). S-EGA analysis is a thermal optical analysis method in which the light transmittance through the sample filter is monitored at multiple wavelengths, rather than the single wavelength currently used by both the IMPROVE_A and modified NIOSH 5040/Sunset methods. This provides additional information regarding the wavelength-dependence of the material in the sample as it evolves during the analysis, and potentially a better measure of POC formation, which is strongly wavelength-dependent.

Another question raised by the results presented in this work involves the partitioning of semivolatile material emitted by biomass burning between the gas and aerosol phases. Gas-phase adsorption artifacts on filters and the OC fraction of TOOC were both functions of OC concentration, suggesting that gas-particle partitioning varied during FLAME. Additional measurements designed to produce a wider range of aerosol concentrations could verify this, and assess the fraction of organic material emitted by fires that is semi-volatile. TOOC emissions could be more accurately quantified by addition of gas-phase instrumentation, such as open path

FTIR, to quantify the concentrations of oxidized-volatile organic compounds not detected by GC-FID. This could provide a better estimate of the potential mass available for SOA formation or condensation on pre-existing smoke particles as plumes age. Aging effects could also be explored through smog chamber studies in which smoke produced by fires is artificially 'aged' by various atmospheric oxidants introduced to the chamber, or produced by photochemical reactions involving gases emitted by the fire itself.

Additional statistical analyses may provide more insight into the FLAME data set and light attenuation measurements. The non-linear regression approach I used to determine the attenuation Ångström exponents could be refined using a Box-Cox transformation. Regression techniques require that the residuals to the fit be normally distributed. A Box-Cox transformation is one particular method for parameterizing the power transformation to obtain more normally distributed residuals. Analysis of variance (ANOVA) would partition the observed variance in a number of the results shown here into several explanatory variables. For example, ANOVA could explain the fraction of variance in the emission factor for a particular aerosol species into that due to MCE, fuel water content, mass loading, burn rate, or any other combination of parameters.

The real-time data could also be explored further using other measurements that, at the time of writing, were being processed and analyzed. The aerosol mass spectrometer that sampled during the FLAME 2 stack burns will provide additional information regarding real-time aerosol composition that could be compared with real-time optical measurements. This could provide additional information regarding the mass scattering and absorption efficiencies, and possibly provide links between combustion phase, aerosol composition, and optical

properties such as the Ångström exponents for scattering and absorption. Photoacoustic absorption measurements were only available for FLAME 1 at the time of writing, so when FLAME 2 data become available this will roughly double the number of fire-integrated samples that could be examined, and provide over 100 additional stack burns with real-time data regarding scattering and absorption.

In this work, aerosol optical property measurements have been examined using combustion and composition data, but aerosol size distributions and refractive index measurements were also performed during the FLAME 1 chamber burns and the FLAME 2 stack and chamber burns. Aerosol size plays a major role in determining the scattering and absorbing behavior of the particles, so it would be worthwhile to examine the size distribution and refractive index results to determine if there is any evidence of changes in particle size or refractive index for different fuels and/or combustion behaviors. For example, the results presented here could not determine if the emitted particles with higher scattering efficiencies had higher scattering efficiencies because they were larger in size, or had a higher refractive index.

References

- Abu-Rahmah, A., W. P. Arnott, and H. Moosmuller (2006), Integrating nephelometer with a low truncation angle and an extended calibration scheme, *Measurement Science & Technology*, 17(7), 1723-1732.
- Alexandrov, M. D., A. A. Lacis, B. E. Carlson, and B. Cairns (2002), Remote sensing of atmospheric aerosols and trace gases by means of multifilter rotating shadowband radiometer. Part I: Retrieval algorithm, *Journal of the Atmospheric Sciences*, 59(3), 524-543.
- Allen, C. D., M. Savage, D. A. Falk, K. F. Suckling, T. W. Swetnam, T. Schulke, P. B. Stacey, P. Morgan, M. Hoffman, and J. T. Klingel (2002), Ecological restoration of Southwestern ponderosa pine ecosystems: A broad perspective, *Ecological Applications*, 12(5), 1418-1433.
- Ames, R. B., and W. C. Malm (2001), Chemical species' contributions to the upper extremes of aerosol fine mass, *Atmos. Environ.*, 35(30), 5193-5204.
- Anderson, T. L., D. S. Covert, S. F. Marshall, M. L. Laucks, R. J. Charlson, A. P. Waggoner, J. A. Ogren, R. Caldow, R. L. Holm, F. R. Quant, G. J. Sem, A. Wiedensohler, N. A. Ahlquist, and T. S. Bates (1996), Performance characteristics of a high-sensitivity, three-wavelength, total scatter/backscatter nephelometer, *Journal of Atmospheric and Oceanic Technology*, 13(5), 967-986.
- Anderson, T. L., and J. A. Ogren (1998), Determining aerosol radiative properties using the TSI 3563 integrating nephelometer, *Aerosol Sci. Technol.*, 29(1), 57-69.
- Andreae, M. O., and P. J. Crutzen (1997), Atmospheric aerosols: Biogeochemical sources and role in atmospheric chemistry, *Science*, 276(5315), 1052-1058.
- Andreae, M. O., and P. Merlet (2001), Emission of trace gases and aerosols from biomass burning, *Global Biogeochemical Cycles*, 15(4), 955-966.
- Andreae, M. O., and A. Gelencser (2006), Black carbon or brown carbon? The nature of light-absorbing carbonaceous aerosols, *Atmos. Chem. Phys.*, 6, 3131-3148.
- Arnott, W. P., H. Moosmuller, C. F. Rogers, T. F. Jin, and R. Bruch (1999), Photoacoustic spectrometer for measuring light absorption by aerosol: instrument description, *Atmos. Environ.*, 33(17), 2845-2852.
- Arnott, W. P., H. Moosmuller, and J. W. Walker (2000), Nitrogen dioxide and kerosene-flame soot calibration of photoacoustic instruments for measurement of light absorption by aerosols, *Review of Scientific Instruments*, 71(12), 4545-4552.
- Arnott, W. P., H. Moosmuller, P. J. Sheridan, J. A. Ogren, R. Rasp, W. V. Slaton, J. L. Hand, S. M. Kreidenweis, and J. L. Collett (2003), Photoacoustic and filter-based ambient aerosol light absorption measurements: Instrument comparisons and the role of relative humidity, *J. Geophys. Res.*, 108(D1), doi:10.1029/2002JD002165.

- Arnott, W. P., K. Hamasha, H. Moosmuller, P. J. Sheridan, and J. A. Ogren (2005a), Towards aerosol light-absorption measurements with a 7-wavelength Aethalometer: Evaluation with a photoacoustic instrument and 3-wavelength nephelometer, *Aerosol Sci. Technol.*, 39(1), 17-29.
- Arnott, W. P., B. Zielinska, C. F. Rogers, J. Sagebiel, K. H. Park, J. Chow, H. Moosmuller, J. G. Watson, K. Kelly, D. Wagner, A. Sarofim, J. Lighty, and G. Palmer (2005b), Evaluation of 1047-nm photoacoustic instruments and photoelectric aerosol sensors in source-sampling of black carbon aerosol and particle-bound PAHs from gasoline and diesel powered vehicles, *Environ. Sci. Technol.*, 39(14), 5398-5406.
- Bae, M. S., J. J. Schauer, J. T. DeMinter, J. R. Turner, D. Smith, and R. A. Cary (2004), Validation of a semi-continuous instrument for elemental carbon and organic carbon using a thermal-optical method, *Atmos. Environ.*, 38(18), 2885-2893.
- Bench, G., and P. Herckes (2004), Measurement of contemporary and fossil carbon contents of PM_{2.5} aerosols: Results from Turtleback Dome, Yosemite National Park, *Environ. Sci. Technol.*, 38(8), 2424-2427.
- Bergstrom, R. W., P. Pilewskie, P. B. Russell, J. Redemann, T. C. Bond, P. K. Quinn, and B. Sierau (2007), Spectral absorption properties of atmospheric aerosols, *Atmos. Chem. Phys.*, 7(23), 5937-5943.
- Bertschi, I., R. J. Yokelson, D. E. Ward, R. E. Babbitt, R. A. Susott, J. G. Goode, and W. M. Hao (2003), Trace gas and particle emissions from fires in large diameter and belowground biomass fuels, *J. Geophys. Res.*, 108(D13), doi:10.1029/2002JD002100.
- Birch, M. E., and R. A. Cary (1996), Elemental carbon-based method for monitoring occupational exposures to particulate diesel exhaust, *Aerosol Sci. Technol.*, 25(3), 221-241.
- Birch, M. E. (1998), Analysis of carbonaceous aerosols: interlaboratory comparison, *Analyst*, 123(5), 851-857.
- Bohren, C. F., and D. R. Huffman (1983), *Absorption and scattering of light by small particles*, Wiley-Interscience, New York.
- Bond, T. C., T. L. Anderson, and D. Campbell (1999a), Calibration and intercomparison of filter-based measurements of visible light absorption by aerosols, *Aerosol Sci. Technol.*, 30(6), 582-600.
- Bond, T. C., M. Bussemer, B. Wehner, S. Keller, R. J. Charlson, and J. Heintzenberg (1999b), Light absorption by primary particle emissions from a lignite burning plant, *Environ. Sci. Technol.*, 33(21), 3887-3891.
- Bond, T. C. (2001), Spectral dependence of visible light absorption by carbonaceous particles emitted from coal combustion, *Geophys. Res. Lett.*, 28(21), 4075-4078.
- Bond, T. C., D. S. Covert, J. C. Kramlich, T. V. Larson, and R. J. Charlson (2002), Primary particle emissions from residential coal burning: Optical properties and size distributions, *J. Geophys. Res.*, 107(D21), doi:10.1029/2001JD000571.
- Bond, T. C., and R. W. Bergstrom (2006), Light absorption by carbonaceous particles: An investigative review, *Aerosol Sci. Technol.*, 40(1), 27-67.
- Bond, T. C., G. Habib, and R. W. Bergstrom (2006), Limitations in the enhancement of visible light absorption due to mixing state, *J. Geophys. Res.*, 111(D20), 13,

doi:10.1029/2006JD007315.

- Brioude, J., O. R. Cooper, M. Trainer, T. B. Ryerson, J. S. Holloway, T. Baynard, J. Peischl, C. Warneke, J. A. Neuman, J. De Gouw, A. Stohl, S. Eckhardt, G. J. Frost, S. A. McKeen, E. Y. Hsie, F. C. Fehsenfeld, and P. Nedelec (2007), Mixing between a stratospheric intrusion and a biomass burning plume, *Atmos. Chem. Phys.*, 7(16), 4229-4235.
- Brown, J. K., and L. S. Bradshaw (1994), Comparisons of particulate-emissions and smoke impacts from presettlement, full suppression, and prescribed natural fire period in the Selway-Bitterroot Wilderness, *International Journal of Wildland Fire*, 4(3), 143-155.
- Brown, S. G., P. Herckes, L. Ashbaugh, M. P. Hannigan, S. M. Kreidenweis, and J. L. Collett (2002), Characterization of organic aerosol in Big Bend National Park, Texas, *Atmos. Environ.*, 36(38), 5807-5818.
- Cachier, H., C. Lioussé, P. Buatmenard, and A. Gaudichet (1995), Particulate content of savanna fire emissions, *Journal of Atmospheric Chemistry*, 22(1-2), 123-148.
- Chakrabarty, R. K., H. Moosmuller, M. A. Garro, W. P. Arnott, J. Walker, R. A. Susott, R. E. Babbitt, C. E. Wold, E. N. Lincoln, and W. M. Hao (2006), Emissions from the laboratory combustion of wildland fuels: Particle morphology and size, *J. Geophys. Res.*, 111(D7), doi:10.1029/2005JD006659.
- Chand, D., O. Schmid, P. Gwaze, R. S. Parmar, G. Helas, K. Zeromskiene, A. Wiedensohler, A. Massling, and M. O. Andreae (2005), Laboratory measurements of smoke optical properties from the burning of Indonesian peat and other types of biomass, *Geophys. Res. Lett.*, 32(12), doi:10.1029/2005GL022678.
- Chand, D., P. Guyon, P. Artaxo, O. Schmid, G. P. Frank, L. V. Rizzo, O. L. Mayol-Bracero, L. V. Gatti, and M. O. Andreae (2006), Optical and physical properties of aerosols in the boundary layer and free troposphere over the Amazon Basin during the biomass burning season, *Atmos. Chem. Phys.*, 6, 2911-2925.
- Chen, L. W. A., J. C. Chow, J. G. Watson, H. Moosmuller, and W. P. Arnott (2004), Modeling reflectance and transmittance of quartz-fiber filter samples containing elemental carbon particles: Implications for thermal/optical analysis, *J. Aerosol. Sci.*, 35(6), 765-780.
- Chen, L. W. A., H. Moosmuller, W. P. Arnott, J. C. Chow, and J. G. Watson (2006), Particle emissions from laboratory combustion of wildland fuels: In situ optical and mass measurements, *Geophys. Res. Lett.*, 33(4), 4, doi:10.1029/2005GL024838.
- Chen, L. W. A., H. Moosmuller, W. P. Arnott, J. C. Chow, J. G. Watson, R. A. Susott, R. E. Babbitt, C. E. Wold, E. N. Lincoln, and W. M. Hao (2007), Emissions from laboratory combustion of wildland fuels: Emission factors and source profiles, *Environ. Sci. Technol.*, 41(12), 4317-4325.
- Chow, J. C., J. G. Watson, L. C. Pritchett, W. R. Pierson, C. A. Frazier, and R. G. Purcell (1993), The DRI Thermal Optical Reflectance carbon analysis system - Description, evaluation and applications in United States air quality studies, *Atmospheric Environment Part a-General Topics*, 27(8), 1185-1201.
- Chow, J. C., J. G. Watson, D. Crow, D. H. Lowenthal, and T. Merrifield (2001), Comparison of IMPROVE and NIOSH carbon measurements, *Aerosol Sci. Technol.*, 34(1), 23-34.
- Chow, J. C., J. G. Watson, L. W. A. Chen, W. P. Arnott, and H. Moosmuller (2004), Equivalence of elemental carbon by thermal/optical reflectance and transmittance with different

- temperature protocols, *Environ. Sci. Technol.*, 38(16), 4414-4422.
- Chow, J. C., J. G. Watson, P. K. K. Louie, L. W. A. Chen, and D. Sin (2005), Comparison of PM_{2.5} carbon measurement methods in Hong Kong, China, *Environ. Pollut.*, 137(2), 334-344.
- Chow, J. C., J. G. Watson, L. W. A. Chen, M. C. O. Chang, N. F. Robinson, D. Trimble, and S. Kohl (2007), The IMPROVE-A temperature protocol for thermal/optical carbon analysis: maintaining consistency with a long-term database, *Journal of the Air & Waste Management Association*, 57(9), 1014-1023.
- Christian, T. J., B. Kleiss, R. J. Yokelson, R. Holzinger, P. J. Crutzen, W. M. Hao, B. H. Saharjo, and D. E. Ward (2003), Comprehensive laboratory measurements of biomass-burning emissions: 1. Emissions from Indonesian, African, and other fuels, *J. Geophys. Res.*, 108(D23), 4719, doi:10.1029/2003JD003704.
- Christian, T. J., B. Kleiss, R. J. Yokelson, R. Holzinger, P. J. Crutzen, W. M. Hao, T. Shirai, and D. R. Blake (2004), Comprehensive laboratory measurements of biomass-burning emissions: 2. First intercomparison of open-path FTIR, PTR-MS, and GC-MS/FID/ECD, *J. Geophys. Res.*, 109(D2), 12, doi:10.1029/JD2003JD003874.
- Christian, T. J., R. J. Yokelson, J. A. Carvalho, D. W. T. Griffith, E. C. Alvarado, J. C. Santos, T. G. S. Neto, C. A. G. Veras, and W. M. Hao (2007), The tropical forest and fire emissions experiment: Trace gases emitted by smoldering logs and dung from deforestation and pasture fires in Brazil, *J. Geophys. Res.*, 112(D18), D18308, doi:10.1029/2006JD008147.
- Chung, S. H., and J. H. Seinfeld (2002), Global distribution and climate forcing of carbonaceous aerosols, *J. Geophys. Res.*, 107(D19), doi:10.1029/2001JD001397.
- Clarke, A., C. McNaughton, V. Kapustin, Y. Shinozuka, S. Howell, J. Dibb, J. Zhou, B. Anderson, V. Brekhovskikh, H. Turner, and M. Pinkerton (2007), Biomass burning and pollution aerosol over North America: Organic components and their influence on spectral optical properties and humidification response, *J. Geophys. Res.*, 112(D12), doi:10.1029/2006JD007777.
- Clinton, N. E., P. Gong, and K. Scott (2006), Quantification of pollutants emitted from very large wildland fires in Southern California, USA, *Atmos. Environ.*, 40(20), 3686-3695.
- Colarco, P. R., M. R. Schoeberl, B. G. Doddridge, L. T. Marufu, O. Torres, and E. J. Welton (2004), Transport of smoke from Canadian forest fires to the surface near Washington, D. C.: Injection height, entrainment, and optical properties, *J. Geophys. Res.*, 109(D6), doi:10.1029/2003JD004248.
- Collins, B. M., P. N. Omi, and P. L. Chapman (2006), Regional relationships between climate and wildfire-burned area in the Interior West, USA, *Can. J. For. Res.-Rev. Can. Rech. For.*, 36(3), 699-709.
- Cooke, W. F., C. Lioussé, H. Cachier, and J. Feichter (1999), Construction of a 1 degrees x 1 degrees fossil fuel emission data set for carbonaceous aerosol and implementation and radiative impact in the ECHAM4 model, *J. Geophys. Res.*, 104(D18), 22137-22162.
- Countess, R. J. (1990), Interlaboratory analyses of carbonaceous aerosol samples, *Aerosol Sci. Technol.*, 12(1), 114-121.
- Cronan, C. S., and G. R. Aiken (1985), Chemistry and transport of soluble humic substances in forested watersheds of the Adirondack Park, New York, *Geochimica Et Cosmochimica*

Acta, 49(8), 1697-1705.

- Crutzen, P. J., and M. O. Andreae (1990), Biomass burning in the tropics - Impact on atmospheric chemistry and biogeochemical cycles, *Science*, 250(4988), 1669-1678.
- Damoah, R., N. Spichtinger, C. Forster, P. James, I. Mattis, U. Wandinger, S. Beirle, T. Wagner, and A. Stohl (2004), Around the world in 17 days - hemispheric-scale transport of forest fire smoke from Russia in May 2003, *Atmos. Chem. Phys.*, 4, 1311-1321.
- Decesari, S., S. Fuzzi, M. C. Facchini, M. Mircea, L. Emblico, F. Cavalli, W. Maenhaut, X. Chi, G. Schkolnik, A. Falkovich, Y. Rudich, M. Claeys, V. Pashynska, G. Vas, I. Kourtchev, R. Vermeylen, A. Hoffer, M. O. Andreae, E. Tagliavini, F. Moretti, and P. Artaxo (2006), Characterization of the organic composition of aerosols from Rondonia, Brazil, during the LBA-SMOCC 2002 experiment and its representation through model compounds, *Atmos. Chem. Phys.*, 6, 375-402.
- Deuze, J. L., P. Goloub, M. Herman, A. Marchand, G. Perry, S. Susana, and D. Tanre (2000), Estimate of the aerosol properties over the ocean with POLDER, *J. Geophys. Res.*, 105(D12), 15329-15346.
- Deuze, J. L., F. M. Breon, C. Devaux, P. Goloub, M. Herman, B. Lafrance, F. Maignan, A. Marchand, F. Nadal, G. Perry, and D. Tanre (2001), Remote sensing of aerosols over land surfaces from POLDER-ADEOS-1 polarized measurements, *J. Geophys. Res.*, 106(D5), 4913-4926.
- Dillon, M. B., M. S. Lamanna, G. W. Schade, A. H. Goldstein, and R. C. Cohen (2002), Chemical evolution of the Sacramento urban plume: Transport and oxidation, *J. Geophys. Res.*, 107(D5-6), doi:10.1029/2001JD000969.
- Diner, D. J., J. C. Beckert, T. H. Reilly, C. J. Bruegge, J. E. Conel, R. A. Kahn, J. V. Martonchik, T. P. Ackerman, R. Davies, S. A. W. Gerstl, H. R. Gordon, J. P. Muller, R. B. Myneni, P. J. Sellers, B. Pinty, and M. M. Verstraete (1998), Multi-angle Imaging SpectroRadiometer (MISR) - Instrument description and experiment overview, *Ieee Transactions on Geoscience and Remote Sensing*, 36(4), 1072-1087.
- Donahue, N. M., A. L. Robinson, C. O. Stanier, and S. N. Pandis (2006), Coupled partitioning, dilution, and chemical aging of semivolatile organics, *Environ. Sci. Technol.*, 40(8), 2635-2643.
- Dubovik, O., B. N. Holben, T. Lapyonok, A. Sinyuk, M. I. Mishchenko, P. Yang, and I. Slutsker (2002), Non-spherical aerosol retrieval method employing light scattering by spheroids, *Geophys. Res. Lett.*, 29(10), doi:10.1029/2001GL014506.
- Duncan, B. N., R. V. Martin, A. C. Staudt, R. Yevich, and J. A. Logan (2003), Interannual and seasonal variability of biomass burning emissions constrained by satellite observations, *J. Geophys. Res.*, 108(D2), doi:10.1029/2002JD002378.
- Echalar, F., A. Gaudichet, H. Cachier, and P. Artaxo (1995), Aerosol emissions by tropical forest and savanna biomass burning - Characteristic trace-elements and fluxes, *Geophys. Res. Lett.*, 22(22), 3039-3042.
- Eck, T. F., B. N. Holben, J. S. Reid, O. Dubovik, A. Smirnov, N. T. O'Neill, I. Slutsker, and S. Kinne (1999), Wavelength dependence of the optical depth of biomass burning, urban, and desert dust aerosols, *J. Geophys. Res.*, 104(D24), 31333-31349.
- Eck, T. F., B. N. Holben, D. E. Ward, O. Dubovik, J. S. Reid, A. Smirnov, M. M. Mukelabai, N. C.

- Hsu, N. T. O'Neill, and I. Slutsker (2001), Characterization of the optical properties of biomass burning aerosols in Zambia during the 1997 ZIBBEE field campaign, *J. Geophys. Res.*, 106(D4), 3425-3448.
- Elliot-Fisk, D. L. (1988), The boreal forest, in *North American terrestrial vegetation*, edited by M. G. Barbour and W. D. Billings, pp. 33-62, Cambridge University Press, Cambridge.
- Engling, G., C. M. Carrico, S. M. Kreidenweis, J. L. Collett, D. E. Day, W. C. Malm, E. Lincoln, W. M. Hao, Y. Iinuma, and H. Herrmann (2006a), Determination of levoglucosan in biomass combustion aerosol by high-performance anion-exchange chromatography with pulsed amperometric detection, *Atmos. Environ.*, 40, S299-S311.
- Engling, G., P. Herckes, S. M. Kreidenweis, W. C. Malm, and J. L. Collett (2006b), Composition of the fine organic aerosol in Yosemite National Park during the 2002 Yosemite Aerosol Characterization Study, *Atmos. Environ.*, 40(16), 2959-2972.
- Ferek, R. J., J. S. Reid, P. V. Hobbs, D. R. Blake, C. Lioussse, and Vl (1998), Emission factors of hydrocarbons, halocarbons, trace gases and particles from biomass burning in Brazil, *J. Geophys. Res.*, 103(D24), 32107-32118.
- Fernandes, S. D., N. M. Trautmann, D. G. Streets, C. A. Roden, and T. C. Bond (2007), Global biofuel use, 1850-2000, *Global Biogeochemical Cycles*, 21(2), doi:Gb2019 Artn gb2019.
- Fine, P. M., G. R. Cass, and B. R. T. Simoneit (2001), Chemical characterization of fine particle emissions from fireplace combustion of woods grown in the northeastern United States, *Environ. Sci. Technol.*, 35(13), 2665-2675.
- Fites-Kaufman, J. A., P. Rundel, N. Stephenson, and D. A. Weixelman (2007), Montane and subalpine vegetation in the Sierra Nevada and Cascade ranges, in *Terrestrial vegetation of California*, edited by M. G. Barbour, et al., pp. 456-501, University of California Press, Los Angeles.
- Flagan, R. C., and J. H. Seinfeld (1988), *Fundamentals of air pollution engineering*, Prentice Hall, Englewood Cliffs, New Jersey.
- Foot, J. S., and C. G. Kilsby (1989), Absorption of light by aerosol particles - An intercomparison of techniques and spectral observations, *Atmos. Environ.*, 23(2), 489-495.
- Formenti, P., W. Elbert, W. Maenhaut, J. Haywood, S. Osborne, and M. O. Andreae (2003), Inorganic and carbonaceous aerosols during the Southern African Regional Science Initiative (SAFARI 2000) experiment: Chemical characteristics, physical properties, and emission data for smoke from African biomass burning, *J. Geophys. Res.*, 108(D13), doi:10.1029/2002JD002408.
- Forster, C., U. Wandinger, G. Wotawa, P. James, I. Mattis, D. Althausen, P. Simmonds, S. O'Doherty, S. G. Jennings, C. Kleefeld, J. Schneider, T. Trickl, S. Kreipl, H. Jager, and A. Stohl (2001), Transport of boreal forest fire emissions from Canada to Europe, *J. Geophys. Res.*, 106(D19), 22887-22906.
- Forster, P., Ramaswamy, A. P. V, T. Berntsen, R. Betts, D. W. Fahey, J. Haywood, J. Lean, D. C. Lowe, M. G. N. J, R. Prinn, G. Raga, M. Schulz, and R. Van Dorland (2007), Changes in atmospheric constituents and in radiative forcing, in *Climate change 2007: The physical science basis. Contribution of Working Group I to the Fourth Assessment Report on the Intergovernmental Panel on Climate Change*, edited by S. Solomon, et al., Cambridge

University Press, Cambridge.

- Franklin, J. F. (1988), Pacific northwest forests, in *North American terrestrial vegetation*, edited by M. G. Barbour and W. D. Billings, pp. 103-130, Cambridge University Press, Cambridge.
- Freeborn, P. H., M. J. Wooster, W. M. Hao, C. A. Ryan, B. L. Nordgren, S. P. Baker, and C. Ichoku (2008), Relationships between energy release, fuel mass loss, and trace gas and aerosol emissions during laboratory biomass fires, *J. Geophys. Res.*, 113(D1), D01301, doi:10.1029/2007JD008679.
- French, N. H. F., E. S. Kasischke, and D. G. Williams (2002), Variability in the emission of carbon-based trace gases from wildfire in the Alaskan boreal forest, *J. Geophys. Res.*, 108(D1), doi:10.1029/2001JD000480.
- Frenklach, M. (2002), Reaction mechanism of soot formation in flames, *Physical Chemistry Chemical Physics*, 4(11), 2028-2037.
- Fuller, K. A., W. C. Malm, and S. M. Kreidenweis (1999), Effects of mixing on extinction by carbonaceous particles, *J. Geophys. Res.*, 104(D13), 15941-15954.
- Fung, K. (1990), Particulate carbon speciation by MnO₂ oxidation, *Aerosol Sci. Technol.*, 12(1), 122-127.
- Fuzzi, S., S. Decesari, M. C. Facchini, E. Matta, M. Mircea, and E. Tagliavini (2001), A simplified model of the water soluble organic component of atmospheric aerosols, *Geophys. Res. Lett.*, 28(21), 4079-4082.
- Gao, S., D. A. Hegg, P. V. Hobbs, T. W. Kirchstetter, B. I. Magi, and M. Sadilek (2003), Water-soluble organic components in aerosols associated with savanna fires in southern Africa: Identification, evolution, and distribution, *J. Geophys. Res.*, 108(D13), doi:8491 Artn 8491.
- Gelencser, A., A. Hoffer, G. Kiss, E. Tombacz, R. Kurdi, and L. Bencze (2003), In-situ formation of light-absorbing organic matter in cloud water, *Journal of Atmospheric Chemistry*, 45(1), 25-33.
- Giglio, L., I. Csiszar, and C. O. Justice (2006a), Global distribution and seasonality of active fires as observed with the Terra and Aqua Moderate Resolution Imaging Spectroradiometer (MODIS) sensors, *Journal of Geophysical Research-Biogeosciences*, 111(G2), doi:10.1029/2005JG000142.
- Giglio, L., G. R. van der Werf, J. T. Randerson, G. J. Collatz, and P. Kasibhatla (2006b), Global estimation of burned area using MODIS active fire observations, *Atmos. Chem. Phys.*, 6, 957-974.
- Goode, J. G., R. J. Yokelson, R. A. Susott, and D. E. Ward (1999), Trace gas emissions from laboratory biomass fires measured by open-path Fourier transform infrared spectroscopy: Fires in grass and surface fuels, *J. Geophys. Res.*, 104(D17), 21237-21245.
- Goode, J. G., R. J. Yokelson, D. E. Ward, R. A. Susott, R. E. Babbitt, M. A. Davies, and W. M. Hao (2000), Measurements of excess O₃, CO₂, CO, CH₄, C₂H₄, C₂H₂, HCN, NO, NH₃, HCOOH, CH₃COOH, HCHO, and CH₃OH in 1997 Alaskan biomass burning plumes by airborne fourier transform infrared spectroscopy (AFTIR), *J. Geophys. Res.*, 105(D17), 22147-22166.
- Gorin, C. A., J. L. Collett, and P. Herckes (2006), Wood smoke contribution to winter aerosol in

- Fresno, CA, *Journal of the Air & Waste Management Association*, 56(11), 1584-1590.
- Graber, E. R., and Y. Rudich (2006), Atmospheric HULIS: How humic-like are they? A comprehensive and critical review, *Atmos. Chem. Phys.*, 6, 729-753.
- Green, M., and J. Xu (2007), Causes of haze in the Columbia River Gorge, *Journal of the Air & Waste Management Association*, 57(8), 947-958.
- Gregoire, J. M., K. Tansey, and J. M. N. Silva (2003), The GBA2000 initiative: developing a global burnt area database from SPOT-VEGETATION imagery, *Int. J. Remote Sens.*, 24(6), 1369-1376.
- Gross, D. S., M. E. Galli, M. Kalberer, A. S. H. Prevot, J. Dommen, M. R. Alfarra, J. Duplissy, K. Gaeggeler, A. Gascho, A. Metzger, and U. Baltensperger (2006), Real-time measurement of oligomeric species in secondary organic aerosol with the aerosol time-of-flight mass spectrometer, *Anal. Chem.*, 78(7), 2130-2137.
- Haines, T. K., R. L. Busby, and D. A. Cleaves (2001), Prescribed burning in the south: trends, purpose, and barriers, *Southern Journal of Applied Forestry*, 25(4), 149-153.
- Hand, J. L., and W. C. Malm (2007), Review of aerosol mass scattering efficiencies from ground-based measurements since 1990, *J. Geophys. Res.*, 112(D18), 24, doi:10.1029/2007JD008484.
- Hansen, A. D. A., H. Rosen, and T. Novakov (1984), The Aethalometer - An instrument for the real-time measurement of optical absorption by aerosol particles, *Science of the Total Environment*, 36(JUN), 191-196.
- Hao, W. M., and M. H. Liu (1994), Spatial and temporal distribution of tropical biomass burning, *Global Biogeochemical Cycles*, 8(4), 495-503.
- Havers, N., P. Burba, J. Lambert, and D. Klockow (1998), Spectroscopic characterization of humic-like substances in airborne particulate matter, *Journal of Atmospheric Chemistry*, 29(1), 45-54.
- Hays, M. D., C. D. Geron, K. J. Linna, N. D. Smith, and J. J. Schauer (2002), Speciation of gas-phase and fine particle emissions from burning of foliar fuels, *Environ. Sci. Technol.*, 36(11), 2281-2295.
- Haywood, J. M., and K. P. Shine (1995), The effect of anthropogenic sulfate and soot aerosol on the clear-sky planetary radiation budget, *Geophys. Res. Lett.*, 22(5), 603-606.
- Haywood, J. M., D. L. Roberts, A. Slingo, J. M. Edwards, and K. P. Shine (1997), General circulation model calculations of the direct radiative forcing by anthropogenic sulfate and fossil-fuel soot aerosol, *Journal of Climate*, 10(7), 1562-1577.
- Haywood, J. M., S. R. Osborne, P. N. Francis, A. Keil, P. Formenti, M. O. Andreae, and P. H. Kaye (2003), The mean physical and optical properties of regional haze dominated by biomass burning aerosol measured from the C-130 aircraft during SAFARI 2000, *J. Geophys. Res.*, 108(D13), doi:10.1029/2002JD002226.
- Heald, C. L., D. J. Jacob, P. I. Palmer, M. J. Evans, G. W. Sachse, H. B. Singh, and D. R. Blake (2003), Biomass burning emission inventory with daily resolution: Application to aircraft observations of Asian outflow, *J. Geophys. Res.*, 108(D21), doi:8811 Artn 8811.
- Heald, C. L., A. H. Goldstein, J. D. Allan, A. C. Aiken, E. Apel, E. L. Atlas, A. K. Baker, T. S. Bates, A. J. Beyersdorf, D. R. Blake, T. Campos, H. Coe, J. D. Crounse, P. F. DeCarlo, J. A. de Gouw, E. J. Dunlea, F. M. Flocke, A. Fried, P. Goldan, R. J. Griffin, S. C. Herndon,

- J. S. Holloway, R. Holzinger, J. L. Jimenez, W. Junkermann, W. C. Kuster, A. C. Lewis, S. Meinardi, D. B. Millet, T. Onasch, A. Polidori, P. K. Quinn, D. D. Riemer, J. M. Roberts, D. Salcedo, B. Sive, A. L. Swanson, R. Talbot, C. Warneke, R. J. Weber, P. Weibring, P. O. Wennberg, D. R. Worsnop, A. E. Wittig, R. Zhang, J. Zheng, and W. Zheng (2008), Total observed organic carbon (TOOC) in the atmosphere: a synthesis of North American observations, *Atmos. Chem. Phys.*, 8(7), 2007-2025.
- Heaton, K. J., M. A. Dreyfus, S. Wang, and M. V. Johnston (2007), Oligomers in the early stage of biogenic secondary organic aerosol formation and growth, *Environ. Sci. Technol.*, 41(17), 6129-6136.
- Hegglin, M. I., U. K. Krieger, T. Koop, and T. Peter (2002), Technical note: Organics-induced fluorescence in Raman studies of sulfuric acid aerosols, *Aerosol Sci. Technol.*, 36(4), 510-512.
- Herman, J. R., P. K. Bhartia, O. Torres, C. Hsu, C. Seftor, and E. Celarier (1997), Global distribution of UV-absorbing aerosols from Nimbus 7/TOMS data, *J. Geophys. Res.*, 102(D14), 16911-16922.
- Hildemann, L. M., G. R. Markowski, and G. R. Cass (1991), Chemical composition of emissions from urban sources of fine organic aerosol, *Environ. Sci. Technol.*, 25(4), 744-759.
- Hille, M. G., and S. L. Stephens (2005), Mixed conifer forest duff consumption during prescribed fires: Tree crown impacts, *Forest Science*, 51(5), 417-424.
- Hodzic, A., S. Madronich, B. Bohn, S. Massie, L. Menut, and C. Wiedinmyer (2007), Wildfire particulate matter in Europe during summer 2003: meso-scale modeling of smoke emissions, transport and radiative effects, *Atmos. Chem. Phys.*, 7(15), 4043-4064.
- Hoffer, A., G. Kiss, M. Blazso, and A. Gelencser (2004), Chemical characterization of humic-like substances (HULIS) formed from a lignin-type precursor in model cloud water, *Geophys. Res. Lett.*, 31(6), doi:10.1029/2003GL018962.
- Hoffer, A., A. Gelencser, P. Guyon, G. Kiss, O. Schmid, G. P. Frank, P. Artaxo, and M. O. Andreae (2006), Optical properties of humic-like substances (HULIS) in biomass-burning aerosols, *Atmos. Chem. Phys.*, 6, 3563-3570.
- Holben, B. N., T. F. Eck, I. Slutsker, D. Tanre, J. P. Buis, A. Setzer, E. Vermote, J. A. Reagan, Y. J. Kaufman, T. Nakajima, F. Lavenu, I. Jankowiak, and A. Smirnov (1998), AERONET - A federated instrument network and data archive for aerosol characterization, *Remote Sensing of Environment*, 66(1), 1-16.
- Holden, Z. A., P. Morgan, M. A. Crimmins, R. K. Steinhorst, and A. M. S. Smith (2007), Fire season precipitation variability influences fire extent and severity in a large southwestern wilderness area, United States, *Geophys. Res. Lett.*, 34(16), doi:10.1029/2007GL030804.
- Hopkins, R. J., K. Lewis, Y. Desyaterik, Z. Wang, A. V. Tivanski, W. P. Arnott, A. Laskin, and M. K. Gilles (2007), Correlations between optical, chemical and physical properties of biomass burn aerosols, *Geophys. Res. Lett.*, 34(18), doi:10.1029/2007GL030502.
- Horvath, H. (1997), Experimental calibration for aerosol light absorption measurements using the integrating plate method - Summary of the data, *J. Aerosol. Sci.*, 28(7), 1149-1161.
- Husar, R. B., J. M. Prospero, and L. L. Stowe (1997), Characterization of tropospheric aerosols over the oceans with the NOAA advanced very high resolution radiometer optical thickness operational product, *J. Geophys. Res.*, 102(D14), 16889-16909.

- Iinuma, Y., E. Brüggemann, T. Gnauk, K. Müller, M. O. Andreae, G. Helas, R. Parmar, and H. Herrmann (2007), Source characterization of biomass burning particles: The combustion of selected European conifers, African hardwood, savanna grass, and German and Indonesian peat, *J. Geophys. Res.*, 112(D8), 26, doi:10.1029/2006JD007120.
- Ito, A., and J. E. Penner (2004), Global estimates of biomass burning emissions based on satellite imagery for the year 2000, *J. Geophys. Res.*, 109(D14), doi:D14s05 Artn d14s05.
- Ito, A., and H. Akimoto (2007), Seasonal and interannual variations in CO and BC emissions from open biomass burning in Southern Africa during 1998-2005, *Global Biogeochemical Cycles*, 21(2), doi:10.1029/2006GB002848.
- Jacobson, M. Z. (1999), Isolating nitrated and aromatic aerosols and nitrated aromatic gases as sources of ultraviolet light absorption, *J. Geophys. Res.*, 104(D3), 3527-3542.
- Jacobson, M. Z. (2001), Global direct radiative forcing due to multicomponent anthropogenic and natural aerosols, *J. Geophys. Res.*, 106(D2), 1551-1568.
- Japar, S. M., A. C. Szkarlat, R. A. Gorse, E. K. Heyerdahl, R. L. Johnson, J. A. Rau, and J. J. Huntzicker (1984), Comparison of solvent-extraction and thermal optical carbon analysis methods - Application to diesel vehicle exhaust aerosol, *Environ. Sci. Technol.*, 18(4), 231-234.
- Johnson, E. A., K. Miyanishi, and J. M. H. Weir (1998), Wildfires in the western Canadian boreal forest: Landscape patterns and ecosystem management, *Journal of Vegetation Science*, 9(4), 603-610.
- Kasischke, E. S., N. L. Christensen, and B. J. Stocks (1995), Fire, global warming, and the carbon balance of boreal forests, *Ecological Applications*, 5(2), 437-451.
- Kaufman, Y. J., D. Tanre, L. A. Remer, E. F. Vermote, A. Chu, and B. N. Holben (1997), Operational remote sensing of tropospheric aerosol over land from EOS moderate resolution imaging spectroradiometer, *J. Geophys. Res.*, 102(D14), 17051-17067.
- Kaufman, Y. J., C. Ichoku, L. Giglio, S. Korontzi, D. A. Chu, W. M. Hao, R. R. Li, and C. O. Justice (2003), Fire and smoke observed from the Earth Observing System MODIS instrument - products, validation, and operational use, *Int. J. Remote Sens.*, 24(8), 1765-1781.
- Keeley, J. E., and F. W. Davis (2007), Chaparral, in *Terrestrial vegetation of California*, edited by M. G. Barbour, et al., pp. 339-366, University of California Press, Los Angeles.
- Keene, W. C., R. M. Lobert, P. J. Crutzen, J. R. Maben, D. H. Scharffe, T. Landmann, C. Hely, and C. Brain (2006), Emissions of major gaseous and particulate species during experimental burns of southern African biomass, *J. Geophys. Res.*, 111(D4), doi:10.1029/2005JD006319.
- Keshtkar, H., and L. L. Ashbaugh (2007), Size distribution of polycyclic aromatic hydrocarbon particulate emission factors from agricultural burning, *Atmos. Environ.*, 41(13), 2729-2739.
- King, M. D., Y. J. Kaufman, D. Tanre, and T. Nakajima (1999), Remote sensing of tropospheric aerosols from space: Past, present, and future, *Bulletin of the American Meteorological Society*, 80(11), 2229-2259.
- Kirchstetter, T. W., C. E. Corrigan, and T. Novakov (2001), Laboratory and field investigation

- of the adsorption of gaseous organic compounds onto quartz filters, *Atmos. Environ.*, 35(9), 1663-1671.
- Kirchstetter, T. W., T. Novakov, and P. V. Hobbs (2004), Evidence that the spectral dependence of light absorption by aerosols is affected by organic carbon, *J. Geophys. Res.*, 109(D21), 12, doi:10.1029/2004JD004999.
- Kirchstetter, T. W., and T. Novakov (2007), Controlled generation of black carbon particles from a diffusion flame and applications in evaluating black carbon measurement methods, *Atmos. Environ.*, 41(9), 1874-1888.
- Kitzberger, T., P. M. Brown, E. K. Heyerdahl, T. W. Swetnam, and T. T. Veblen (2007), Contingent Pacific-Atlantic Ocean influence on multicentury wildfire synchrony over western North America, *Proc. Natl. Acad. Sci. U. S. A.*, 104(2), 543-548.
- Koch, D. (2001), Transport and direct radiative forcing of carbonaceous and sulfate aerosols in the GISS GCM, *J. Geophys. Res.*, 106(D17), 20311-20332.
- Koch, D., T. C. Bond, D. Streets, N. Unger, and G. R. van der Werf (2007), Global impacts of aerosols from particular source regions and sectors, *J. Geophys. Res.*, 112(D2), doi:10.1029/2005JD007024.
- Kreidenweis, S. M., L. A. Remer, R. Bruintjes, and O. Dubovik (2001), Smoke aerosol from biomass burning in Mexico: Hygroscopic smoke optical model, *J. Geophys. Res.*, 106(D5), 4831-4844.
- Krotkov, N., P. K. Bhartia, J. Herman, J. Slusser, G. Scott, G. Labow, A. P. Vasilkov, T. F. Eck, O. Dubovik, and B. N. Holben (2005), Aerosol ultraviolet absorption experiment (2002 to 2004), part 2: absorption optical thickness, refractive index, and single scattering albedo, *Optical Engineering*, 44(4), doi:10.1117/1.1886819.
- Lamanna, M. S., and A. H. Goldstein (1999), In situ measurements of C-2-C-10 volatile organic compounds above a Sierra Nevada ponderosa pine plantation, *J. Geophys. Res.*, 104(D17), 21247-21262.
- Lee, T., S. M. Kreidenweis, and J. L. Collett (2004), Aerosol ion characteristics during the Big Bend Regional Aerosol and Visibility Observational Study, *Journal of the Air & Waste Management Association*, 54(5), 585-592.
- Levelt, P. F., G. H. J. Van den Oord, M. R. Dobber, A. Malkki, H. Visser, J. de Vries, P. Stammes, J. O. V. Lundell, and H. Saari (2006), The Ozone Monitoring Instrument, *Ieee Transactions on Geoscience and Remote Sensing*, 44(5), 1093-1101.
- Lewis, K., W. P. Arnott, H. Moosmuller, and C. E. Wold (in press), Strong spectral variation of biomass smoke light absorption and single scattering albedo observed with a novel dual wavelength photoacoustic instrument, *J. Geophys. Res.*, doi:10.1029/2007JD009699.
- Lim, H. J., B. J. Turpin, E. Edgerton, S. V. Hering, G. Allen, H. Maring, and P. Solomon (2003), Semicontinuous aerosol carbon measurements: Comparison of Atlanta Supersite measurements, *J. Geophys. Res.*, 108(D7), 12, doi:10.1029/2001JD001214.
- Limbeck, A., M. Kulmala, and H. Puxbaum (2003), Secondary organic aerosol formation in the atmosphere via heterogeneous reaction of gaseous isoprene on acidic particles, *Geophys. Res. Lett.*, 30(19), doi:10.1029/2003GL017738.
- Lindberg, J. D., R. E. Douglass, and D. M. Garvey (1999), Atmospheric particulate absorption and black carbon measurement, *Applied Optics*, 38(12), 2369-2376.

- Lioussé, C., J. E. Penner, C. Chuang, J. J. Walton, H. Eddleman, and H. Cachier (1996), A global three-dimensional model study of carbonaceous aerosols, *J. Geophys. Res.*, *101*(D14), 19411-19432.
- Lipsky, E. M., and A. L. Robinson (2005), Design and evaluation of a portable dilution sampling system for measuring fine particle emissions from combustion systems, *Aerosol Sci. Technol.*, *39*(6), 542-553.
- Lipsky, E. M., and A. L. Robinson (2006), Effects of dilution on fine particle mass and partitioning of semivolatile organics in diesel exhaust and wood smoke, *Environ. Sci. Technol.*, *40*(1), 155-162.
- Lobert, J. M., D. H. Scharffe, W. M. Hao, T. A. Kuhlbusch, R. Seuwen, P. Warneck, and P. J. Crutzen (1991), Experimental evaluation of biomass burning emissions: Nitrogen and carbon containing compounds, in *Global Biomass Burning: Atmospheric, Climatic, and Biospheric Implications*, edited by J. S. Levine, pp. 289-304, MIT Press, Cambridge.
- Lunden, M. M., D. R. Black, M. McKay, K. L. Revzan, A. H. Goldstein, and N. J. Brown (2006), Characteristics of fine particle growth events observed above a forested ecosystem in the Sierra Nevada Mountains of California, *Aerosol Sci. Technol.*, *40*(5), 373-388.
- Mader, B. T., and J. F. Pankow (2001), Gas/solid partitioning of semivolatile organic compounds (SOCs) to air filters. 3. An analysis of gas adsorption artifacts in measurements of atmospheric SOC and organic carbon (OC) when using Teflon membrane filters and quartz fiber filters, *Environ. Sci. Technol.*, *35*(17), 3422-3432.
- Madronich, S. (1993), UV radiation in the natural and perturbed atmosphere, in *Environmental effects of ultraviolet radiation*, edited, Lewis, Boca Raton, Fla.
- Malm, W. C., J. F. Sisler, D. Huffman, R. A. Eldred, and T. A. Cahill (1994), Spatial and seasonal trends in particle concentration and optical extinction in the United States, *J. Geophys. Res.*, *99*(D1), 1347-1370.
- Malm, W. C., B. A. Schichtel, M. L. Pitchford, L. L. Ashbaugh, and R. A. Eldred (2004), Spatial and monthly trends in speciated fine particle concentration in the United States, *J. Geophys. Res.*, *109*(D3), 33, doi:10.1029/2003JD003739.
- Malm, W. C., and J. L. Hand (2007), An examination of the physical and optical properties of aerosols collected in the IMPROVE program, *Atmos. Environ.*, *41*(16), 3407-3427.
- Martin, R. V., D. J. Jacob, R. M. Yantosca, M. Chin, and P. Ginoux (2003), Global and regional decreases in tropospheric oxidants from photochemical effects of aerosols, *J. Geophys. Res.*, *108*(D3), 19, doi:10.1029/2002JD002622.
- Martins, J. V., P. Artaxo, P. V. Hobbs, C. Lioussé, H. Cachier, Y. J. Kauffman, and A. Planafattori (1996), Particle size distributions, elemental compositions, carbon measurements, and optical properties of smoke from biomass burning in the Pacific Northwest of the United States, in *Global biomass burning and global change*, edited by J. S. Levine, pp. 716-732, MIT Press, Cambridge, MA.
- Mayol-Bracero, O. L., P. Guyon, B. Graham, G. Roberts, M. O. Andreae, S. Decesari, M. C. Facchini, S. Fuzzi, and P. Artaxo (2002), Water-soluble organic compounds in biomass burning aerosols over Amazonia - 2. Apportionment of the chemical composition and importance of the polyacidic fraction, *J. Geophys. Res.*, *107*(D20), doi:10.1029/2001JD000522.

- Mazzoleni, L. R., B. Zielinska, and H. Moosmuller (2007), Emissions of levoglucosan, methoxy phenols, and organic acids from prescribed burns, laboratory combustion of wildland fuels, and residential wood combustion, *Environ. Sci. Technol.*, 41(7), 2115-2122.
- McCarty, J. L., C. O. Justice, and S. Korontzi (2007), Agricultural burning in the Southeastern United States detected by MODIS, *Remote Sensing of Environment*, 108(2), 151-162.
- McKenzie, D., S. M. O'Neill, N. K. Larkin, and R. A. Norheim (2006), Integrating models to predict regional haze from wildland fire, *Ecol. Model.*, 199(3), 278-288.
- McMeeking, G. R., S. M. Kreidenweis, C. M. Carrico, T. Lee, J. L. Collett, and W. C. Malm (2005), Observations of smoke-influenced aerosol during the Yosemite Aerosol Characterization Study: Size distributions and chemical composition, *J. Geophys. Res.*, 110(D9), doi:10.1029/2004JD005389.
- McMeeking, G. R., S. M. Kreidenweis, M. Lunden, J. Carrillo, C. M. Carrico, T. Lee, P. Herckes, G. Engling, D. E. Day, J. Hand, N. Brown, W. C. Malm, and J. L. Collett (2006), Smoke-impacted regional haze in California during the summer of 2002, *Agricultural and Forest Meteorology*, 137(1-2), 25-42.
- Mendoza, A., M. R. Garcia, P. Vela, D. F. Lozano, and D. Allen (2005), Trace gases and particulate matter emissions from wildfires and agricultural burning in Northeastern Mexico during the 2000 fire season, *Journal of the Air & Waste Management Association*, 55(12), 1797-1808.
- Mitchell, J. B. A., and D. J. M. Miller (1989), Studies of the effects of metallic and gaseous additives in the control of soot formation in diffusion flames, *Combustion and Flame*, 75(1), 45-55.
- Moosmuller, H., and W. P. Arnott (2003), Angular truncation errors in integrating nephelometry, *Review of Scientific Instruments*, 74(7), 3492-3501.
- Morvan, D., J. L. Dupuy, B. Porterie, and M. Larini (2000), Multiphase formulation applied to the modeling of fire spread through a forest fuel bed, *Proceedings of the Combustion Institute*, 28, 2803-2809.
- Muhle, J., T. J. Lueker, Y. Su, B. R. Miller, K. A. Prather, and R. F. Weiss (2007), Trace gas and particulate emissions from the 2003 southern California wildfires, *J. Geophys. Res.*, 112(D3), D03307, doi:10.1029/2006JD007350.
- Mukai, H., and Y. Ambe (1986), Characterization of a humic acid-like brown substance in airborne particulate matter and tentative identification of its origin, *Atmos. Environ.*, 20(5), 813-819.
- Mulholland, G. W., and N. P. Bryner (1994), Radiometric model of the transmission cell-reciprocal nephelometer, *Atmos. Environ.*, 28(5), 873-887.
- Myhre, G., T. K. Berntsen, J. M. Haywood, J. K. Sundet, B. N. Holben, M. Johnsrud, and F. Stordal (2003), Modeling the solar radiative impact of aerosols from biomass burning during the Southern African Regional Science Initiative (SAFARI-2000) experiment, *J. Geophys. Res.*, 108(D13), doi:10.1029/2002JD002313.
- O'Neill, K. P., E. S. Kasischke, and D. D. Richter (2002a), Environmental controls on soil CO₂ flux following fire in black spruce, white spruce, and aspen stands of interior Alaska, *Can. J. For. Res.-Rev. Can. Rech. For.*, 32(9), 1525-1541.
- O'Neill, N. T., T. F. Eck, B. N. Holben, A. Smirnov, A. Royer, and Z. Li (2002b), Optical

- properties of boreal forest fire smoke derived from Sun photometry, *J. Geophys. Res.*, 107(D11), doi:10.1029/2001JD000877.
- Park, K., J. C. Chow, J. G. Watson, D. L. Trimble, P. Doraiswamy, W. P. Arnott, K. R. Stroud, K. Bowers, R. Bode, A. Petzold, and A. D. A. Hansen (2006), Comparison of continuous and filter-based carbon measurements at the Fresno Supersite, *Journal of the Air & Waste Management Association*, 56(4), 474-491.
- Park, R. J., D. J. Jacob, M. Chin, and R. V. Martin (2003), Sources of carbonaceous aerosols over the United States and implications for natural visibility, *J. Geophys. Res.*, 108(D12), doi:10.1029/2002JD003190.
- Park, R. J., D. J. Jacob, and J. A. Logan (2007), Fire and biofuel contributions to annual mean aerosol mass concentrations in the United States, *Atmos. Environ.*, 41, 7389-7400.
- Patterson, E. M., and C. K. McMahon (1984), Absorption characteristics of forest fire particulate matter, *Atmos. Environ.*, 18(11), 2541-2551.
- Peet, R. K. (1988), Forests of the Rocky Mountains, in *North American terrestrial vegetation*, edited by M. G. Barbour and W. D. Billings, pp. 63-101, Cambridge University Press, Cambridge.
- Penner, J. E., C. C. Chuang, and K. Grant (1998), Climate forcing by carbonaceous and sulfate aerosols, *Climate Dynamics*, 14(12), 839-851.
- Penner, J. E., S. Y. Zhang, and C. C. Chuang (2003), Soot and smoke aerosol may not warm climate, *J. Geophys. Res.*, 108(D21), doi:10.1029/2003JD003409.
- Pfister, G. G., P. G. Hess, L. K. Emmons, P. J. Rasch, and F. M. Vitt (2008), Impact of the summer 2004 Alaska fires on top of the atmosphere clear-sky radiation fluxes, *J. Geophys. Res.*, 113(D2), doi:10.1029/2007JD008797.
- Phuleria, H. C., P. M. Fine, Y. F. Zhu, and C. Sioutas (2005), Air quality impacts of the October 2003 Southern California wildfires, *J. Geophys. Res.*, 110(D7), doi:10.1029/2004JD004626.
- Poschl, U. (2003), Aerosol particle analysis: challenges and progress, *Analytical and Bioanalytical Chemistry*, 375(1), 30-32.
- Posfai, M., R. Simonics, J. Li, P. V. Hobbs, and P. R. Buseck (2003), Individual aerosol particles from biomass burning in southern Africa: 1. Compositions and size distributions of carbonaceous particles, *J. Geophys. Res.*, 108(D13), doi:10.1029/2002JD002291.
- Quinn, P. K., T. S. Bates, D. J. Coffman, and D. S. Covert (2008), Influence of particle size and chemistry on the cloud nucleating properties of aerosols, *Atmos. Chem. Phys.*, 8(4), 1029-1042.
- Radke, L. F., D. A. Hegg, P. V. Hobbs, J. D. Nance, J. H. Lyons, K. K. Laursen, R. E. Weiss, P. J. Riggan, and D. E. Ward (1991), Particle and trace emissions from large biomass fires in North America, in *Global biomass burning: Atmospheric, climatic, and biospheric implications*, edited by J. S. Levine, pp. 209-224, MIT Press, Cambridge, MA.
- Reid, J. S., and P. V. Hobbs (1998), Physical and optical properties of young smoke from individual biomass fires in Brazil, *J. Geophys. Res.*, 103(D24), 32013-32030.
- Reid, J. S., P. V. Hobbs, R. J. Ferek, D. R. Blake, J. V. Martins, M. R. Dunlap, and C. Liou (1998), Physical, chemical, and optical properties of regional hazes dominated by smoke in Brazil, *J. Geophys. Res.*, 103(D24), 32059-32080.

- Reid, J. S., T. F. Eck, S. A. Christopher, R. Koppmann, O. Dubovik, D. P. Eleuterio, B. N. Holben, E. A. Reid, and J. Zhang (2005a), A review of biomass burning emissions part III: intensive optical properties of biomass burning particles, *Atmos. Chem. Phys.*, 5, 827-849.
- Reid, J. S., R. Koppmann, T. F. Eck, and D. P. Eleuterio (2005b), A review of biomass burning emissions part II: intensive physical properties of biomass burning particles, *Atmos. Chem. Phys.*, 5, 799-825.
- Remer, L. A., Y. J. Kaufman, D. Tanre, S. Mattoo, D. A. Chu, J. V. Martins, R. R. Li, C. Ichoku, R. C. Levy, R. G. Kleidman, T. F. Eck, E. Vermote, and B. N. Holben (2005), The MODIS aerosol algorithm, products, and validation, *Journal of the Atmospheric Sciences*, 62(4), 947-973.
- Robinson, A. L., N. M. Donahue, M. K. Shrivastava, E. A. Weitkamp, A. M. Sage, A. P. Grieshop, T. E. Lane, J. R. Pierce, and S. N. Pandis (2007), Rethinking organic aerosols: Semivolatile emissions and photochemical aging, *Science*, 315(5816), 1259-1262.
- Roden, C. A., T. C. Bond, S. Conway, A. Benjamin, and O. Pinel (2006), Emission factors and real-time optical properties of particles emitted from traditional wood burning cookstoves, *Environ. Sci. Technol.*, 40(21), 6750-6757.
- Rogge, W. F., M. A. Mazurek, L. M. Hildemann, G. R. Cass, and B. R. T. Simoneit (1993), Quantification of urban organic aerosols at a molecular level - Identification, abundance and seasonal variation, *Atmospheric Environment Part a-General Topics*, 27(8), 1309-1330.
- Rosen, H., and T. Novakov (1983), Optical transmission through aerosol deposits on diffusely reflective filters - A method for measuring the absorbing component of aerosol particles, *Applied Optics*, 22(9), 1265-1267.
- Roy, D. P., P. E. Lewis, and C. O. Justice (2002), Burned area mapping using multi-temporal moderate spatial resolution data - a bi-directional reflectance model-based expectation approach, *Remote Sensing of Environment*, 83(1-2), 263-286.
- Ryu, S. Y., J. E. Kim, H. Zhuanshi, Y. J. Kim, and G. U. Kang (2004), Chemical composition of post-harvest biomass burning aerosols in Gwangju, Korea, *Journal of the Air & Waste Management Association*, 54(9), 1124-1137.
- Sandradewi, J., A. S. H. Prevot, E. Weingartner, R. Schmidhauser, M. Gysel, and U. Baltensperger (2008), A study of wood burning and traffic aerosols in an Alpine valley using a multi-wavelength Aethalometer, *Atmos. Environ.*, 42(1), 101-112.
- Savage, M., and T. W. Swetnam (1990), Early 19th-century fire decline following sheep pasturing in a Navajo ponderosa pine forest, *Ecology*, 71(6), 2374-2378.
- Schade, G. W., and A. H. Goldstein (2001), Fluxes of oxygenated volatile organic compounds from a ponderosa pine plantation, *J. Geophys. Res.*, 106(D3), 3111-3123.
- Schmid, H., L. Laskus, H. J. Abraham, U. Baltensperger, V. Lavanchy, M. Bizjak, P. Burba, H. Cachier, D. Crow, J. Chow, T. Gnauk, A. Even, H. M. ten Brink, K. P. Giesen, R. Hitznerberger, E. Hueglin, W. Maenhaut, C. Pio, A. Carvalho, J. P. Putaud, D. Toom-Sauntry, and H. Puxbaum (2001), Results of the "carbon conference" international aerosol carbon round robin test stage I, *Atmos. Environ.*, 35(12), 2111-2121.
- Schmid, O., P. Artaxo, W. P. Arnott, D. Chand, L. V. Gatti, G. P. Frank, A. Hoffer, M. Schnaiter,

- and M. O. Andreae (2006), Spectral light absorption by ambient aerosols influenced by biomass burning in the Amazon Basin. I: Comparison and field calibration of absorption measurement techniques, *Atmos. Chem. Phys.*, 6, 3443-3462.
- Schnaiter, M., O. Schmid, A. Petzold, L. Fritzsche, K. F. Klein, M. O. Andreae, G. Helas, A. Thielmann, M. Gimmler, O. Mohler, C. Linke, and U. Schurath (2005), Measurement of wavelength-resolved light absorption by aerosols utilizing a UV-VIS extinction cell, *Aerosol Sci. Technol.*, 39(3), 249-260.
- Schnaiter, M., M. Gimmler, I. Llamas, C. Linke, C. Jager, and H. Mutschke (2006), Strong spectral dependence of light absorption by organic carbon particles formed by propane combustion, *Atmos. Chem. Phys.*, 6, 2981-2990.
- Schulz, M., C. Textor, S. Kinne, Y. Balkanski, S. Bauer, T. Berntsen, T. Berglen, O. Boucher, F. Dentener, S. Guibert, I. S. A. Isaksen, T. Iversen, D. Koch, A. Kirkevag, X. Liu, V. Montanaro, G. Myhre, J. E. Penner, G. Pitari, S. Reddy, O. Seland, P. Stier, and T. Takemura (2006), Radiative forcing by aerosols as derived from the AeroCom present-day and pre-industrial simulations, *Atmos. Chem. Phys.*, 6, 5225-5246.
- Seinfeld, J. H., and S. N. Pandis (1998), *Atmospheric chemistry and physics: From air pollution to climate change*, Wiley-Interscience, New York.
- Shafizadeh, F., and W. F. Degroot (1976), Combustion characteristics of cellulosic fuels, *Abstracts of Papers of the American Chemical Society*, 172(SEP3), 125-125.
- Simon, M., S. Plummer, F. Fierens, J. J. Hoelzemann, and O. Arino (2004), Burnt area detection at global scale using ATSR-2: The GLOBSCAR products and their qualification, *J. Geophys. Res.*, 109(D14), doi:10.1029/2003JD003622.
- Simoneit, B. R. T. (2002), Biomass burning - A review of organic tracers for smoke from incomplete combustion, *Appl. Geochem.*, 17(3), 129-162.
- Sinha, P., P. V. Hobbs, R. J. Yokelson, I. T. Bertschi, D. R. Blake, I. J. Simpson, S. Gao, T. W. Kirchstetter, and T. Novakov (2003), Emissions of trace gases and particles from savanna fires in southern Africa, *J. Geophys. Res.*, 108(D13), doi:10.1029/2002JD002325.
- Spracklen, D. V., J. A. Logan, L. J. Mickley, R. J. Park, R. Yevich, A. L. Westerling, and D. A. Jaffe (2007), Wildfires drive interannual variability of organic carbon aerosol in the western U.S. in summer, *Geophys. Res. Lett.*, 34, L16816, doi:10.1029/2007GL030037.
- Stanturf, J. A., D. D. Wade, T. A. Waldrop, D. K. Kennard, and G. L. Achtemeier (2002), Background paper: Fire in southern forest landscapes, in *Southern Forest Resource Assessment, Gen. Tech. Rep. SRS-53*, edited by W. D. N and J. G. Greis, pp. 607-630, USDA Forest Service, Southern Research Station, Asheville, North Carolina.
- Stephens, S. L., and J. J. Moghaddas (2005), Experimental fuel treatment impacts on forest structure, potential fire behavior, and predicted tree mortality in a California mixed conifer forest, *Forest Ecology and Management*, 215(1-3), 21-36.
- Stohl, A., E. Andrews, J. F. Burkhardt, C. Forster, A. Herber, S. W. Hoch, D. Kowal, C. Lunder, T. Mefford, J. A. Ogren, S. Sharma, N. Spichtinger, K. Stebel, R. Stone, J. Strom, K. Torseth, C. Wehrli, and K. E. Yttri (2006), Pan-Arctic enhancements of light absorbing aerosol concentrations due to North American boreal forest fires during summer 2004, *J. Geophys. Res.*, 111(D22), doi:10.1029/2006JD007216.

- Subramanian, R., A. Y. Khlystov, J. C. Cabada, and A. L. Robinson (2004), Positive and negative artifacts in particulate organic carbon measurements with denuded and undenuded sampler configurations, *Aerosol Sci. Technol.*, 38, 27-48.
- Subramanian, R., A. Y. Khlystov, and A. L. Robinson (2006), Effect of peak inert-mode temperature on elemental carbon measured using thermal-optical analysis, *Aerosol Sci. Technol.*, 40(10), 763-780.
- Subramanian, R., C. A. Roden, P. Boparai, and T. C. Bond (2007), Yellow beads and missing particles: Trouble ahead for filter-based absorption measurements, *Aerosol Sci. Technol.*, 41(6), 630-637.
- Sullivan, A. P., and R. J. Weber (2006), Chemical characterization of the ambient organic aerosol soluble in water: 2. Isolation of acid, neutral, and basic fractions by modified size-exclusion chromatography, *J. Geophys. Res.*, 111(D5), doi:10.1029/2005JD006486.
- Sullivan, A. P., A. S. Holden, L. A. Patterson, S. M. Kreidenweis, W. C. Malm, W. M. Hao, C. E. Wold, and J. L. Collett, Jr. (submitted), A method for smoke marker measurements and its potential application for determining the contribution of biomass burning from wildfires and prescribed fires to ambient PM_{2.5} organic carbon.
- Sun, H. L., L. Biedermann, and T. C. Bond (2007), Color of brown carbon: A model for ultraviolet and visible light absorption by organic carbon aerosol, *Geophys. Res. Lett.*, 34(17), doi:10.1029/2007GL029797.
- Tauc, J., Grigorov, R., and A. Vancu (1966), Optical properties and electronic structure of amorphous germanium, *Physica Status Solidi*, 15(2), 627-&.
- Tolocka, M. P., M. Jang, J. M. Ginter, F. J. Cox, R. M. Kamens, and M. V. Johnston (2004), Formation of oligomers in secondary organic aerosol, *Environ. Sci. Technol.*, 38(5), 1428-1434.
- Torres, O., P. K. Bhartia, J. R. Herman, A. Sinyuk, P. Ginoux, and B. Holben (2002), A long-term record of aerosol optical depth from TOMS observations and comparison to AERONET measurements, *Journal of the Atmospheric Sciences*, 59(3), 398-413.
- Trentmann, J., G. Luderer, T. Winterrath, M. D. Fromm, R. Servranckx, C. Textor, M. Herzog, H. F. Graf, and M. O. Andreae (2006), Modeling of biomass smoke injection into the lower stratosphere by a large forest fire (Part I): reference simulation, *Atmos. Chem. Phys.*, 6, 5247-5260.
- Turpin, B. J., J. J. Huntzicker, and S. V. Hering (1994), Investigation of organic aerosol sampling artifacts in the Los Angeles basin, *Atmos. Environ.*, 28(19), 3061-3071.
- Turpin, B. J., P. Saxena, and E. Andrews (2000), Measuring and simulating particulate organics in the atmosphere: problems and prospects, *Atmos. Environ.*, 34(18), 2983-3013.
- Turpin, B. J., and H. J. Lim (2001), Species contributions to PM_{2.5} mass concentrations: Revisiting common assumptions for estimating organic mass, *Aerosol Sci. Technol.*, 35(1), 602-610.
- van der Werf, G. R., J. T. Randerson, L. Giglio, G. J. Collatz, P. S. Kasibhatla, and A. F. Arellano (2006), Interannual variability in global biomass burning emissions from 1997 to 2004, *Atmos. Chem. Phys.*, 6, 3423-3441.
- Venkatachari, P., L. M. Zhou, P. K. Hopke, J. J. Schwab, K. L. Demerjian, S. Weimer, O. Hogrefe, D. Felton, and O. Rattigan (2006), An intercomparison of measurement methods for

- carbonaceous aerosol in the ambient air in New York City, *Aerosol Sci. Technol.*, 40(10), 788-795.
- Venkataraman, C., G. Habib, D. Kadamba, M. Shrivastava, J. F. Leon, B. Crouzille, O. Boucher, and D. G. Streets (2006), Emissions from open biomass burning in India: Integrating the inventory approach with high-resolution Moderate Resolution Imaging Spectroradiometer (MODIS) active-fire and land cover data, *Global Biogeochemical Cycles*, 20(2), doi:10.1029/2005GB002547.
- Virkkula, A., N. C. Ahlquist, D. S. Covert, W. P. Arnott, P. J. Sheridan, P. K. Quinn, and D. J. Coffman (2005), Modification, calibration and a field test of an instrument for measuring light absorption by particles, *Aerosol Sci. Technol.*, 39(1), 68-83.
- Vuilleumier, L., J. T. Bamer, R. A. Harley, and N. J. Brown (2001a), Evaluation of nitrogen dioxide photolysis rates in an urban area using data from the 1997 Southern California Ozone Study, *Atmos. Environ.*, 35(36), 6525-6537.
- Vuilleumier, L., R. A. Harley, N. J. Brown, J. R. Slusser, D. Kolinski, and D. S. Bigelow (2001b), Variability in ultraviolet total optical depth during the Southern California Ozone Study (SCOS97), *Atmos. Environ.*, 35(6), 1111-1122.
- Ward, D. E., and C. C. Hardy (1991), Smoke emissions from wildland fires, *Environment International*, 17(2-3), 117-134.
- Ward, D. E., and L. F. Radke (1993), Emission measurements from vegetation fires: a comparative evaluation of methods and results, in *Fire in the environment: the ecological, atmospheric, and climatic importance of vegetation fires*, edited by P. J. Crutzen and Goldammer, pp. 53-76, Wiley, Chichester, UK.
- Warnatz, J., U. Maas, and R. W. Dibble (1996), *Combustion: Physical and chemical fundamentals, modeling and simulation, experiments, pollutant formation*, Springer, New York.
- Watson, J. G. (2002), Visibility: Science and regulation, *Journal of the Air & Waste Management Association*, 52(6), 628-713.
- Watson, J. G., J. C. Chow, and L.-W. Antony Chen (2005), Summary of organic and elemental/black carbon analysis methods and intercomparisons, *Aerosol and Air Quality Research*, 5(1), 65-102.
- Weingartner, E., H. Saathoff, M. Schnaiter, N. Streit, B. Bitnar, and U. Baltensperger (2003), Absorption of light by soot particles: determination of the absorption coefficient by means of aethalometers, *J. Aerosol. Sci.*, 34(10), 1445-1463.
- West, N. E., and J. A. Young (2000), Intermountain valleys and lower mountain slopes, in *North American terrestrial vegetation*, edited by M. G. Barbour, Cambridge University Press, Cambridge.
- Westerling, A. L., H. G. Hidalgo, D. R. Cayan, and T. W. Swetnam (2006), Warming and earlier spring increase western US forest wildfire activity, *Science*, 313(5789), 940-943.
- Wiedinmyer, C., B. Quayle, C. Geron, A. Belote, D. McKenzie, X. Y. Zhang, S. O'Neill, and K. K. Wynne (2006), Estimating emissions from fires in North America for air quality modeling, *Atmos. Environ.*, 40(19), 3419-3432.
- Winker, D. M., W. H. Hunt, and M. J. McGill (2007), Initial performance assessment of CALIOP, *Geophys. Res. Lett.*, 34(19), doi:L19803 Artn 119803.
- Wooster, M. J., and Y. H. Zhang (2004), Boreal forest fires burn less intensely in Russia than in

- North America, *Geophys. Res. Lett.*, 31(20), doi:L20505 Artn I20505.
- Wotawa, G., and M. Trainer (2000), The influence of Canadian forest fires on pollutant concentrations in the United States, *Science*, 288(5464), 324-328.
- Yamasoe, M. A., Y. J. Kaufman, O. Dubovik, L. A. Remer, B. N. Holben, and P. Artaxo (1998), Retrieval of the real part of the refractive index of smoke particles from Sun/sky measurements during SCAR-B, *J. Geophys. Res.*, 103(D24), 31893-31902.
- Yamasoe, M. A., P. Artaxo, A. H. Miguel, and A. G. Allen (2000), Chemical composition of aerosol particles from direct emissions of vegetation fires in the Amazon Basin: water-soluble species and trace elements, *Atmos. Environ.*, 34(10), 1641-1653.
- Yokelson, R. J., D. W. T. Griffith, and D. E. Ward (1996), Open-path Fourier transform infrared studies of large-scale laboratory biomass fires, *J. Geophys. Res.*, 101(D15), 21067-21080.
- Yokelson, R. J., R. Susott, D. E. Ward, J. Reardon, and D. W. T. Griffith (1997), Emissions from smoldering combustion of biomass measured by open-path Fourier transform infrared spectroscopy, *J. Geophys. Res.*, 102(D15), 18865-18877.
- Yokelson, R. J., J. G. Goode, D. E. Ward, R. A. Susott, R. E. Babbitt, D. D. Wade, I. Bertschi, D. W. T. Griffith, and W. M. Hao (1999), Emissions of formaldehyde, acetic acid, methanol, and other trace gases from biomass fires in North Carolina measured by airborne Fourier transform infrared spectroscopy, *J. Geophys. Res.*, 104(D23), 30109-30125.
- Yokelson, R. J., T. Karl, P. Artaxo, D. R. Blake, T. J. Christian, D. W. T. Griffith, A. Guenther, and W. M. Hao (2007a), The Tropical Forest and Fire Emissions Experiment: overview and airborne fire emission factor measurements, *Atmos. Chem. Phys.*, 7(19), 5175-5196.
- Yokelson, R. J., S. P. Urbanski, E. L. Atlas, D. W. Toohey, E. C. Alvarado, J. D. Crouse, P. O. Wennberg, M. E. Fisher, C. E. Wold, T. L. Campos, K. Adachi, P. R. Buseck, and W. M. Hao (2007b), Emissions from forest fires near Mexico City, *Atmos. Chem. Phys.*, 7(21), 5569-5584.
- Yokelson, R. J., T. J. Christian, T. G. Karl, and A. Guenther (2008), The tropical forest and fire emissions experiment: laboratory fire measurements and synthesis of campaign data, *Atmospheric Chemistry and Physics Discussions*, 8, 4221-4266.
- Zhuang, Q., A. D. McGuire, K. P. O'Neill, J. W. Harden, V. E. Romanovsky, and J. Yarie (2002), Modeling soil thermal and carbon dynamics of a fire chronosequence in interior Alaska, *J. Geophys. Res.*, 108(D1), doi:10.1029/2001JD001244.
- Ziemba, L. D., E. Fischer, R. J. Griffin, and R. W. Talbot (2007), Aerosol acidity in rural New England: Temporal trends and source region analysis, *J. Geophys. Res.*, 112(D10), doi:10.1029/2006JD007605.

Appendix A Carbonaceous aerosol measurements

Table A.1 Filter-integrated combustion properties and aerosol emission factors during FLAME. C = fuel carbon fraction (dry weight fraction), which is assumed to be 0.45 if not directly measured. Emission factors reported in g kg^{-1} dry fuel divided by the fuel carbon content yields emission factors in units of g kg^{-1} carbon emitted.

ID	Sample	C	MCE	CE	EC/TC	Emission factors (g kg^{-1} dry fuel)					
						TOOC	OC	EC	Σ IN	RFM	PM _{2.5}
FLAME 1 chamber burns											
1	Cellulose filter (plain)	-	-	-	0	-	-	-	-	-	-
2	Cellulose filter (K doped 1)	0.45	-	-	0	-	-	-	-	-	-
3	Cellulose filter (K doped 2)	0.45	-	-	0	-	-	-	-	-	-
4	Cellulose powder	0.45	-	-	0	-	-	-	-	-	-
5	Mt. Grass (dry)	0.42	-	-	0.047	-	-	-	-	-	-
6	Mt. Grass (fresh)	0.42	-	-	0	-	-	-	-	-	-
7	Rice Straw	0.43	0.874	0.833	0	13.2	7.5	0	2.4	10	13.8
8	PP Duff	0.46	-	-	0.013	-	-	-	-	-	-
9	PP Needle Litter	0.49	0.922	-	0.019	-	11.1	0.2	0.5	11.8	17.3
10	PP Needle Litter	0.49	0.911	0.855	0.001	28.1	22.8	0	0.5	23.3	34.7
11	PP Needle Litter	0.49	0.933	-	0.022	-	8.9	0.2	0.5	9.5	14
12	PP Needle Litter	0.327	-	-	0.005	-	-	-	-	-	-
13	PP Needle Litter	0.49	0.92	-	0.007	-	12.7	0.1	0.5	13.3	19.7
14	PP Branches (dead, small)	0.48	0.946	0.914	0.45	12.9	3.6	2.9	0.7	7.2	9
15	PP Branches (dead, large)	0.48	0.954	0.941	0.433	4.2	1.9	1.5	0.3	3.8	4.7
16	PP Branches (fresh, small)	0.48	0.924	-	0.007	-	-	-	-	-	-
17	PP Needles (fresh)	0.52	0.87	0.79	0.003	45.8	37.7	0.1	0.7	38.5	57.4
18	PP Branches (fresh, large)	0.48	-	-	0.005	-	-	-	-	-	-
19	LP Needle Litter	-	-	-	0.057	-	-	-	-	-	-
20	LP Needles (fresh)	0.50	0.868	0.777	0.005	50.9	33.8	0.2	1.3	35.3	52.2
21	LP Branches (dead, small)	0.48	0.946	0.936	0.51	3.1	1.5	1.5	0.5	3.5	4.2
22	LP Needle Duff	0.42	0.932	0.881	0	18	7.6	0	0.8	8.4	12.2
23	Rice Straw	0.43	0.917	-	0.052	-	4.7	0.3	2.2	7.1	9.5
24	Rice Straw	-	-	-	-	-	-	-	-	-	-
25	Rice Straw	0.43	0.91	-	-	-	6.4	-	-	-	-
26	Palmetto Leaf (dry)	0.48	0.916	-	0.242	-	1.5	0.5	4.4	6.4	7.1
27	Chamise Leaf (dry)	0.45	0.893	0.866	0.016	10	6.8	0.1	1.6	8.4	11.8
28	Chamise Branches (dry)	0.45	0.909	0.89	0	7.6	4.1	0	0.7	4.8	6.8
29	Chamise Leaf (fresh)	0.45	0.866	-	0	-	-	-	-	-	-
30	Chamise Branches (fresh)	0.45	0.926	0.902	0.003	8.9	3.5	0	0.7	4.3	6
31	Manzanita Leaves (fresh)	-	-	-	0	-	-	-	-	-	-
32	Manzanita Branches (fresh)	0.45	0.886	0.855	0	14.2	10.7	0	1.2	11.9	17.3
33	Manzanita leaves (dry)	0.45	0.87	0.763	0.005	52.7	40	0.2	1.1	41.2	61.2
34	Chamise Branches and Leaves (dry)	0.45	0.935	0.924	0.324	3.8	1.5	0.7	0.9	3.2	3.9

ID	Sample	C	MCE	CE	EC/TC	Emission factors (g kg ⁻¹ dry fuel)					
						TOOC	OC	EC	ΣIN	RFM	PM _{2.5}
FLAME 1 chamber burns											
35	PP Pine Complex (dried needles, sticks)	0.485	0.972	0.89	0.036	34	2.4	0.1	0.1	2.6	3.7
36	S. CA Chamise Complex	0.51	0.949	0.935	0.678	6	0.3	0.7	0.7	1.8	1.9
37	PP Pine Complex (dried needles, sticks)	0.49	0.942	0.916	0.08	11.3	7.4	0.6	0.2	8.3	12
38	S. CA Chamise Complex	0.51	0.952	0.938	0.219	6.2	2.4	0.7	0.8	3.8	5
39	S. CA Chamise Complex	-	-	-	-	-	-	-	-	-	-
40	Taiwanese Rice Straw	0.43	0.945	0.935	0	3.6	1.5	0	2.2	3.6	4.3
41	PP Pine Duff	0.46	0.93	0.91	0	8.6	5	0	0.3	5.3	7.8
42	Alaskan Duff (feather moss)	0.36	0.901	0.871	0	10	3.6	0	0.2	3.8	5.5
43	S. CA Manzanita	0.50	0.972	0.962	0.523	3.8	0.7	0.7	0.3	1.7	2
44	Utah Juniper Foliage/Sticks	0.49	0.959	0.951	0.797	1.3	0.7	2.7	0.4	3.8	4.2
45	Utah Rabbitbrush/Sage foliage/sticks	0.45	0.942	0.93	0.722	3.7	0.5	1.4	1.2	3.1	3.4
46	Lignin	0.45	0.977	0.926	0.234	22.1	3.5	1.1	0.2	4.8	6.6
47	LP needles/branches, dried (equal mass)	0.49	0.97	0.923	0.028	21.4	2.3	0.1	0.2	2.6	3.7
48	Puerto Rico fern, dried foliage	0.46	0.952	0.937	0.055	6	2.2	0.1	0.4	2.8	3.9
49	S. CA Chamise (dry)	0.51	0.949	0.937	0.585	4.2	0.8	1.1	0.7	2.5	2.9
50	SE Wax Myrtle, foliage/sticks	0.50	0.928	0.897	0.085	14.3	4.5	0.4	2.3	7.2	9.4
51	Southern Pine needle, dried	0.50	0.962	0.9	0.064	31.5	18.6	1.3	1.2	21.1	30.4
52	Puerto Rico mixed wood/dry sticks	0.45	0.954	-	0.109	-	-	-	-	-	-
53	SE Palmetto leaves	0.48	0.952	0.945	0.217	1.8	1.3	0.3	-	-	-
54	S. CA Ceanothus	0.50	0.925	0.911	0.036	6.1	3.9	0.1	0.8	4.9	6.9
FLAME 2 stack burns											
55	PP Needles	-	-	-	-	-	-	-	-	-	-
56	Ethanol	0.45	0.984	-	-	-	-	-	-	-	-
57	Propane Torch	0.45	0.995	-	-	-	-	-	-	-	-
58	PP Needles	-	-	-	0.001	-	-	-	-	-	-
59	MS Palmetto	0.51	0.938	0.921	0.06	7.6	6	0.4	1.7	8	11
60	FL inland Palmetto	0.26	-	-	0.132	-	-	-	-	-	-
61	FL coastal Palmetto	0.51	0.944	0.925	0.106	7.8	5.3	0.6	2.8	8.7	11.4
62	MS Gallberry	0.56	0.947	0.913	0.534	10	7.1	8.1	1.8	17	20.5
63	MS Longleaf Pine Needles	0.50	0.926	0.878	0.041	21.8	18.6	0.8	1.9	21.3	30.6
64	NC Oak Leaves	0.50	0.941	0.912	0.037	13.6	10.6	0.4	1.9	12.9	18.2
65	NC Hickory Leaves	0.48	0.933	0.908	0.041	10	7.1	0.3	1.6	9	12.5
66	MS Wiregrass	0.48	0.961	0.951	0.089	4.2	3.5	0.3	0.8	4.7	6.4
67	FL Titi	0.27	-	-	0.255	-	-	-	-	-	-
68	LA Phragmites	0.49	0.957	0.91	0.019	22.8	19.7	0.4	6.3	26.4	36.2
69	MS Wax Myrtle	0.50	0.91	0.884	0.037	11.3	8.1	0.3	2.5	11	15
70	GA Kudzu	0.47	0.857	0.73	0	57.4	44.2	0	4.1	48.3	70.5
71	MS Palmetto and Gallberry	0.54	0.914	0.866	0	24	19.1	0	3	22.1	31.7
72	MS Longleaf Pine Needles and Wiregrass	0.52	0.927	-	0.004	-	-	-	-	-	-
73	Oak and Hickory	0.245	-	-	0	-	-	-	-	-	-
74	PP Needles 25g	0.52	-	-	0.033	-	-	-	-	-	-
75	PP Needles 250g	0.52	0.907	0.808	0.001	51.8	45.6	0.1	1.2	46.9	69.7
76	PP Needles 2460g	0.52	0.935	-	0.09	-	-	-	-	-	-
77	PP Needles 80g	0.52	0.903	0.786	0	61	52	0	4.2	56.1	82.1
78	PP Needles 500g	0.52	0.939	0.891	0.028	22	17.8	0.5	0.8	19.2	28.1

ID	Sample	C	MCE	CE	EC/TC	Emission factors (g kg ⁻¹ dry fuel)					
						TOOC	OC	EC	ΣIN	RFM	PM _{2.5}
79	AK Black Spruce dried	0.45	0.952	0.928	0.08	10.3	8.5	0.7	0.7	10	14.2
80	AK Black Spruce fresh	0.45	0.954	0.932	0.01	9.3	6.9	0.1	0.6	7.6	11.1
81	MT Fir Needles fresh	0.54	0.852	0.74	0	61.3	49.6	0	1.6	51.2	76
82	MT Fir Branches fresh	0.54	0.927	-	0.062	33.7	25.2	1.7	11.7	38.6	51.2
83	MT Fir Needles and Branches dried	0.54	0.926	0.85	0	37.4	18.8	0	1.3	20.1	29.4
84	MT Fir Needles and Branches fresh	0.54	0.882	0.805	0.004	41.1	27	0.1	1.5	28.6	42.1
85	MT Fir Needles dried	-	-	-	0	-	-	-	-	-	-
86	MT Fir Branches dried	0.54	0.922	0.896	0	13.6	9.4	0	1.5	10.9	15.6
87	CA Manzanita	0.50	0.918	0.889	0.063	12.6	7.7	0.5	1.5	9.8	13.6
88	CA Ceanothus	0.50	0.907	0.891	0.136	6.8	3.8	0.6	2.4	6.8	8.6
89	PP sticks small	0.54	0.967	0.957	0.652	2.5	1.6	3.1	0.5	5.2	6.1
90	PP sticks medium	0.52	0.965	0.953	0.47	3	2.5	2.2	1.1	5.9	7.1
91	PP sticks large	0.52	0.957	0.949	0.347	2.7	2.1	1.1	0.8	4	5.1
92	UT Sage	0.47	0.905	0.87	0.017	16.6	14.6	0.3	4.5	19.4	26.8
93	UT Sage washed	0.48	0.892	0.844	0.069	21	14.5	1.1	7.6	23.2	30.5
94	CA Chamise	0.26	-	-	0.206	-	-	-	-	-	-
95	CA Chamise washed	0.51	0.908	0.888	0.151	9.1	6.5	1.2	2.9	10.5	13.8
96	PP Needles Flaming	0.55	0.993	-	0.501	-	2.5	2.5	0.7	5.6	6.9
97	PP Needles Flaming feeding	0.55	0.983	0.97	0.404	4.6	3.9	2.6	-	-	-
98	PP Needles smoldering	0.55	0.8	-	0	-	45.3	0	0.9	46.1	68.8
99	PP Needles smoldering feeding	0.55	0.725	-	0	-	21.2	0	-	-	-
100	Rice Straw flaming	0.45	0.977	-	0	-	3.4	0	2.5	5.9	7.6
101	Rice Straw smoldering	0.45	-	-	0	-	-	-	-	-	-
102	PP Needles heading	0.45	0.939	0.887	0.047	22.9	20.7	1	1.3	23	33.3
103	PP Needles backing	0.45	0.946	0.928	0.36	5.6	2.9	1.6	1	5.5	7
104	MT Sage heading	0.50	0.86	0.778	0.032	39.8	24.9	0.8	6.2	32	44.5
105	MT Sage backing	0.50	0.881	0.833	0.075	21	12.5	1	5.8	19.3	25.5
106	MT Sage Ammonium Sulfate coated	0.51	0.898	0.859	0.048	17.1	10.7	0.5	4.1	15.3	20.6
107	CA Chamise Ammonium Sulfate coated	0.54	0.925	0.908	0.318	5.9	4.2	1.9	3.4	9.5	11.6
108	MT Sage KCl coated	0.50	0.878	0.838	0.033	18.8	12.1	0.4	4.4	16.9	22.9
109	CA Chamise coated	0.55	0.93	0.915	0.347	6.2	3.2	1.7	2.2	7.2	8.8
110	MT Sage	0.46	0.853	0.789	0.028	28.1	16.7	0.5	4.1	21.2	29.6
111	Rice Straw	0.43	0.922	0.887	0	14.2	11	0	3	14.1	19.6
112	NC Turkey Oak	0.53	0.886	0.811	0.043	39.5	32.5	1.4	2	35.9	52.2
113	NC Black Needle Rush and Salt Marsh Grass	0.50	0.891	0.845	0.016	21.8	18.3	0.3	10.6	29.2	38.4
114	LA Saw Grass	0.48	0.901	0.872	0.111	11.5	9.2	1.1	9.6	20	24.6
115	AK Duff Core	0.36	0.811	-	0	-	25	0	2.1	27.2	39.7
116	US Charcoal	0.65	0.811	-	-	-	-	-	-	-	-
117	Asian Charcoal	0.72	0.841	-	-	-	-	-	-	-	-
FLAME 2 chamber burns											
118	PP Needles	-	-	-	0.04	-	-	-	-	-	-
119	Longleaf Pine Needles and Wiregrass	0.52	0.983	-	0.045	-	-	-	-	-	-
120	Black Needle Rush	0.49	-	-	0.088	-	-	-	-	-	-
121	NC Hickory and Oak Leaves	0.49	0.964	-	0.084	-	-	-	-	-	-
122	MT Fir Needles & Branches (fresh)	0.54	0.95	-	0.325	-	-	-	-	-	-
123	MT Fir Needles & Branches (dry)	-	-	-	0.006	-	-	-	-	-	-
124	FL Palmetto Leaves (coastal)	0.51	0.966	0.959	0.573	1.9	0.8	1.1	1.5	3.4	3.8

ID	Sample	C	MCE	CE	EC/TC	Emission factors (g kg ⁻¹ dry fuel)					
						TOOC	OC	EC	ΣIN	RFM	PM _{2.5}
125	MS Palmetto Leaves	0.51	0.963	0.956	0.25	2.3	1.2	0.4	1.2	2.9	3.5
126	Burn 119 continued overnight	-	-	-	-	-	-	-	-	-	-
127	Rice Straw	0.43	0.953	-	0.026	-	-	-	-	-	-
128	AK Duff Core	0.36	0.933	0.91	0.007	7.3	5.4	0	0.3	5.8	8.5
129	NC Rhododendron	0.51	0.967	0.957	0.091	3.8	2.1	0.2	0.3	2.6	3.7
130	AK Black Spruce	0.53	0.982	0.968	0.238	6	3.1	1	0.2	4.3	5.8
131	MT Fir Needles & Branches (dry- 50g)	0.54	0.953	-	0	-	-	-	-	-	-
132	AK Duff Core (40g)	0.36	0.942	0.916	0	7.8	6.8	0	0.3	7.2	10.6
133	FL Wiregrass	0.48	0.977	-	0.062	-	-	-	-	-	-
134	CA Chamise	0.51	0.95	-	0.502	-	-	-	-	-	-
135	FL Black Needlerush	-	-	-	0.038	-	-	-	-	-	-
136	MT Sage- Undiluted	0.50	0.946	-	0.377	-	-	-	-	-	-
137	MT Sage- Dilution #1	-	-	-	-	-	-	-	-	-	-
138	MT Sage- Dilution #2	-	-	-	-	-	-	-	-	-	-
139	MS Longleaf Pine Needles- Undiluted	0.50	0.956	0.887	0.021	36.9	34.1	0.7	2.2	36.9	54
140	MS Longleaf Pine Needles- Dilution #1	-	-	-	-	-	-	-	-	-	-
141	MS Longleaf Pine Needles- Dilution #2	-	-	-	-	-	-	-	-	-	-
142	MS Longleaf Pine Needles- Dilution #3	-	-	-	-	-	-	-	-	-	-
143	MS Gallberry	-	-	-	0.497	-	-	-	-	-	-
144	China Sugar Cane	0.48	0.981	-	0.105	-	-	-	-	-	-
145	AK White Spruce	0.52	0.979	0.966	0	5.1	3.5	0	0.7	4.2	5.9

Table A.2 Emission factors for inorganic species during FLAME.

ID	Filter name	Emission factors (g kg ⁻¹ dry fuel)							
		Cl ⁻	K ⁺	Na ⁺	Ca ²⁺	Mg ²⁺	SO ₄ ²⁻	NH ₄ ⁺	NO ₃ ⁻
FLAME 1 stack burns									
1	Cellulose filter (plain)	-	-	-	-	-	-	-	-
2	Cellulose filter (K doped 1)	-	-	-	-	-	-	-	-
3	Cellulose filter (K doped 2)	-	-	-	-	-	-	-	-
4	Cellulose powder	-	-	-	-	-	-	-	-
5	Mt. Grass (dry)	-	-	-	-	-	-	-	-
6	Mt. Grass (fresh)	-	-	-	-	-	-	-	-
7	Rice Straw	1.33	0.54	0.09	0.17	0.02	0.08	0.13	0.09
8	PP Duff	-	-	-	-	-	-	-	-
9	PP Needle Litter	0.13	0.04	0.05	0.05	0.06	0.04	0.02	0.06
10	PP Needle Litter	0.08	0.04	0.09	0.09	0.05	0.06	0.02	0.08
11	PP Needle Litter	0.09	0.03	0.06	0.08	0.09	0.04	0.02	0.07
12	PP Needle Litter	-	-	-	-	-	-	-	-
13	PP Needle Litter	0.14	0.03	0.1	0.07	0.04	0.04	0.02	0.07
14	PP Branches (dead, sm)	0.07	0	0.26	0.26	0.07	0.03	0	0
15	PP Branches (dead, large)	0.07	0	0.09	0.07	0.03	0.04	0.01	0.05
16	PP Branches (fresh, small)	-	-	-	-	-	-	-	-
17	PP Needles (fresh)	0.2	0.15	0.12	0	0	0.11	0.03	0.1
18	PP Branches (fresh, large)	-	-	-	-	-	-	-	-
19	LP Needle Litter	-	-	-	-	-	-	-	-
20	LP Needles (fresh)	0.19	0.4	0.17	0.23	0	0.17	0.04	0.14
21	LP Branches (dead, small)	0.09	0.02	0.07	0.11	0.05	0.03	0.02	0.06
22	LP Needle Duff	0.23	0.04	0.18	0.24	0	0.09	0.03	0
23	Rice Straw	1.23	0.48	0.14	0	0	0.09	0.16	0.08
24	Rice Straw	-	-	-	-	-	-	-	-
25	Rice Straw	-	-	-	-	-	-	-	-
26	Palmetto Leaf (dry)	2.24	1.34	0.25	0	0	0.31	0.24	0.05
27	Chamise Leaf (dry)	0.3	0.58	0.13	0.08	0.12	0.26	0.02	0.07
28	Chamise Branches (dry)	0.13	0.07	0.16	0.08	0.02	0.1	0.02	0.1
29	Chamise Leaf (fresh)	-	-	-	-	-	-	-	-
30	Chamise Branches (fresh)	0.07	0.09	0.17	0.12	0.1	0.06	0.03	0.09
31	Manzanita Leaves (fresh)	-	-	-	-	-	-	-	-
32	Manzanita Branches (fresh)	0.19	0.18	0.33	0.15	0.06	0.1	0.05	0.11
33	Manzanita leaves (dry)	0.20	0.29	0.13	0.14	0.08	0.13	0.03	0.11
34	Chamise Branches and Leaves (dry)	0.15	0.31	0.12	0.06	0	0.17	0.01	0.05
FLAME 1 chamber burns									
35	PP Pine Complex (dried needles, sticks)	0.04	0	0.01	0.01	0	0.01	0	0
36	S. CA Chamise Complex	0.15	0.38	0.02	0	0	0.14	0.01	0.02
37	PP Pine Complex (dried needles, sticks)	0.05	0.01	0.02	0.02	0	0.03	0.02	0.04
38	S. CA Chamise Complex	0.16	0.35	0.05	0	0	0.16	0	0.05
39	S. CA Chamise Complex	-	-	-	-	-	-	-	-
40	Taiwanese Rice Straw	1.23	0.42	0.03	0.02	0	0.05	0.38	0.03
41	PP Pine Duff	0.05	0.02	0.04	0.03	0.01	0.05	0.02	0.05
42	Alaskan Duff (feather moss)	0.04	0.02	0.04	0.03	0.01	0.04	0.02	0
43	S. CA Manzanita	0.06	0.16	0.02	0	0	0.09	0	0.01
44	Utah Juniper Foliage/Sticks	0.11	0.2	0.02	0	0	0.08	0	0.02

ID	Filter name	Emission factors (g kg ⁻¹ dry fuel)							
		Cl ⁻	K ⁺	Na ⁺	Ca ²⁺	Mg ²⁺	SO ₄ ²⁻	NH ₄ ⁺	NO ₃ ⁻
45	Utah Rabbitbrush/Sage foliage/sticks	0.28	0.67	0.03	0	0	0.18	0.01	0.02
46	Lignin	0.07	0.01	0.05	0.02	0	0.03	0.02	0.03
47	LP needles/branches, dried (equal mass)	0.01	0	0.03	0.02	0	0.03	0.02	0
48	Puerto Rico fern, dried foliage	0.01	0.06	0.01	0	0	0.04	0.02	0.03
49	S. CA Chamise (dry)	0.15	0.28	0.02	0	0	0.19	0	0.02
50	SE Wax Myrtle, foliage/sticks	1.13	0.58	0.29	0.02	0	0.17	0.02	0.06
51	Southern Pine needle, dried	0.4	0.1	0.11	0.11	0	0.15	0.11	0.22
52	Puerto Rico mixed wood/dry sticks	-	-	-	-	-	-	-	-
53	SE Palmetto leaves	-	-	-	-	-	-	-	-
54	S. CA Ceanothus	0.29	0.31	0.03	0.02	0	0.17	0	0.04
FLAME 2 stack burns									
55	PP Needles	-	-	-	-	-	-	-	-
56	Ethanol	-	-	6.01	3.53	3.24	0	3.21	0
57	Propane Torch	-	-	4.15	2.15	2.17	0	1.99	0
58	PP Needles	-	-	-	-	-	-	-	-
59	MS Palmetto	0.99	0.28	0.16	0.08	0	0	0.19	0
60	FL inland Palmetto	-	-	-	-	-	-	-	-
61	FL coastal Palmetto	1.21	0.43	0.23	0.09	0.08	0.31	0.26	0.14
62	MS Gallberry	0.16	0.61	0.16	0.07	0.08	0.45	0.14	0
63	MS Longleaf Pine Needles	0.88	0.33	0.23	0.10	0.08	0	0.15	0.15
64	NC Oak Leaves	0.23	0.54	0.28	0.14	0.14	0.40	0.21	0
65	NC Hickory Leaves	0.23	0.46	0.24	0.13	0.12	0	0.2	0
66	MS Wiregrass	0.18	0.19	0.17	0.11	0.1	0	0.09	0
67	FL Titi	-	-	-	-	-	-	-	-
68	LA Phragmites	2.54	1.08	0.98	0.52	0.52	0	0.64	0
69	MS Wax Myrtle	0.77	0.66	0.28	0.08	0.08	0.36	0.18	0
70	GA Kudzu	0.39	1.06	0.65	0.34	0.33	0.99	0.35	0
71	MS Palmetto and Gallberry	1.56	0.49	0.16	0.12	0.09	0.20	0.23	0.16
72	MS Longleaf Pine Needles and Wiregrass	-	-	-	-	-	-	-	-
73	Oak and Hickory	-	-	-	-	-	-	-	-
74	PP Needles 25g	-	-	-	-	-	-	-	-
75	PP Needles 250g	0.22	0.3	0.23	0.19	0.13	0	0.13	0
76	PP Needles 2460g	-	-	-	-	-	-	-	-
77	PP Needles 80g	0.52	0.99	1	0.69	0.51	0	0.44	0
78	PP Needles 500g	0.11	0.17	0.11	0.1	0.06	0.23	0.07	0
79	AK Black Spruce dried	0.16	0.25	0.12	0.07	0.06	0	0.06	0
80	AK Black Spruce fresh	0.13	0.16	0.12	0.07	0.06	0	0.1	0
81	MT Fir Needles fresh	0.11	0.31	0.2	0.14	0.12	0.29	0.22	0.21
82	MT Fir Branches fresh	1.03	3.09	2.95	1.7	1.53	0	1.36	0
83	MT Fir Needles and Branches dried	0.15	0.34	0.29	0.2	0.17	0	0.13	0
84	MT Fir Needles and Branches fresh	0.11	0.37	0.18	0.12	0.11	0.36	0	0.21
85	MT Fir Needles dried	-	-	-	-	-	-	-	-
86	MT Fir Branches dried	0.16	0.41	0.35	0.22	0.21	0	0.17	0
87	CA Manzanita	0.19	0.46	0.14	0.09	0.09	0.3	0.14	0
88	CA Ceanothus	0.47	0.88	0.16	0.08	0	0.45	0.1	0
89	PP sticks small	0.06	0.16	0.12	0.07	0.07	0	0.06	0
90	PP sticks medium	0.1	0.23	0.23	0.11	0.11	0	0.15	0

ID	Filter name	Emission factors (g kg ⁻¹ dry fuel)							
		Cl ⁻	K ⁺	Na ⁺	Ca ²⁺	Mg ²⁺	SO ₄ ²⁻	NH ₄ ⁺	NO ₃ ⁻
91	PP sticks large	0.08	0.14	0.14	0.07	0.07	0.12	0.06	0.14
92	UT Sage	1.87	1.16	0.64	0.3	0.31	0	0.26	0
93	UT Sage washed	2.88	2.5	0.81	0.35	0.34	0	0.3	0
94	CA Chamise	-	-	-	-	-	-	-	-
95	CA Chamise washed	0.52	0.96	0.73	0.06	0	0.27	0.01	0
96	PP Needles Flaming	0.11	0.16	0.25	0.02	0	0.03	0	0
97	PP Needles Flaming feeding	-	-	-	-	-	-	-	-
98	PP Needles smoldering	0.18	0.14	0.5	0.05	0	0	0	0
99	PP Needles smoldering feeding	-	-	-	-	-	-	-	-
100	Rice Straw flaming	1.15	0.78	0.14	0.02	0	0.2	0.1	0
101	Rice Straw smoldering	-	-	-	-	-	-	-	-
102	PP Needles heading	0.27	0.31	0.32	0.05	0	0.13	0	0
103	PP Needles backing	0.25	0.23	0.43	0.03	0	0.07	0	0
104	MT Sage heading	1.02	2.94	0.44	0.04	0	0.65	0	0.66
105	MT Sage backing	1.09	2.96	0.47	0.04	0	0.75	0.01	0
106	MT Sage Ammonium Sulfate coated	0.99	1.65	0.57	0.08	0	0.42	0.01	0
107	CA Chamise Ammonium Sulfate coated	0.58	1.11	0.76	0.07	0	0.36	0	0
108	MT Sage KCl coated	1.11	1.74	0.56	0.05	0	0.48	0	0
109	CA Chamise coated	0.54	0.68	0.87	0.09	0	0	0	0
110	MT Sage	0.72	1.84	0.37	0.03	0	0.43	0	0.48
111	Rice Straw	0.98	0.83	0.32	0.05	0	0.24	0.06	0.54
112	NC Turkey Oak	0.33	1.01	0.37	0.04	0	0.23	0.01	0
113	NC Black Needle Rush and Salt Marsh Grass	4.73	3.19	2.06	0.06	0	0.49	0.1	0
114	LA Saw Grass	3.87	4.69	0.68	0.05	0	0.35	0.02	0
115	AK Duff Core	0.46	0.43	1.13	0.12	0	0	0	0
116	US Charcoal	-	-	0.41	0.08	0	0	0	0
117	Asian Charcoal	-	-	1.12	0.08	0	0	0.02	0
FLAME 2 chamber burns									
118	PP Needles	-	-	-	-	-	-	-	-
119	Longleaf Pine Needles and Wiregrass	-	-	-	-	-	-	-	-
120	Black Needle Rush	-	-	-	-	-	-	-	-
121	NC Hickory and Oak Leaves	-	-	-	-	-	-	-	-
122	MT Fir Needles & Branches (fresh)	-	-	-	-	-	-	-	-
123	MT Fir Needles & Branches (dry)	-	-	-	-	-	-	-	-
124	FL Palmetto Leaves (coastal)	0.93	0.16	0.11	0.01	0	0.12	0.18	0
125	MS Palmetto Leaves	0.72	0.12	0.03	0.01	0	0.05	0.15	0.1
126	Burn 119 continued overnight	-	-	-	-	-	-	-	-
127	Rice Straw	-	-	-	-	-	-	-	-
128	AK Duff Core	0.03	0.07	0.04	0.02	0.01	0.05	0.04	0.06
129	NC Rhododendron	0.08	0.08	0.03	0.01	0	0.04	0.02	0.02
130	AK Black Spruce	0.02	0.05	0.04	0.01	0	0.04	0.03	0.03
131	MT Fir Needles & Branches (dry- 50g)	-	-	-	-	-	-	-	-
132	AK Duff Core (40g)	0.02	0.09	0.09	0.03	0.01	0	0.07	0
133	FL Wiregrass	-	-	-	-	-	-	-	-
134	CA Chamise	-	-	-	-	-	-	-	-
135	FL Black Needlerush	-	-	-	-	-	-	-	-
136	MT Sage- Undiluted	-	-	-	-	-	-	-	-

ID	Filter name	Emission factors (g kg ⁻¹ dry fuel)							
		Cl ⁻	K ⁺	Na ⁺	Ca ²⁺	Mg ²⁺	SO ₄ ²⁻	NH ₄ ⁺	NO ₃ ⁻
137	MT Sage- Dilution #1	-	-	-	-	-	-	-	-
138	MT Sage- Dilution #2	-	-	-	-	-	-	-	-
139	MS Logleaf Pine Needles- Undiluted	1.27	0.28	0.14	0.04	0.01	0.14	0.21	0.06
140	MS Logleaf Pine Needles- Dilution #1	-	-	-	-	-	-	-	-
141	MS Logleaf Pine Needles- Dilution #2	-	-	-	-	-	-	-	-
142	MS Logleaf Pine Needles- Dilution #3 (overnight)	-	-	-	-	-	-	-	-
143	MS Gallberry	-	-	-	-	-	-	-	-
144	China Sugar Cane	-	-	-	-	-	-	-	-
145	AK White Spruce	0.31	0.16	0.08	0.02	0.01	0	0.08	0

Table A.3 Organic and elemental carbon concentrations and loadings on IMPROVE PM_{2.5} and high volume filter samples during the FLAME 1 and 2 chamber burns.

Fuel	IMPROVE PM _{2.5}							High volume			
	ID	Primary filters		Secondary filters				OC ($\mu\text{g m}^{-3}$)	OC ($\mu\text{g cm}^{-2}$)	EC ($\mu\text{g m}^{-3}$)	EC ($\mu\text{g cm}^{-2}$)
		OC ($\mu\text{g m}^{-3}$)	OC ($\mu\text{g cm}^{-2}$)	EC ($\mu\text{g m}^{-3}$)	EC ($\mu\text{g cm}^{-2}$)	OC ($\mu\text{g m}^{-3}$)	EC ($\mu\text{g m}^{-3}$)				
ponderosa pine	35	121.8	117.5	31.4	30.3	4.7	0.3	133.7	45.5	5	1.7
chamise	36	46.1	37.5	108.8	88.3	3.9	0	26.8	8.9	56.5	18.8
ponderosa pine	37	477.2	314.8	83	54.8	11.3	1.5	390.8	107.3	34.1	9.4
chamise	38	46.7	35.2	51	38.4	3.6	0	125.2	7	35.2	2
	39	-	-	-	-	-	-	-	-	-	-
rice straw	40	60.7	62.8	4.8	5	3.9	0.2	62.1	20.9	0	0
ponderosa duff	41	154.5	150.8	18.4	18	8.3	0.6	129.9	44.9	0	0
Alaskan duff	42	130.7	115.9	4.9	4.4	6.5	0.3	106.5	37.3	0	0
manzanita	43	38	35.5	56.9	53.2	3.7	0.2	43.6	13.5	47.9	14.9
juniper	44	28.9	26.5	160.4	146.7	4	0	36.3	13.3	142.6	52.4
sage/rabbitbrush	45	33.5	33.3	88.6	88.1	3.3	0.1	31.9	11.5	83	29.8
lignin	46	80	76.3	57.8	55.1	6.2	0.3	98.1	33.3	29.9	10.1
lodgepole pine	47	170.8	121.3	28.1	20	9	0.3	83.4	21.8	2.4	0.6
Puerto Rican fern	48	121.8	115.4	18.7	17.8	6	0.7	116.3	41.5	6.8	2.4
chamise	49	41.9	37.2	61.2	54.4	4.1	0.3	38.5	13.3	54.2	18.7
wax myrtle	50	96.7	90.9	47.6	44.7	4.8	0.6	107.7	37.1	10	3.4
longleaf pine	51	91.6	88.2	25.9	24.9	5	0.7	93	30	6.4	2.1
PR mixed woods	52	38.6	38.4	23	22.9	3.9	0.3	47.6	16.8	5.8	2
palmetto	53	60.3	58.4	27.1	26.3	3.3	0.1	61.5	20.9	17	5.8
ceanothus	54	162.3	148.1	11.1	10.2	6.6	0.3	110.6	35.8	4.1	1.3
longleaf											
pine/wiregrass	119	178.4	133.8	21.6	16.2	8.5	1.4	189.8	71.4	8.8	3.3
black needlerush	120	415.9	311.9	83.8	62.8	8.8	0.8	438.8	142.8	42.2	13.7
hickory/oak	121	89.6	73.4	11.2	9.2	11.8	0.8	115	41.7	10.5	3.8
Douglas fir (fresh)	122	49.8	3.1	31	2	16.7	0	57	19.3	27.5	9.3
Douglas fir (dry)	123	76	48.2	8.8	5.5	6.4	0.3	98.6	28.7	0.6	0.2
palmetto (coastal)	124	13.9	10.1	34.2	24.9	2.6	0	25.8	8.6	34.5	11.5
palmetto	125	23.4	17.9	19	14.5	3.8	0.1	40.6	13.8	13.5	4.6
palmetto overnight	126	-	-	-	-	-	-	-	-	-	-
rice straw	127	22.5	17.4	3.6	2.8	3.1	0	33.3	11.2	0.9	0.3
Alaskan duff	128	111	85.9	5.3	4.1	6.4	0.2	126.4	42.2	0.9	0.3
rhododendron	129	51.5	39.9	10.4	8.1	4.7	0.3	68.4	22.2	6.9	2.2
black spruce	130	46.7	36.2	33.4	25.9	4.6	0.2	77.3	24.5	24.1	7.6
Douglas fir	131	58.3	33.9	5	2.9	6.6	0.5	86.7	21.6	0	0
Alaskan duff (40 g)	132	79.5	44.1	2.3	1.3	6.5	0.2	95.9	23.3	0	0
Wiregrass	133	23.4	13.4	5.9	3.4	4.3	0	39.8	9.6	2.6	0.6
chamise	134	32.7	18.3	42	23.5	4.5	0	43.6	10.6	44	10.7
black needlerush	135	60.1	35.5	10.1	6	5.5	0.3	83.6	20.3	3.3	0.8
sagebrush	136	181.3	69.3	101.7	38.9	7.2	0	206	32.9	124.5	19.9
continued	137	-	-	-	-	-	-	-	-	-	-
continued	138	-	-	-	-	-	-	-	-	-	-
longleaf pine	139	744.2	289.9	41.6	16.2	15.8	0.7	722.6	118.5	15.4	2.5
continued	140	-	-	-	-	-	-	-	-	-	-
continued	141	-	-	-	-	-	-	-	-	-	-
continued	142	-	-	-	-	-	-	-	-	-	-
gallberry	143	37.8	21.6	45.5	26.1	5	0.2	52.4	12.7	51.9	12.6
sugar cane	144	20.8	11.4	6.8	3.7	2.5	0	32.6	8.1	3.8	1
white spruce	145	38.2	20.8	6.6	3.6	3.8	0	55.1	13.7	0	0